REPORT DOCUMENTATION PAGE

Form Approved
OMB No. 0704-0188

1. AGENCY USE ONLY *(Leave blank)*

2. REPORT DATE
May 23, 1996

3. REPORT TYPE AND DATES COVERED
FINAL TECHNICAL REPORT

4. TITLE AND SUBTITLE
Development of Regional Discriminants

5. FUNDING NUMBERS
AFOSR Grant:
F49620-93-1-0221

6. AUTHOR(S)
Donald V. Helmberger and David G. Harkrider

7. PERFORMING ORGANIZATION NAME(S) AND ADDRESS(ES)
California Institute of Technology
1201 East California Blvd.
Pasadena, CA 91125

AFOSR-TR-96
0309

9. SPONSORING/MONITORING AGENCY NAME(S) AND ADDRESS(ES)
AFOSR/NL
110 Duncan Avenue, Suite B115
Bolling AFB
Washington, DC 20332-0001

10. SPONSORING/MONITORING AGENCY REPORT NUMBER

11. SUPPLEMENTARY NOTES

12a. DISTRIBUTION/AVAILABILITY STATEMENT ...ic release, distribution unlimited

12b. DISTRIBUTION CODE

13. ABSTRACT *(Maximum 200 words)*

The research performed under the grant, during the period May 1, 1994 through December 15, 1995, can be divided into three main topics: (1) Regional source parameters, seismic energy, and discrimination; (2) Determining surface-wave magnitudes from regional Nevada Test Site data; and (3) Isotropic and deviatoric moment inversion of regional surface waves from Nevada test site explosions: implications for yield estimation and seismic discrimination.

19960624 252

14. SUBJECT TERMS
NTS, seismic energy, North America, nuclear explosions, surface waves, Rayleigh and Love waves, discrimination

15. NUMBER OF PAGES

16. PRICE CODE

17. SECURITY CLASSIFICATION OF REPORT	18. SECURITY CLASSIFICATION OF THIS PAGE	19. SECURITY CLASSIFICATION OF ABSTRACT	20. LIMITATION OF ABSTRACT
Unclassified			Unlimited

NSN 7540-01-280-5500

DTIC QUALITY INSPECTED 1

Standard Form 298 (Rev. 2-89)
Prescribed by ANSI Std 239-18
298-102

GENERAL INSTRUCTIONS FOR COMPLETING SF 298

The Report Documentation Page (RDP) is used in announcing and cataloging reports. It is important that this information be consistent with the rest of the report, particularly the cover and title page. Instructions for filling in each block of the form follow. It is important to ***stay within the lines*** to meet ***optical scanning requirements***.

Block 1. Agency Use Only *(Leave blank)*.

Block 2. Report Date. Full publication date including day, month, and year, if available (e.g. 1 Jan 88). Must cite at least the year.

Block 3. Type of Report and Dates Covered. State whether report is interim, final, etc. If applicable, enter inclusive report dates (e.g. 10 Jun 87 - 30 Jun 88).

Block 4. Title and Subtitle. A title is taken from the part of the report that provides the most meaningful and complete information. When a report is prepared in more than one volume, repeat the primary title, add volume number, and include subtitle for the specific volume. On classified documents enter the title classification in parentheses.

Block 5. Funding Numbers. To include contract and grant numbers; may include program element number(s), project number(s), task number(s), and work unit number(s). Use the following labels:

C	- Contract	**PR**	- Project
G	- Grant	**TA**	- Task
PE	- Program Element	**WU**	- Work Unit Accession No.

Block 6. Author(s). Name(s) of person(s) responsible for writing the report, performing the research, or credited with the content of the report. If editor or compiler, this should follow the name(s).

Block 7. Performing Organization Name(s) and Address(es). Self-explanatory.

Block 8. Performing Organization Report Number. Enter the unique alphanumeric report number(s) assigned by the organization performing the report.

Block 9. Sponsoring/Monitoring Agency Name(s) and Address(es). Self-explanatory.

Block 10. Sponsoring/Monitoring Agency Report Number. *(If known)*

Block 11. Supplementary Notes. Enter information not included elsewhere such as: Prepared in cooperation with...; Trans. of...; To be published in.... When a report is revised, include a statement whether the new report supersedes or supplements the older report.

Block 12a. Distribution/Availability Statement. Denotes public availability or limitations. Cite any availability to the public. Enter additional limitations or special markings in all capitals (e.g. NOFORN, REL, ITAR).

DOD - See DoDD 5230.24, "Distribution Statements on Technical Documents."
DOE - See authorities.
NASA - See Handbook NHB 2200.2.
NTIS - Leave blank.

Block 12b. Distribution Code.

DOD - Leave blank.
DOE - Enter DOE distribution categories from the Standard Distribution for Unclassified Scientific and Technical Reports.
NASA - Leave blank.
NTIS - Leave blank.

Block 13. Abstract. Include a brief *(Maximum 200 words)* factual summary of the most significant information contained in the report.

Block 14. Subject Terms. Keywords or phrases identifying major subjects in the report.

Block 15. Number of Pages. Enter the total number of pages.

Block 16. Price Code. Enter appropriate price code *(NTIS only)*.

Blocks 17. - 19. Security Classifications. Self-explanatory. Enter U.S. Security Classification in accordance with U.S. Security Regulations (i.e., UNCLASSIFIED). If form contains classified information, stamp classification on the top and bottom of the page.

Block 20. Limitation of Abstract. This block must be completed to assign a limitation to the abstract. Enter either UL (unlimited) or SAR (same as report). An entry in this block is necessary if the abstract is to be limited. If blank, the abstract is assumed to be unlimited.

DISCLAIMER NOTICE

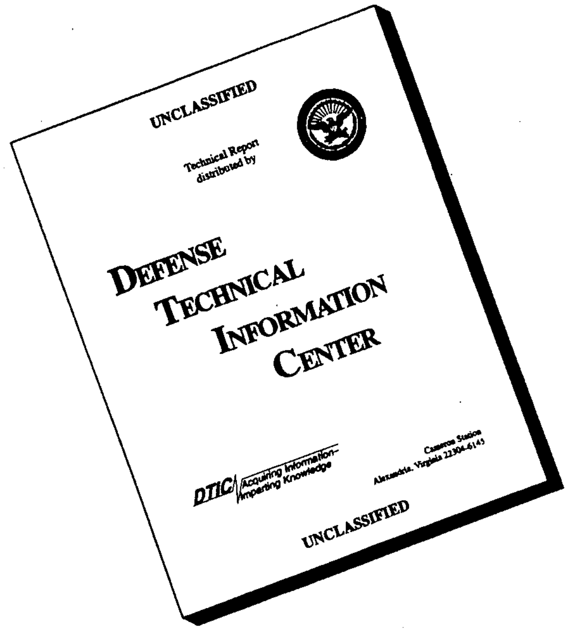

THIS DOCUMENT IS BEST QUALITY AVAILABLE. THE COPY FURNISHED TO DTIC CONTAINED A SIGNIFICANT NUMBER OF PAGES WHICH DO NOT REPRODUCE LEGIBLY.

Final Technical Report
May 1, 1994 - December 15, 1995

Name of Contractor:	California Institute of Technology
Effective Date of Contract:	1 May 1993
Contract Expiration Date:	15 December 1995
Contract Number:	F49620-93-~~J~~ I-0221
Principal Investigators:	Donald V. Helmberger (818) 395-6998 David G. Harkrider (818) 395-6910
Program Manager:	Dr. Stanley K. Dickinson Code NL
Title of Work:	Development of Regional Discriminants

Sponsored by

AFOSR/NL
110 Duncan Avenue, Suite B115
Bolling AFB
Washington, DC 20332-0001
Contract No. F49620-93-J-0221

Seismological Laboratory 252-21
Division of Geological and Planetary Sciences
California Institute of Technology
Pasadena, California 91125

Table of Contents

Summary

Regional Source Parameters, Seismic Energy, and Discrimination

Determining Surface-Wave Magnitudes from Regional Nevada Test Site Data

Isotropic and Deviatoric Moment Inversion of Regional Surface Waves from Nevada Test Site Explosions: Implications for Yield Estimation and Seismic Discrimination

Summary

The research performed under the grant, during the period 1 May 1994 through 30 April 1995, can be divided into three main topics; (1) regional source parameters, seismic energy, and discrimination, (2) determining surface-wave magnitudes from regional Nevada Test Site data, and (3) isotopic and deviatoric moment inversion of regional surface waves from Nevada Test Site explosions: implications for yield estimation and seismic discrimination.

In section 1, we have examined broadband waveforms from a large number of NTS explosions and earthquakes throughout the southwestern United States in order to characterize seismic sources. Explosions were found to be richer in coda energy than earthquakes. Most earthquakes show relatively little long-period (T>4 sec) coda energy and tend to be richer in long-period and shear-wave energy than explosions. We have developed several seismic discriminants based on these observations and our modeling experience. One promising discrimant is the ratio of short-period vertical component, P-wavetrain energy, to long-period surface wave energy, averaged over three components. Explosions tend to have a higher ratio than do earthquakes, essentially an extension of M_b:M_S. Magnitude threshold for this discriminant is about 3.5. Another useful discriminant is based on the total broadband energy to moment ratio where explosions are distinguished by their stronger energy levels relative to their long-period amplitudes. This approach requires Green's functions, a source estimator program, and processes all events as earthquakes. For this method to be effective requires the calibration of the region using relatively large earthquakes, M>5, but does not require calibrations of explosions.

In section 2, we re-examine the use of surface-wave magnitudes to determine the yield of underground nuclear explosions and the associated magnitude-yield scaling relationship. We have calculated surface-wave magnitudes for 190 Nevada Test Site (NTS) shots using regional long-period seismograms from a combined super-network of 55 north American stations. Great effort went towards making the data set comprehensive and diverse in terms of yield, source location and shot medium in order to determine the portability of surface-wave magnitude scales. In particular, we examine Pahute Mesa, Rainier Mesa and Yucca Flat explosions detonated above and below the water table, and which range over three orders of magnitude in yield. By observation we find a low-yield measure threshold of approximately one kiloton (kt) for (assumedly) moderately well-coupled explosions recorded at near-regional (<500 km) stations, which have little microseismic noise. In order to utilize regional surface waves (Δ<15 °) for quantifying sources and for discrimination purposes, we have developed related methods for determining time-domain surface-wave magnitudes and scalar moments from regional Rayleigh waves. Employing regional surface-wave data lowers the effective magnitude threshold. One technique employs synthetic seismograms to establish a relationship between the amplitude of the regional Airy phase, or Rayleigh pulse of the Rayleigh wavetrain and an associated surface-wave magnitude, based on conventional M_S determinations, calculated from synthetic seismograms propagated to 40°. The other method uses synthetic seismograms in a similar fashion, but the relationship used is a more straightforward one between scalar moment and peak Rayleigh wave amplitude. Path corrections are readily implemented to both methods. The inclusion of path corrections decreases the M_S variance by a factor of two and affects the absolute scaling relationship by up to a factor of 0.1 magnitude units. This latter effect is attributed to the particular station network used and the Green's functions used to obtain the 40° M_S values. Using a generic structure for the distance traveled past the actual source-receiver path minimizes the difference between magnitudes determined with and without path

corrections. The method gives stable M_S values that correlate well with other magnitude scale values over a range of three orders of magnitude in source yield. Our M_S value scale very similarly to more standard teleseismic M_S values from other studies, although the absolute M_S values vary by ±0.5 magnitude units about ours. Such differences are due in part to the choice of M_S formula used. For purposes of future user comparisons, we give conversion values to the previous studies. Our most refined M_S values give the relationship $M_S = 1.00 \times \log_{10}$ (yield) + B, where B is dependent upon source region and shot medium. This yield exponent of unity holds for events of all sizes and is in line with M_S-yield scaling relations found by other studies. When events are grouped with respect to source region, significantly better fits to these individual-site linear-regression curves are obtained compared to the fits obtained using a single, all-inclusive model. This observation implies that shot-site parameters and source structure can significantly affect surface-wave-magnitude measurements. We present these M_S values primarily to augment the extensive historical analysis of explosion data based on surface-wave magnitudes by using regional data to increase the number of events with surface-wave magnitudes. These magnitudes are consistent with the teleseismically determined magnitudes of larger events.

In section 3, seismic moments of Nevada Test Site (NTS) explosions are determined from regional surface wave spectra. Two methods are used. In one the moment is solved for assuming only an explosive source, or average scalar moment; in the other a joint inversion for an isotropic (explosive) source plus a constrained double couple moment component representing tectonic strain release. Although the general moment tensor solution to this joint inversion problem is non-unique, if some assumptions are made concerning the non-isotropic moment components, then the remaining source parameters can be solved by a linear least-squares inversion scheme. We examine the errors in determining the isotropic moment component (M_I) by this latter method of constrained linear inversion solutions in a canonical study using a theoretical network of long-period (6-60 sec.) surface wave data. The network azimuthal coverage was chosen to represent that of a long-period North American super-network of 55 stations used for the actual NTS events. We compare these errors in moment estimate to those obtained from surface wave magnitude (M_S) measurements for the same surface wave observations. For a ratio of $M_{(expl)}/M_{(eq)}$ less than 1.0 we find that the inverted M_I solution is a much better estimate of the actual isotropic moment than either M_S or M_O, and the standard deviation in this estimate is substantially less than that using the other two methods for the great majority of isotropic source + double couple sources. Even when the inversion constraints are off in dip and rake each by 30°, the mis-estimate of the isotropic moment is less than 35 percent of the actual value. In the case of a vertical strike-slip fault, the inverted isotropic moment solution which assumes this fault orientation is exact to three figures, whereas M_S and M_O under-estimate the moment by 45 percent and 32 percent, respectively because of uneven azimuthal coverage. This moment tensor inversion method is applied to determine the isotropic source for 109 NTS underground explosions using vertical and tangential component surface wave data from this regional network. We also calculate M_S and M_O for these same events and compare the results. Isotropic source errors are smallest using the spectral domain inversion method. However, this spectral domain method cannot attain as low a magnitude threshold as the time domain moment or M_S method. The extensive moment data set analyzed here were combined with larger yield explosions from prior moment studies to create a comprehensive data set with which to obtain conclusive, well-constrained long-period explosion source scaling relationships at the separate NTS sub-sites.

SECTION 1

Regional Source Parameters, Seismic Energy, and Discrimination

REGIONAL SOURCE PARAMETERS, SEISMIC ENERGY, AND DISCRIMINATION

DON V. HELMBERGER
Seismological Laboratory 252-21
California Institute of Technology
Pasadena, CA 91125

and

BRAD WOODS
Woodward Clyde Consultants
566 El Dorado Street, Suite 100
Pasadena, CA 91101

1. Abstract

We have examined broadband waveforms from a large number of NTS explosions and earthquakes throughout the southwestern United States in order to characterize seismic sources. Explosions were found to be richer in coda energy than earthquakes. Most earthquakes show relatively little long-period (T>4 sec) coda energy and tend to be richer in long-period and shear-wave energy than explosions. We have developed several seismic discriminants based on these observations and our modeling experience. One promising discriminant is the ratio of short-period vertical component, P-wavetrain energy, to long-period surface wave energy, averaged over three components. Explosions tend to have a higher ratio than do earthquakes, essentially an extension of m_b:M_S. Magnitude threshold for this discriminant is about 3.5. Another useful discriminant is based on the total broadband energy to moment ratio where explosions are distinguished by their stronger energy levels relative to their long-period amplitudes. This approach requires Green's functions, a source estimator program, and processes all events as earthquakes. For this method to be effective requires the calibration of the region using relatively large earthquakes, M>5, but does not require calibrations of explosions.

2. Introduction

A number of broadband arrays have been introduced in recent years. One such array, TERRAscope, is presently being installed in southern California, see figure 1. These stations are a part of the global IRIS (International Research Institution for Seismology) network. Presumably the IRIS network, in conjunction with short-period arrays, will provide some of the essential data necessary for worldwide monitoring of seismic activity. Unfortunately, station spacing in remote areas is rather sparse. Thus, we may have

E.S. Husebye and A.M. Dainty (eds.), Monitoring a Comprehensive Test Ban Treaty, 365-383.

to rely on a single station to characterize events and to distinguish an explosion from an earthquake. This task will be difficult, but may be possible in regions that have an abundance of earthquakes that can be used to calibrate regional paths. We envision an environment not unlike that of western United States and thus we can use the population of NTS events and the natural seismicity to construct and test such a methodology. Before discussing regional calibration and the development of energy discrimination techniques, we will first briefly review the observational differences between explosions and earthquakes.

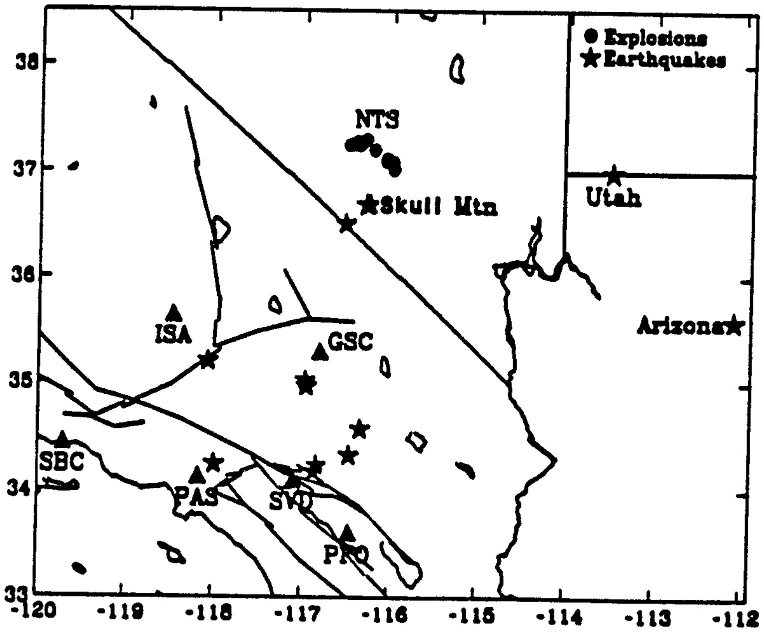

Figure 1. Map of southwestern United States displaying the locations of a number of recent earthquakes and NTS explosions; also included is the TERRAscope array as existed in early 1993.

Most of the useful regional discriminants for populations of explosions and earthquakes in this region have been discussed by Taylor et al., (1989). Their results suggest that m_b:M_s works very well for well-calibrated paths but they had difficulty in determining M_s for explosions smaller than about m_b=4. In contrast, they report M_s for earthquakes with m_b's as small as 2.5. The characteristics of events as described above are quite compatible with TERRAscope observations, as displayed in figure 2, where seismograms of the Kearsarge explosion (m_b=5.6) is compared with the Skull Mountain earthquake (m_b=5.7). Simulations of the broadband data appropriate for various instruments are included since this type of data is normally used in defining m_b and M_L (WASP), and M_s(LP). Note that the ratio of peak short-period to long-period amplitudes (averaged over the components) is an order of magnitude larger for the explosion. Because the paths are nearly identical, this difference must be caused either by the source excitation and/or epicenter depth. Thus, it appears that m_b:M_s can be extended to small events if the Rayleigh waves can be detected.

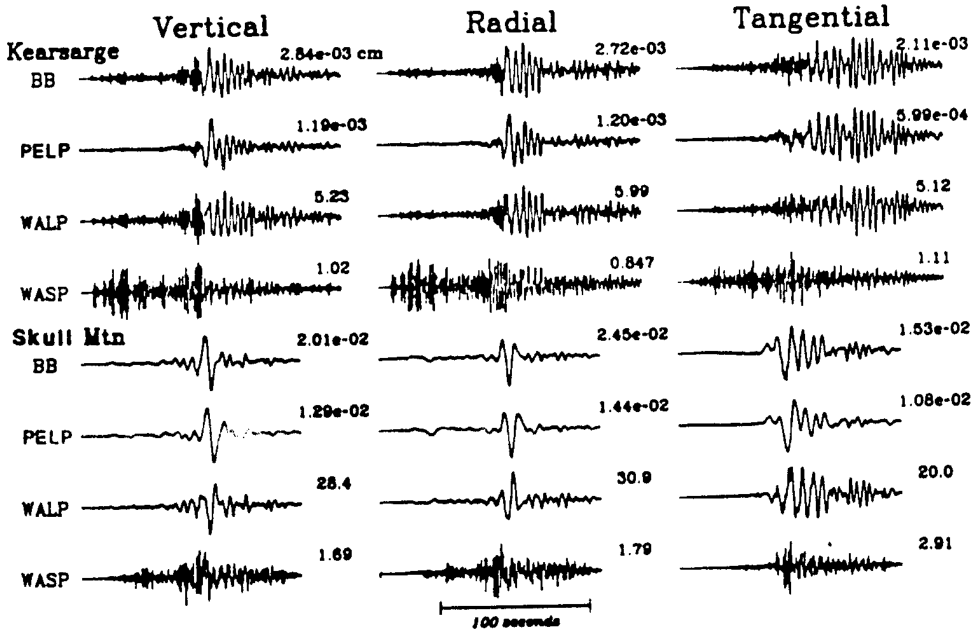

Figure 2. Comparison of the broadband observations and assorted simulated instrumental responses of a 150 kt NTS explosion (JVE) and a recent earthquake at Skull Mountain as recorded at PAS (Δ=350 km). Note that the paths are nearly identical but the motions are quite distinct.

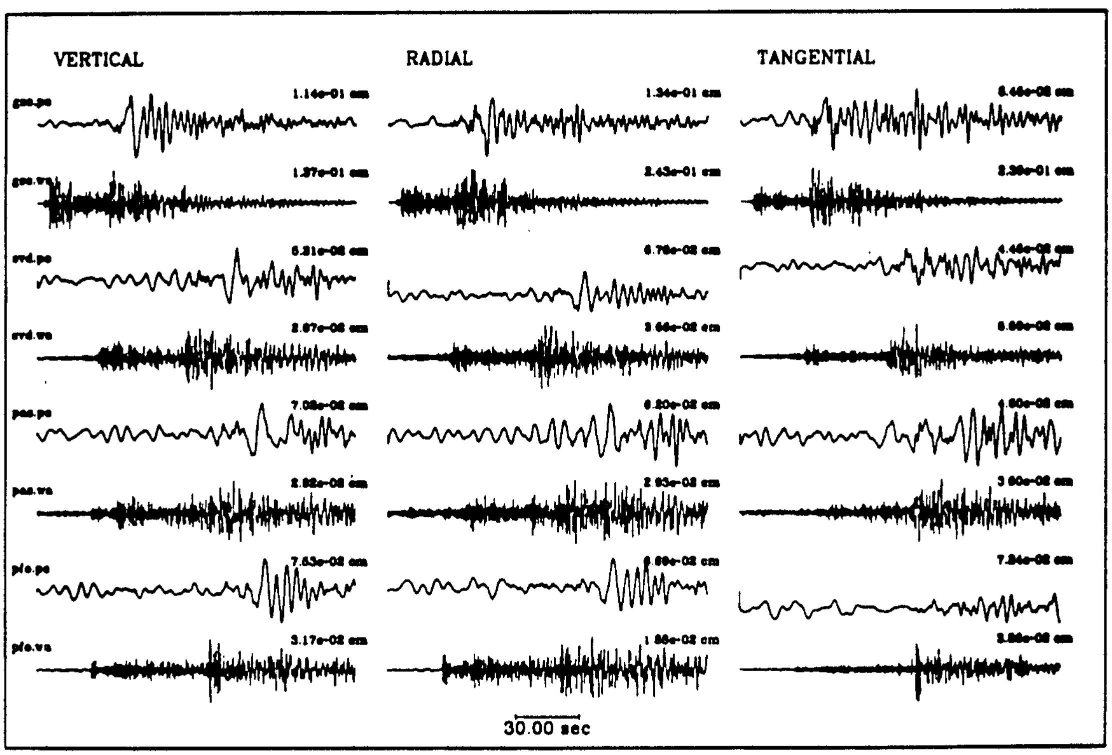

Figure 3. A small Yucca Flat explosion, Floydada (M_L=4.0), recorded at TERRAscope stations and simulated Press-Ewing (long-period) and Wood-Anderson (short-period), after Woods et al. (1993).

In figure 3, we display the TERRAscope data from a small NTS explosion where the Rayleigh waves are quite apparent even at long-periods. Note that the surface wave amplitudes indicate that these signals would not be discernible on the actual analog instruments. M_L for this event is 4.0 and its log moment is 14.20, Woods et al., (1993). Assuming it is a shallow explosion above the water table, the yield can be inferred to be less than 10 kt from the moment-yield scaling relationships determined for NTS by Woods and Harkrider (1994). Were it detonated in hard rock below the water table it would correspond to a two kiloton explosion. We estimate that were this event 2.5 times lower in yield, it would still be possible to obtain its moment, yielding a magnitude threshold of about 3.5. These observations are quite typical of small NTS events where only the fundamental Rayleigh wave Airy phase is detectable and reasonably predictable across the array.

Thus, it appears that regional seismograms from explosions are indeed higher frequency than earthquakes with comparable Rayleigh wave excitation. This feature is explored by Patton and Walter (1993), in a study of well-calibrated m_b:Ms and the m_b:M_o discriminants. Their results produced a clear separation as does the M_L:M_o discriminant proposed by Woods et al., (1993). The latter results are displayed in figure 4. Note there is a significant separation of earthquakes and explosions with no real overlap over all scales. However, many of the M_o's for these explosions were determined by assuming shallow isotropic excitation (Woods et al., 1993), and thus while this approach demonstrates that the high-frequency vs. low-frequency source characterizations remain valid to small magnitudes, it may have limited usefulness as a direct discriminant.

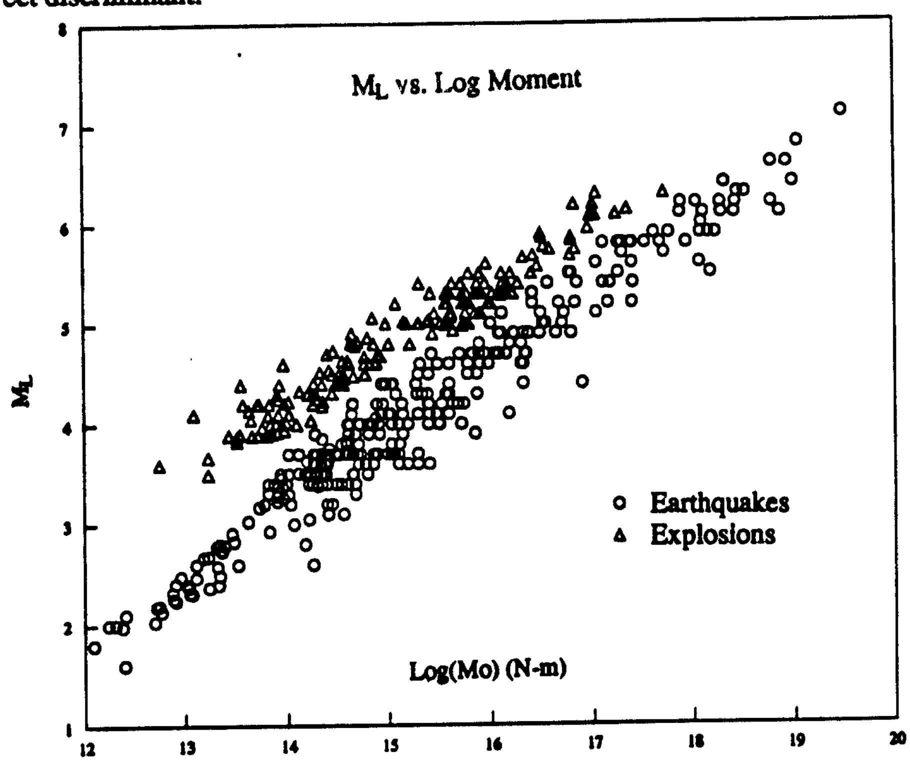

Figure 4. Plot of M_L vs. M_o for a population of explosions and earthquakes, after Woods et al. (1993).

Another difficulty with the M_L:M_0 discriminant is in the development of a physical basis. While the M_L measure is easily simulated for earthquakes it proves problematical for explosions. For example, in examining figures 2 and 3, we find that the peak short-period amplitude usually occurs on the tangential component. This is difficult to explain with the conventional symmetric RDP (Reduced Displacement Potential) formalism and require some type of mode conversion. Presumably, the large amount of local Rayleigh wave energy released by the source into the slow-velocity source region gets scattered into the crustal wave guide (e.g., Stead and Helmberger, 1988). We find the broadband (BB) records from earthquakes occurring in the normal seismogenic depths of 4 to 15 kms to be relatively simple as displayed in figure 2. Thus, we will explore the possibility of using the ratio of accumulated energy to surface wave magnitude or M_0 as a discriminant.

To pursue this approach we will assume all events are earthquakes with respect to estimating source parameters. Explosions are then distinguished by their excess short-period energy. However, to obtain meaningful estimates of source parameters from regional waveforms does require a crustal model and useful Green's functions. These can be obtained by modeling moderate sized earthquakes.

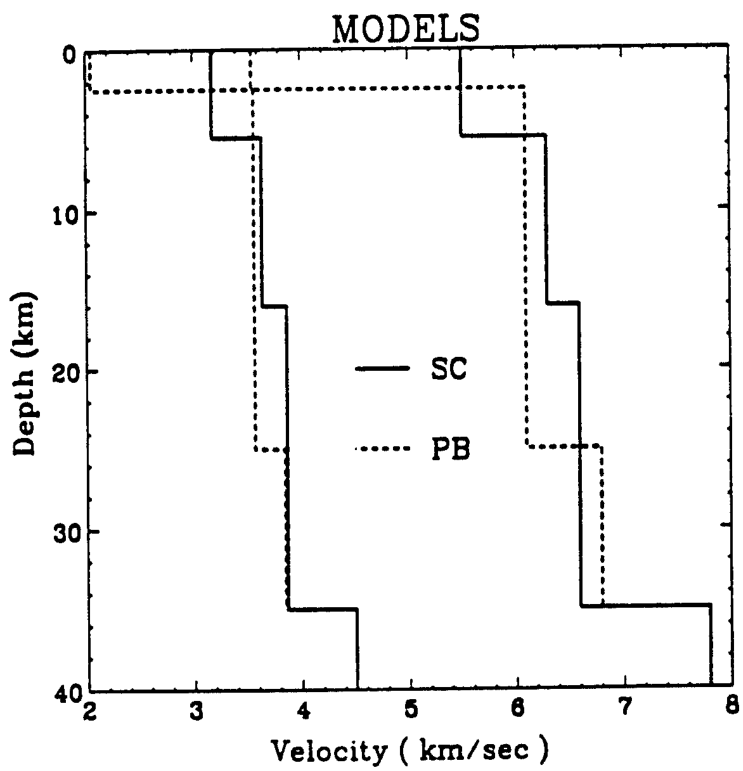

Figure 5. Display of velocity vs. depth models for a southern California model (SC) and a basin-and-range model (PB).

3. Estimation Of Earthquake Parameters

Essentially, three new methods have been developed to take advantage of the new instrumentation: the CMT (Centroid Moment Tensor) solution at long-periods (Ritsema and Lay, 1993), inversion of long-period body waveforms (Dreger and Helmberger, 1993), and a broadband cut and paste method by Zhao and Helmberger (1994).

For events larger than $M_W>5$, it is possible to invert surface wave records for periods greater than 50 seconds assuming the PREM model (Dziewonski and Anderson, 1981) by employing a CMT procedure. At shorter periods the surface waves show regional variation, and corresponding regionalized models are required (see for example, Patton and Zandt, 1991; Thio and Kanamori, 1992).

The second method uses the relative strengths of the observed bodywaves compared with synthetics to determine mechanisms, moment, and depth. Often, only one station is sufficient to fix the source parameters, since S (SV and SH) and sS (SV and SH) are strongly dependent upon source orientation. Cycling through source depths the proper timing between P and pP, S and sS, etc. allows accurate depth estimates. This approach works best at periods greater than a few seconds and therefore we usually work with long-period bandpassed records. The Southern California model (SC), Dreger and Helmberger (1991), displayed in figure 5 works well in terms of waveform matching throughout the entire region, as reported by Dreger and Helmberger (1993).

The third approach uses a direct grid search for the fault parameters (strike (θ), dip (δ), rake (λ)). This method matches complete broadband observed seismograms against synthetics over discrete phases so that timing shifts between particular wave groups are allowed. That is, in matching a synthetic seismogram to the observed record, we may allow the Rayleigh wave to be shifted relative to the P_{nl} wavetrain. This allows a better correlation, thus the name cut-and-paste method. This feature desensitizes the effect of the crustal model used in generating the synthetics and allows stable estimates of the source parameters with imperfect Green's functions. We demonstrate this conclusion by generating fault parameters for a number of regional events using two strongly contrasting crustal models, the SC model and a basin and range model (PB) by Priestley and Brune (1978), displayed in figure 5. The source parameter determinations are given in Table 1 for three large events in the region: the Utah event, the Little Skull Mountain event, and the Arizona event. Paths connecting these events to the TERRAscope stations provide a good sample of the propagational features of the region, see figure 1.

A comparison of the waveform fits assuming the PB model is displayed in figures 6 and 7. The numbers above each trace indicates the peak amplitude and the moment estimate comes from a least square fit where the individual amplitude comparison indicates the relative contribution of that trace to the average moment. The relative shifts of the various phases is discussed in Zhao and Helmberger (1994).

4. Estimation of Seismic Energy and Discriminants

With the advent of broadband instrumentation, it is possible to make some useful estimates of the energy levels of sources. This is especially attractive at local and regional distances before the strong attenuation of the upper mantle has stripped away the higher frequencies. However, we must be able to correct for the strong propagational effects produced by the crust before obtaining accurate energy estimates.

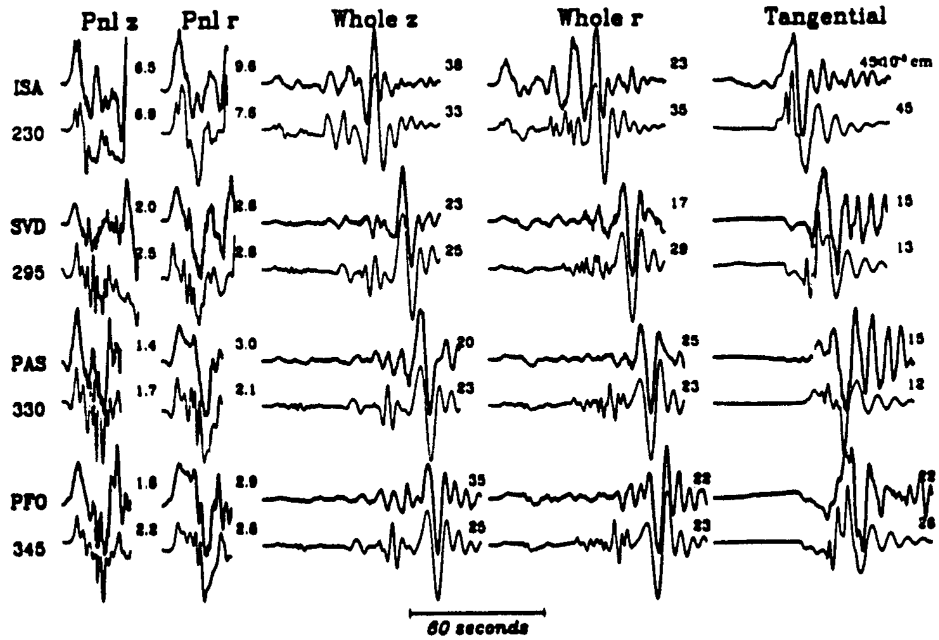

Figure 6. Comparison of broadband observations (Utah event) and corresponding synthetics (PB) as determined in obtaining the best fitting mechanism. The numbers indicate the peak amplitudes in cm. The numbers below the stations indicate the distance from that station to the event in kms.

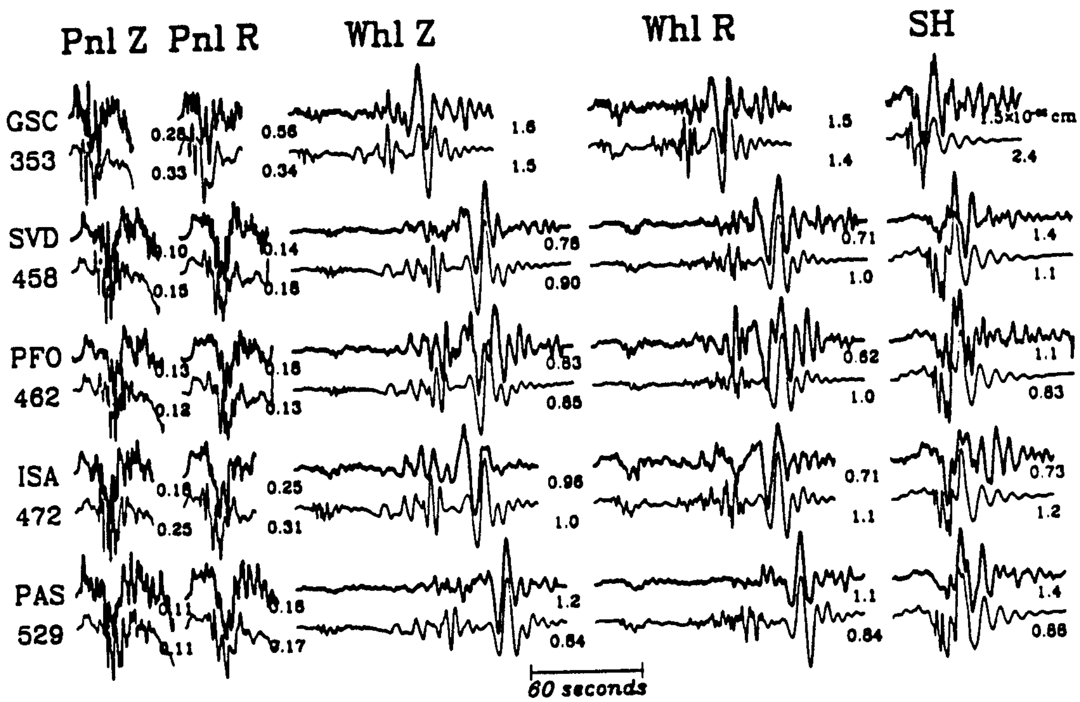

Figure 7. Comparison of synthetics vs. observations for the Utah event where the time history has been adjusted such that the energy ratio between the synthetic (WASP/LP) in the Pnl window is equal to that observed as averaged over the 5 stations.

We proceed by making some useful definitions in terms of a source time history needed to make definitive broadband moment estimates. Because energy depends on velocity, we must be careful in defining the time history, especially at the highest frequency. The approach followed here is to base this estimate on the P_{nl} window which we think is the least contaminated by the complex surface layer. Since the WASP records are difficult to match in waveform, we choose to base the time history on that triangle, δt_i, which best predicts the energy ratio of synthetic (WASP/LP) to that of the observations. The broadband moment (M_B) is defined as the best fitting synthetic to the observed data assuming this time history with the orientation parameters determined by the long-period fit.

In the same fashion as M_B we define the energy moment, M_E, to be the ratio of the total integrated broadband energy (3 components) divided by the corresponding integrated Green's functions. To be more specific we will write down the explicit expressions for the tangential component, we define

$$M = V_{obs}(t) / V_g(t) \tag{1}$$

where
M = moment
V_g (t) = synthetic for a particular far-field source history, $\dot{D}$ (t)
V_{obs} (t) = observed record
We define M= M_o when these amplitude comparisons are performed at long-periods, and M_B when performed with the $\dot{D}(t)$ fixed by the (SPZ/LP) ratio. The energy strength is defined by

$$M_E = \left[\int_o^T \dot{V}_{obs}^2 \ (t)dt \ / \ \int_o^T \dot{V}_g^2 \ (t)dt \right]^{1/2} \tag{2}$$

where T is the length of the records. This same procedure is applied to all components and averaged to define the M's for a particular event. If the synthetics fit the observed data exactly, we would obtain M_E equal to M_B or a ratio (M_E/M_B) of 1.

Applying this formalism to the Little Skull Mountain main event we obtain broadband fits nearly identical to those in figure 6. We obtain a time history given by δt_i = 0.3 secs. The corresponding short-period comparisons of synthetics with observations are displayed in figure 8. These comparisons are quite good and are typical of results from other events, see Zhao and Helmberger (1994).

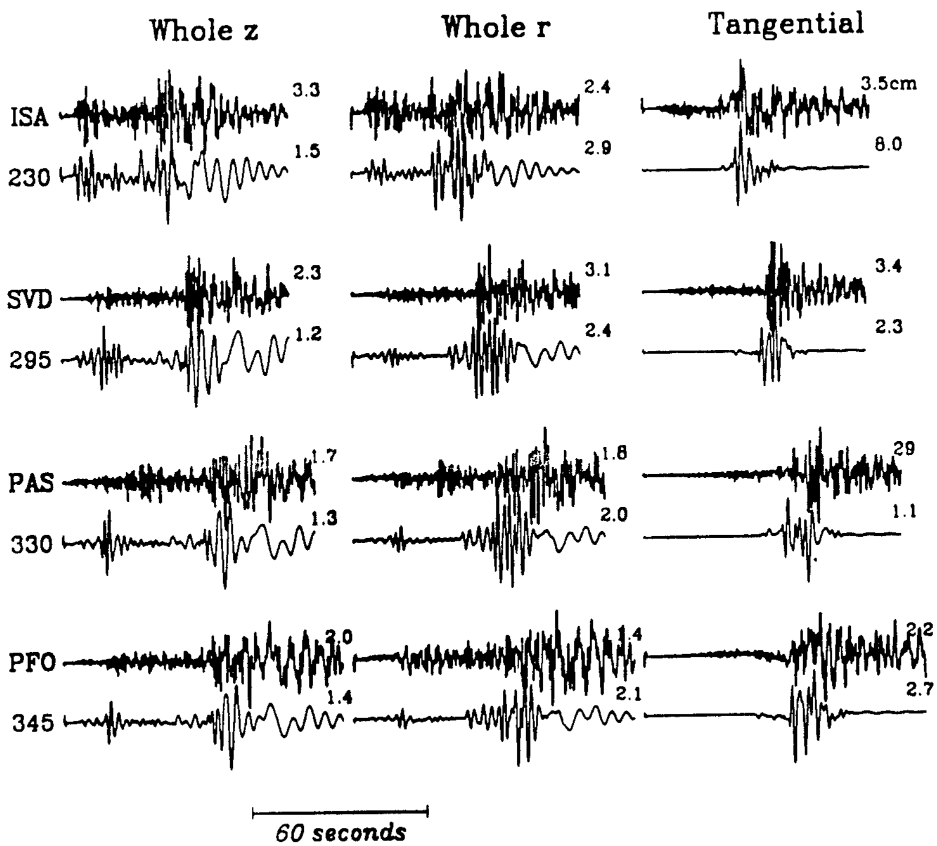

Figure 8. Comparison of predicted short-period synthetics vs. observations for the Utah event assuming the broadband time history.

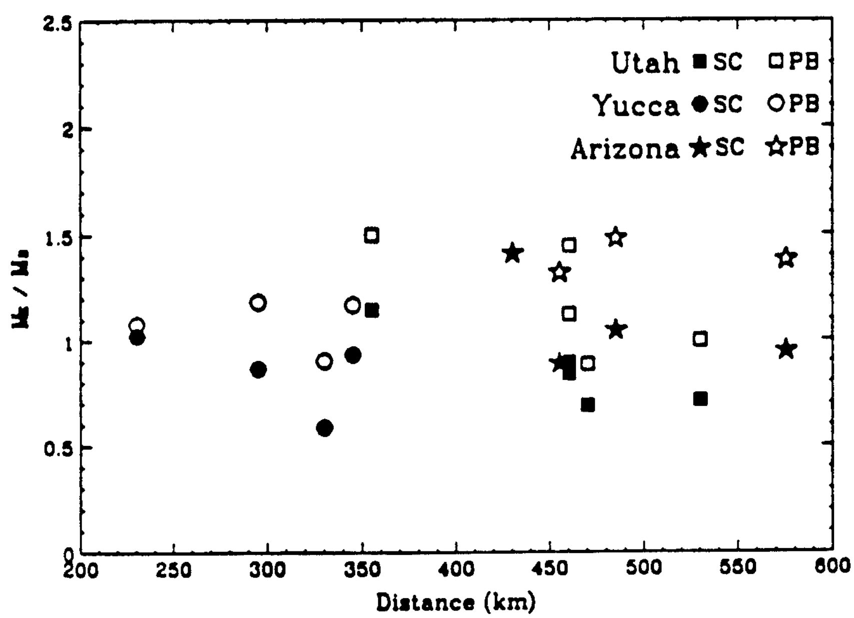

Figure 9. Plot of accumulated energy for all three components (broadband) vs. distance for the three calibration events.

We do not want definitions of source properties such as moment and energy to depend on the range or receiver. Thus, we can check the usefulness of our definitions by plotting (M_E/M_B) as a function of distance and model as in figure 9. Most of the points fall between .5 and 1.5. This plot shows no obvious distance dependence suggesting that our path corrections are adequate. However, there is a slight baseline shift with the PB model yielding slightly higher values. But in general, the various moments and source parameter appear to be quite independent of model if we treat deep sources, i.e., d>5 km. Note that the more detailed the upper portion of the model becomes, the more likely it will become path dependent. If we want to use the same model for a large region, we want to keep the model simple and restrict the source depths accordingly.

With this brief review of source estimation, we return to the observations displayed in figure 2. If we simply compare the top-traces, we see that while the peak short-period (SP) amplitudes are similar, the long-period outputs are an order-of-magnitude different. This comparison is typical (Woods et al., 1993). Also, note that the explosion data contains many more arrivals or energy than do the earthquake traces. Therefore, if we simply compare the ratio of (M_E/M_B), we should distinguish the two types of events. But to do this, we must first obtain estimates of M_O, M_B, and M_E from explosions. We do this by assuming all events are earthquakes or double-couple's. An example calculation is given in figure 10.

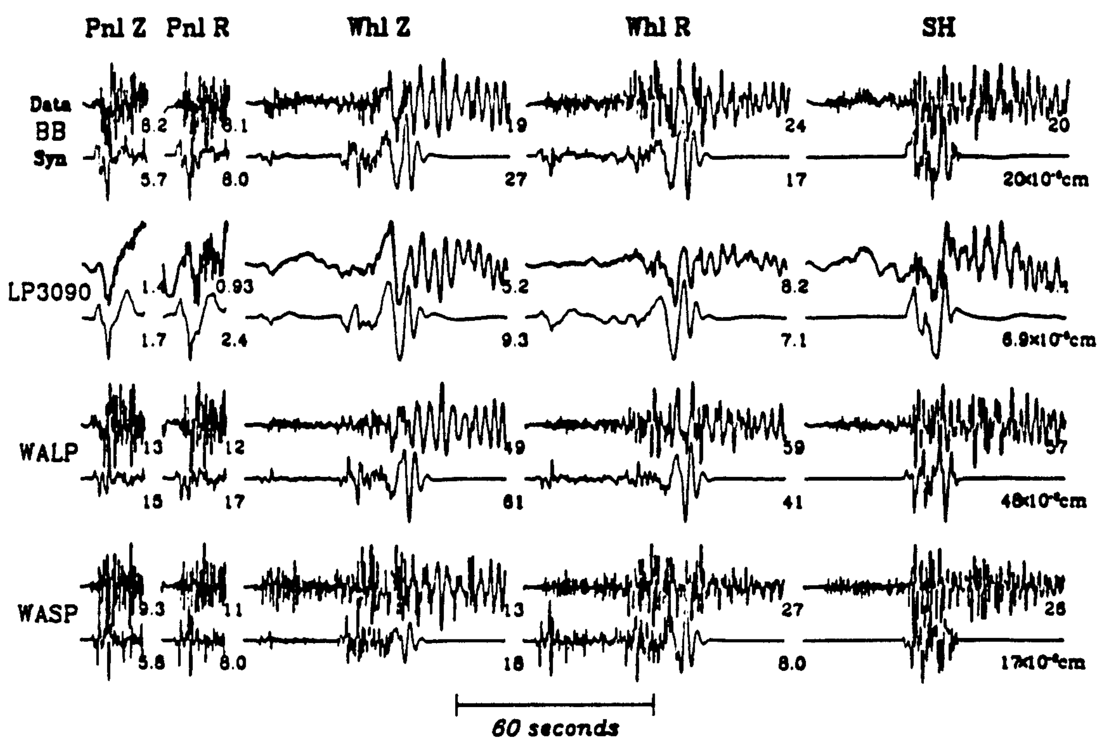

Figure 10. Comparison of data (small explosion) with synthetics (assumed to be double-couple). In this case the code found essentially a strike-slip solution. The depth of 5 km was determined by the best fitting solution. Note that there are many more scattered arrivals in the data that are not in the nature earthquake.

In this match of synthetics to observations, we have used the (WASP/WALP) ratio to fit the time history because of the noise in the LP bandpass. A value of (.1,.1) triangle was obtained. While the short-period details are not well explained, the overall estimate of long-period waveform fits is reasonable. We obtain a moment of 1.1 x 10^{22} dyne-cm and a source orientation of (220°, 30°, 115°) for strike, dip, and rake. The source depth search preferred the depth of 5 km which is the shallowest depth allowed. Woods et al., (1993) obtained a M_O = 3 x 10^{21} dyne-cm for this event or about 4 times smaller than the above estimate. This difference is expected because of the relative strengths of Rayleigh wave Green's functions for two reasons. First, since the excitation of Rayleigh waves per unit of moment is stronger at the shallower depth, we can understand why a larger moment is needed to fit the data assuming a depth of 5 km. Second, since the radiation pattern for an earthquake is always less than for an explosion, we again require an increased moment to compensate. The M_B moment is obtained by matching the amplitudes in the upper two plots yielding .5 x 10^{22} dyne-cm, which is lower than M_O. This is caused by the short-period spikes riding on top of the observed Rayleigh waves; something which does not occur in the synthetics but holds true for most observations of explosions. Thus, the M_B measure from explosions is not a very good measure of source strength since it appears to be affected by these short-period spikes. The M_E measure is also strongly affected by these spikes and decreased accordingly. However, the extra arrivals occurring in the observations increase M_E, yielding M_E = 1.2 x 10^{22} dyne-cm or a ratio of M_E/M_B = 2.3. Earthquakes yield values near unity as discussed above, thus it is an effective depth discriminant.

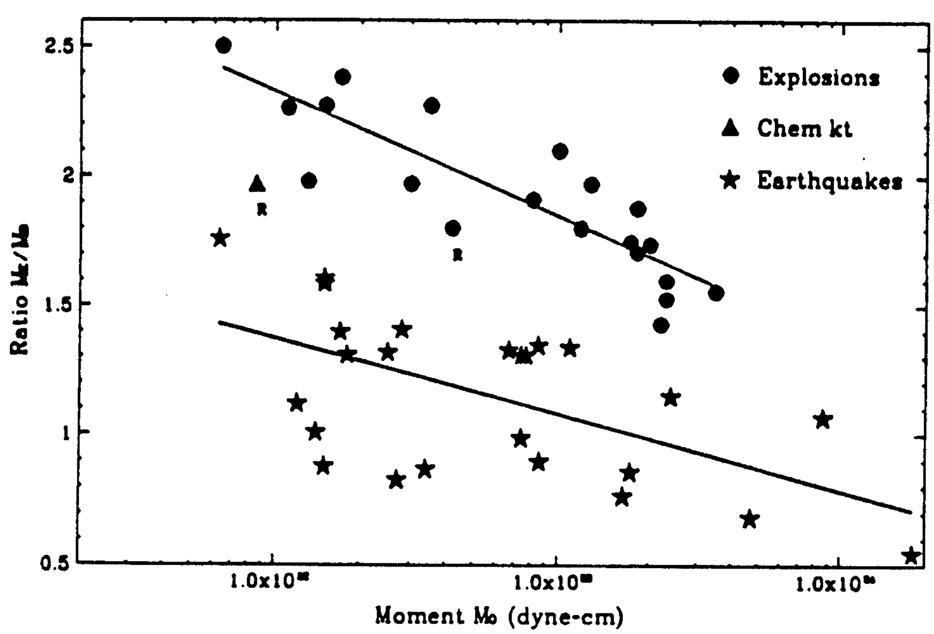

Figure 11. Plot of (M_E/M_B) vs. M_O for a small population of earthquakes and NTS explosions displaying good separation.

Figure 11 shows the results for NTS explosions and southwestern U. S. earthquakes. Each point represents one event. The chemical NPE (non-proliferation explosion) also has been added to the data set. This event and a normal Rainier shot (denoted with an "R") lie at the lower limit of the explosion population, but they are still separated from the earthquake population.

A more empirical approach is to use the short-period:long-period (SP:LP) ratio. The source properties that we want to quantify are the short-period (1 Hz) P-wave and long-period (0.14 to 0.05 Hz) surface wave energy levels, the ratio of which is used as the discrimination criterion. The short-period bandpass is the same used to measure teleseismic P-wave amplitudes for the m_b:M_s discriminant. The long-period bandpass represents the predominant frequency range of the fundamental-mode Airy Phase at regional distances (Alewine, 1972). This short-period vs. long-period energy ratio ($E_{SP:LP}$) is defined as:

$$E_{SP:LP} = \frac{\int_{t_{P_n}}^{t_{S_n}} \upsilon_{sp}\ (t)^2\, dt}{\sum_{i=1}^{3} \int_{t_1}^{t_2} \upsilon_{lp}(t)^2\, dt}, \qquad (3)$$

with the summation being for the three components and t_i representing the windowing times determined from travel path length and the wave train of interest; t_{pn} corresponds to the time before the onset of the P-wave and t_{sn} the time prior to the S-wave onset time, and t_1 and t_2 bracket the time window of the fundamental Rayleigh and Love waves. v_{sp} and v_{lp} are the short-period and long-period ground bandpass velocities, respectively. v_{sp} is obtained by convolving the broadband velocity record convolved with a Wood-Anderson (WA) short-period instrument and v_{lp} is the broadband velocity record convolved with a long-period instrument (PE). The velocities are squared in order to obtain units of energy; the factor of $m/2$ in the numerator and denominator, where m is the unit mass of the particle of motion, cancel out.

Figure 12 displays the log SP:LP integrated energy ratio vs. distance for all data; each data point represents one event-station pair. Crosses represent earthquakes, circles signify nuclear explosions, and stars are data points for the chemical kt test. The explosions tend to have higher SP:LP integrated energy ratios than do the earthquakes at all distance ranges. Although there isn't complete separation of the two populations, the portion of the earthquake population which overlaps with the explosion population is small (approximately 10 percent).

5. Discussion

In order to better appreciate the robustness of these energy measurements and their application to particularly small events, we will show a suite of regional waveforms and their associated integrated energy curves for small explosions from the three NTS subsites and for earthquakes near NTS, namely the Little Skull Mountain sequence. We will also briefly discuss some 2-D scattering effects produced by surface geology.

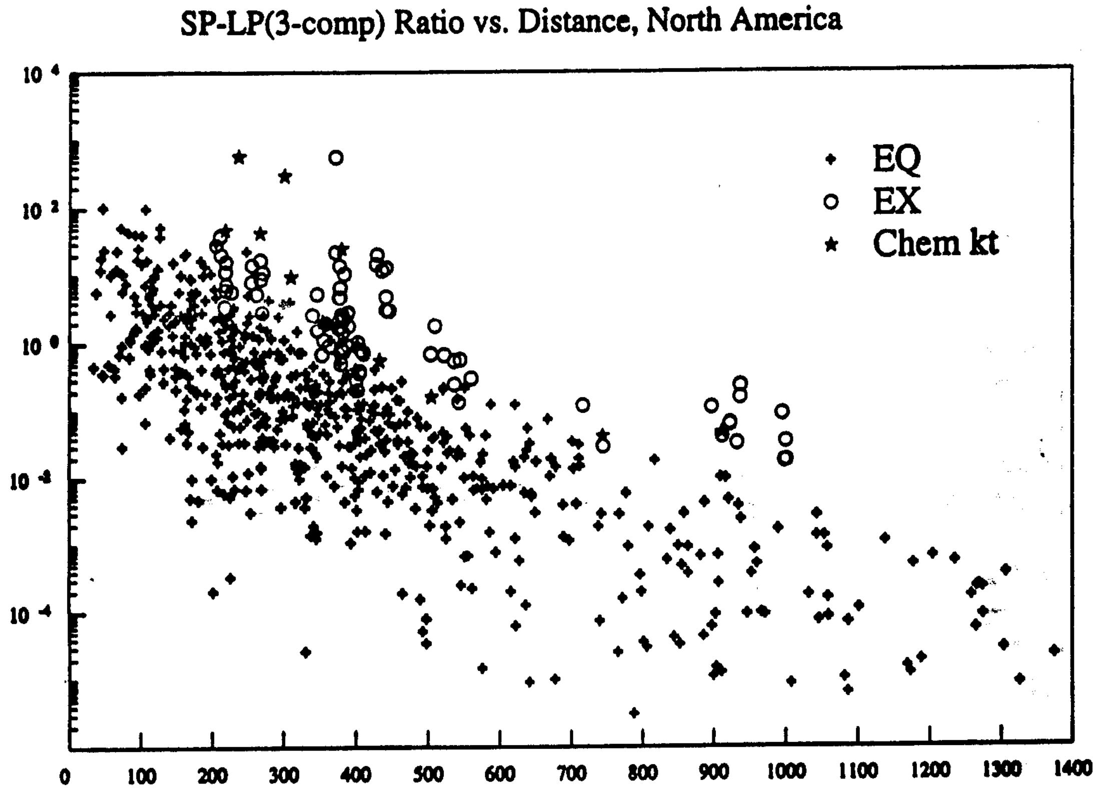

Figure 12. Plot of the short period:long period discriminant for a population of events, after Woods and Helmberger (1994).

Figure 13 displays vertical component records of NTS shots recorded at GSC (top four rows) and ISA (bottom four rows). The first column is the broadband displacement, followed by a convolution with the WA instrument on the right. The test site or name of the event is to the left of each row. At both these stations, long-period fundamental-mode Rayleigh wave energy is evident for all four events, with $T < 7$ sec. dispersed coda waves having the largest amplitudes. In making comparisons between events, it should be noted that the Pahute shot is larger than the others, so that it has a much better signal to noise ratio. On the broadband recordings there are no distinguishing waveform characteristics between the three test sites. This holds true for all TERRAscope records, Woods and Helmberger (1994). On inspection of the WA records, certain patterns emerge. Recordings of the Pahute shot have a strong, prominent P-wavetrain followed by relatively small short-period coda compared to the other test-site shots. The Yucca shot shows a great deal of what appears to be scattered shear-wave energy at both stations, which equals or exceeds the peak P-wave amplitude. The Ranier shots seem to be an intermediate case, for which the shear-wave energy may nearly rival, but not exceed the peak P-wave amplitudes. In all cases the shear-wavetrain does not have a sharp onset, but rather is a dispersive wavetrain.

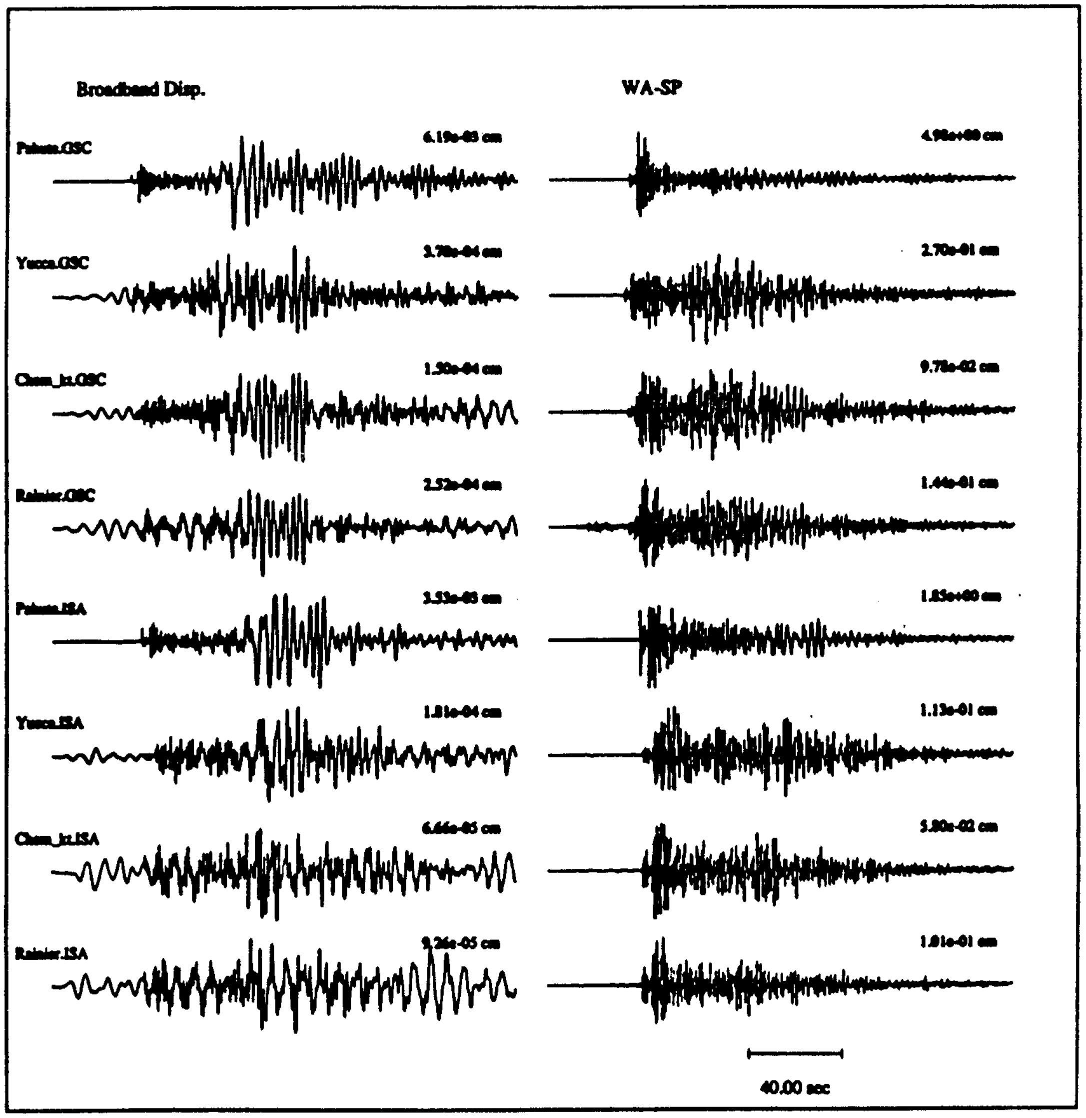

Figure 13. Comparison of NTS events at GSC (Δ ≈ 330 km). Note that the seismograms of the chemical explosion fit nicely into the other underground explosion population. Pahute events appear distinct in their simplicity at this azimuth.

These NTS records are in sharp contrast to natural earthquake records as displayed in figure 14 where the onset of shear waves is quite clear. These recordings are at fairly near distances (200 < D <280 km), so that propagation effects are minimized. However, these characteristics persist to larger ranges, Woods and Helmberger (1994). These waveform characteristics are displayed in the integrated energy curves as well.

The panel on the left in figure 15 displays the short-period, vertical component, integrated energy curves vs. time for explosions recorded at the four TERRAscope stations. All curves are normalized to unity, with the actual integrated energy value given to the right in the legend. We will refer to these plots as E(t), or accumulated energy up to time t. For records with a prominent P-wavetrain arrival, the curves resemble step functions. This is particularly true of the Pahute shot and expected on theoretical grounds, i.e., RDP source. For the Yucca shot, the P-wavetrain energy comprises less than half of the short-period energy. The Rainier nuclear explosion and chemical blast are intermediate in shape to the Pahute and Yucca energy curves. At the more distant stations (PAS and PFO), the Rainier energy curves more closely resemble those of Yucca than Pahute, whereas at the closer stations, particularly ISA, the opposite is true.

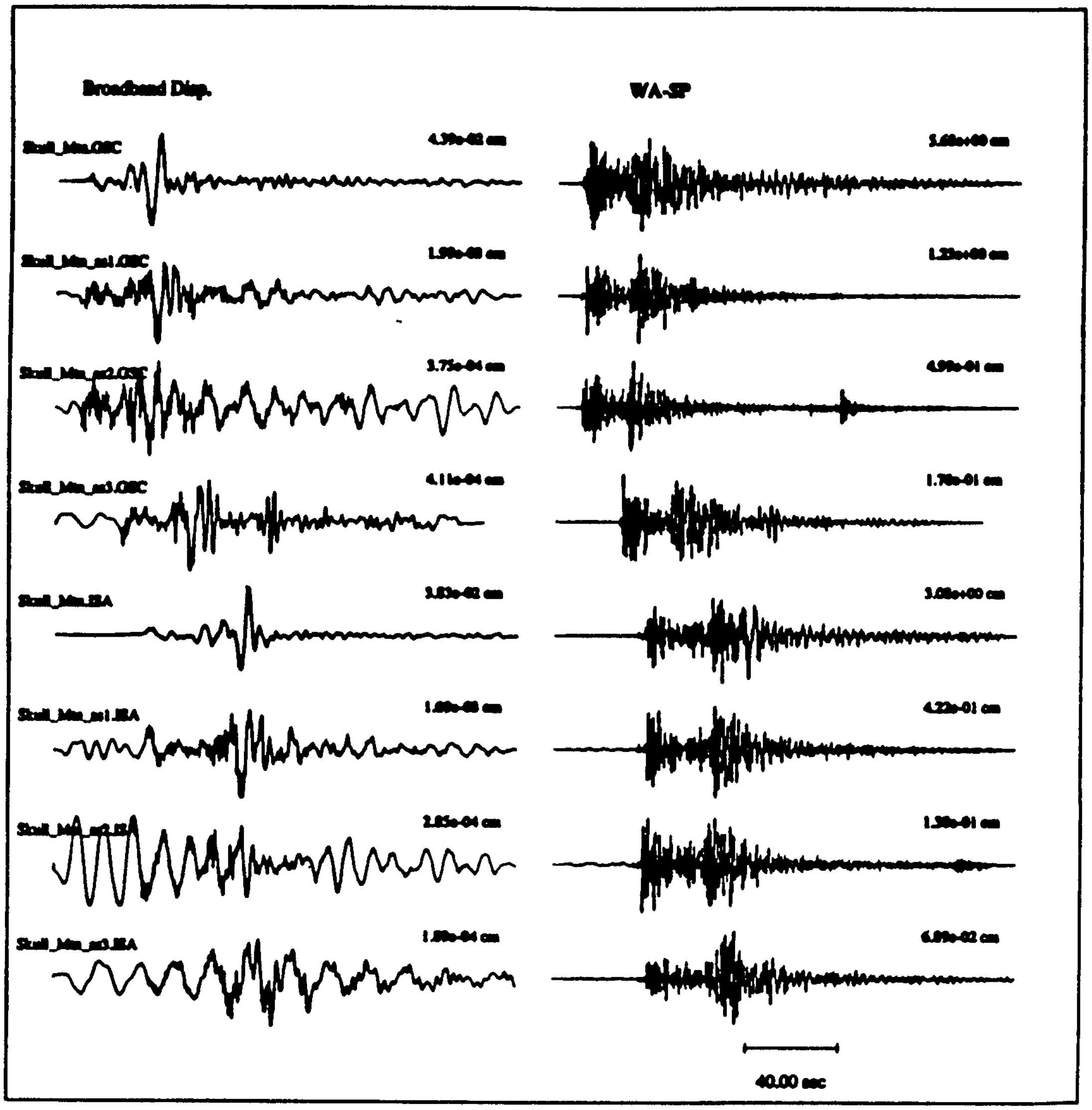

Figure 14. Comparison of the Skull Mountain events at GSC and ISA.

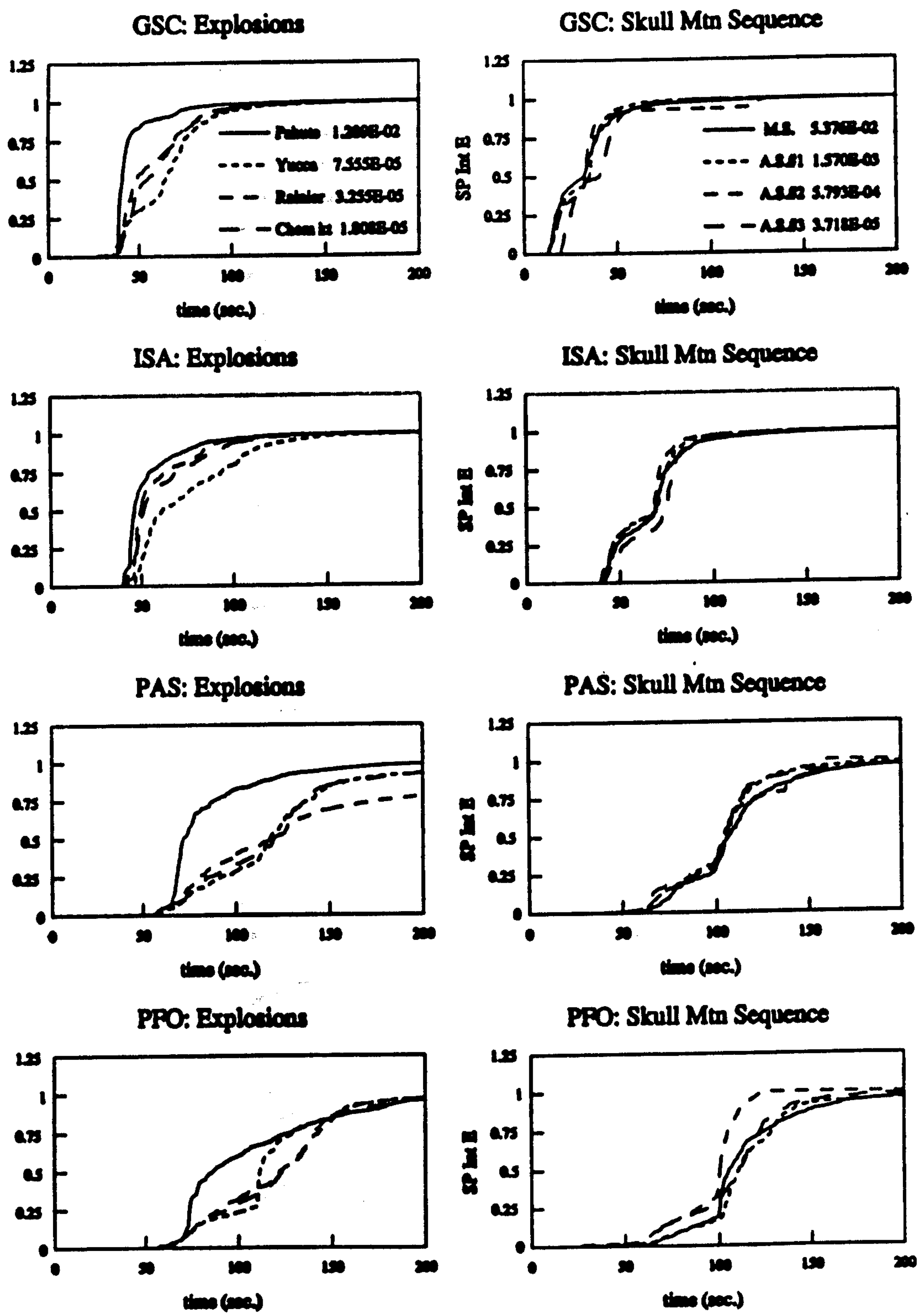

Figure 15. Comparison of short-period energy curves of explosions and earthquakes (Skull Mtn) at the various stations.

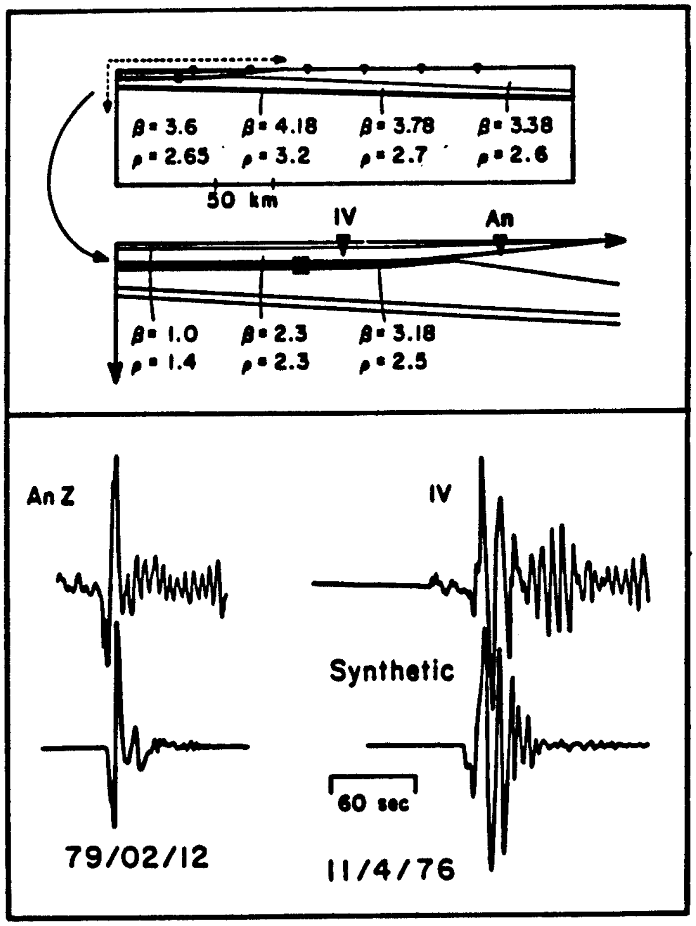

Figure 16. Upper panel displays a 2D cross-section from Imperial Valley (left) to Pasadena (right), distance is about 260 km. Lower panel displays the comparison of a relatively simple event (AN) compared to the more complex-looking event which occurred in the basin (IV). These are long-period comparisons with synthetics predicted from the above model.

The panel on the right in figure 16 displays analogous plots of integrated energy curves for earthquakes from the Little Skull Mountain sequence. Here the onset of the S-wave energy is pronounced and sharp. For explosions, in general, the S-wave onset is much more gradual, with the exception of the Yucca event recorded at PFO, which looks very much like the earthquake energy curves. It is not clear whether these differences are due to near-source or propagation effects. In the case of Yucca Flat for which the energy curve at each station deviates significantly from the "cleaner" Pahute curve, it seems likely that shallow structure in the source region is at least partly responsible for the large amount of scattered energy in the waveforms.

Several investigations have discussed the scattering of locally trapped Rayleigh waves encountering NTS type structures, see for example, McLaughlin and Jih (1987), and Stead and Helmberger (1988). However, explaining all three components of regional NTS events (figure 3) proves especially difficult because of the amount of tangential energy generally observed. Thus, the scattering must be due to a 3-D feature and/or requires secondary sources such as spall, etc. In short, it is difficult to predict regional records using the conventional RDP formalism.

An easier problem that has been studied quite successfully involves modeling events occurring along a corridor from Imperial Valley to Pasadena, essentially events on the San Jacinto fault zone, see Helmberger et al., (1992), and Ho and Helmberger (1988). Events occurring in the Imperial Valley arrive at Pasadena with extensive coda compared to events occurring outside the basin, see figure 16. The upper panel displays a 2-D model connecting Imperial Valley to Pasadena (260 km). The (AN) event occurred near the edge while the (IV) event is located well into the basin. Basin events not only have well developed dispersion but many times have secondary arrivals. The shallower the event, the stronger these later arrivals. These signals can be modeled as shallow surface waves propagating slowly in the upper layer and re-radiating at the basin edge, and can be the strongest signals on the record if the source extends to the surface, see Ho and Helmberger (1988). Thus, it is relatively easy to explain the excess energy associated with shallow events occurring in soft materials.

Applying this experience to the NTS data, we suggest that the Yucca Flat basin is responsible for the complicated records occurring in figure 13 and that natural earthquakes (figure 14), which normally occur at deeper depths, are generally easier to model. Thus, the similarity in waveshapes and energy curves (figure 15) allows us to model the large earthquake (M>5) where the signals are above the noise, identify the paths of short-period arrivals and predict their behavior for small events. In short, we think it is easier to understand the short-period phases produced by the Little Skull Mountain events (figure 14) than those produced by the NTS shots (figure 13). Thus, we propose to identify earthquakes by their waveshapes and energy distributions and identify explosions as being not-like-earthquakes.

In conclusion, we demonstrated that regional seismograms from earthquakes can be used to estimate their fault parameters, moment, and depths applying a procedure developed in Zhao and Helmberger (1994). Next we examined the energy content of the various phases, defined M_B (broadband moment) and M_E (energy strength), and introduced a new method of discrimination. In this method all events are processed as earthquakes, and explosions are distinguished by their stronger energy levels relative to their long-period amplitudes. This was followed by a discussion of a discriminant based on the ratio of short-period (1 Hz), vertical component, P_{nl} wavetrain energy to intermediate-period (0.05 to 0.16 Hz), three component, surface wave energy, for which explosions tend to have a higher ratio than earthquakes. This discriminant works on the same premise as the teleseismic M_s:m_b ratio, for which earthquakes are richer in long-period surface wave energy relative to explosions.

6. Acknowledgments.

We thank Evelina Cui for producing this camera-ready manuscript and Dave Harkrider for his review. This research was supported by the Department of Defense as monitored by the Air Force Office of Scientific Research under contract F49620-93-1-0221. Contribution no. 5472, Division of Geological & Planetary Sciences, Caltech, Pasadena, CA.

7. References

1. Alewine, R. W. (1972) Theoretical and observed distance corrections for Rayleigh-Wave magnitude, ***Bull. Seismol. Soc. Am.*** **62,** no. 6, 1611-1619.
2. Dreger, D. S. and Helmberger, D. V. (1991) Source parameters of the Sierra Madre earthquake from regional and local body waves, *Geophys. Res. Lett.* **18,** 2015-2018.
3. Dreger, D. S. and Helmberger, D. V. (1993) Determination of source parameters at regional distances with three-component sparse network data, *J. Geophys. Res.* **98**, B5, 8107-8125.
4. Dziewonski, A. M. and Anderson, D. L. (1981) Preliminary reference Earth model, *Phys. Earth Planet. Inter.* **25**, 297-356.
5. McLaughlin, K. L. and Jih, R.-S. (1987) Finite-difference simulations of Rayleigh wave scattering by shallow heterogeneity, *Report AFGL-TR-87-0322*, Air Force Geophysics Laboratory, Hanscom AFB, MA, ADA194961.
6. Patton, H. J. and Walter, W. R. (1993) Regional moment: magnitude relations for earthquakes and explosions, *Geophys. Res. Lett.* **20**, *277-280.*
7. Patton, H. J. and Zandt, G. (1991) Seismic moment tensors of western U. S. earthquakes and implications for the tectonic stress field, *J. Geophys. Res.* **96**, 18,245-18,259.
8. Priestley, K. and Brune, J. (1978) Surface waves and the structure of the Great Basin of Nevada and western Utah, *J. Geophys. Res.* **83**, 2,265-2,276.
9. Ritsema, J. and Lay, T. (1994) Rapid source mechanism determination of large ($M_w \geq 5$) earthquakes in the western United States, Geophys. Res. Lett. **20**, 1611-1614.
10. Stead, R. J. and Helmberger, D. V. (1988) Numerical-analytical interfacing in two dimensions with applications to modeling NTS seismograms, *PAGEOPH* **128**, 157-193.
11. Taylor, S. R., Denney, M. D., Vergino, E. S., and Glaser, R. E. (1989) Regional discrimination between NTS explosions and western U. S. Earthquakes, *Bull. Seismol. Soc. Am.* **79**, 1142-1176.
12. Thio, H. K. and Kanamori, H. (1992) Moment tensor inversions in Southern California using surface waves recorded by TERRAscope, (abstract), *EOS Trans., AGU* **73**, 376.
13. Woods, B. and Helmberger, D. V. (1994) Regional seismic discriminants using wavetrain energy ratios, submitted to *BSSA*.
14. Woods, B., Kedar, S., and Helmberger, D. V. (1993) M_L:M_o as a regional seismic discriminant, ***Bull. Seismol. Soc. Am.*** **83**, 1167-1183.
15. Woods, B. and Harkrider, D. G. (1994) Investigating long-period source spectra of Nevada Test Site explosions using regional surface wave data with applications to yield estimation and discrimination, *Geophys. J. Int.* (in press).
16. Zhao, L. S. and Helmberger, D. V. (1994) Source estimation from broadband regional seismograms, ***Bull. Seismol. Soc. Am.*** **84,** 91-104.
17. Zhao, L. S. and Helmberger, D. V. (1994) Regional moments, energy levels, and a new discriminant, submitted to *Phys. Earth Planet. Inter.*

SECTION 2

Determining Surface-Wave Magnitudes from Regional Nevada Test Site Data

Geophys. J. Int. (1995) **120**, 474–498

Determining surface-wave magnitudes from regional Nevada Test Site data

Bradley B. Woods and David G. Harkrider
Seismological Laboratory 252-21, *California Institute of Technology, Pasadena,* CA 91125, *USA*

Accepted 1994 July 21. Received 1994 July 21; in original form 1994 April 23

SUMMARY

We re-examine the use of surface-wave magnitudes to determine the yield of underground nuclear explosions and the associated magnitude-yield scaling relationship. We have calculated surface-wave magnitudes for 190 Nevada Test Site (NTS) shots using regional long-period seismograms from a combined super-network of 55 North American stations. Great effort went towards making the data set comprehensive and diverse in terms of yield, source location and shot medium in order to determine the portability of surface-wave magnitude scales. In particular, we examine Pahute Mesa, Rainier Mesa and Yucca Flat explosions detonated above and below the water table, and which range over three orders of magnitude in yield. By observation we find a low-yield measure threshold of approximately one kiloton (kt) for (assumedly) moderately well-coupled explosions recorded at near-regional (<500 km) stations, which have little microseismic noise. In order to utilize regional surface waves ($\Delta < 15°$) for quantifying sources and for discrimination purposes, we have developed related methods for determining time-domain surface-wave magnitudes and scalar moments from regional Rayleigh waves. Employing regional surface-wave data lowers the effective magnitude threshold. One technique employs synthetic seismograms to establish a relationship between the amplitude of the regional Airy phase, or Rayleigh pulse of the Rayleigh wavetrain and an associated surface-wave magnitude, based on conventional M_S determinations, calculated from synthetic seismograms propagated to 40°. The other method uses synthetic seismograms in a similar fashion, but the relationship used is a more straightforward one between scalar moment and peak Rayleigh wave amplitude. Path corrections are readily implemented to both methods. The inclusion of path corrections decreases the M_S variance by a factor of two and affects the absolute scaling relationship by up to a factor of 0.1 magnitude units. This latter effect is attributed to the particular station network used and the Green's functions used to obtain the 40° M_S values. Using a generic structure for the distance travelled past the actual source–receiver path minimizes the difference between magnitudes determined with and without path corrections. The method gives stable M_S values that correlate well with other magnitude scale values over a range of three orders of magnitude in source yield. Our M_S values scale very similarly to more standard teleseismic M_S values from other studies, although the absolute M_S values vary by ±0.5 magnitude units about ours. Such differences are due in part to the choice of M_S formula used. For purposes of future user comparisons, we give conversion values to the previous studies. Our most refined M_S values give the relationship $M_S = 1.00 \times \log_{10}(\text{yield}) + B$, where B is dependent upon source region and shot medium. This yield exponent of unity holds for events of all sizes and is in line with M_S-yield scaling relations found by other studies. When events are grouped with respect to source region, significantly better fits to these individual-site linear-regression curves are obtained compared to the fits obtained using a single, all-inclusive model. This observation implies that shot-site parameters and source structure can significantly affect surface-wave-magnitude measurements. We present these M_S values primarily to augment the extensive historical analysis of explosion data based on surface-wave magnitudes by using regional data to increase the number of events with surface-wave magnitudes. These magnitudes are consistant with the teleseismically determined magnitudes of larger events. We present our preferred surface-wave moment values in a sequel paper.

Key words: North America, nuclear explosions, surface waves.

INTRODUCTION

We re-examine the use of surface waves for determining underground nuclear-explosion magnitudes, particularly for smaller yield, Y ($Y < 20$ kt), events. The surface-wave magnitude-yield scaling relationship for such low-yield events is not well defined. Even for larger yield explosions there is some debate as to the scaling relation between yield and the long-period energy radiation, as well as the relationship between M_S and m_b. Evernden & Filson (1971) found that $M_S = 1.4 + 1.3 \times \log(Y)$ for hard rock sites in North America, where log is understood to be $\log_{10}$. Marshall, Douglas & Hudson (1971) found that M_S scales with yield to the first power, with consolidated rock (tuff, salt, granite, andesite and sandstone) coupling 10 times more efficiently than detonations in alluvium. More recently Marshall, Springer & Rodean (1979) found that for events detonated in hard rock (salt or granite) or water-saturated material (below the water table) that $M_S = 2.16 + 0.97 \times \log(Y)$ and that $M_S = 1.88 + 1.06 \times \log(Y)$ for explosions above the water table. Taken together, these two populations yield the relationship $M_S = 2{\cdot}05 + \log(Y)$ (Bache 1982). Basham & Horner (1973) found the scaling relationship for explosions in consolidated rock at sites throughout the world (a majority of the events being from NTS) to be $M_S = 1{\cdot}56 + 1{\cdot}24 \times \log(Y)$. Sykes & Cifuentes (1984) found a worldwide empirical relationship of $M_S = 2.16 + 0.95 \times \log(Y)$ for explosions. Murphy (1977) found that the scaling law varied between events larger than 100 kt [$M_S = 1.2 + 1.33 \times \log(Y)$] and smaller events [$M_S = 2.14 + 0.84 \times \log(Y)$].

The above studies utilized data from a suite of sites to determine magnitude-yield relationships. Doing so is likely to add scatter to the results, for the shot medium, the source region, and regional propagation effects may all affect surface-wave amplitudes. We subgrouped our data set into specific source-region data subsets in order to ascertain whether or not the separated explosion populations have different magnitude-scaling relationships.

The data for this study are long-period vertical-component surface-wave records for 190 Nevada Test Site (NTS) events. The stations used are from several North American networks. Their respective instruments all have passbands that lie within the 6 to 60 s range. Surface waves are very useful for yield estimation purposes, for M_S is determined from relatively long-period seismic waves that are insensitive to high-frequency near-source effects, which may be caused by asymmetries in the shot cavity (Zhao & Harkrider 1991), spall (Taylor & Randall 1989; Day & McLaughlin 1991) or other possible mechanisms. These high-frequency source effects may cause appreciable bias in magnitudes that are based on higher frequency waves, such as the m_b and L_g scales. There are advantages to using body-wave measurements. Teleseismic body waves traverse mantle paths that are relatively homogeneous, whereas surface waves travel in crustal and upper-mantle waveguides that are known to have strong lateral inhomogeneities.

Evernden & Filson (1971) suggest, based on their observations of body-wave and surface-wave magnitudes of U.S. underground explosions detonated both within and outside of NTS, that the change in $M_S - m_b$ relationship from site to site is due to abnormal m_b values, rather than abnormal M_S values, and that regional-crustal and upper-mantle attenuation variations near the source (Δt^*) are responsible for the larger scatter in m_b-yield correlations. M_S measurements are also less sensitive to source-depth effects than are body-wave measured magnitudes (Marshall & Basham 1972). If it was not for contamination due to tectonic release, which has a more pronounced effect on long-period surface waves than body waves, and lateral inhomogeneity along the surface-wave propagation path near the surface of the earth, the long-period energy measured from surface waves might be a more stable measure of seismic yield than teleseismic body-wave measurements. It is the purpose of this paper to develop and apply a technique for reducing the contaminating effect of lateral propagation on M_S measurements.

Another advantage of using seismic moment or M_S is that empirical evidence and theoretical studies show that the scaling relationship between M_S (or log moment) and yield has an approximate slope of unity, i.e. $M_S = \log(\text{yield}) + B$, whereas the m_b-yield and $m_b(L_g)$-yield relationships have slopes between 0.65 and 0.90. As Evernden & Filson (1971) point out, a 0.3 error in m_b corresponds to a three-fold error in yield determination, while an equivalent error in M_S results in only a two-fold error in the yield estimate. Thus the error in yield estimation is inherently larger when obtained from higher-frequency magnitude measurements.

For lower-yield events it becomes necessary to include the data from regional stations ($\Delta < 25°$), for teleseismic surface-wave recordings have too low a signal-to-noise ratio (SNR), which makes them unusable. At regional distances surface waves are not well dispersed, having a prominent Airy phase pulse with a period between 6 and 20 s (Alewine 1972), so that it is not possible to measure M_S conventionally (that is measuring the amplitude of a stable, prominent 20 s surface wave). For North America in general, there is a minimum in the group velocity curve near 12 s for the fundamental Rayleigh wave (Marshall *et al.* 1979). To make accurate surface-wave magnitude measurements, this energy bandwidth ought to be modelled as well as possible, for it is the predominant signal of the wavetrain.

To measure M_S we first model regional Rayleigh waves with theoretical seismograms. These synthetic wavefields are then propagated out to 40°, at which distance stable 20 s surface-wave magnitudes can be measured. In using this procedure several propagation-path models were tested to determine the effect of attenuation and seismic-velocity structure upon the M_S values. These calculated M_S values remain stable, have reasonably small errors and correlate well with associated m_b magnitudes and log yield for the event data set. The $M_S - m_b$ relationships are determined by a weighted least-square linear regression; both free- and fixed-slope curves were fitted to the data.

We also determine time-domain moment measurements from the same data. The moment is determined from the ratio of the maximum peak-to-peak amplitude of the surface wave train to that of a synthetic, with a given input-step moment, propagated to the same distance as the data. These two time-domain magnitude measurements (M_S and log M_0) give very consistent scaling results.

Besides comparing the M_S results with several different independent magnitude scales, the data have also been separated with respect to source region and shot material. No corrections were made in magnitude for shot-medium coupling effects, although such effects can be considerable, even for long-period energy (Werth & Herbst 1963), because such shot-site information would not necessarily be available for events detonated in other countries. This study is meant to test the effectiveness and portability of a surface-wave magnitude scale in the most general case.

We do not account for tectonic-release effects upon the magnitude measurements. Such effects are best accounted for with moment-tensor inversions of sources which involves more sophisticated data analysis. Standard M_S measurement techniques ignore this factor as well. The effects of tectonic release are considered in a sequel paper.

DATA

The data are long-period vertical seismograms recorded at North American stations for 190 explosions at NTS and consist of digitized World Wide Standard Seismographic Network (WWSSN) and Canadian Seismographic Network (CSN) records, Digital World Wide Seismographic Network (DWWSN), Lawrence Livermore Regional Seismic Network (LLNL) and Regional Seismic Test Network (RSTN) digital data. The analogue WWSSN and CSN data were digitized by ENSCO Inc. Fig. 1 shows a map of this 58 station super-network. Epicentral distances range from 220 km for NTS to GSC (Goldstone, California), to 4350 km for NTS to MBC (Mould Bay, Northwest Territories). For the smaller events, particularly Rainer Mesa explosions, only the nearer stations (distance < 1000 km) had usable data. Station coverage varies widely

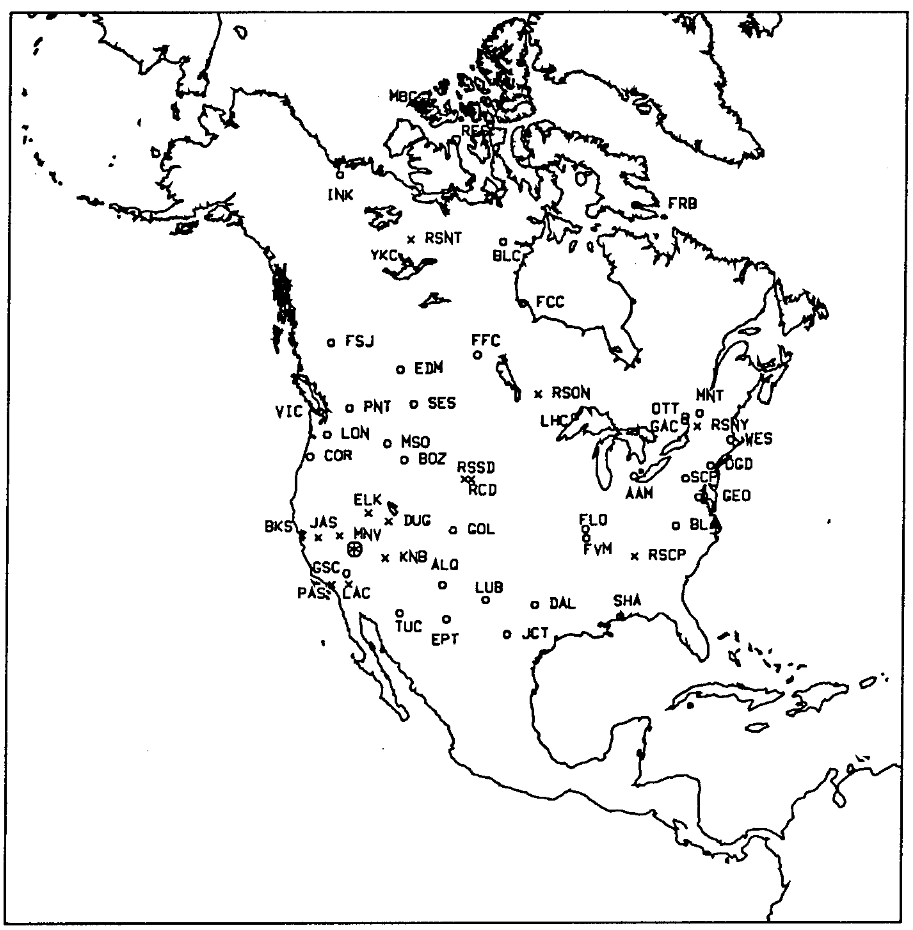

Figure 1. Map of the North American station network used in this study. The 'spoked wheel' is the Nevada Test Site.

between events. 22 of the smaller events (or very early events) only had one usable station seismogram each, while some events had over 30. The average number of stations reporting per event is approximately 10. For current and future geographical areas of monitoring interest it is reasonable to assume that only sparse networks will be able to record any given event, particularly smaller explosions (below 10 kt) or intentionally 'muffled' explosions, so it is important to see how well an explosion magnitude can be estimated with only a few observations.

Because our methods for determining magnitudes are done by means of time-domain measurements, analogue records can be readily used as well. We took advantage of this fact to add considerably more events (72 of the 190) to the sample population. These events were chosen with a mind to filling out the data set with respect to yield, depth to water table and geographic location.

We chose to confine our study to surface waves travelling solely along continental paths, i.e. within North America. Surface waves that propagate across oceanic-continental margins undergo significant modification in their waveforms because of the great lateral variation in crustal and upper-mantle structure at such boundaries. These propagation effects are not straightforward to model, and hence meaningful Green's functions, or transfer functions, are difficult to obtain. Without robust Green's functions it is hard to infer accurate source information from the data. Also, smaller events are not likely to be observed at the distant stations, which often include oceanic structure along their propagation path, and make these longer paths even less attractive to include in the monitoring network.

Of the 190 events, 48 are from Pahute Mesa, 30 are from Rainer Mesa, 105 are from Yucca Flat and seven others are from other sites in or around NTS, but outside of the three major test sites. Of these seven events, PILEDRIVER (detonated at Climax stock) was the only one for which digital data were available. For some specific stations, waveforms varied somewhat between events, depending upon source location. The PILEDRIVER data from a given station look appreciably different from those of any other events recorded at that same station. This was true for every station recording PILEDRIVER and probably is caused by differences in the source region for this explosion. PILEDRIVER was detonated in a granitic source region, north of the other sites. The source-to-receiver geometries for this event are approximately the same as those at the other NTS events, so the difference in waveforms appears to be a source effect rather than a propagation effect. Because PILEDRIVER was the only Climax Stock event with readily available data, no further examination of this site was carried out.

Figure 2 compares representative NTS vertical-component long-period data with synthetic Rayleigh waves for each source–receiver path. More than one event was used since no one event was observed at every station. The darker traces are the observations and the lighter trace below each

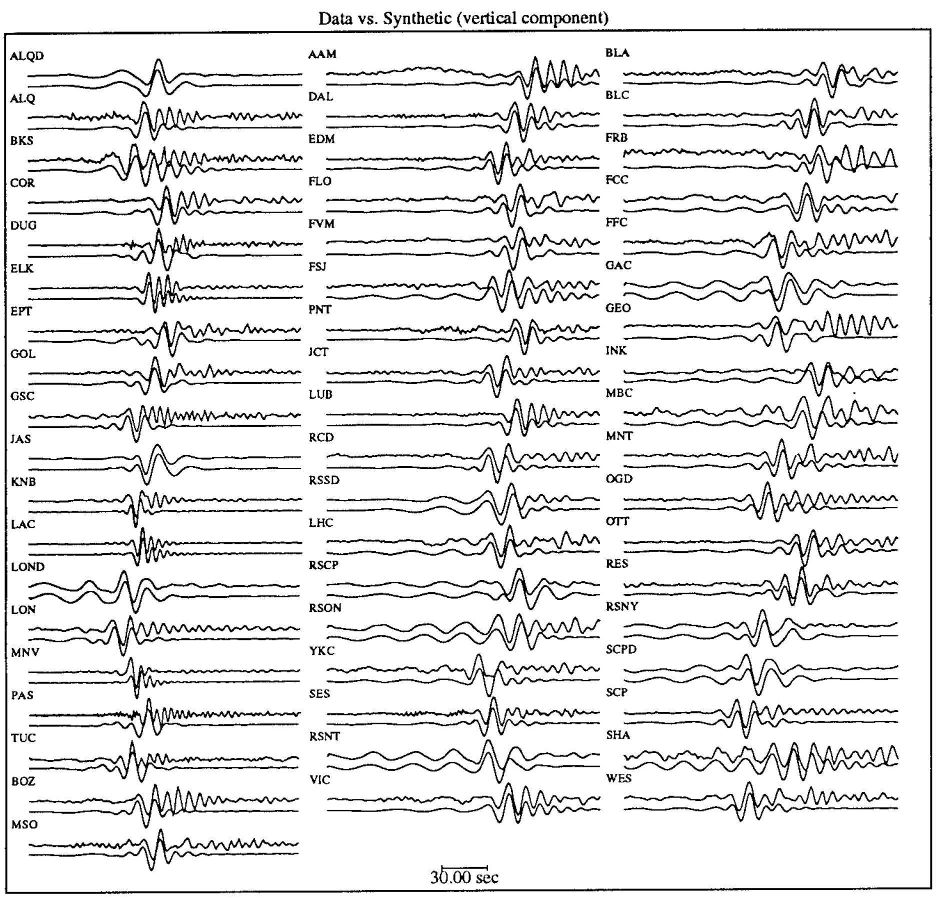

Figure 2. Comparison of vertical-component Rayleigh-wave waveforms. The data time series are the upper, thicker traces; the lower trace in each case is the fundamental-mode synthetic. All time series band-passed between 60 and 6 s.

is a synthetic seismogram made with the fundamental-mode Rayleigh wave only. The seismograms were bandpassed filtered between 6 and 60 s to suppress the long-period and short-period noise that would otherwise affect the peak-to-peak measurement of the Rayleigh pulse.

MAGNITUDE CALCULATION TECHNIQUE

We have developed a method to measure surface magnitudes indirectly. Because a large portion of the data for low-yield events is from stations recording at regional distances ($\Delta < 25°$), it is not possible to calculate M_S conventionally, for the Rayleigh wave is pulse-like, which precludes measuring a well-dispersed 20 s phase (Alewine 1972). We address this problem with the use of synthetic seismograms of the fundamental Rayleigh wave using an asymptotic relation for mixed-path surface waves.

For our mixed path expressions, we follow Levshin (1985) or Yanovskyaya (1989, page 44) and write the spectral Rayleigh wave vertical displacement for approximate propagation in a slowly varying laterally inhomogeneous media (e.g. Burridge & Veinberg 1977; Babich, Chikhachev & Yanovskyaya 1976; Woodhouse 1974; Yomogida 1985) as

$$w_0 = \frac{\exp(-i3\pi/4)}{\sqrt{8\pi\omega}} \frac{\exp\left[-i\omega\int_{P_0}^{P} ds/c\right]}{\sqrt{[J]_P}} \exp\left[-\int_{P_0}^{P} \gamma\, ds\right] \times \left[\frac{1}{\sqrt{UI}}\right]_P \left[\frac{W}{\sqrt{UIc}}\right]_{P_0} \tag{1}$$

where the energy integral is

$$I = \int_0^\infty \rho(z)[y_1^2(z) + y_3^2(z)]\, dz, \tag{2}$$

$\rho(z)$ is the local density distribution in the medium and we have used Saito's (1967) Rayleigh wave eigenfunction notation, $y_i(z)$. The eigenfunctions are normalized in such a way that the vertical-displacement eigenfunction, $y_1(z)$ is equal to 1 at the free surface, $z = 0$. This results in the horizontal displacement eigenfunction, $y_3(z)$, being equal to the Rayleigh mode surface ellipticity at this boundary. U and c are respectively the local group and phase velocities. By local we mean the eigenvalues and eigenfunctions that one would obtain for a laterally homogeneous half-space consisting of the vertical elastic and density distribution at that location. P is the receiver location and P_0 is the point-source location and quantities within the P or P_0 subscripted square brackets are evaluated at these locations. The integrals are taken along the phase-velocity-determined ray path between the two surface locations. J describes the geometrical spreading of the surface-wave energy. γ is the frequency-dependent attenuation coefficient due to the anelastic structure of the path, i.e. $\gamma = \omega/(2QU)$, where Q is the attenuation quality factor. The above expression is applicable in the absence of foci or shadow zones in the vicinity of the receiver. If there are foci along the path an additional phase factor of $\exp(i\pi/2)$ should be included for each foci. For an explosion, W is

$$W = M(\omega)\left[\frac{dy_1}{dz} - \frac{\omega}{c} y_3(z)\right], \tag{3}$$

where $M(\omega)$ is the isotropic or explosion spectral seismic moment. We also assume a step for our explosion history, i.e. $M(\omega) = M_0/(i\omega)$.

Since we will assume that the directions of the horizontal gradients of the material properties are approximately aligned in the direction of the source to receiver, the ray path is a straight line and $J = r$, which is the distance between the two locations. We further assume that the lateral inhomogeneity can be considered to be made up of n homogeneous segments of radius r_i, i.e. $\Sigma r_j = r$. For comparison with Stevens (1986), who used a similar expression to estimate seismic moments for explosions, and earlier works on which his expressions were based (e.g. Bache, Rodi & Harkrider 1978; Harkrider 1981), we write W in terms of K where

$$K = y_3(z) - \frac{c}{2\mu\omega} y_2(z) \tag{4}$$

and y_2 is the normalized vertical normal stress eigenfunction. The relation between K and W is obtained by substituting

$$\frac{dy_1}{dz} = \frac{1}{(\lambda + 2\mu)}\left[y_2(z) + \frac{\omega}{c}\lambda y_3(z)\right] \tag{5}$$

into the previous W expression.

Now we can write the multipath displacement as

$$w_0 = -\frac{\exp(-i3\pi/4)}{\sqrt{2\pi\omega}} \frac{\beta_1^2}{\alpha_1^2} \frac{M_0}{c_1} \frac{\exp[-i\omega(r_j/c_j)]}{\sqrt{r}} \times \exp(-\gamma_j r_j)\left[\frac{1}{\sqrt{UI}}\right]_n \left[\frac{K}{\sqrt{UIc}}\right]_1 \tag{6}$$

where the summation convention of repeated subscripts is used. The subscript '1' denotes the local quantities for the source medium and the subscript 'n' the local quantities at the receiver. The shear velocity is denoted by β and the compressional velocity by α. For a given moment, M_0, the ratio of the square of these two quantities plays a key role in determining the amplitude effect of various shot media. To this order of approximation the spectral amplitude neglecting attenuation is only dependent on the local properties at the source and receiver. The attenuation and phase are dependent on the local properties along the whole path.

With the substitution

$$\underset{-}{A} = \frac{1}{2cUI} \tag{7}$$

(Harkrider & Anderson 1966; Harkrider 1981) and multiplying by $-\sqrt{c_n/c_1}$, we obtain the same expression as used by Stevens (1986) to obtain his path corrections from NTS to 24 WWSSN station in United States and Canada and to 12 SRO stations. For his models $n = 2$. The negative sign results from the differences in our sign criteria for vertical displacement. In Stevens (1986) vertical displacement is positive up while in this article it is positive down. The phase-velocity factor is due to the use of wavenumber spreading by Bache *et al.* (1978), Harkrider (1981), and Stevens (1986) compared to geometric spreading by the others. Bache *et al.* (1978) based their expressions on the conservation of lateral-energy flux while these expressions are from the main term in an asymptotic expansion.

Glover & Harkrider (1986) performed numerical tests in order to estimate the frequency range for which these approximations were valid for Rayleigh waves generated at NTS where the source region may be limited by sharp boundaries such as in the low-velocity basin at Yucca Flat. Rayleigh wave seismograms were calculated for explosive sources at depth in a finite vertical cylinder with contrasting elastic properties representative of the various test areas at NTS embedded in a vertically stratified propagation media. The technique couples laterally inhomogeneous finite-element calculations of the source region with Green's functions for teleseismic Rayleigh waves using the elastodynamic representation theorem. The details of the technique can be found in Harkrider (1981) and Bache, Day & Swanger (1982). The spectra for these Rayleigh waves were then compared with those, which used the two approximations to cross the sharp boundary. It is surprising that both approximations worked as well as they did since they are based on a gradual transition. It was found that both approximations worked equally well for periods greater than four seconds, and that for shorter periods the asymptotic approximation used in this paper is better. The period range is dependent on the material contrast and the vertical extent of the contrast but this mixed path approximation is certainly adequate for the determination of long-period moments and surface-wave magnitudes from NTS Rayleigh wave observations at continental stations.

It is interesting to note that for this geometry, i.e. $n = 2$, the Rayleigh wave transmission coefficient, $T(\omega)$, of Bache *et al.* (1978)

$$T(\omega) = \left(\frac{c_2 A_2}{c_1 A_1}\right)^{1/2} = \left(\frac{U_1 I_1}{U_2 I_2}\right)^{1/2} \tag{8}$$

is identical to the factor R of Levshin (1985) and was used in both articles to illustrate the effect of mixed paths on the amplitude of Rayleigh waves.

For each source-to-receiver path, a theoretical Rayleigh wave is generated. The earth model used to create this synthetic is meant to reflect the average earth structure between NTS and the given station. The earth models used in this study were determined from inversions of dispersion and attenuation data as well as forward modelling of the waveform to fine tune the models. The criteria for determining the goodness of fit of the synthetic to the data are dispersion, absolute traveltime and waveform fit (relative amplitude of different dispersed phases). Hence the synthetic seismogram displays the same spectral and time-domain waveform characteristic as the data which it simulates (see Fig. 2). This was done for all paths. The paths to WWSSN and Canadian stations were taken from the explosion moment study by Stevens (1986). We determined the RSTN, LLNL and DWWSN path structures.

To determine M_S for a particular source–receiver geometry two synthetics are generated. One, which is propagated the actual path distance, that is meant to simulate the data and one which is propagated to 40°. At 40° the surface wave train is well dispersed and stable, so that a conventional M_S value can be calculated. Fig. 3 illustrates this method. The upper set of seismograms are a comparison of data to its corresponding synthetic seismogram. For this particular example the station COR (Corvallis, Oregon) and the event LOWBALL are used. The data is the solid line and the dashed line is the synthetic time series. Note that the waveform fit (dispersion and relative amplitude) is exceptional. This feature is important in order to make maximum peak-to-peak amplitude comparisons. The middle figure schematically shows the propagation paths for the synthetic seismograms. The path of length R is the actual source-to-receiver distance. The longer path is of length 40°. The bottom figures are of the two synthetic seismograms. The left one is calculated for the distance R (10.4° in this case) and the right seismogram is the one propagated out to 40°. They are plotted to the same time-scale. Note the much better dispersed wave train in the 40° case. The arrows in the right-hand figure mark the cycle or phase of the record which is used to obtain a M_S value.

To calculate M_S we use a modified version of the von Seggern formula (von Seggern 1977):

$$M_S = \log(A/T) + 1.08 \times \log(\Delta) + 4.38, \tag{9}$$

where A is one-half the maximum peak-to-peak amplitude (in microns) for periods between 17 and 23 s of a well-dispersed wave train measured from the vertical record, T is the period of the arrival measured in seconds, and Δ is the propagation distance in degrees. The original formula was modified to include the period correction and is the same at a period of 20 s. This formula was chosen because the distance coefficient (1.08) more closely approximates the effect of attenuation along continental paths (Basham 1971; Marshall & Basham 1972). Evernden (1971) found the distance coefficient to be 0.92 for M_S measurements at less than 25° and 1.66 for measurements at greater distances. This latter attenuation coefficient is more characteistic of mixed continental-oceanic path 20 s surface waves. Basham (1971) also found that the surface-wave magnitude distance coefficient for regional Rayleigh waves ($10 < T < 14$ s) is between 0.7 and 0.8. Marshall & Basham (1972) make similar assertions, but employ a distance correction which is a function of distance as well.

A vertical-component measurement has two advantages over horizontal-component measurements. The horizontal components usually have lower signal-to-noise ratios than the vertical component and generally are more likely to be contaminated by Love wave signals which may be generated by tectonic release, source effects, or scattering due to lateral variations in the earth's structure.

Both the regional and teleseismic (40°) synthetics are generated with the same site and source function, so that the peak-to-peak amplitude of the Rayleigh pulse of the regional synthetic can be directly related to the M_S value determined for a theoretical Rayleigh wave train propagated out to 40°. In order to reduce the effect of the various network instruments on the M_S measurement and any path correction, which might be made, the magnitude measurement was made on synthetics generated with the same long-period WWSSN instrument while the amplitude of the synthetic Rayleigh pulse was generated using the actual station instrument response. The relationship between the data peak-to-peak amplitude and its indirectly determined M_S is:

$$M_S(\text{data}) = M_S(\text{synth}\,|_{40°}) + \log[(PPA\,|_{\text{data}})/(PPA\,|_{\text{synth}})], \tag{10}$$

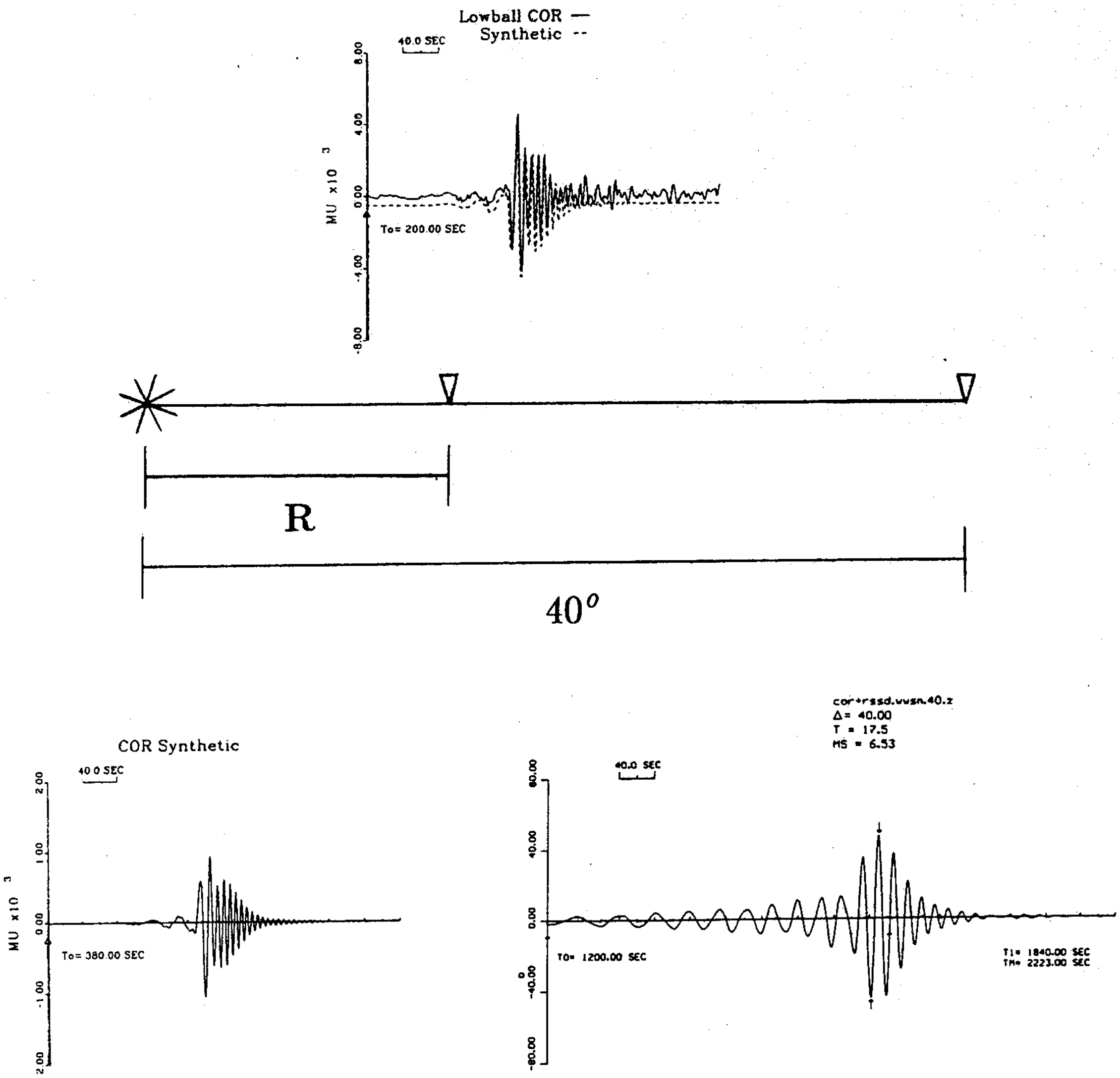

Figure 3. Schematic of the M_S calculation method: (a) the top figure is a comparison of observed-to-synthetic seismograms for the event Lowball recorded at the WWSN station COR ($\Delta = 10.4°$). This record shows a prominent Airy phase with a dominant period that is considerably less than 20 s. The solid line is the observed time series, and the dashed line is that of the synthetic seismogram. Both time series have been bandpass filtered between 60 and 6 s. (b) The middle figure shows the paths for which synthetic Rayleigh waves are calculated. There are two receiver distances. One, R, is the distance between the actual receiver and the source. The other distance is 40°. A synthetic generated for the distance R is made with a structure that best models the regional seismogram. (c) The bottom two figures show synthetic seismograms calculated for the two receiver distances for the COR path model. The left-hand one is for the actual regional path distance R; it is flipped in polarity with respect to the same synthetic in the top figure. The right-hand one is a Rayleigh wave propagated to 40°; the arrows denote the pulse that is used to calculate M_S. Notice that the dominant period for this case is 17.5 s. This pulse is considerably closer in period to 20 s than that of the regional seismogram which has a period near 12 s.

where PPA is the peak-to-peak amplitude of the Rayleigh pulse. A path correction may be included in this expression. This path correction is the difference between the individual path synthetic-derived M_S and the average theoretical M_S for the entire network. It also differs from a classical station correction that comes from the data and not the synthetics. Secondary station corrections based on the data were not used in this paper. For each source–receiver pair, a M_S is calculated from a synthetic seismogram propagated to 40°. Each such synthetic has the same site and source size, so ideally one would want all M_S values so measured to be equal in value. Yet this is not so, for each path's dispersion and effective attention at the periods measured may be different. The difference between the mean network synthetic M_S and a particular receiver M_S is the path correction. A negative path-correction value implies that the theoretical 40° station M_S is larger than the network average. Table 1 lists the network path corrections used.

The question arises whether or not it is valid to use the average earth structure for a particular path to propagate a surface wave to 40° when the earth model is only meant to reflect the seismic properties of the earth for a path that may only be a small fraction of this distance. This is particularly true of the shortest paths for which the seismic waves traverse only western North America, an area of relatively high attenuation compared to the continental craton and shield areas. A surface wave propagated 40° along a characteristic tectonic North American crust and mantle

Table 1. Network path corrections.

Dominant Period	Path Correction Dispersion	Path Correction Single Path	Path Correction Mixed Path 1	Path Correction Mixed Path 2	Station Name
11.5	-0.64	0.20	-0.07	-0.11	AAM
12.0	-0.61	0.18	-0.02	0.17	ALQ
13.5	-0.50	0.57	0.08	0.27	BKS
15.0	-0.38	-0.24	-0.28	-0.32	BLA
10.5	-0.71	0.18	0.00	-0.47	BLC
11.0	-0.67	-0.26	-0.02	0.16	BOZ
11.5	-0.64	-0.12	0.07	0.14	COR
11.0	-0.67	0.35	-0.12	0.09	DAL
12.0	-0.61	-0.03	-0.02	0.19	DUG
11.0	-0.67	-0.26	0.10	0.03	EDM
11.2	-0.66	0.26	-0.03	0.20	ELK
12.0	-0.61	-0.03	-0.03	0.12	EPT
12.0	-0.61	-0.22	0.06	0.01	FCC
12.5	-0.57	-0.22	-0.02	0.01	FFC
12.0	-0.61	-0.24	-0.12	-0.09	FLO
11.5	-0.64	0.18	0.18	-0.02	FRB
13.5	-0.50	0.45	0.20	0.25	FSJ
11.5	-0.64	-0.24	-0.12	-0.09	FVM
16.0	-0.30	0.18	0.40	-0.29	GAC
15.0	-0.38	-0.24	-0.15	-0.47	GEO
11.5	-0.64	-0.11	0.03	0.08	GOL
11.0	-0.67	0.26	-0.04	0.22	GSC
12.0	-0.61	-0.40	-0.11	-0.23	INK
11.0	-0.67	0.18	0.04	0.13	JCT
11.2	-0.66	1.06	0.02	0.26	KNB
11.2	-0.66	0.26	-0.05	0.20	LAC
12.5	-0.57	-0.13	-0.01	0.00	LHC
11.0	-0.67	0.20	0.01	0.17	LON
11.5	-0.64	-0.19	0.06	0.03	LUB
12.5	-0.57	-0.44	0.26	0.06	MBC
11.5	-0.64	0.18	0.37	-0.39	MNT
11.5	-0.64	0.26	-0.04	0.22	MNV
11.0	-0.67	-0.26	-0.03	0.14	MSO
10.5	-0.71	0.16	0.30	0.19	OGD
11.5	-0.64	0.18	0.40	-0.28	OTT
12.5	-0.57	1.12	0.03	0.27	PAS
11.0	-0.67	-0.26	-0.03	0.11	PNT
11.0	-0.67	-0.26	-0.04	0.10	RCD
11.5	-0.64	-0.39	-0.39	-0.59	RES
11.0	-0.67	-0.53	-0.17	-0.31	SCP
11.0	-0.67	-0.26	-0.05	0.07	SES
12.5	-0.57	0.03	0.04	0.09	SHA
11.5	-0.64	-0.03	-0.04	0.15	TUC
11.5	-0.64	0.45	0.16	0.27	VIC
11.5	-0.64	0.22	-0.30	-0.41	WES
12.5	-0.57	-0.40	-0.20	-0.23	YKC
19.5	-0.04	0.18	-0.02	0.17	ALQD
16.5	-0.27	0.20	0.01	0.17	LOND
16.5	-0.27	-0.53	-0.17	-0.31	SCPD
15.0	-0.38	-0.51	0.02	0.02	RSCP
16.0	-0.30	-0.09	-0.05	0.09	RSSD
15.5	-0.34	-0.19	-0.07	-0.05	RSON
16.0	-0.30	0.18	0.33	0.22	RSNY
15.5	-0.34	-0.40	-0.20	-0.23	RSNT
18.0	-0.16	1.21	0.01	0.19	JAS

model (NTS to DUG, for example) for 40° will be much more attenuated than a wave propagated the same distance through an average structure from NTS to eastern North America (NTS to SCP, for example). Hence the calculated M_S for the NTS to DUG structure would be smaller than the NTS to SCP M_S.

There are several methods to correct for this path-dependent effect. As explained above one may implement path corrections that account for the theoretical difference in attenuation between paths. Another means is to make a mixed-path structure that has the appropriate path structure from the source to the actual station distance, with the rest of the path out to 40° being a generic seismic velocity and attenuation model. For the cases in this study where the structures that comprise the mixed path are both continental structures (i.e. not too dissimilar) the approximation is robust enough for the synthetic-seismogram calculations.

We have implemented both procedures individually and in conjunction to see what their effects are. Another method would be to include empirical station corrections (Yacoub 1983; Given & Mellman 1986). Path correction effects are discussed in the results section.

Besides the M_S determination, we also calculated a time-domain moment for the same data. This time-domain, scalar moment is determined as follows:

$$M_0(\text{data}) = M_0(\text{synth}) \times [(PPA\,|_{\text{data}})/(PPA\,|_{\text{synth}})], \tag{11}$$

where PPA is the peak-to-peak amplitude of the Rayleigh pulse or Airy phase. This method is simpler than the M_S method and has the added advantage that the synthetic involves only two structures: the source region and the propagation path to the station. Path corrections were not incorporated into the time-domain M_0 determinations since the propagation-path synthetic takes the place of a path correction and we are not correcting to a generic (RSSD) structure. Making a correction based on the difference between the average station value and some mean for a collection of events is a form of the classical empirical station correction and is most useful when there are only a few stations reporting since a zero sum of the corrections is the usual constraint (Given & Mellman 1986). The mean moment can then be converted to an M_S using the moment-M_S relation for the generic structure (RSSD) propagated to 40°, i.e. the theoretical RSSD station magnitude

$$M_S(PPA) = \log M_0(PPA) - 11.38. \tag{12}$$

Figure 4 plots M_S versus $M_0(PPA)$ for the entire data set. The correlation between the two types of magnitude measurements is extremely good. The regression constant 11.43 is very close to the theoretical value 11.38 given above. Thus the difference between our best mixed-path M_S regression with moment, and the M_S moment relation for a pure path of the generic RSSD model is only 0.05 magnitude units. On first glance it might appear that both techniques are identical. However, even if all the stations had the same moment, the individual station magnitudes would be different due to different extended path lengths and possibly different structures from the station out to 40°. We try to reduce this difference by making the additional correction to a mean of the theoretical values for all stations

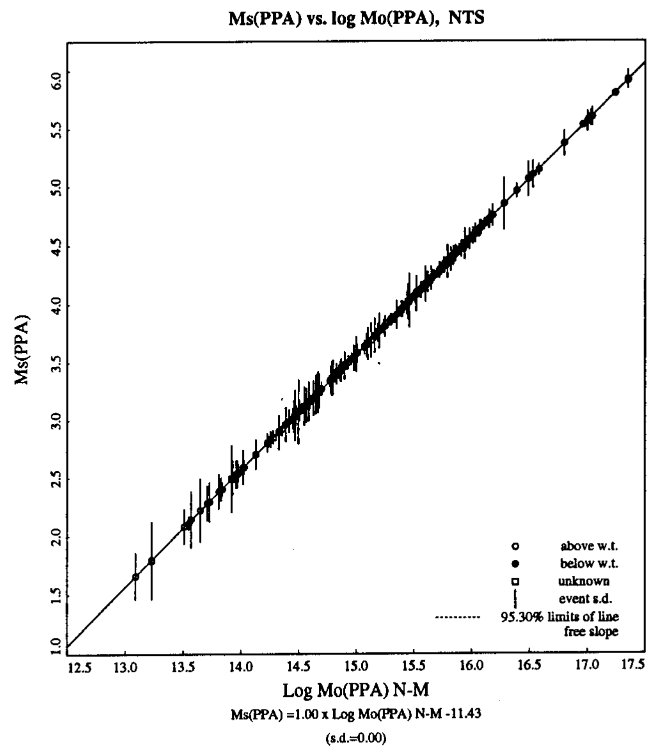

Figure 4. Time-domain M_S values regressed versus time-domain moments for all the events in this study. Note the extremely good correlation between the two scales. Vertical error bars are the variance for the individual events.

in the mixed-path evaluation. These observations imply that the RSSD model is a good average model for the network and that our M_S calculations are sound and result in robust measurements of surface-wave magnitude, which are not too dependent on which of the two techniques we use. In our analysis of the data we will use only M_S measurements. A table of the $\log M_0$ and their standard deviations will be given in Woods & Harkrider (1995).

Source structure significantly affects absolute surface-wave amplitudes, and hence surface-wave magnitudes or moments. For all of the synthetic seismograms generated, we used the Stevens (1986) and Given & Mellman (1986) NTS-source elastic structure, which is basically a Pahute Mesa velocity structure. By numerical simulations using a variety of different NTS structures, we found that for the frequencies of interest and sources in the upper 6 km the primary effect was due to the difference in shot-point velocity ratios. The size of the effect can be predicted extremely well from their explicit presence in the mixed-path expression, eq. (6). As an example, our Green's functions are computed for an explosive source at a depth of 600 m. In the Stevens (1986) source structure, the second layer starts at a depth of 500 m. There is a significant difference between the Poisson's ratio of the surface and second layer in the source earth structure. The log difference between the square of their compressional to shear velocities would predict from eq. (6) an M_S difference of 0.17. The actual difference between the M_S of a surface explosion and our Green's function is 0.16 with the near-surface explosion smaller as predicted. In order to reduce the effect of differing shot-point velocity ratios, Stevens (1986) suggested a new explosion moment, M_0', defined by

$$M_0' = 3\frac{\beta^2}{\alpha^2}M_0. \tag{13}$$

For a shot-point medium with Poisson's ratio of 0.25 ($\alpha^2/\beta^2 = 3$) the value of the moment is unchanged.

In Fig. 2, we see that for the WWSSN stations, denoted by three letters, the period of the dominant phase is significantly lower than the recommended lower cut-off of 17 s for the standard M_S formula. This period was determined by taking twice the time difference between the arrival of the largest peak and trough. We also calculated the 'instantaneous period' of this arrival and found it to be essentially the same value. The dominant period at each station is given in Table 1. For the WWSSN stations, the periods are between 10 and 15 s. Most are near 11 s. For the digital stations, denoted by four letters, the dominant period is between 15 and 19.5 s, with the average being 16.5 s. An alternative approach for using the maximum amplitude of Rayleigh wave observations where the dominant period is significantly different from 20 s was developed by Marshall & Basham (1972). Using the stationary-phase approximation they determined a path correction, which corrected for the dispersive characteristics of the path. Using observed dispersion curves for North America, Eurasia, mixed ocean-continent, and pure ocean paths, they were able to determine an M_S correction based on the period of an observed Airy phase to the 20 s period arrival in North America or Eurasia. The North American dispersion correction appropriate for the dominant period measured at each station in our network is also given in Table 1 (column 2). An advantage of our technique is that our path corrections are independent of recording instrument whereas Marshall & Basham's correction depends on the dominant period, which depends not only on dispersion but also instrument response. As an example, the station ALQ has a dominant period of 12 s and ALQD has a dominant period of 19.5 s.

An advantage that time-domain estimates of M_S or M_0 have over spectral estimates can be seen in Fig. 2. Except for the work of Patton (e.g. Patton 1991), the Green's functions used for spectral estimates of explosions have been fundamental Rayleigh and Love waves. As can be seen from the figure, it is very important to isolate the fundamental surface wave in the data for taking its spectra for moment estimates. The Rayleigh waves at almost every station show the additional presence of higher modes. The higher modes are primarily due to constructive interference of multiple reflected shear waves and are therefore very sensitive to lateral variations in crust and upper-mantle structure. This is especially true for non-parallel layers with sharp contrasts. Therefore, in the presence of nearby signals or noise, it makes more sense to use the larger time-domain amplitudes of the fundamental-mode Airy phases at regional distances. Because of the possibility of tectonic release, it is also necessary to determine the polarity of the surface wave. Again this is best done in the time domain, especially for Love waves.

If a spectral estimate is desired, comparing the Green's function with the data in the time domain should allow one to determine time windows and tapers so as reduce the contamination of spectral-amplitude estimates with higher modes and spurious scattered arrivals at intermediate ranges. And at close ranges where this may not be possible, it should help in deciding which time-domain amplitude measurements best represent the spectral amplitudes of the fundamental modes.

The question remains how well do either of these two measurements compare to spectral-moment estimates. For the events for which digital data were available, spectral-domain moments were also determined. Spectral moments were calculated using the method of Stevens (1986), with the exception that station corrections were not included in our moment calculations. Spectral moments were calculated in the bandwidth between 6 and 60 s. These spectral moments will be referred to as M_0. Moments were also obtained by inverting for an isotropic (explosion source) component (M_I) and a deviatoric component (caused by tectonic release or an asymmetric source cavity) of moment ($M_{\#}$). Details of these moments are the subject of a later paper by the authors (Woods & Harkrider, in preparation).

We compare the time-domain moments with these two types of spectral-domain moments. Fig. 5(a) compares $M_0(PPA)$ to $M_0(\omega)$ and Fig. 5(b) compares $M_0(PPA)$ to $M_I(\omega)$. $M_0(\omega)$ refers to the average spectral scalar moment and $M_I(\omega)$ refers to the isotropic source component determined from a moment-tensor inversion scheme (Woods & Harkrider, in preparation). $M_0(PPA)$ correlates well with the two types of spectral moments. The advantage of time-domain moments is that analogue data can be used directly and the effective SRN is lower than for spectral-moments methods, thus smaller events can be measured.

In the top figure there is some scatter in the moment correlation for several of the smaller events, with the time-domain moments being significantly larger than the spectral-domain moments. Most of these outlying events are Rainier shots, none is from Yucca and only one, REX, is from Pahute. REX ($M_0(PPA) = 15.35$, $M_0(\omega) = 14.87$) was detonated below the water table and had an anomalously large deviatoric moment component (Woods & Harkrider, in preparation). Since many more stations were used in the determination of the time-domain moments with a more complete azimuthal coverage, one would expect them to be less affected by the deviatoric component, which at NTS is speculated to be such that it will average out with adequate azimuthal coverage. The scatter is somewhat less in the $M_0(PPA){:}M_I(\omega)$ curve (Fig. 5b). In particular, REX no longer stands out, although several of the Rainer events lie well off the scaling curve. These outlying Rainier events can be explained in several ways. First, these events are relatively small and are only measured at very few stations (sometimes only one to three stations), thus the scatter, or error, in the moment measurement is larger. Also the spectral moment is more susceptible to noise contamination since it requires the isolation of a segment of the surface wave train from noise and the time-domain measurement only requires that the maximum amplitude not be too distorted by noise. One problem with this explanation is that there are other small events recorded at Pahute Mesa and Yucca Flat that lie right on the moment scaling curve (Fig. 5a) and these events are no better recorded than the Rainier events. Another possibility is that these outlying events

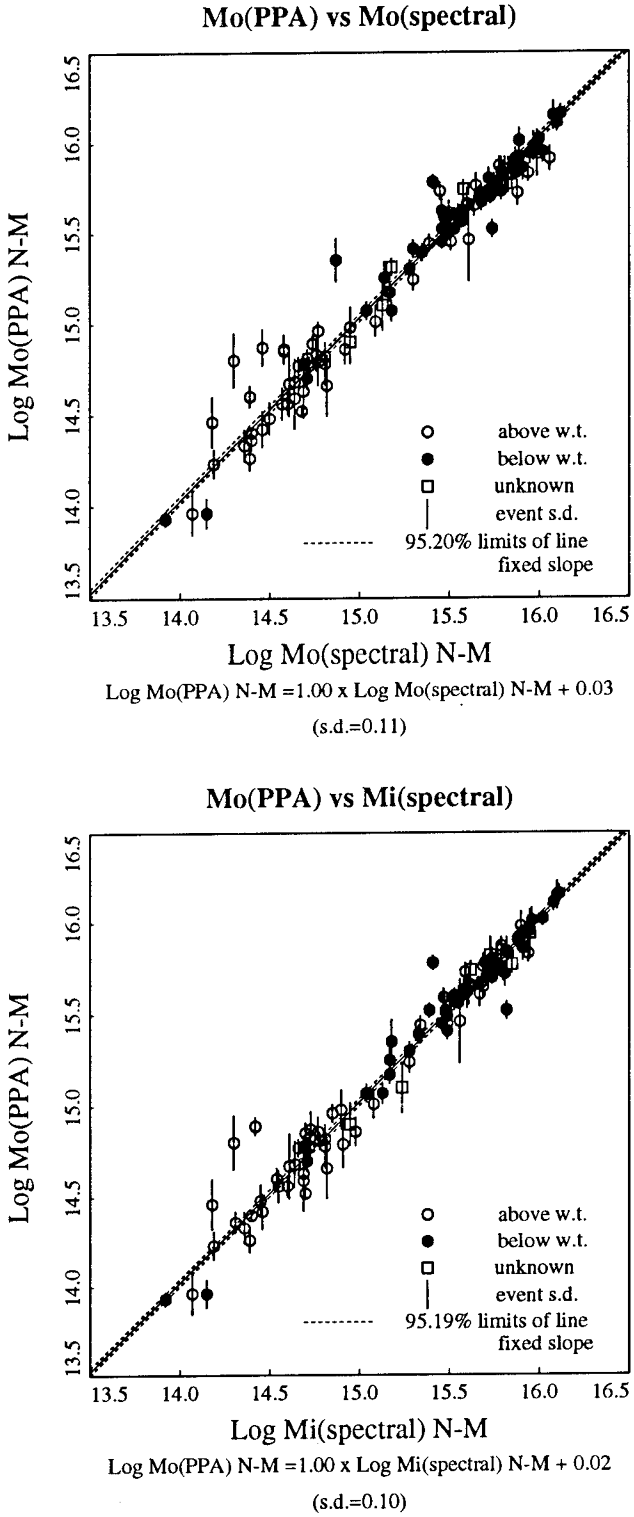

Figure 5. Time-domain log moments regressed against spectral-domain log moments. In the top figure spectral moments were determined assuming an isotropic source only, while in the bottom figure the spectral moments were determined by inverting for a isotropic source + a double-couple source. The regressions were constrained to a slope of unity.

reflect differences in source spectra. As discussed previously, the time-domain moments measure energy predominantly in the 10–14 s range, the period range of the continental Airy phase, whereas the spectral moment is an average of the spectral ratio between 6 and 60 s. So, it is possible that the Rainier test sites excite more high-frequency energy than do either the Phaute or Yucca site. This effect was seen in data at several of the closer stations, in particular.

DATA ANALYSIS AND RESULTS

The seismograms were bandpassed filtered between 6 and 60 s to minimize contaminating noise as described previously. The vertical records were visually inspected to ensure that the correct time window was used and that their signal-to-noise ratio was about 2.0 (approximately). M_S values were then calculated for the data as per the method described above (eq. 9) with several variations. The synthetic seismograms were also bandpassed filtered between 6 and 60 s for consistency. The M_S values are plotted against seismic magnitudes of several scales for the same set of events. It should be noted that no complete magnitude list was available for all 190 events.

We chose to compare or plot our data primarily with body-wave magnitudes determined by Lilwall & McNeary (1985). The Lilwall–McNeary (LM) data set contains 143 of the 190 events examined by us and is believed to be a well-determined and self-consistent list of m_b values that have small errors due to, among other things, the inclusion of network station corrections. Fig. 6 shows the m_b–yield relationship for events in this study for which m_b and yield information were available. It is important to notice that events above and below the water table separate into two distinct populations. For this data set this separation is only apparent near the cluster of events with m_b's around 5.4.

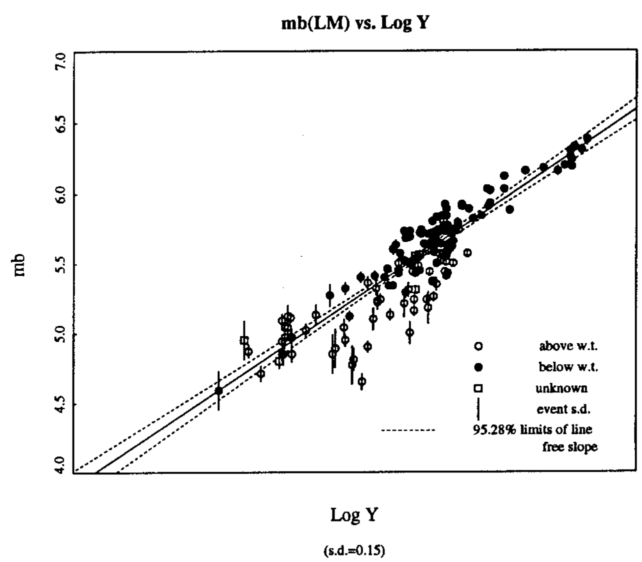

Figure 6. Lilwall m_b versus log Yield for events from this study. The solid line is the best-fitting regression line. The dashed lines show the 95 per cent confidence interval of this line. Lines through the data points represent one standard deviation in a datum measurement. Blackened circles represent sources beneath the water table, open circles are events above the water table and open squares are events for which this information is not known. Events detonated below the water table have a larger m_b for a given yield. Besides this separation of data, there is little scatter to the data. The consistency of the m_b–yield relationship makes it reasonable to use these m_b values to plot our M_S measurements against.

Also notice the very small error bars for this data; for many events the error bars are smaller than the symbols demarking a data point. The solid line is the best-fitting, least-squares curve, with the dashed curves being the two-sigma confidence interval of the regression relationship. The correlation between m_b and yield is good, with the scatter mostly being due to the above-water table shots. The slope of the regression curve is 0.67.

This scaling curve slope is slightly lower than that found in other studies of teleseismic m_b–yield scaling relationships. Marshall *et al.* (1979) found that m_b was proportional to $Y^{0.74}$ for well-coupled Yucca flat explosions, and proportional to $Y^{0.78}$ for explosions throughout NTS and Amchitka. Longer period telesiesmic body-wave magnitudes m_{LPP} introduced by Basham & Horner (1973) show that for events in tuff and rhyolite the amplitude of the arrivals is proportional to $Y^{0.72}$. Murphy (1977) compared theoretical m_b–yield scaling relations for cube-root scaling models and the modified Mueller & Murphy (1971) source model. He found that the yield exponent varies between 0.6 and 1.0 for the cube-root model in the yield range of interest, whereas the exponent is a constant 0.85 for their modified source model. Schlittenhardt (1988) found m_b to be proportional to $Y^{0.82}$ for NTS explosions. The empirically derived curves have errors in their slopes of the order of 0.05 to 0.1 units and are based on small sampling populations. The LM m_b–yield scaling relationship is determined from a significantly larger data set, making it at least as reliable as any other empirical scaling curve.

The same scaling law slope (~0.67) holds for the LM data when they were separated with respect to test-site and shot-medium coupling (whether detonated above or below the water table). There is consensus in the literature that that seismic coupling is a function of the percentage dry (or gaseous) porosity of a material. In a study of small-scale, high-explosive experiments with 15 rock types, Larson (1981) found for a given size explosion that the elastic radius of a porous material (such as tuff) increased with increasing water content. The dominant non-linear mechanism (within the plastic radius) working at low yields appears to be pore crushing of the surrounding material (Stevens 1991). Non-linear finite-difference calculations (Bache 1982) also indicate that porosity is the most important characteristic of NTS tuff for seismic-coupling purposes. In the same study, source functions for Yucca Flat wet and dry tuff are significantly different, with the long-period amplitude of wet tuff being larger by 50 per cent and its corner frequency being lower. Springer (1966) has observed this effect for teleseismic P-wave amplitudes. Patton (1988), Gupta *et al.* (1989), and Vergino & Mensing (1989) have observed this coupling effect in regional phases such as L_g, P_n and P_g.

Several sets of synthetic Rayleigh waves were generated at the 40° distance for calculating M_s. One set was propagated along the single-structure model (hereafter referred to as the single-path case) which reflects the average earth structure between NTS and a given station. We also generated mixed-path synthetics for which that part of the path beyond the actual source–receiver distance, out to 40°, the surface wave is propagated along a generic earth structure. The NTS–RSSD Earth structure was chosen for this generic path section, as it is a relatively simple structure that generates stable surface waves and it is roughly an intermediate range station (distance < 1900 km), so that its structure can be considered to be an 'average' North American structure for the network.

Surface magnitudes were first calculated from the 40° synthetics generated with a single-structure propagation path. Figs 7(a) and (b) display single-path m_S values, calculated as described above, versus body-wave magnitude (m_b). These m_b's are those of Lilwall & McNeary (1985). In the upper figure (7a) M_S is calculated without path corrections, whereas M_S is calculated with path corrections in the lower figure. The vertical error bars represent the one standard-deviation confidence interval for each M_S value. The solid line is the best-fitting weighted least-squares regression of the data, with the weighting factor being inversely proportional to individual event variances. The dashed lines represent the two standard-deviation error (assuming a Student t distribution) of the fit of the line to the data. Since Student t statistics (Lapin 1983) are functions of the sample size, the confidence level will vary with data set size. Solid black circles are shots below the water table, open circles are shots above the water table, and open squares are shots for which this information is not known. Note the error bars are approximtely 50 per cent larger for the uncorrected M_S's (Fig. 7a) than for the case of path-corrected M_S's (Fig. 7b). The scatter in the data is also significantly less for the path-corrected M_S's as evidenced by the reduction of the standard deviation of the free-slope regression. Although, it should be noted here and for the following discussion that the success of these techniques is not in how well they reduce the standard deviation from some assumed linear relation between surface and body-wave magnitudes, but how well they reduce the variance or standard deviation of the magnitude determination of an individual event, and even more important, their ability to include small events in the data base where teleseimic data was too sparse for determining a classical M_S. On the other hand, it is interesting that the standard deviation for the LM body-wave magnitudes versus yield is 0.15 and our best regression between M_S and their m_b for the same explosion data set is 0.26. Both regressions are improved when the events are separated into different populations. When we get to Figs 15 and 16, which are our regressions on log yield, you will see that our regression standard deviations are quite competitive with those of m_b for events restricted to NTS below the water table and Rainier.

There are two significant effects of including path corrections. One is the reduction in variance of individual magnitudes. Without path corrections the individual station magnitudes have a bi-modal distribution reflecting the two generic earth models of North America: the tectonic western and stable cratonic eastern crust and upper-mantle structures. The path corrections bring in the outlying station magnitude values towards the mean value. Including path corrections for the single-path derived M_S's increases the average value by 0.14 units (or 32 per cent). This effect can be attributed to the smaller events that are brought more in line with the curve containing larger events. This in turn is due to the fact that the smaller events are only observed at nearer stations in tectonic North America (TNA), for which path structures exhibit higher attenuation than do more cratonic or shield-like models, so that surface

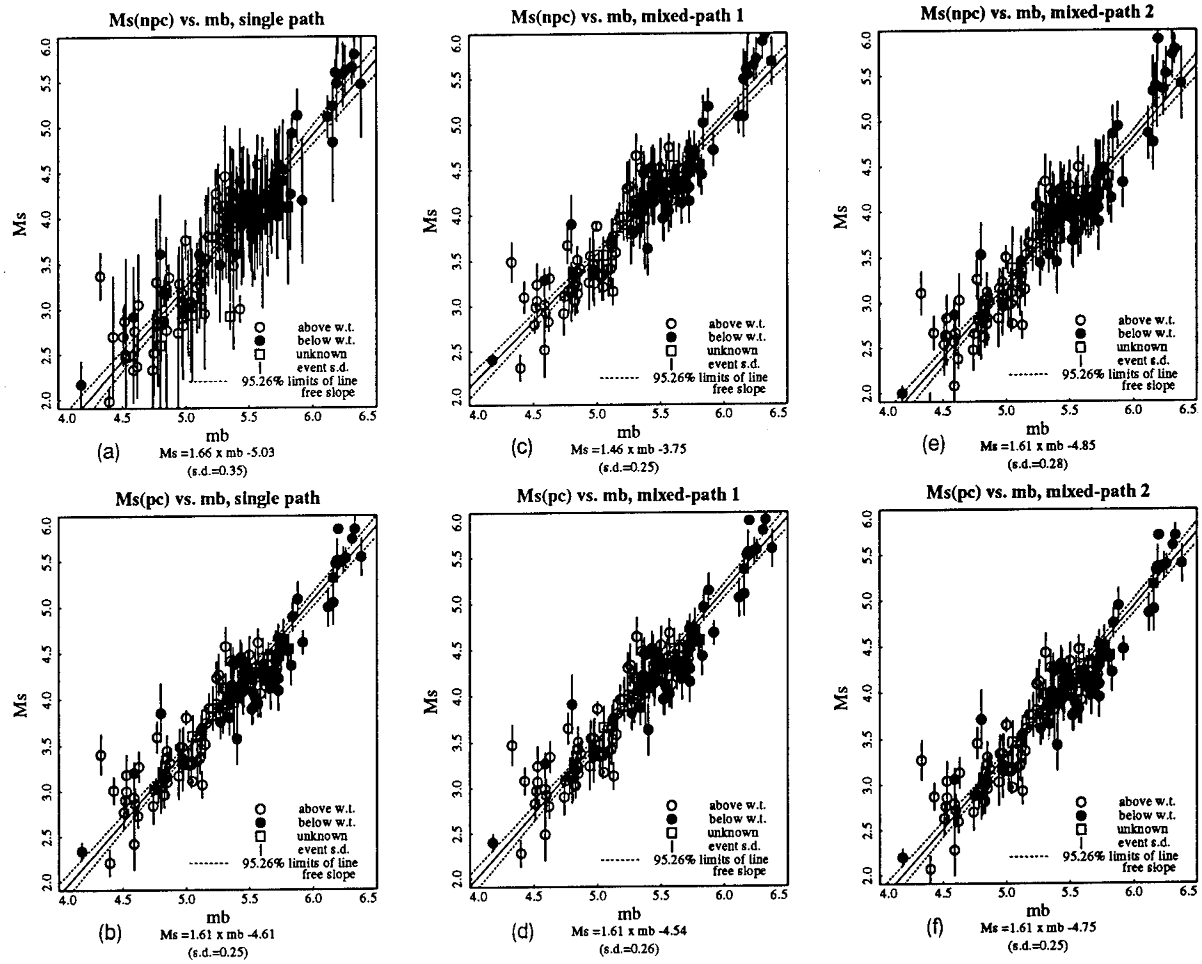

Figure 7. Here M_S is plotted versus Lilwall m_b's. For the left figures M_S is calculated with single-path Green's functions, without path corrections (npc) and with path corrections (pc). The best-fitting regression model is the solid line running through the data points. The dashed lines are the two-sigma confidence intervals of the line. The M_S–m_b relationship and the rms error of the data are at the bottom of each figure. The middle figure M_S values are determined using the mixed-path-1 synthetics and in the right two figures mixed-path-2 Green's functions were used.

waves propagated along a TNA path for 40° will be significantly more attenuated than waves propagated along a craton or shield path for that same distance. Path corrections reduce this effect significantly for the single-path derived magnitudes. Table 1 lists these network-path corrections. The third column lists the corrections for single-path synthetics. A positive value denotes that the M_S for a station is smaller than the network theoretical average.

We next explored the effect of mixed-path transfer functions upon the M_S calculations. As described above, we chose the path to RSSD as a generic structure for the second portion of the mixed-path synthetic seismogram calculations. We generate two sets of these synthetics. The difference between these two mixed-path earth structures is their spectral attenuation coefficients, with $\gamma(\omega)$ being twice as large, at a given frequency, for the mixed-path-2 case as for the mixed-path-1 case. Fig. 8 is a plot of the attenuation factor ($\gamma(\omega)$) as a function of period. The line labelled RSSD $\times$ 2 is that of the increased attenuation model. It is referred to as 'mixed-path 2' throughout this study. The lower, dashed curve is the attenuation curve for the RSSD structure. Synthetics made with this RSSD generic structure for the latter portion of the 40° travel path will be referred to as 'mixed-path 1'. Table 1 gives the path corrections for each station for these two cases, also.

The network averages and their standard deviations for the three different path assumptions are

Single path

$$M_S(PPA) = \log M_0 - 11.50, \tag{14}$$

with a standard deviation of 0.38.

Mixed-path 1

$$M_S(PPA) = \log M_0 - 11.44, \tag{15}$$

with a standard deviation of 0.17.

Mixed path 2

$$M_S(PPA) = \log M_0 - 11.64, \tag{16}$$

with a standard deviation of 0.22.

These standard deviations are only a measure of the spread of the theoretical network path corrections for a given moment. The above standard deviations could also be found from squaring and summing the path-correction values in their respective columns in Table 1 after removing the three digital stations that have the same correction as

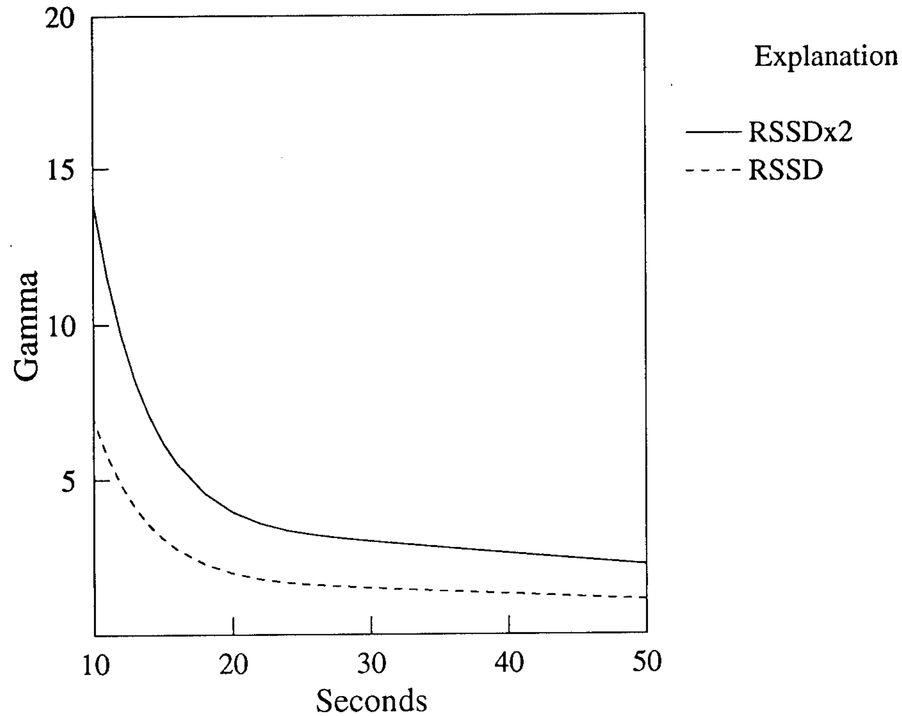

Figure 8. The two attenuation models for the generic portion of the hybrid propagation model are plotted versus period. Gamma is the attenuation coefficient (eq. 1) at a given period. Model RSSD × 2's attenuation is twice that of the RSSD model. M_S values calculated with synthetics using model RSSD are referred to as mixed-path 1, while values determined from synthetics created using attenuation model RSSD × 2 are referred to as mixed-path 2.

their analogue entries. It should be remembered that the 40° M_S were all calculated using the same WWSSN long-period instrument response and thus the path corrections are instrument-independent. In relating theoretical station amplitudes to M_S, the actual station instrument response is removed. The previously discussed regression constant of 11.43 for the entire data set differs slightly from the theoretical network value of 11.44 given in eq. (15) primarily because the individual observed values are not always determined using the full network of stations.

In Figs 7(c) and (d) the M_S magnitudes were calculated using synthetic seismograms using the mixed-path-1 model. In Fig. 7(c) the M_S's are calculated without path-correction terms, while in Fig. 7(d) path corrections are included. The addition of the path-correction terms cuts the data variance, but by no more than 25 per cent, and then not in all cases. Assuming a fixed-slope regression ($m = 1.50$), there is no offset in the intercept between the uncorrected and path-corrected M_S's. So using a generic structure for the remainder of the 40° path acts as a path correction as well.

Figures 7(e) and (f) are M_S versus m_b plots for the mixed-path-2 case without and with path corrections, respectively. It should be noted that the slope of the regression line is nearly the same (1.61) for all three path-corrected cases (Figs 7b, d and f) and that the difference in the regression intercept between the three cases is essentially what one would predict from the three theoretical network intercepts given in eqs (14), (15) and (16). This should not be surprising since the determined moment for each event is the same from figure to figure and on average their slopes should be equal and the differences in M_S between the three figures should be close to the difference in the theoretical network values. If explosions at only one site are plotted, the slope of the curve is closer to 1.5, so that we will take the M_S–m_b scaling relationship to be:

$$M_S = 1.50 \times m_b + B. \tag{17}$$

For this fixed-slope scaling relationship, the uncorrected and path-corrected mixed-path-1 M_S curves have the same intercept, whereas for the mixed-path-2 case the intercept is 0.10 units larger for the path-corrected curve than for the uncorrected curve. For path-corrected M_S's, the mixed-path-1 intercept is 0.21 log units greater than that of the mixed-path-2 curve. Because mixed-path synthetics are propagated to 40° along a more attenuative path, the M_S measured also will be smaller.

For the single-path case, path-corrected M_S values give the same relationship (slope = 1.61), but the slope is larger (1.66) for the uncorrected magnitudes, although the difference lies within the errors bounds. It would seem that both path corrections and mixed-path Green's functions improve M_S determinations for the method used here. The most consistent, reliable magnitudes are obtained using mixed-path-generated synthetics in conjunction with path corrections for the 40° M_S measurements. The variance among the mixed-path-based M_S values for the network is smaller than that when M_S is derived from single-path synthetics, so that magnitude measurements will be more consistent when they are determined from mixed-path synthetics. This is particularly important for events with few reporting stations. All further plots of M_S in this study use values obtained from the mixed-path-1 case with path corrections, unless stated otherwise.

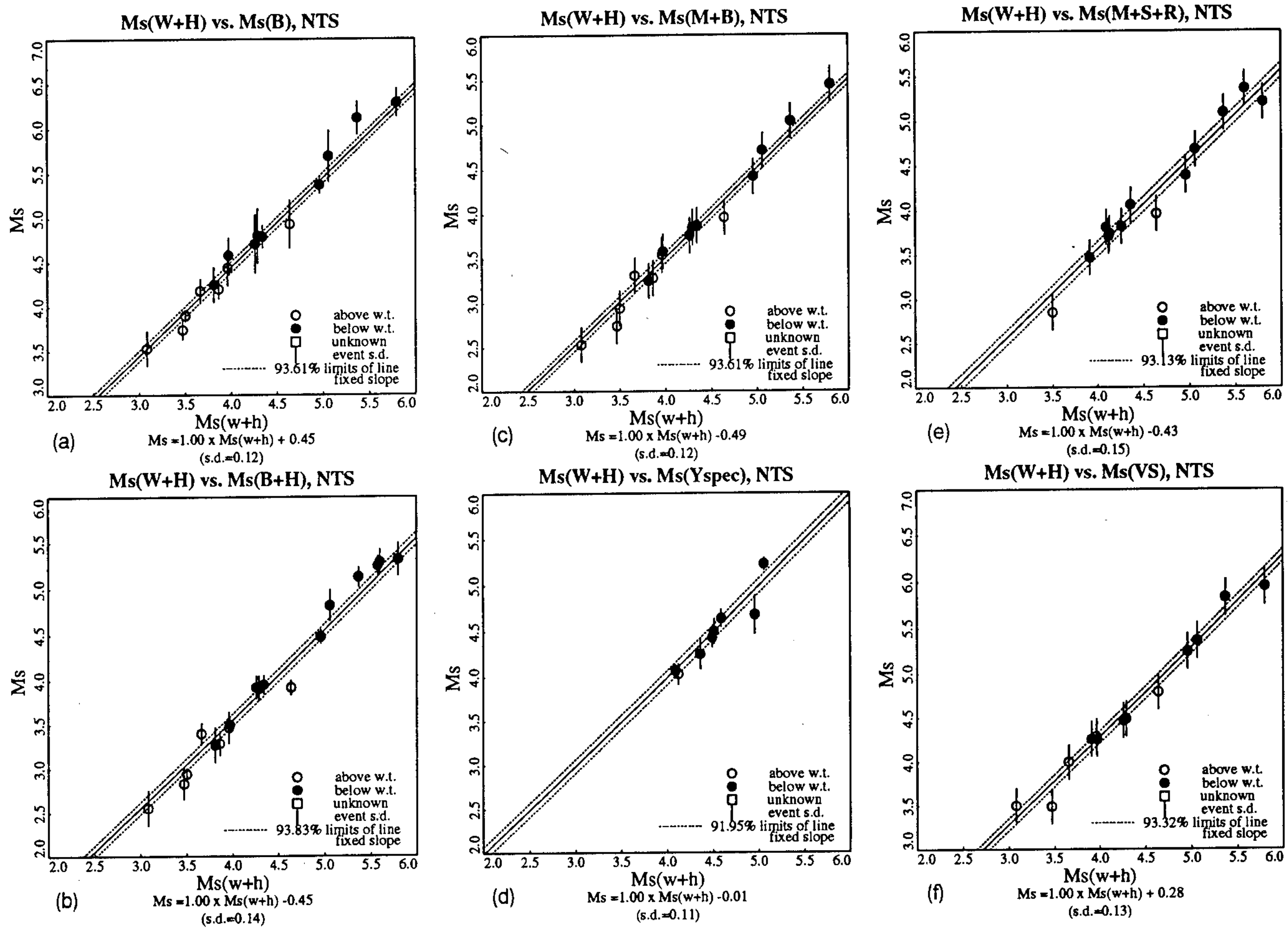

Figure 9. M_S of this study regressed against those determined by other studies.

How well the final M_S values reflect the actual seismic magnitude of these events necessitates having another measure of their size. In the event of anomalously high or low seismic-source coupling, for example, both body waves and surface waves should be affected similarly by coupling effects. A magnitude parameter independent of seismic observations would be useful to plot the M_S against, so we have also fitted our results to estimate log yields. These relationships are shown and discussed later in the paper. Yield values are estimated to be within 10 per cent of the actual yield (Springer & Kinnaman 1971). Yield information was available for 174 of the events, thus yields make up the most comprehensive data set with which to compare our results. The yields for this data set range over three orders of magnitude in size. The greatest scatter, as in the case of m_b versus log yield, is due to shots above the water table. It should also be kept in mind that the scatter would be further reduced if the data were separated into populations based on their location at NTS (i.e. Pahute Mesa, Rainier Mesa and Yucca Flat).

Since our magnitude values are based on theoretical continental structures, as well as the particular network used, we wanted to compare our M_S values to those obtained from more standard M_S methods. In addition, the reference distance of 40° is arbitrary and along with differing magnitude formulae will result in an offset from previous studies. In order to make it possible for readers to convert our values to the results of others, we regressed on magnitudes of mutual events. Fig. 9 shows our M_S values (x axis) versus those from six other studies (y axis) (Basham 1969; Marshall & Basham 1972; Marshall *et al.* 1979; Basham & Horner 1973; Yacoub 1983; von Seggern 1973). The overlap in data sets varies between 8 and 16 events. We performed a fixed-slope (slope = 1.0), linear regression of our M_S values to those of the six outside studies; in general the correlation is very good. It is important to note that with our method we are able to measure M_S for events one tenth the size of the smallest events measured in the other studies (i.e. $M_S = 1.75$ to 2.0). This is after having corrected for differences in absolute M_S scales. We are able to measure M_S for these smaller events because we are able to make use of near-regional (<500 km) records with the method described in this paper.

The offsets in M_S values vary considerably. This offset is due in part to the difference in definition of M_S for each study, in particular the distance-correction term. As discussed earlier, we chose the distance-correction term $(1.08 \times \log(\Delta))$, whereas the other studies use a variety of terms. Yacoub (1983) and Basham (1969) use variations of the Prague formula: $(1.66 \times \log(\Delta))$ Båth (1967). von Seggern (1973) used a slightly smaller distance factor $(0.9 \times \log(\Delta))$ than that of his later study which we use. The other three studies use distance corrections developed by Marshall & Basham (1972) and all are approximately

0.45 magnitude units smaller than ours. If we had used the Prague formula at a distance of 40°, our magnitudes would have been only 0.15 units smaller. The difference in distance-correction factor is believed to be the primary cause of the offset in magnitude between their results and ours. Our distance correction is also dependent upon the generic path structure chosen to generate the 40° synthetics.

These three studies, as well as that of Basham (1969), use mostly, if not all, data recorded at Canadian stations; thus their networks have strong azimuthal and distance biases as well, which may also affect magnitude measurements. It should be noted that the method described in this study to calculate M_S also is based upon a theoretical network average M_S, so it will have a bias attached to it which is dependent upon the network used. This network bias may be responsible for part of the offset, as well. Our network does have considerably better azimuthal coverage than these other studies, so that tectonic-release effects upon the long-period radiation, assuming strike-slip faulting, should be mitigated, thus giving more accurate M_S measurements.

A significant difference between our M_S calculations and those of the other studies is that we include data from close-in stations. Since the 40° synthetics used to calculate M_S travel further along an arbitrary path model for these nearer stations, it is important to consider whether or not our M_S values have some functional dependence upon distance. Fig. 10(a) plots relative station M_S versus distance for the entire data set. No apparent distance dependence is observed. We also examined this relation for individual events and found the evidence more compelling that there is no distance dependence for the M_S values, which makes this M_S method very attractive, particularly for small events, for which Rayleigh wave amplitudes are measurable only at near distances, since there will be no bias in magnitude values between large and small events. Fig. 10(b) shows the relative station M_S versus azimuth. There is some variation with azimuth. This is to be expected for we do not take into account tectonic release in our M_S calculations. Azimuthal variations in propagation paths, caused, perhaps, by different tectonic regions may also contribute to this effect. The potential bias due to azimuthal averaging of our network and those of previous studies is discussed in the sequel paper as a function of the orientation and strength of tectonic release at NTS.

As pointed out by an anonymous reviewer, there is no physical significance to the magnitude-offset constant, and it only matters for comparison with other studies. It was suggested that we could renormalize our M_S values, i.e. change the constant in the our modified M_S formula, eq. (9), so that they then could be used together with other M_S measurements, e.g. on an m_b versus M_S plot with earthquakes where the earthquake is determined by standard means. Unfortunately, very few explosion studies have been made using standard means. We recommend the use of explosion moments for that purpose since they have a physical interpretation and have very few arbitrary assumptions in their determination. In this paper, we prefer to give the regression-conversion constants between the various explosion studies. They can be found in the labels on Fig. 9 but for convenience, we give them here. In order to convert our values to those of Basham (1969), add 0.45; Marshall & Basham (1972), subtract 0.49; Basham & Horner (1973), subtract 0.45; von Seggern (1973), add 0.28; Marshall *et al.* (1979), subtract 0.43; and Yacoub (1983), subtract 0.01. As an example, if we modify our regression relation between M_S and $\log M_0$ for NTS (Fig. 4) to Marshall *et al.* (1979) M_S values using the above, we obtain $M_S = \log M_0 - 11.85$. This is in fair agreement with the observation by Stevens & McLaughlin (1986) that $M_S = \log M_0 - 12.00$ fit well for NTS, Novaya Zemla and Amchitka explosions using Marshall *et al.* (1979) M_S values for NTS and Amchitka. Only six NTS events were on the figure showing this. Later in the report, 15 NTS explosions, with 11 Marshall, Lilwall & Farthing (1986) and 4 NEIC determinations of M_S, were plotted versus $\log M_0$ and these were in much better agreement with our converted constant of 11.85 than their three-test-site value of 12.00. In Stevens (1986), it was found that 11.86 fitted his East Kazakh explosion moments using Sykes & Cifuentes (1984) M_S values for the 10 events they had in common.

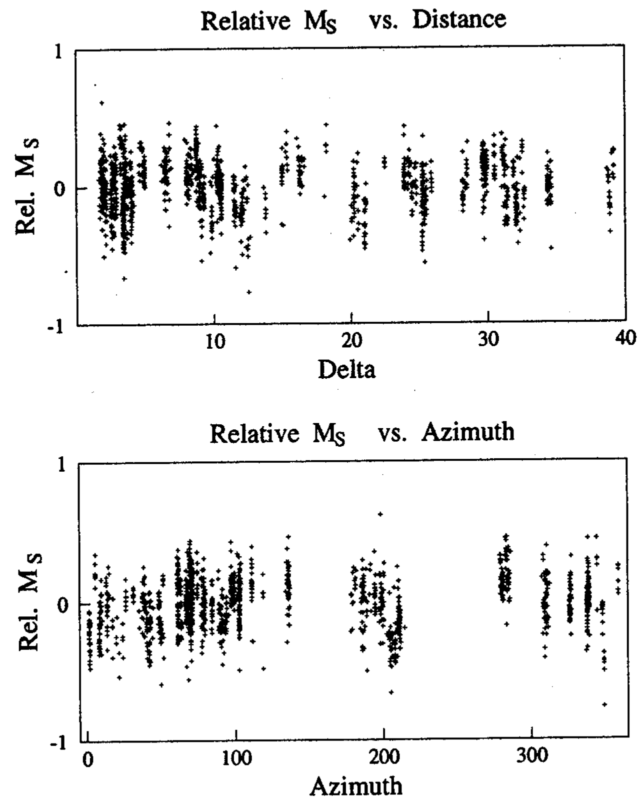

Figure 10. Relative M_S (individual station–network average) versus distance (top figure) and azimuth (bottom figure). M_S values do not appear to be a function of distance. There also is no apparent functional relationship between azimuth and M_S; some azimuths are not covered, however.

Table 2 lists the final mixed-path-1, path-corrected M_S values for the 190 events of this study. The first column lists the number of stations recording the event. Next the surface-wave magnitude and associated error for the event are given. This is followed by a three-letter shot-information code. The first letter denotes its geographic location: Yucca (Y), Pahute (P), Rainer (R), or Climax Stock (C). The second is whether its shot depth was above (A) or below (B) the water table. The last letter describes the shot-site rock as tuff (T), rhyolite (R), granite (G), or alluvium (A). An underscore means that the information is not known.

Table 2. Event information.

No. Sta.	M_S	M_S s.e.	Shot Info.	Event	Julian Date	No. Sta.	M_S	M_S s.e.	Shot Info.	Event	Julian Date
1	2.49	-	R__	Rainier	57262	5	3.86	0.04	YAT	Yard	67250
1	3.25	-	R__	Logan	58289	1	2.08	-	YAA	Marvel	67264
1	3.73	-	R__	Blanca	58303	9	3.64	0.05	YBT	Cobbler	67312
1	2.96	-	NBG	Hardhat	62046	10	5.40	0.06	NBT	Faultless	68019
1	2.89	-	YAA	Dormouseprime	62095	6	3.53	0.05	RAT	Dorsalfin	68060
1	3.57	-	YA_	Aardvark	62132	4	2.85	0.06	N__	Buggy1	68072
1	3.12	-	YAA	Haymaker	62178	3	5.80	0.01	PBR	Boxcar	68117
1	3.69	-	YAA	Sedan	62187	10	4.75	0.09	PAT	Rickey	68167
1	3.66	-	YA_	Mississippi	62278	11	4.48	0.06	PAR	Chateaugay	68180
2	4.85	0.22	YBT	Bilby	63256	9	3.43	0.08	RAT	Hudsonseal	68268
1	3.77	-	RAT	Clearwater	63289	1	3.14	-	YAA	Crew	68309
2	3.07	0.28	YAL	Handcar	64310	4	3.66	0.10	PAT	Schooner	68343
2	2.54	0.08	YAA	Merlin	65047	4	5.92	0.08	PBT	Benham	68354
1	2.82	-	NAA	Wishbone	65049	11	4.03	0.05	RAT	Wineskin	69015
12	3.97	0.06	YBT	Wagtail	65062	1	3.20	-	RAT	Cypress	69043
6	3.96	0.07	YAT	Cup	65085	15	4.06	0.04	YBT	Blenton	69120
1	2.59	-	PAR	Palanquin	65104	9	5.58	0.05	PBT	Jorum	69259
4	2.40	0.06	PBT	Buteo	65132	9	4.68	0.05	PAR	Pipkin	69281
4	3.08	0.09	NAA	Dilutedwaters	65167	3	2.11	0.06	YAT	Cruet	69302
7	3.66	0.05	YAT	Charcoal	65253	3	2.53	0.12	YAT	Pod	69302
5	3.81	0.09	YBT	Lampblack	66018	4	4.36	0.14	YBT	Calabash	69302
8	3.91	0.12	PBT	Rex	66055	2	3.17	0.02	R__	Dieseltrain	69339
13	3.96	0.07	PAR	Duryea	66104	2	3.34	0.05	RAT	Dianamist	70042
5	3.47	0.11	NAT	Pinstripe	66115	2	3.46	0.05	YAT	Cumarin	70056
3	2.81	0.05	YAA	Cyclamen	66125	2	3.22	0.18	YAA	Yannigan	70057
11	4.01	0.10	PAR	Chartreuse	66126	3	2.14	0.24	YAT	Cyathus	70065
15	4.34	0.04	YBT	Piranha	66133	3	1.66	0.20	YAT	Arabis	70065
6	3.50	0.06	YAT	Discusthrower	66147	2	2.22	0.27	YAA	Jal	70078
26	4.27	0.04	CBG	Piledriver	66153	17	4.29	0.05	YBT	Shaper	70082
18	4.29	0.03	YBT	Tan	66154	8	5.56	0.08	PBT	Handley	70085
3	2.70	0.13	YAA	Vulcan	66176	5	3.35	0.13	RAT	Mintleaf	70125
3	5.06	0.15	PBR	Halfbeak	66181	7	3.76	0.08	YAT	Cornice	70135
3	5.37	0.11	PBT	Greeley	66354	13	3.54	0.06	YAT	Morrones	70141
2	2.39	0.05	YAA	Ward	67039	2	1.79	0.33	YAT	Manzanas	70141
1	2.38	-	YAA	Persimmon	67053	5	3.12	0.06	RAT	Hudsonmoon	70146
5	4.55	0.09	YAA	Agile	67054	16	4.12	0.07	YAT	Flask	70146
7	4.96	0.06	YBT	Commodore	67140	2	2.40	0.10	YAA	Embudo	71167
10	4.64	0.07	PAR	Knickerbocker	67146	4	3.01	0.09	YAT	Laguna	71174
3	3.46	0.05	RAT	Midimist	67177	4	3.21	0.02	YAT	Harebell	71175
2	3.03	0.14	RAT	Doormist	67243	10	3.16	0.06	RAT	Camphor	71180
15	4.13	0.03	YBT	Miniata	71189	11	4.40	0.05	YAT	Baseball	81015
21	3.63	0.06	YBT	Algodones	71230	10	4.18	0.07	YBT	Rousanne	81316
2	2.59	0.06	YAT	Pedernal	71272	9	4.67	0.05	YBT	Jornada	82028
4	2.59	0.04	YAT	Cathay	71281	10	4.52	0.06	PBR	Molbo	82043
4	2.29	0.17	YAA	Longchamps	72110	8	4.41	0.08	PAR	Hosta	82043
7	3.44	0.10	RAT	Mistynorth	72123	4	2.99	0.10	YAT	Tenaja	82107
5	3.27	0.06	YBT	Monero	72140	6	4.44	0.05	PAT	Gibne	82115
7	3.35	0.06	RBT	Diamondsculls	72202	15	4.29	0.04	YBT	Bouschet	82127
1	2.50	-	YA_	Delphinium	72270	9	4.52	0.05	PAR	Nebbiolo	82175
12	4.09	0.04	YBT	Miera	73067	9	3.04	0.10	YAT	Monterey	82210
22	4.09	0.03	YBT	Starwort	73116	9	4.73	0.05	YBT	Atrisco	82217
8	3.35	0.08	RAT	Didoqueen	73156	8	3.38	0.05	RAT	Huronlanding	82266
5	5.10	0.12	PBR	Almendro	73157	5	3.54	0.11	RAT	Frisco	82266
15	4.35	0.05	YBT	Latir	74058	2	2.49	0.29	YAA	Seyval	82316
8	3.43	0.08	RAT	Mingblade	74170	6	3.13	0.09	YAA	Manteca	82344
20	4.59	0.05	YBT	Escabosa	74191	2	1.80	0.01	YAA	Cerro	82245
13	3.96	0.05	YBT	Stanyan	74269	3	2.52	0.08	YBT	Borrego	82272

Table 2. (*Continued.*)

No. Sta.	M_S	M_S s.e.	Shot Info.	Event	Julian Date	No. Sta.	M_S	M_S s.e.	Shot Info.	Event	Julian Date
15	4.02	0.04	YBA	Cabrillo	75066	11	4.01	0.05	PAR	Cabra	83085
3	3.24	0.18	RAT	Diningcar	75095	20	4.15	0.05	YBT	Torquoise	83104
13	3.74	0.05	YBT	Obar	75120	7	2.83	0.07	YAA	Crowdie	83125
10	4.65	0.06	PBR	Stilton	75154	12	3.34	0.05	YAT	Fahada	83146
23	4.51	0.06	YBT	Mizzen	75154	10	2.93	0.06	YAA	Danablu	83160
3	5.53	0.02	PBT	Camembert	75177	12	4.17	0.06	PAR	Chancellor	83244
1	3.37	-	RAT	Huskypup	75297	3	3.04	0.22	R__	Midnitezephyr	83264
4	5.59	0.07	PBT	Kasseri	75301	5	2.50	0.04	YBT	Techado	83265
3	5.91	0.02	PBT	Muenster	76003	11	3.81	0.06	YAT	Romano	83350
14	4.49	0.05	YBT	Keelson	76035	9	3.42	0.06	RAT	Midasmyth	84046
8	5.56	0.09	PBT	Fontina	76043	1	2.28	-	YAA	Agrini	84091
13	5.15	0.05	PBR	Cheshire	76045	19	4.40	0.04	YBT	Mundo	84122
6	5.62	0.11	PBT	Colby	76074	11	4.48	0.06	YBT	Caprock	84152
3	3.23	0.17	RAT	Mightyepic	76133	4	3.16	0.17	YAT	Duoro	84172
8	4.24	0.05	YBT	Rudder	76363	21	4.18	0.07	PAR	Kappeli	84207
18	4.17	0.04	YBT	Bulkhead	77117	6	2.90	0.09	YAT	Correo	84215
10	4.09	0.05	YBT	Crewline	77145	3	3.08	0.03	YAT	Dolcetto	84243
27	4.29	0.04	YBT	Lowball	78193	5	3.58	0.08	YAT	Breton	84257
4	3.12	0.17	R__	Diablohawk	78256	4	2.80	0.08	YAA	Villita	84315
13	3.87	0.05	YBT	Quargel	78322	12	4.23	0.06	PAT	Egmont	84344
21	4.35	0.04	YBT	Quinella	79039	14	4.22	0.06	PAR	Tierra	84350
22	4.14	0.05	YBT	Pyramid	80107	11	4.43	0.07	YBT	Tortugas	84061
6	3.36	0.13	RAT	Minersiron	80305	5	3.39	0.06	YAT	Vaughn	85074
4	4.03	0.23	YAT	Cottage	85082	10	4.42	0.07	PAR	Cybar	86198
8	4.72	0.08	YBT	Hermosa	85092	2	2.97	0.02	YAA	Cornucopia	86205
7	3.47	0.12	R_T	Mistyrain	85096	8	4.29	0.07	PAR	Labquark	86273
19	4.37	0.06	PBT	Towanda	85122	7	4.34	0.05	P__	Belmont	86289
13	4.46	0.05	PBR	Salut	85163	5	4.58	0.07	YBT	Gascon	86318
12	4.30	0.05	PAR	Serena	85206	7	4.55	0.08	P__	Bodie	86347
4	3.24	0.13	YAT	Ponil	85270	4	4.38	0.10	P__	Delamar	87108
8	4.19	0.09	YBT	Kinibito	85339	8	4.47	0.07	PAT	Hardin	87120
8	4.19	0.06	P__	Goldstone	85362	4	3.66	0.14	Y__	Midland	87197
4	4.07	0.06	YBT	Glencoe	86081	5	4.60	0.08	Y__	Tahoka	87225
7	3.40	0.09	RAT	Mightyoak	86100	4	4.51	0.13	P__	Lockney	87267
12	4.33	0.07	PAR	Jefferson	86112	3	3.87	0.06	Y__	Borate	87296
2	2.53	0.12	YAA	Panamint	86141	1	4.09	-	PAT	Kernville	88046
7	4.22	0.10	YAT	Tajo	86156	1	4.17	-	PAT	Kearsarge	88230
15	4.31	0.05	P__	Darwin	86176	1	3.36	-	Y__	Kawich	89055

The final two columns give the name and Julian data of each event, respectively. The events are listed in chronological order. The error listed is the standard deviation of the mean or standard error and the standard deviation of the observations can be obtained by multiplying by the square root of the number of observations or stations used. The average standard deviation for the list is 0.15. It is questionable as to what that statistic means, however, since there are events in the table with M_S determined with only one station or infinite standard deviation, and these were obviously not used in determining the average. There are not a lot of NTS studies that give the error for M_S but the standard deviations or the more frequently used standard error of path-corrected log M_0, which is very similar to our M_S method, for NTS can be found in Stevens (1986) and Stevens & McLaughlin (1988). Stevens (1986) notes that the network standard deviations in (log) moment for his study of 40 NTS events are quite small, about 0.1, and that even for recent NTS explosions, which included data from several distant SRO stations, the standard deviations are only 0.15.

To determine the portability of this M_S calculation method the events need to be separated into groups based on their source regions and then compared, one group to another, in order to see if there are systematic differences in M_S values relative to any other magnitude scale. Three main geographic source regions comprise the event data set: Pahute Mesa, Rainier Mesa and Yucca Flat.

Whether or not a shot occurs within saturated material is another criterion by which to separate events in order to look for systematic differences in M_S values. Other studies have found significant seismic-coupling differences between explosions detonated above and below the water table (Marshall *et al.* 1979; Gupta *et al.* 1989; Vergino & Mensing 1989). It is important to quantify this seismic-coupling effect.

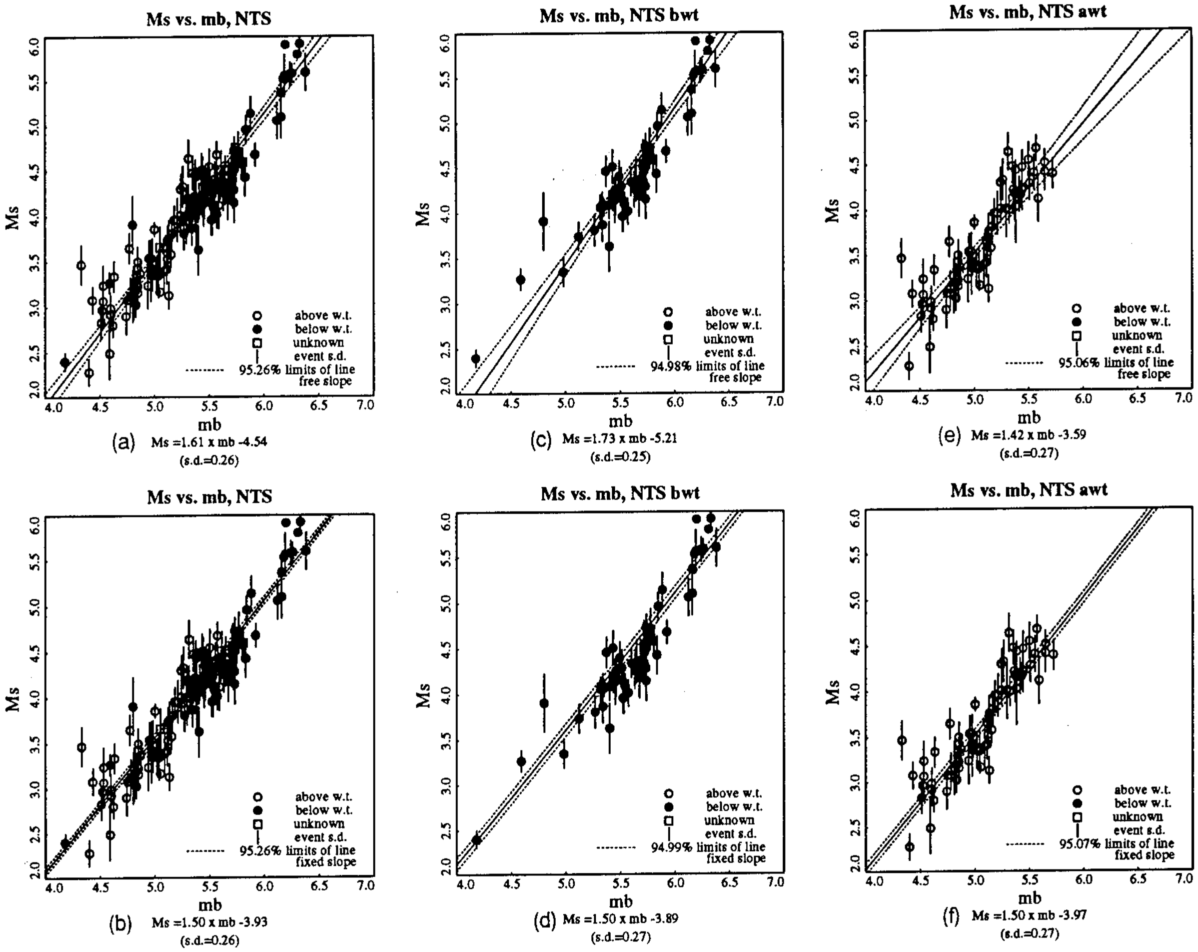

Figure 11. M_S regressed versus Lilwall m_b for all NTS events. The data are also separated with respect to shot point being above or below the water table. The bottom figures are constrained least-square regressions assuming a slope of 1.5.

Reviewing Fig. 6, it is also apparent that shots fired-off below the water table have a larger body-wave magnitude than those detonated above the water table.

Figure 11(a) shows the M_S:m_b (Lilwall) relationship for all NTS events. The surface-wave magnitudes were all calculated using mixed-path Green's functions (with the RSSD-1 structure for the generic path part) and path corrections. Figs 11(b) and (c) divide the data populations into above and below the water table, respectively; shots for which water-table information was not available were left out. Although all but one Rainier Mesa events were detonated above the water level, we found that their coupling (M_S versus log yield) was diagnostic of explosions detonated below the water table. Taylor (1983) notes that Rainier Mesa sports a perched aquifer. We believe that the Rainier Mesa events are detonated within this zone, hence they are assumed to be well-coupled events, i.e. the pore space of the shot medium is filled with water and thus pore-space crushing will not be a strong effect.

The bottom three figures (11d, e and f) plot the same data, but a constrained least-squares fit was performed with the slope = 1.50. The offset in curves between events detonated above and below the water table is 0.08. This amount is within the scatter of the data (i.e. statistically insignificant), but it would appear that shot-medium coupling effects associated with pore-filling phenomena are similar for surface waves and P waves.

Figures 15(a)–(c) are M_S versus log-yield plots analogous to Figs 11(a)–(c). It is important to note that the individual explosion variances are about the same size for the entire range of yields, so that our predicted yield values for small events should be as accurate as for the larger events. The slope of the M_S and log-yield scaling-relation curves was found to be near unity for all populations. Assuming the scaling relationship has a slope of 1, BWT shots couple more strongly than AWT shots by 0.52 units—a substantial amount; for m_b-yield scaling the coupling effect found in this study is 0.28 units. This coupling factor depends on the slope of the scaling curve and has been found to be as large as 0.7 to 0.9 throughout the literature. For individual source regions, the offset in the M_S–yield and m_b–yield scaling curves for shots fired above and below the water table vary slightly from these values determined from the entire data set. There is some scatter in the data which is not surprising considering the diversity of the sampled populations. However the best-fitting M_S–m_b curves are well constrained, for the population covers a wide range of magnitudes.

The various M_S:m_b relationships for Yucca events are shown in Figs 12(a)–(c). The scatter in the data is reduced by 25 per cent over that of the general population (Figs

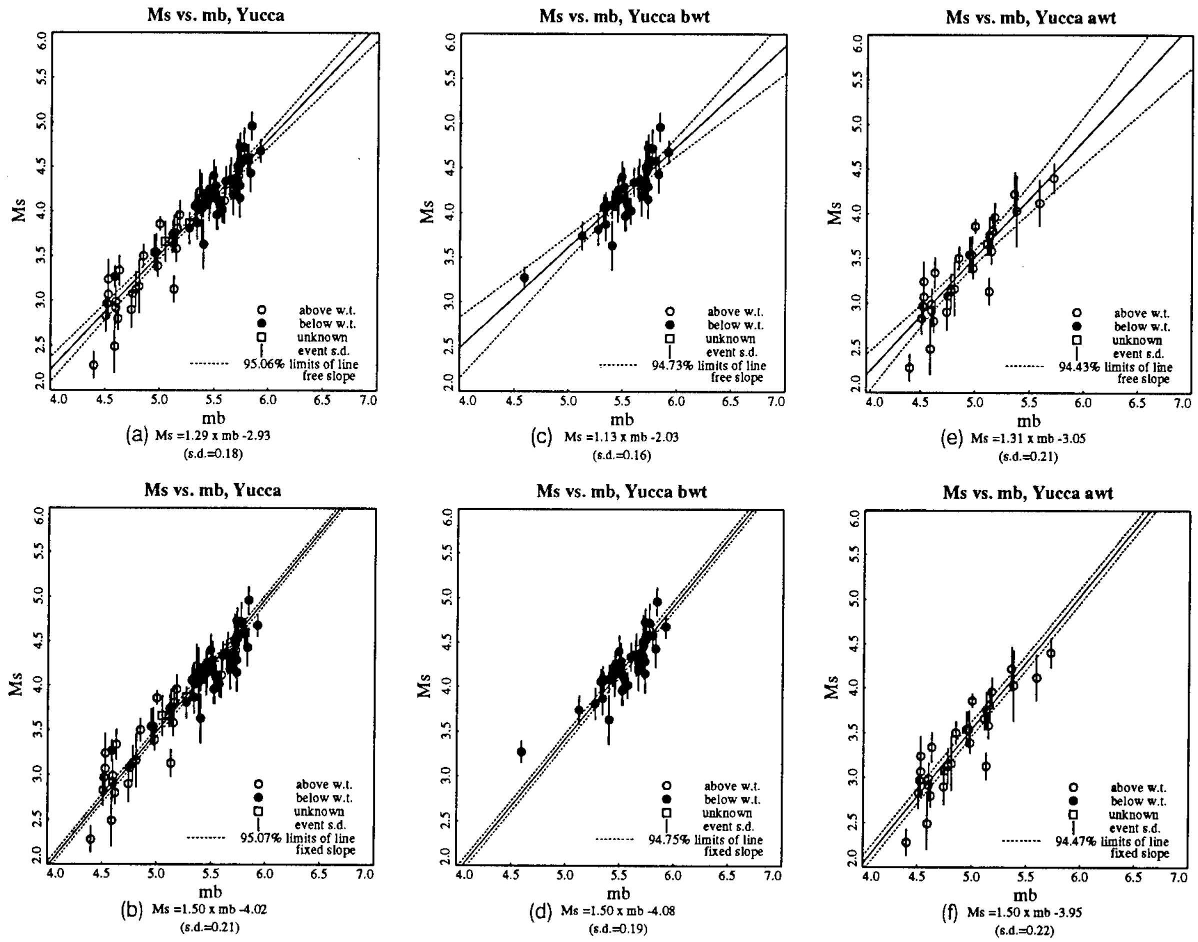

Figure 12. M_S regressed versus Lilwall m_b for Yucca events. The data are also separated with respect to shot point being above or below the water table. The bottom figures are constrained least-square regressions assuming a slope of 1.5.

11a–c). The free-slope regression curves are not as well constrained as those of Fig. 11 because the yield range for Yucca explosions is smaller than that of the entire data set. Fixing the slope to 1.5 (Figs 12d–f) leads to AWT shots coupling 0.13 M_S units more strongly than BWT shots for a given m_b. The error in the fit to the curve is larger than this variation, so it is not a statistically significant result. It would appear the pore-filling coupling affects surface wave and body waves similarly. When the Yucca M_S data are regressed with respect to log yield, as shown in Figs 15(d)–(f), it is found that BWT events couple four times more efficiently than AWT shots ($\Delta M_S = 0.61$). This is a significant amount and the data set on which it is based is more extensive than that of the M_S–m_b regression. Springer (1966) found that high dry porosity (60 per cent) shot mediums coupled four to five times less effectively than in saturated alluvium. Most Yucca Flat shots are detonated in alluvium.

Figure 13(a) plots all Pahute event M_S's versus their respective m_b's. The scaling relationship is significantly different than that of the Yucca data above. Comparing the unconstrained below- and above-water-table curves (Figs 13b and c) to their Yucca counterparts (Figs 12b and c), it is apparent that explosions at the two sites do not display the same scaling relationships. One possible explanation for this difference is that there is not enough data to constrain the scaling curves, particularly for Yucca BWT and Pahute AWT events. Another possible explanation is that this scaling relationship difference is real and may be caused by differences in the source medium, source structure or tectonic-strain release associated with the sites. Figs 12(d)–(f) and 13(d)–(f) show constrained (slope = 1.5) regression curves for the Yucca and Pahute data, respectively. For a given m_b, surface-wave magnitudes for events at Pahute Mesa are larger than those at Yucca Flat by 0.39 and 0.18 log units for BWT and AWT shots, respectively. There is also an appreciable difference in the M_S:log-yield relationship between Yucca and Pahute events detonated in water-saturated material (0.23 units). The Pahute data are plotted in Figs 16(d)–(f). For the case of events exploded in dry material there is a significant difference with Yucca events having a M_S 0.44 units smaller than Pahute events.

Figures 14(a)–(f) display the M_S–m_b regression curves and data for Rainier Mesa events in combination with and without Pahute Mesa data. Figs 16(a)–(c) are analogous figures for the M_S versus log-yield data to Figs 14(a)–(c). Although the clustering of Rainier data near $m_b = 5.0$ causes the curve to be poorly constrained, a slope is obtained that is close to that for Pahute and Yucca BWT shots. Comparison of the equations at the bottom of Figs 13(e) and 14(e) give an offset of 0.47 between M_S estimates

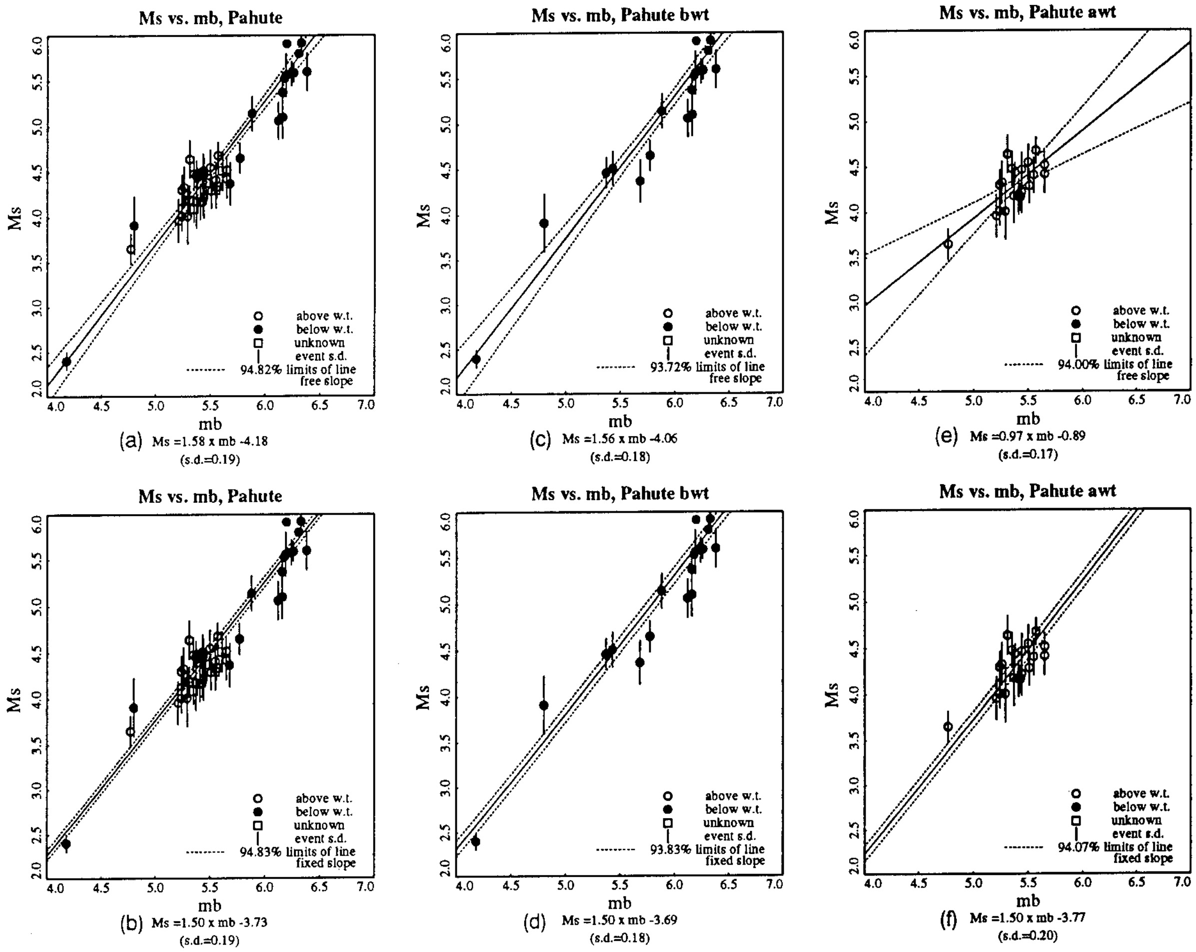

Figure 13. M_S regressed versus Lilwall m_b for Pahute events. The data are also separated with respect to shot point being above or below the water table. The bottom figures are constrained least-square regressions assuming a slope of 1.5.

at Pahute and Rainier (for a given m_b). Either the Pahute site is more efficient at producing surface waves or the Rainier site is more efficient at coupling body-wave energy. Rainier events are tunnel shots. The immediate source region ($R < 200$ m) may behave like an asymmetric cavity, resulting in a source that is non-isotropic (Zhao & Harkrider 1992) and/or seismic coupling that has strong frequency dependence. Either of these effects may account for this difference. The difference in the M_S–log-yield scaling relationship is somewhat less (0.31 units), implying that Rainier more efficiently couples short-period energy than Pahute.

Comparing Fig. 11(b) with 15(b), we see that regressing against log yield has reduced the regression standard deviation from 0.25 to 0.18 for NTS BWT events plus Rainier events. This is probably caused by the reduced standard deviation of the Pahute BWT events, 0.18 to 0.13 (Figs 13b and 16e) and the combined Pahute BWT plus Rainier events, 0.22 to 0.16 (Fig 14b and 16b). The opposite is true for the 'all' NTS events. This is because of the increase in standard deviation for Yucca AWT events when regressed against yield due primarily to the inclusion of a lot of small-yield Yucca events for which we did not have m_b's.

CONCLUSION

In this study we have determined surface-wave magnitudes for small as well as large underground nuclear explosions. Our technique allows us to include smaller events in a consistant manner with the historic set of large events for which surface-wave magnitudes have been determined by classical means. Thus it was not primarily an attempt to improve M_S for large events but to extend it to lower-sized events by including regional stations not usually used in NTS M_S determinations. The M_S formula used was one that had previously been found appropriate for NTS explosions and not the Prague formula used for earthquakes. In the process of making these determinations, we also calculated station and network moments. Since the assumptions and corrections used in the moment determinations were more straightforward, we feel that future estimates of surface-wave energy should be moment and until that time we feel that our technique is best for including small events in the historical surface-wave magnitude data base. The moment values will be given in the sequel paper.

The method we have described to calculate surface-wave magnitudes allows the measurement of M_S for nuclear explosions over a wider magnitude distribution than was

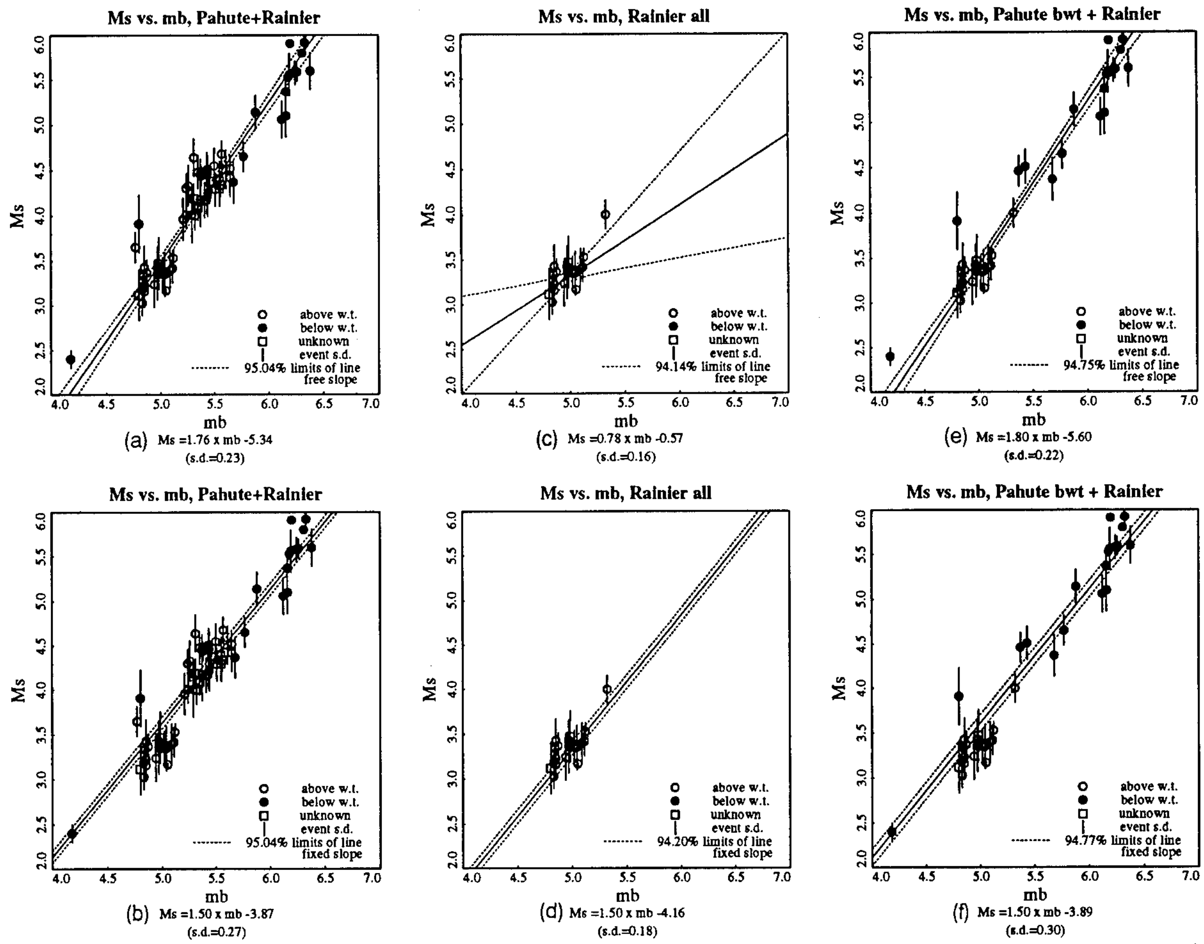

Figure 14. M_S regressed versus Lilwall m_b for Pahute and Rainier events. Regression of Rainier data alone (middle figures), all Rainier and Pahute events (left figures), and all Rainier events with Pahute shots below the water table (right figures) are shown. The bottom figures are constrained least-square regressions assuming a slope of 1.5.

previously possible. These M_S values scale consistently (within a constant factor) with other seismic-magnitude scales. Using our technique, it is now possible to use near-regional ($\Delta < 8°$) long-period records, as well as more conventional far-regional ($\Delta < 15°$) and teleseismic observations, in order to measure surface-wave magnitudes. As it is a time-domain measurement, it is easy to calculate M_S from historical analogue waveforms, since it is only necessary to measure the peak-to-peak Rayleigh wave amplitude.

This M_S method is very useful for quantifying small explosions, because time-domain magnitude measurements of regional waveforms lowers the effective magnitude threshold. Small events, for which teleseismic surface waves are not observed, can now be analysed with regional surface-wave data, thus lowering the effective measuring M_S threshold. Fig. 17 illustrates this point, showing unrotated three-component data for FLOYDADA (8/15/91, $m_b = 4.2$) detonated at Yucca Flat and recorded by three TERRAscope stations convolved with a Press–Ewing 30–90 response. The source-to-receiver distances are between 210 and 390 km. The maximum peak-to-peak amplitudes are quite small (<0.5 mm). On the actual analogue instrument it would not be possible to measure the surface-wave amplitude. Because of the low signal-to-noise ratio a spectral moment would be of dubious value. However, the M_s and M_0(PPA) methods described in this paper would furnish an accurate surface-wave magnitude with which to estimate its yield.

These small surface-wave magnitudes, based on near-regional data would also be of considerable value for discrimination methods that make use of the difference between the long-period and short-period spectral content of earthquakes and explosions, for it is possible to lower the discrimination threshold using such data.

The increase in nearer observations has several other advantages. Station-network coverage is enhanced in terms of overall numbers as well as in azimuthal coverage. In this study stations a few hundred kilometers away from NTS in the south-western U.S. were included in the network that otherwise would have no coverage to the west or south-west. These improvements make the network M_S's more stable and statistically robust. Potential monitoring areas may well have similar geographical constraints requiring the use of near-regional ($\Delta < 8°$) seismic data. Also, the effect of inaccuracies in estimating Q are negligible for very near-regional recordings.

From the results obtained with the data set used here, there do appear to be significant differences in seismic

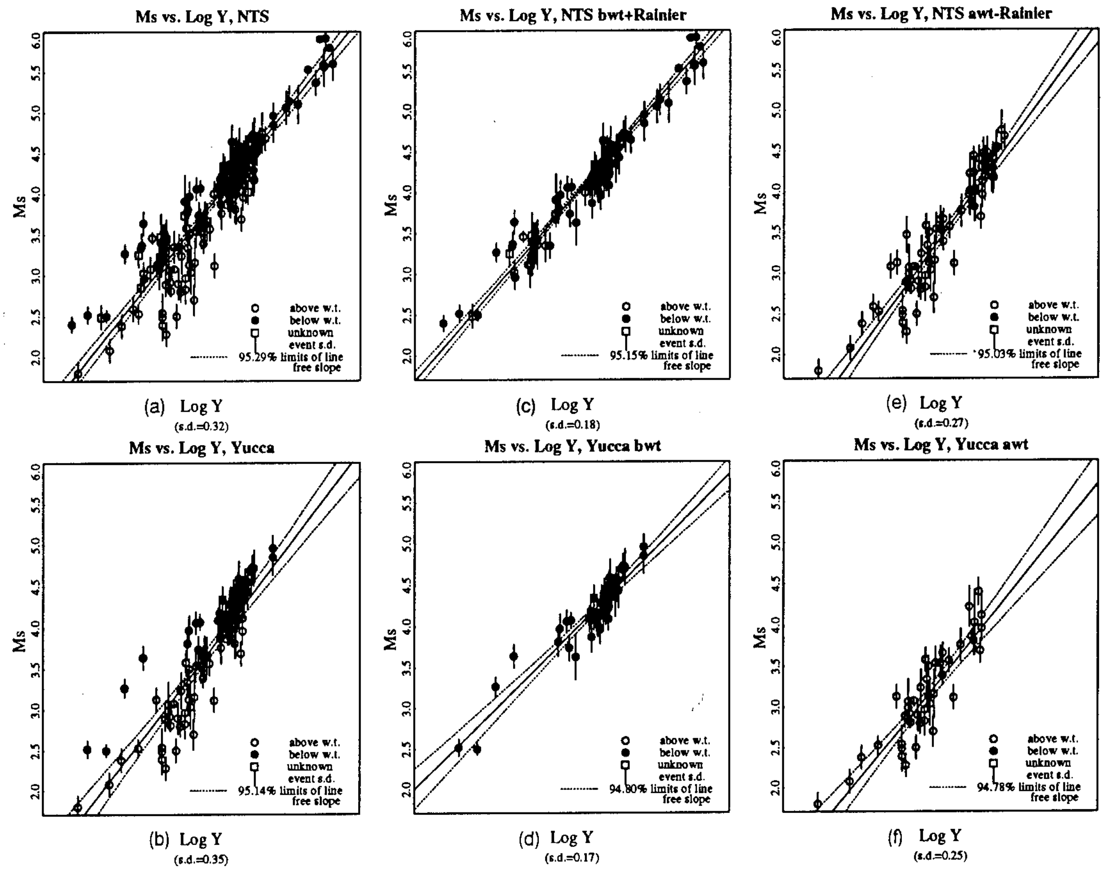

Figure 15. M_S regressed versus log yield for all NTS events (top figures) and for Yucca events (bottom figures). Event populations have also been grouped with respect to shot-point water-table location.

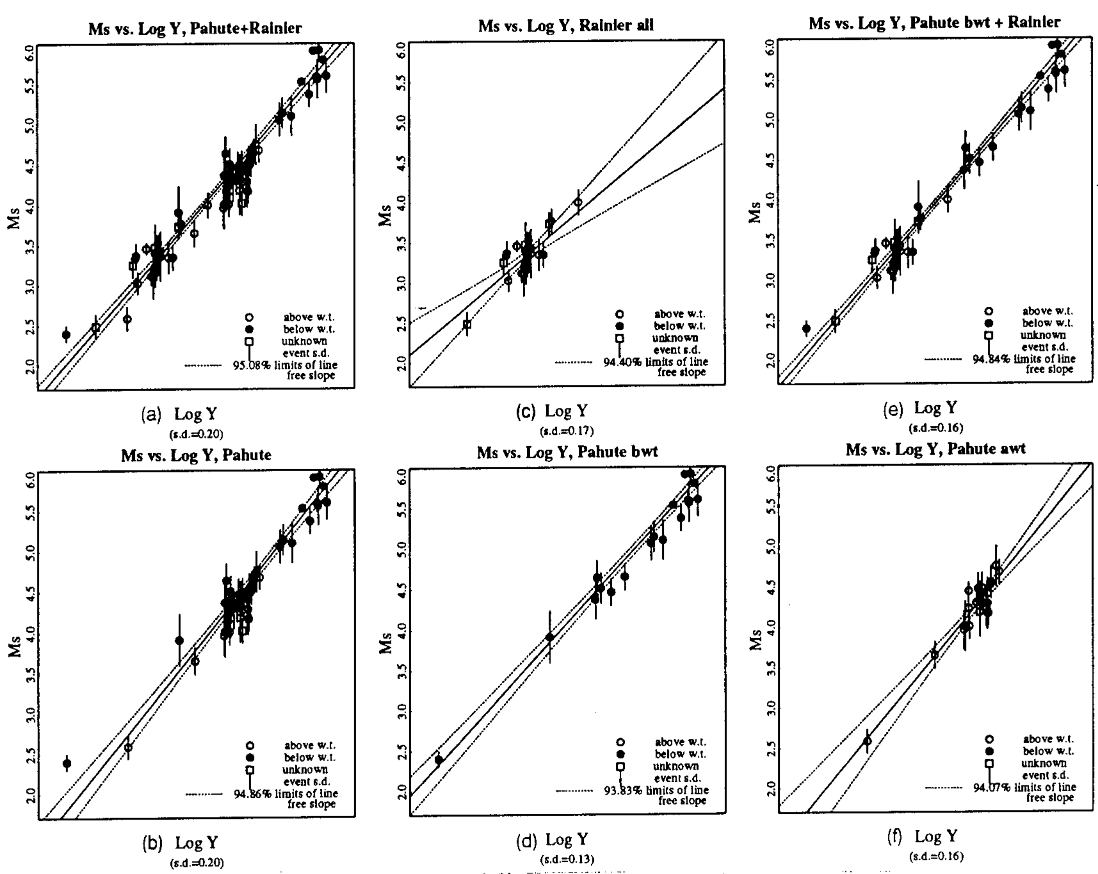

Figure 16. M_S regressed versus log yield for Pahute and Rainier events (top figures) and for Pahute events alone (bottom figures). Event populations have also been grouped with respect to shot-point water-table location.

Floydada (Yucca Flat, Y < 10 kt)

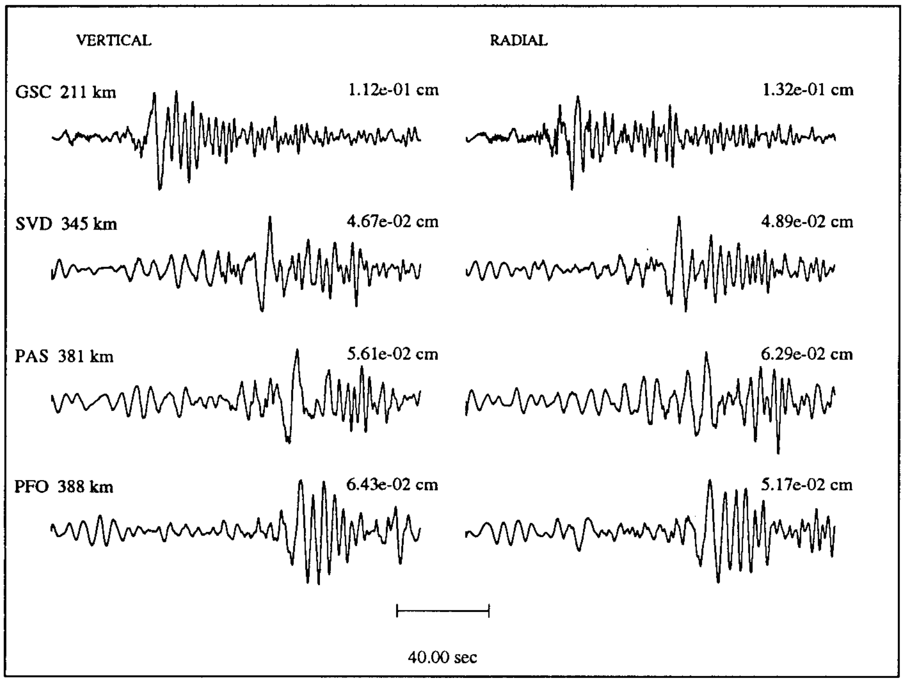

Figure 17. TERRAscope streckeisen recordings of an NTS explosion Floydada at Yucca Flat on 8/15/91 with an estimated yield of <10 kt. ($m_b = 4.2$, $M_L = 4.0$, and $\log M_0 = 14.16$ N–M). The broad-band records have been convolved with a Press–Ewing 30–90 instrument response. All four stations record the surface wave train well enough to measure the Airy-phase peak amplitudes. Records from an actual 30–90 long-period instrument would be unusable.

coupling between NTS subsites, with events at Pahute Mesa producing larger surface-wave magnitudes for a given m_b than at Rainier Mesa or Yucca Flat. For well-coupled events this discrepancy is largest for Rainier Mesa events. M_S values at Yucca Flat tend to be larger than those at Rainier Mesa by 0.08 magnitude units for a given m_b. There also appears to be some difference in waveforms between events of these two source regions. Pahute Mesa events are 0.39 magnitude units larger than those at Yucca flat for explosions set off below the water table and with the same m_b.

Although L_g measurements with a calibration shot give more accurate estimates of explosion yields, there may be cases where L_g 'blockage' caused by strong lateral variations in the propagation path may occur, and one must use other methods, such as surface-wave magnitudes, to estimate yields or for discriminating the event.

ACKNOWLEDGMENTS

This research was supported by the Defense Advanced Research Projects Agency (DOD), Nuclear Monitoring Research Office and was monitored by Air Force Geophysics Laboratory under Contract F19628-89-K-0028, and also was supported by Phillips Laboratory (formerly Geophysics Laboratory) of the Air Force Systems Command under Contract F19628-90-K-0049, and contribution No. 5187, Division of Geological and Planetary Sciences, California Institute of Technology, Pasadena, California.

REFERENCES

Alewine, R.W., 1972. Theoretical and observed distance corrections for Rayleigh-wave magnitude, *Bull. seism. Soc. Am.*, **62,** 6133–6142.

Babich, V.M., Chikhachev, B.A. & Yanovskaya, T.B., 1976. Surface waves in a vertically inhomogeneous halfspace with a weak lateral inhomogeneity. *Izv. AN SSSR, Fiz. Zem.* **4,** 24–31.

Bache, T.C., 1982. Estimating the yield of underground nuclear explosions, *Bull. seism. Soc. Am.*, **72,** S131–S168.

Bache, T.C., Day, S.M. & Swanger, H.J., 1982. Rayleigh wave synthetic seismograms from multidimensional simulations of underground explosions, *Bull. seism. Soc. Am.*, **72,** 15–28.

Bache, T.C., Rodi, W.L. & Harkrider, D.G., 1978. Crustal structures inferred from Rayleigh-wave signatures of NTS explosions, *Bull. seism. Soc. Am.*, **68,** 1399–1413.

Båth, M., 1967. Recommendations of the IASPEI committee on magnitudes, *Seism. Bull.*, May volume, Seismological Institute, Uppsala.

Basham, P.W., 1969. Canadian magnitudes of earthquakes and nuclear explosions in south-western North America, *Geophys. J. R. astr. Soc.*, **17,** 1–13.

Basham, P.W., 1971. A new magnitude formula for short period continental Rayleigh waves, *Geophys. J. R. astr. Soc.*, **23,** 255–260.

Basham, P.W. & Horner, R.B., 1973. Seismic magnitudes of underground nuclear explosions, *Bull. siesm. Soc. Am.*, **63,** 105–131.

Burridge, R. & Weinberg, H., 1977. Horizontal rays and vertical modes, *Wave Propagation and underwater acoustics,* Springer-Verlag, New York.

Day, S.M. & McLaughlin, K.L., 1991. Seismic Source Representation for Spall, *Bull. seism. Soc. Am.*, **81,** 191–201.

Evernden, J.F., 1971. Variation of Rayleigh-wave amplitude with distance, *Bull. seism. Soc. Am.*, **67,** 405–411.

Evernden, J.F. & Filson, J., 1971. Regional dependence of surface-waves versus body-wave magnitudes, *J. geophys. Res.*, **76,** 3303–3308.

Given, J.W. & Mellman, G.R., 1986. Estimating explosion and tectonic release source parameters of underground nuclear explosions from Rayleigh and Love wave observations, *Sierra Geophysics Inc. Rept. No. SGI-R-86-126,* AFGL-TR-86-0171, Kirkland, WA.

Glover, P. & Harkrider, D.G., 1986. Numerical tests of surface wave path corrections, *Science Applications International Corp. Rept. No. C86-05,* MDA903-84-C-0020, McLean, VA.

Gupta, I.N., Lynnes, C.S., Chan, W.W. & Wagner, R.A., 1989. A comparison of the spectral characteristics of nuclear explosions detonated below and above the water table, *Teledyne Geotech Rept. No, TGAL-89-04,* GL-TR-89-0151, Alexandria, VA.

Harkrider, D.G., 1981. Coupling near source phenomena into surface wave generation, *Identification of Seismic Sources—Earthquake or Underground Explosion,* pp. 277–326, eds Husebye & Mykkeltveit, D. Reidel, Dordrecht.

Harkrider, D.G. & Anderson, D.L., 1966. Surface wave energy from point sources in plane layered earth models, *J. geophys. Res.*, **71,** 2967–2980.

Lapin, L.L., 1983. *Probability and Statistics for Modern Engineering,* Brooks/Cole, Monterey, CA.

Larson, D.B., 1981. Explosive energy coupling in geologic materials, *Lawrence Livermore National Laboratory, Report UCID-85662.*

Levshin, A.L., 1985. Effects of lateral inhomogeneities on surface wave amplitude measurements, *Annales Geophysicae,* **3,** 511–518.

Lilwall, R.C. & Neary, J.M., 1985. Redetermination of earthquake body-wave magnitudes using ISC Bulletin data, United Kingdom Atomic Energy Authority, *AWRE Rept. No. O 21/85,* H.M.S.O., London.

Marshall, P.D. & Basham, P.W., 1972. Discrimination between earthquakes and underground explosions employing an improved M_S scale, *Geophys. J. R. astr. Soc.,* **28,** 431–458.

Marshall, P.D., Douglas, A. & Hudson, J.A., 1971. Surface waves from underground nuclear explosions, *Nature,* **234,** 8–9.

Marshall, P.D., Lilwall, R.C. & Farthing, J., 1986. Body wave magnitudes and locations of underground nuclear explosions at Nevada Test Site 1971-1980, United Kingdom Atomic Energy Authority, *AWRE Rept. No O 21/86,* H.M.S.O., London.

Marshall, P.D., Springer, D.L. & Rodean, H.C., 1979. Magnitude corrections for attenuation in the upper mantle, *Geophys. J. R. astr. Soc.,* **57,** 609–638.

Mueller, R.A. & Murphy, J.R., 1971. Seismic characteristics of underground nuclear detonations, *Bull. seism. Soc. Am.,* **61,** 1675–1692.

Murphy, J.R., 1977. Seismic source functions and magnitude determinations for underground nuclear detonations, *Bull. seism. Soc. Am.,* **67,** 135–158.

Patton, H.J., 1988. Application of Nuttli's method to estimate yield of Nevada Test Site explosions recorded on Lawrence Livermore National Laboratory's Digital Seismic Systems, *Bull. seism. Soc. Am.,* **78,** 1759–1772.

Patton, H.J., 1991. Seismic moment estimation and the scaling of the explosion source, *Geophysical Monograph 65: Explosion Source Phenomenology,* pp. 171–183, eds Taylor, S.R., Patton, H.J. & Richards, P.G., *Am. geophys. Un. Monogr.,* Washington, DC.

Saito, M., 1967. Excitation of free oscillations and surface waves by joint sources in a vertically heterogeneous earth. *J. geophys. Res.,* **72,** 3689-3699.

Schlittenhardt, J., 1988. Seismic Yield Estimation Using Teleseismic *P*- and *PKP*-waves Recorded at the GRF-(Graefenberg) array, *Geophys. J.,* **95,** 163–179.

Springer, D.L., 1966. *P*-wave coupling of underground explosions, *Bull. seism. Soc. Am.,* **56,** 861–876.

Stevens, J.L., 1986. Estimation of scalar moments from explosion-generated surface waves, *Bull. seism. Soc. Am.,* **76,** 123–151.

Stevens, J.L., 1991. Seismic source characteristics of cavity decoupled explosions in salt and tuff, *Bull. seism. Soc. Am.,* **81,** 1272–1291.

Springer, D.L. & Kinnaman, R.L., 1971. Seismic source summary for U.S. underground nuclear explosions, 1961–1970, *Bull. seism. Soc. Am.,* **61,** 1073–1098.

Stevens, J.L. & McLaughlin, K.L., 1988. Analysis of surface waves from the Novaya Zemlya, Mururoa, and Amchitka Test Sites, and maximum likelihood estimation of scalar moments from earthquakes, *S-CUBED Technical Rept. No. SSS-TR-89-9953,* F08606-85-c-0028, La Jolla, CA.

Sykes, L.R. & Cifuentes, I.L., 1984. Yields of Soviet underground nuclear explosions from seismic surface waves: compliance with the Threshold Test Ban Treaty, *Proc. Natl Acad. Sci. U.S.A.,* 1922–1925.

Taylor, S.R., 1983. Three-dimensional crust and upper mantle structure at the Nevada Test Site, *J. geophys. Res.,* **88,** 2220–2232.

Taylor, S.R. & Randall, G.E., 1989. The effects of spall on regional seismograms, *Geophys. Res. Lett.,* **16,** 211–221.

Vergino, E.S. & Mensing, R.W., 1989. Yield estimation using regional mb(Pn), *Lawrence Livermore National Laboratory Report UCID-101600.*

von Seggern, D., 1973. Joint magnitude determination and analysis of variance for explosion magnitude estimates, *Bull. seism. Soc. Am.,* **63,** 827–845.

von Seggern, D., 1977. Amplitude distance relation for 20-Second Rayleigh waves, *Bull. seism. Soc. Am.,* **67,** 405–511.

Werth, G.C. & Herbst, R.F., 1963. Comparison of amplitudes of seismic waves from nuclear explosions in four mediums, *J. geophys. Res.,* **68,** 1463–1475.

Woodhouse, J.H., 1974. Surface waves in a laterally varying layered structure, *Geophys. J. R. astr. Soc.,* **37,** 461–490.

Yacoub, N.K., 1983. Instantaneous amplitudes: a new method to measure seismic magnitude, *Bull. seism. Soc. Am.,* **73,** 1345–1355.

Yanovskaya, T.B., 1989. 2. Surface waves in media with weak lateral inhomogeneity, in *Seismic Surface Waves in a Laterally Inhomogeneous Earth,* ed. Keilis-Borok, V.I., Kluwer Academic Publishers, Dordrecht.

Yomogida, K., 1985. Surface waves in a laterally slowly-varying media, *Geophys. J. R. astr. Soc.,* **82,** 511–533.

Zhao, L.S. & Harkrider, D.G., 1992. Wavefields from an off-center explosion in an imbedded solid sphere, *Bull. seism. Soc. Am.,* **82,** 1927–1955.

SECTION 3

Isotropic and deviatoric Moment Inversion of Regional Surface Waves from Nevada Test Site Explosions: Implications for Yield Estimation and Seismic Discrimination

Isotropic and Deviatoric Moment Inversion of Regional Surface Waves from Nevada Test Site Explosions: Implications for Yield Estimation and Seismic Discrimination

BRADLEY B. WOODS AND DAVID G. HARKRIDER
Seismological Laboratory 252-21,
California Institute of Technology

SUMMARY

Seismic moments of Nevada Test Site (NTS) explosions are determined from regional surface wave spectra. Two methods are used. In one the moment is solved for assuming only an explosive source, or average scalar moment; in the other a joint inversion for an isotropic (explosive) source plus a constrained double couple moment component representing tectonic strain release (TSR). Although the general moment tensor solution to this joint inversion problem is non-unique, if some assumptions are made concerning the non-isotropic moment components, then the remaining source parameters can be solved by a linear least-squares inversion scheme. We examine the errors in determining the isotropic moment component (M_I) by this latter method of constrained linear inversion solutions in a canonical study using a theoretical network of long-period (6-60 sec.) surface wave data. The network azimuthal coverage was chosen to represent that of a long-period North American super-network of 55 stations used for the actual NTS events. We compare these errors in moment estimate to those obtained from surface wave magnitude (M_S) and spectral scalar moment (M_0) measurements for the same surface wave observations. For a ratio of $M_{(expl)}/M_{(eq)}$ less than

1.0 we find that the inverted M_I solution is a much better estimate of the actual isotropic moment than either M_S or M_0, and the standard deviation in this estimate is substantially less than that using the other two methods for the great majority of isotropic source + double couple sources. Even when the inversion constraints are off in dip and rake each by 30^o, the mis-estimate of the isotropic moment is less than 35 percent of the actual value. In the case of a vertical strike-slip fault, the inverted isotropic moment solution which assumes this fault orientation is exact to three figures, whereas M_S and M_0 under-estimate the moment by 45 percent and 32 percent, respectively because of uneven azimuthal coverage. This moment tensor inversion method is applied to determine the isotropic source for 109 NTS underground explosions using vertical and tangential component surface wave data from this regional network. We also calculate M_S and M_0 for these same events and compare the results. Isotropic source errors are smallest using the spectral domain inversion method. However, this spectral domain method cannot attain as low a magnitude threshold as the time domain moment or M_S method. The extensive moment data set analyzed here were combined with larger yield explosions from prior moment studies to create a comprehensive data set with which to obtain conclusive, well-constrained long-period explosion source scaling relationships at the separate NTS sub-sites.

INTRODUCTION

The purpose of this work is to determine the precision of seismic moment (M_0) estimates of underground nuclear explosions determined from spectral measurements of intermediate-period (6 to 60 sec.), regional surface waves. Seismic moment is a measure of low frequency seismic source spectrum. Besides being useful as a quantifier of earthquake sources, it also can be used to estimate seismic yields of explosions and employed in long-period:short-period discriminants (Woods *et al.*, 1993). Woods & Harkrider (1994) dealt with time-domain moment and magnitude (M_S) measurements of regional surface waves. A criticism of time domain amplitude measurements of regional surface waves is that lateral variations in the crustal structure cause multi-pathing and scattering which affect the peak amplitude of the Airy Phase, particularly for paths shorter than 1000 km for which the longer-period wave-train is not well dispersed. Spectral moment $M(\omega)$ measurements reduce this problem by averaging over the frequency band of interest. They are also insensitive to spall effects which are significant primarily in this 0.2 to 2 Hz frequency bandwidth (Taylor & Randall, 1989), since the spectral moment is calculated between 0.0167 and 0.167 Hz.

Unlike short-period body wave amplitudes, surface waves are relatively insensitive to source region attenuation effects which give rise to m_b biases in yield-magnitude relationships between inter-regional testing sites.

Previous moment studies of explosions have relied on distant regional ($D > 1000$ km) and teleseismic surface wave measurements and as such only the larger explosions ($m_b \geq 5.5$) could be examined. Stevens (1986) determined scalar moments, assuming a pure isotropic (explosive) source, for Nevada Test Site (NTS) and East Kazakhstan Test Site events. Given & Mellman (1986) inverted fundamental-mode Rayleigh and Love wave spectral data to obtain the isotropic component and double-couple component (due to tectonic strain release) of the source moment tensor for virtually the same data set. Both studies relied on seismic networks with poor azimuthal coverage and included mixed continental-oceanic paths which, as discussed in Woods & Harkrider (1995), can significantly alter surface wave-train waveforms and spectral content. Although both studies made use of uniquely derived path structures to account for propagation effects, they also made use of empirically derived "station corrections" directly or indirectly, but which are, in fact, path corrections to reduce the scatter in the network averaged moment caused by apparent errors in modeling the paths. These two studies also relied heavily on hand-digitized data for events in the 70's; the digital data available was, for the most part, from stations with oceanic paths. One would rather use digitized data from pure continental paths, since waveforms should be more reliable and the signal to noise ratio (SNR) should be better, particularly for smaller events. The mixed-path approximation theory for synthetic surface wave generation discussed in Woods & Harkrider (1995) works best for paths that aren't radically different, so it is not clear that this approximation would work well for ocean-continent paths.

Evernden *et al.* (1971) suggest, that with high dynamic range digital seismometers, it should be possible to observe surface waveforms from small earthquakes ($m_b \approx 4.0$) up to 6000 km distance away; for explosions which have relatively lower level long-period source spectra, a higher detection threshold would be expected.

This study re-investigates the long-period source spectrum (seismic moment) of explosions using surface wave spectral amplitude measurements from digitally recorded, reasonably high dynamic range, regional (375 km < 5000 km) waveforms. Such data have been used in earthquake source studies (Patton & Zandt, 1991; Yelin & Patton, 1991; and Thio & Kanamori, 1992), but until now has not been applied to underground explosion source studies. We wish to determine whether such data better constrain moment estimates of explosions and whether the observational magnitude threshold for measuring surface moments can be lowered. This study is confined to NTS events; however, it is a more comprehensive data set in that it includes 109 events–nearly three times as many events as the previous studies and events from Rainier Mesa are examined as well. As in Woods & Harkrider (1995) localized site effects on moment estimates can be studied. The digital data for this study is not as comprehensive as that in Woods & Harkrider (1995) which included many analog data, so that it will not be possible to constrain the magnitude-moment scaling relationships as well as the in time-domain moment-M_S moment study.

With the use of nearer regional stations, better azimuthal coverage of NTS is attainable. This is important for obtaining unbiased average scalar moments and/or to invert for non-isotropic moment components. Also with shorter paths, errors in propagation effects, principally because of attenuation, Q, will be smaller than for the longer paths.

Particular attention is paid to error analysis in this study, since high confidence levels in nuclear monitoring are a primary concern. Standard deviations in scalar moments estimates by Stevens (1986) ranged between 12 and 200 percent , with most being under 25 percent. While no error analysis appears to have been conducted in the moment tensor inversion study, it was found that some explosions exhibited radiation patterns which have double-couple moment components as large as 50 percent of the isotropic moment component. The explosions with the largest apparent tectonic strain release moments in the Given & Mellman study also tended to have the largest error estimates in the Stevens (1986) scalar moment study. Hence it would be instructive to examine how well correcting for tectonic release effects would reduce the variance in moment estimates.

The assumption that the radiation pattern from an explosive source has no azimuthal dependence, while theoretically sound, is not born out in practice. Many researchers have reported evidence for a non-isotropic component for explosion sources (Press & Archambeau, 1962; Brune & Pomeroy, 1963; Toksöz *et al.*, 1971; Toksöz & Kehrer, 1972; Tsai & Aki, 1972; Wallace *et al.*, 1985) and has been attributed predominantly to tectonic strain release

(Archambeau & Sammis, 1970) and, more recently, to asymmetric explosion cavities (Zhao & Harkrider, 1992). This additional source can have appreciable long-period content, and as such can effect surface wave radiation patterns (Helle & Rygg, 1984; Given & Mellman, 1986), and thus bias moment estimates if it is not accounted for.

The most general moment tensor inversion solution for a joint isotropic + double-couple source is non-unique (Mendiguren, 1977; Ekström & Richards, 1994). And for very shallow sources some off-diagonal elements of the moment tensor become unresolvable (Kanamori & Given, 1981; and Patton, 1988). If one is to invert for source depth and source time functions, the problem becomes non-linear and even more complicated. In the inversion procedure developed herein, several assumptions are made concerning the sources. The tectonic release source and explosion sources are both modeled as step moment source time functions coincident in time and depth, which are reasonable assumptions for the periods measured (6-60 sec.). Secondly, as described later in the Inversion Method Section, certain moment tensor components and source excitation functions are assumed to be negligible when source depth is taken as the limit $h \rightarrow 0$ (see Given & Mellman, 1986, for details). The tectonic release radiation pattern is assumed to be modeled as a double-couple source. Further, the dip and rake of the double-couple fault plane are constrained by previous studies of tectonic release at NTS to be predominantly vertical, strike-slip in nature with a $sin2\phi$ radiation pattern (Toksöz *et al.*, 1965; Aki & Tsai, 1972; Wallace *et al.*, 1983 and 1985; Lay *el al*, 1984; Given & Mellman, 1986), with the strike angle varying between N10°W and N60°W.

The tectonic release strike angle (ϕ), moment ($M_{\#}$), and the explosion moment (M_I) are then inverted from fundamental-mode Rayleigh wave and Love wave spectra in what is then a one-step linear least-squares inversion. The errors in M_I are compared to those of scalar moments (M_0). The source parameters and yield-magnitude relationships are compared between the three major NTS sub-sites: Pahute Mesa, Rainier Mesa, and Yucca Flats.

Data Processing and Analysis

The digital and digitized data of Woods & Harkrider (1995) are used in this study. Table 1 lists, in chronological order, the events used along with available source information. In the date column is the Julian date. The three-letter site code (3rd column) gives the NTS sub-site location (P=Pahute Mesa, Y=Yucca Flat, R=Rainier Mesa (Tunnel shots), or C=Climax Stock), whether the shot was detonated above (A) or below (B) the water table, and rock type (T=Volcanic Tuff, G=Granite, R=Rhyolite, A=Alluvium). When available, the shot point elevation and depth of burial are given. Also listed, when available, are body wave magnitudes determined by the International Seismic Centre (ISC) and Lilwall & Neary (1985) (L), and local magnitudes. Data for events before 1982 are digitized records, while all later events rely on digital recordings. In most cases the vertical and two horizontal components are all available for any particular event-station pair, although for a small minority of the data pairs only the vertical or horizontal component records were usable/existent. Horizontal components were rotated to their great circle path to obtain the transverse component; the radial components were not used as they yield only redundant P-SV wavefield (Rayleigh wave) information and can be contaminated with scattered transverse component energy. Horizontal components also, in general, have a lower SNR than vertical components.

The SNR for some observations is low, particularly for the smaller events ($m_b \approx 5.0$ and below), with long-period ($T > 60$ sec) noise overwhelming the transient signal. High-pass filtering improved the time-domain SNR significantly, making positive identification of Love

NAME	Date	Site	Lat.	Lon.	Elev.	Depth	$m_{b(I)}$	$m_{b(L)}$	σ_{m_b}	M_L
Table 1 (a): Event Information										
WAGTAIL	65062	YBT	37.06	-116.04	1237	-750		5.53	0.06	5.0
LAMPBLACK	66018	YBT	37.09	-116.02	1294	-561	5.2	5.27	0.08	5.2
REX	66055	PBT	37.27	-116.43	1998	-672	4.8			4.8
PIRANHA	66133	YBT	37.09	-116.03	1264	-549	5.6	5.60	0.04	5.1
PILEDRIVER	66153	CBG	37.23	-116.06	1535	-463	5.6	5.63	0.04	5.0
TAN	66154	YBT	37.07	-116.04	1249	-561	5.7	5.69	0.03	4.9
MIDIMIST	67177	RAT	37.20	-116.21	2226	-374	5.1			4.5
DOORMIST	67243	RAT	37.18	-116.21	2325	-446	5.0	4.83		4.8
COBBLER	67312	YBT	37.09	-116.04	1269	-671	5.1			
DORSALFIN	68060	RAT	37.18	-116.21	2287	-410	5.0	5.12	0.08	
HUDSONSEAL	68268	RAT	37.20	-116.21	2191	-333	5.0	4.97	0.08	
WINESKIN	69015	RAT	37.21	-116.23	2290	-518	5.3	5.32	0.05	5.0
CYPRESS	69043	RAT	37.17	-116.21	2292	-412		4.83		
BLENTON	69120	YBT	37.08	-116.01	1281	-558	5.3	5.32	0.04	
DIANAMIST	70042	RAT	37.18	-116.21	2225	-399	4.6	4.84	0.08	4.5
SHAPER	70082	YBT	37.09	-116.02	1279	-561	5.5	5.51	0.03	
MINTLEAF	70125	RAT	37.22	-116.18	2121	-405	5.2	5.04	0.06	4.6
HUDSONMOON	70146	RAT	37.18	-116.21	2301	-422	5.0			4.6
CAMPHOR	71180	RAT	37.18	-116.21			4.9	4.85	0.08	
MINIATA	71189	YBT	37.11	-116.05	1274	-529	5.5	5.53	0.03	5.3
ALGODONES	71230	YBT	37.06	-116.04	1233	-528	5.4	5.40	0.04	5.2
MISTYNORTH	72123	RAT	37.21	-116.21	2226	-377	5.0	4.85	0.06	
MONERO	72140	YBT	37.06	-116.00	1272	-537	4.9	4.59	0.04	4.5
DIAMONDSCULLS	72202	RBT	37.21	-116.18	2140	-424	5.0	4.98	0.04	4.6
MIERA	73067	YBT	37.10	-116.03	1306	-569	5.4	5.34	0.03	5.4
STARWORT	73116	YBT	37.12	-116.06	1288	-564	5.6	5.54	0.02	5.3
DIDOQUEEN	73156	RAT	37.18	-116.22	2274	-391	5.1	5.02	0.05	4.8
LATIR	74058	YBT	37.10	-116.05			5.8	5.64	0.02	5.4

Table 1: NTS Event source information

Table 1 (b)										
NAME	Date	Site	Lat.	Lon.	Elev.	Depth	$m_{b(I)}$	$m_{b(L)}$	σ_{m_b}	M_L
MINGBLADE	74170	RAT	37.21	-116.21			5.0	4.97	0.04	
ESCABOSA	74191	YBT	37.08	-116.03			5.7	5.74	0.02	5.6
STANYAN	74269	YBT	37.13	-116.07			5.6	5.52	0.03	5.0
CABRILLO	75066	YBA	37.13	-116.08	1315	-600	5.5	5.57	0.03	5.2
DININGCAR	75095	RAT	37.19	-116.21	2265	-305	4.8	4.94	0.03	4.5
OBAR	75120	YBT	37.11	-116.03			5.2	5.12	0.04	5.0
MIZZEN	75154	YBT	37.09	-116.04	1274	-637	5.7	5.71	0.02	5.6
HUSKYPUP	75297	RAT	37.22	-116.18	2063	-348	4.7	4.87	0.05	4.7
KEELSON	76035	YBT	37.07	-116.03	1285	-655	5.8	5.72	0.02	5.8
MIGHTYEPIC	76133	RAT	37.21	-116.21	2251		4.9	4.85	0.05	4.6
RUDDER	76363	YBT	37.10	-116.04	1282	-640	5.5	5.69	0.02	5.5
BULKHEAD	77117	YBT	37.09	-116.03	1286	-594	5.4	5.43	0.03	5.1
CREWLINE	77145	YBT	37.09	-116.04	1252	-564	5.3	5.40	0.03	5.3
LOWBALL	78193	YBT	37.08	-116.04	1252	-564	5.5	5.72	0.02	5.4
QUARGEL	78322	YBT	37.13	-116.08	1302	-542	5.1	5.34	0.03	5.2
QUINELLA	79039	YBT	37.10	-116.05	1302	-542	5.5	5.71	0.02	5.2
PYRAMID	80107	YBT	37.10	-116.03	1293	-579	5.3	5.45	0.03	5.3
MINERSIRON	80305	RAT	37.24	-116.21	2239	-390	4.7	4.97	0.06	4.9
BASEBALL	81015	YAT	37.09	-116.04	1259	-564	5.6	5.72	0.02	5.5
JORNADA	82028	YBT	37.09	-116.05	1260	-640	5.9	5.92	0.02	5.6
MOLBO	82043	PBR	37.22	-116.46	1900	-651	5.6	5.43	0.03	5.4
HOSTA	82044	PAR	37.35	-116.32	2103	-640	5.6	5.55	0.02	5.5
TENAJA	82107	YAT	37.02	-116.01	1210	-357	4.5	4.59	0.15	4.4
GIBNE	82115	PAT	37.26	-116.42	1964	-570	5.4	5.38	0.03	5.4
KRYDDOST	82126	Y__	37.12	-116.13	1390	-325	4.3			4.4
BOUSCHET	82127	YBT	37.07	-116.05	1244	-564	5.7	5.73	0.02	5.4
NEBBIOLO	82175	PAR	37.24	-116.37	2065	-640	5.6	5.65	0.02	5.6
MONTEREY	82210	YAT	37.10	-116.07	1280	-400	4.5	4.97	0.06	4.6

Table 1 (c)										
NAME	Date	Site	Lat.	Lon.	Elev.	Depth	$m_{b(I)}$	$m_{b(L)}$	σ_{m_b}	M_L
ATRISCO	82217	YBT	37.08	-116.01	1295	-640	5.7	5.73	0.02	5.4
HURONLANDING	82266	RAT	37.21	-116.01	2260	-408	4.9	5.04	0.04	4.8
BORREGO	82272	YBT	37.09	-116.04	1261	-564				4.1
FRISCO	82267	YAT	37.17	-116.09	1374	-451	4.9	4.97	0.06	4.8
MANTECA	82344	YAA	37.03	-116.07	1263	-413	4.6	4.78	0.06	4.7
CABRA	83085	PAR	37.30	-116.46	1934	-543	5.1	5.24	0.03	5.2
TORQUOISE	83104	YBT	37.07	-116.05	1246	-533	5.7	5.73	0.03	5.5
CROWDIE	83125	YAA	37.01	-116.09	1336	-390	4.5	4.51	0.06	4.3
FAHADA	83146	YAT	37.10	-116.01	1339	-384	4.4	4.63	0.10	4.4
DANABLU	83160	YAT	37.16	-116.09	1353	-320	4.5	4.60	0.06	4.6
CHANCELLOR	83244	PAR	37.27	-116.36	2040	-625	5.4	5.41	0.03	5.3
MIDNITEZEPHYR	83264	RAT	37.21	-116.21	2257	-405				4.1
TECHADO	83265	YBT	37.11	-116.05	1268	-533				4.1
ROMANO	83350	YAT	37.14	-116.07	1314	-515	5.1	5.16	0.04	5.0
MILAGRO	84046	RAT	37.22	-116.18	2076	-361	5.0	5.11	0.04	4.8
TORTUGAS	84061	YBT	37.07	-116.05	1243	-639	5.9	5.83	0.02	5.5
MUNDO	84122	YBT	37.11	-116.02	1319	-567	5.3	5.49	0.03	5.3
CAPROCK	84152	YBT	37.10	-116.05	1264	-600	5.8	5.72	0.02	5.6
DUORO	84172	YAT	37.00	-116.04	1207	-381	4.6	4.81	0.07	4.5
KAPPELI	84207	PAR	37.27	-116.41	2010	-640	5.3	5.37	0.03	5.2
CORREO	84215	YAT	37.02	-116.01	1209	-335	4.7	4.74	0.07	4.4
DOLCETTO	84243	YAT	37.09	-115.99	1318	-366	4.5	4.75	0.10	4.3
BRETON	84257	YAT	37.09	-116.07	1265	-483	5.0	5.15	0.04	5.0
VILLITA	84315	YAA	37.00	-116.02	1205	-373	4.5	4.62	0.10	4.4
EGMONT	84344	PAT	37.27	-116.49	1867	-551	5.5	5.44	0.03	5.4
TIERRA	84350	PAR	37.28	-116.31	2145	-640	5.4	5.44	0.03	5.4
VAUGHN	85074	YAT	37.06	-116.05	1238	-427	4.8	4.98	0.05	4.6
COTTAGE	85082	YAT	37.18	-116.09	1389	-515	5.3	5.38	0.04	5.1

Table 1 (d)										
NAME	Date	Site	Lat.	Lon.	Elev.	Depth	$m_{b(I)}$	$m_{b(L)}$	σ_{m_b}	M_L
HERMOSA	85092	YBT	37.10	-116.03	1278	-640	5.7	5.77	0.02	5.6
MISTYRAIN	85096	R_T	37.20	-116.21	1850	-389	4.8	4.98	0.04	4.8
TOWANDA	85122	PBT	37.25	-116.33	2112	-661	5.7	5.68	0.02	5.4
SALUT	85163	PBR	37.25	-116.49	1900	-608	5.5	5.37	0.03	5.3
SERENA	85206	PAR	37.30	-116.44	1969	-597	5.2	5.24	0.03	5.1
PONIL	85270	YAT	37.09	-116.00	1312	-366	4.6	4.53	0.07	4.5
ROQUEFORT	85289	YAT	37.11	-116.12	1368	-415	4.6	4.50	0.07	4.6
KINIBITO	85339	YBT	37.05	-116.05	1235	-600	5.7	5.67	0.02	5.2
GOLDSTONE	85362	P__	37.24	-116.47	1914	-500	5.3	5.31	0.03	5.1
GLENCOE	86081	YBT	37.08	-116.07	1260	-600	5.4	5.35	0.03	5.0
MIGHTYOAK	86100	RAT	37.22	-116.18	2111	-400	4.9	5.09	0.05	4.9
JEFFERSON	86112	PAR	37.26	-116.44	1982	-600	5.3	5.26	0.03	5.4
PANAMINT	86141	YAT	37.13	-116.06	1286	-480	4.8			3.9
TAJO	86156	YAT	37.10	-116.02	1316	-518	5.3	5.36	0.03	5.3
DARWIN	86176	P__	37.27	-116.50	1876	-549	5.5	5.55	0.03	5.3
CYBAR	86198	PAR	37.28	-116.36	2044	-628	5.7	5.65	0.02	5.5
CORNUCOPIA	86205	YAA	37.14	-116.07	1314	-400	4.4	4.52	0.07	4.4
LABQUARK	86273	PAR	37.30	-116.31	2127	-600	5.5	5.51	0.03	5.2
BELMONT	86289	P__	37.22	-116.46	1898	-600	5.6	5.56	0.03	5.5
GASCON	86318	YAT	37.10	-116.05	1263	-600	5.8	5.80	0.03	5.6
BODIE	86347	PAT	37.26	-116.41	2018	-600	5.5	5.50	0.03	5.4
DELAMAR	87108	P__	37.25	-116.51	1902	-500	5.5	5.46	0.03	5.3
HARDIN	87120	PAT	37.23	-116.42	1970	-600	5.5	5.44	0.03	5.3
PANCHUELA	87181	YAA	36.99	-116.04	1206	-300	4.6	4.64		4.0
TAHOKA	87225	Y_A	37.06	-116.05	1239	-600	5.9	5.81	0.03	5.5
LOCKNEY	87267	P__	37.23	-116.38	2072	-600	5.7	5.61	0.03	5.4
BORATE	87296	Y__	37.14	-116.08	1321	-500	5.2	5.27	0.03	5.0

waves much easier. In examining the ensemble of records, it became apparent that Love waves were observed for almost all events. The largest Love waves are associated with Pahute Mesa and Rainier events; however, most Yucca shots also showed evidence of Love wave generation. Most of the low-magnitude events were from Yucca Flat, so that the lack of Love wave observations may be due to the extremely low SNR. Also, the smaller events can only be observed at the nearer stations, so that the Rayleigh and Love wavefields have not separated enough in time by dispersion to identify the Love wave, since the Love wave is a pulse and arriving near and within the Rayleigh wave time window. Figures 1 and 2 plot the three component records for LON (Longmire, WA) and ALQ-ANMO (Albequerque, NM), respectively. These two stations were the best-reporting for the network used in this study. Both stations were upgraded with longer-period instruments for events after 1982, which explains the oberved difference in frequency content between the two types of records. Love waves are present on all but the lowest SNR records, implying that tectonic strain release or some other effect is generating a non-isotropic source. Given & Mellman (1986) found that all events they studied displayed evidence of tectonic strain release. However, their study was confined to large ($m_b > 5.5$) events.

Poor quality data such as ANMO: 85092, 82217(tang), 82127, 84152, 86318 and 87197(vert) were removed. Low SNR tangential components were removed in cases where the vertical component was kept, such as ANMO: 87181 and 86141, or ALQ: 65062 and 72140. All seismograms were bandpass-filtered between 6 and 60 seconds to best observe the wavetrain and for data analysis. Synthetic seismograms were filtered identically. Next, cosine-tapered time windows were applied to vertical and tangential records in an attempt to remove all but the fundamental-mode Rayleigh wave and Love wave respectively. A more robust alternative

Figure 1: Explosion-generated surface waves observed at Albequerque, N.M. (ALQ), some 900 km from NTS.

ALQ (a)

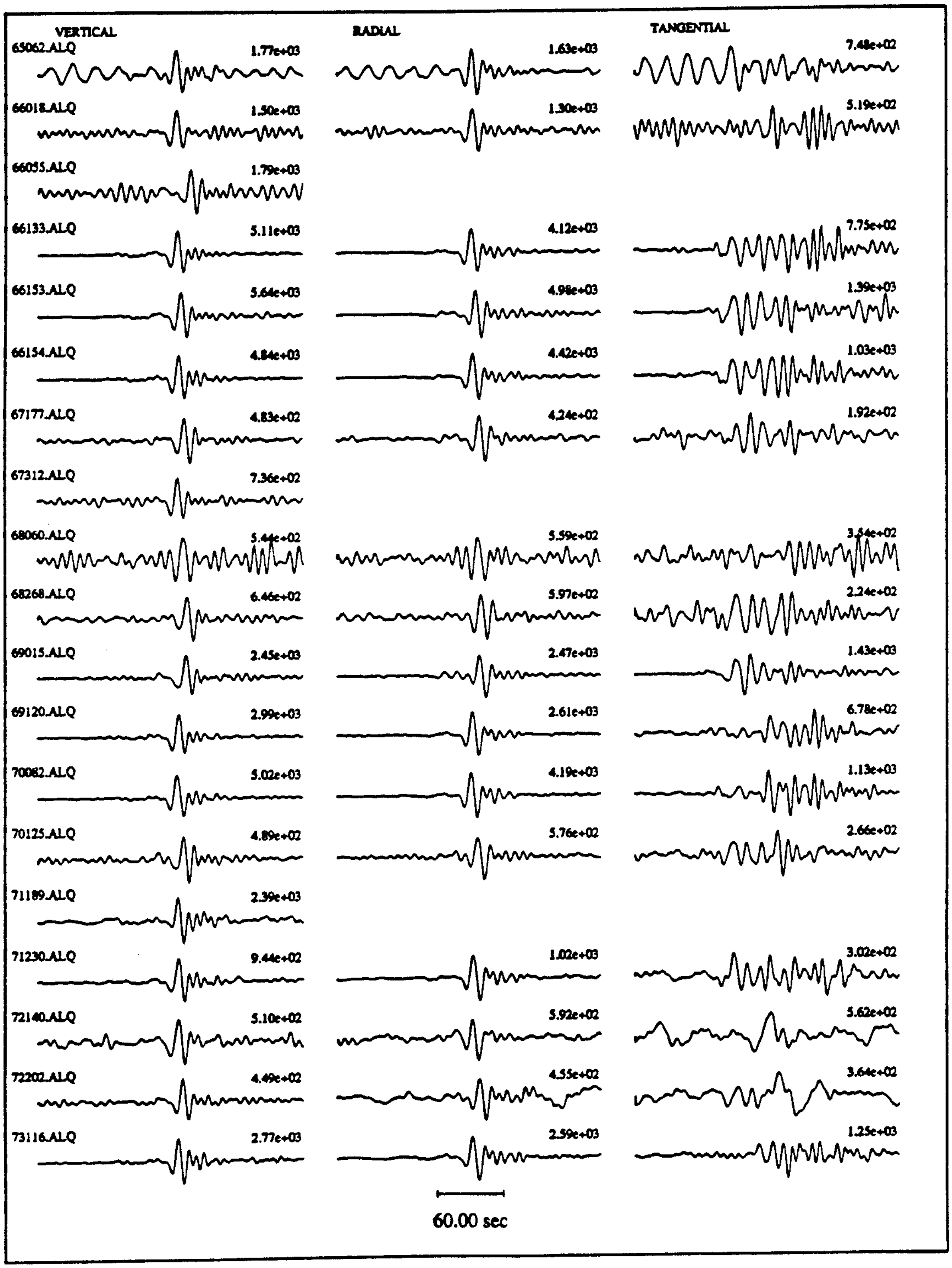

VERTICAL
RADIAL
TANGENTIAL
65062.ALQ 1.77e+03 1.63e+03 7.48e+02
66018.ALQ 1.50e+03 1.30e+03 5.19e+02
66055.ALQ 1.79e+03
66133.ALQ 5.11e+03 4.12e+03 7.75e+02
66153.ALQ 5.64e+03 4.98e+03 1.39e+03
66154.ALQ 4.84e+03 4.42e+03 1.03e+03
67177.ALQ 4.83e+02 4.24e+02 1.92e+02
67312.ALQ 7.36e+02
68060.ALQ 5.44e+02 5.59e+02 3.54e+02
68268.ALQ 6.46e+02 5.97e+02 2.24e+02
69015.ALQ 2.45e+03 2.47e+03 1.43e+03
69120.ALQ 2.99e+03 2.61e+03 6.78e+02
70082.ALQ 5.02e+03 4.19e+03 1.13e+03
70125.ALQ 4.89e+02 5.76e+02 2.66e+02
71189.ALQ 2.39e+03
71230.ALQ 9.44e+02 1.02e+03 3.02e+02
72140.ALQ 5.10e+02 5.92e+02 5.62e+02
72202.ALQ 4.49e+02 4.55e+02 3.64e+02
73116.ALQ 2.77e+03 2.59e+03 1.25e+03
60.00 sec

ALQ (b)

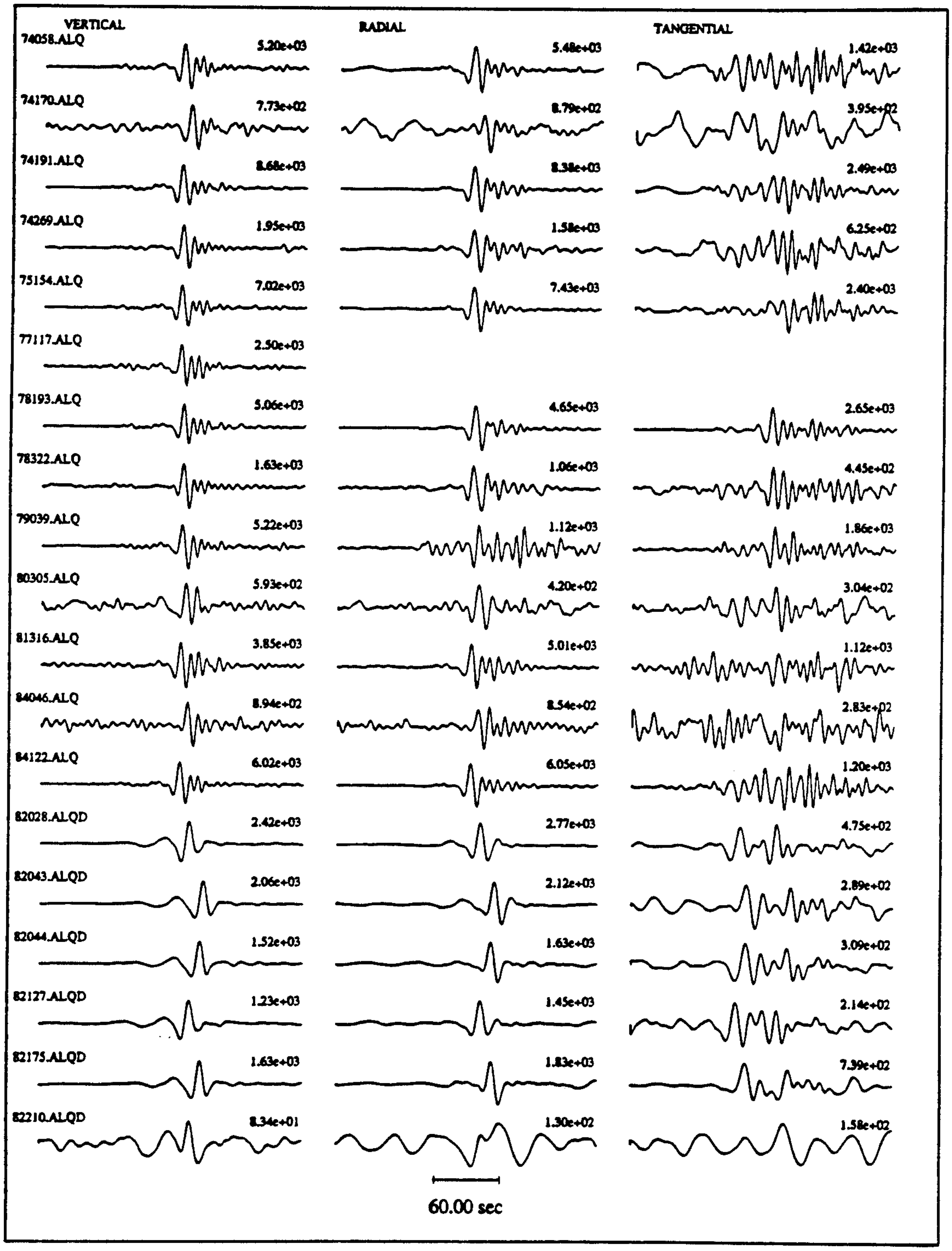
VERTICAL
RADIAL
TANGENTIAL
74058.ALQ 5.20e+03 5.48e+03 1.42e+03
74170.ALQ 7.73e+02 8.79e+02 3.95e+02
74191.ALQ 8.68e+03 8.38e+03 2.49e+03
74269.ALQ 1.95e+03 1.58e+03 6.25e+02
75154.ALQ 7.02e+03 7.43e+03 2.40e+03
77117.ALQ 2.50e+03
78193.ALQ 5.06e+03 4.65e+03 2.65e+03
78322.ALQ 1.63e+03 1.06e+03 4.45e+02
79039.ALQ 5.22e+03 1.12e+03 1.86e+03
80305.ALQ 5.93e+02 4.20e+02 3.04e+02
81316.ALQ 3.85e+03 5.01e+03 1.12e+03
84046.ALQ 8.94e+02 8.54e+02 2.83e+02
84122.ALQ 6.02e+03 6.05e+03 1.20e+03
82028.ALQD 2.42e+03 2.77e+03 4.75e+02
82043.ALQD 2.06e+03 2.12e+03 2.89e+02
82044.ALQD 1.52e+03 1.63e+03 3.09e+02
82127.ALQD 1.23e+03 1.45e+03 2.14e+02
82175.ALQD 1.63e+03 1.83e+03 7.39e+02
82210.ALQD 8.34e+01 1.30e+02 1.58e+02
60.00 sec

ANMO (c)

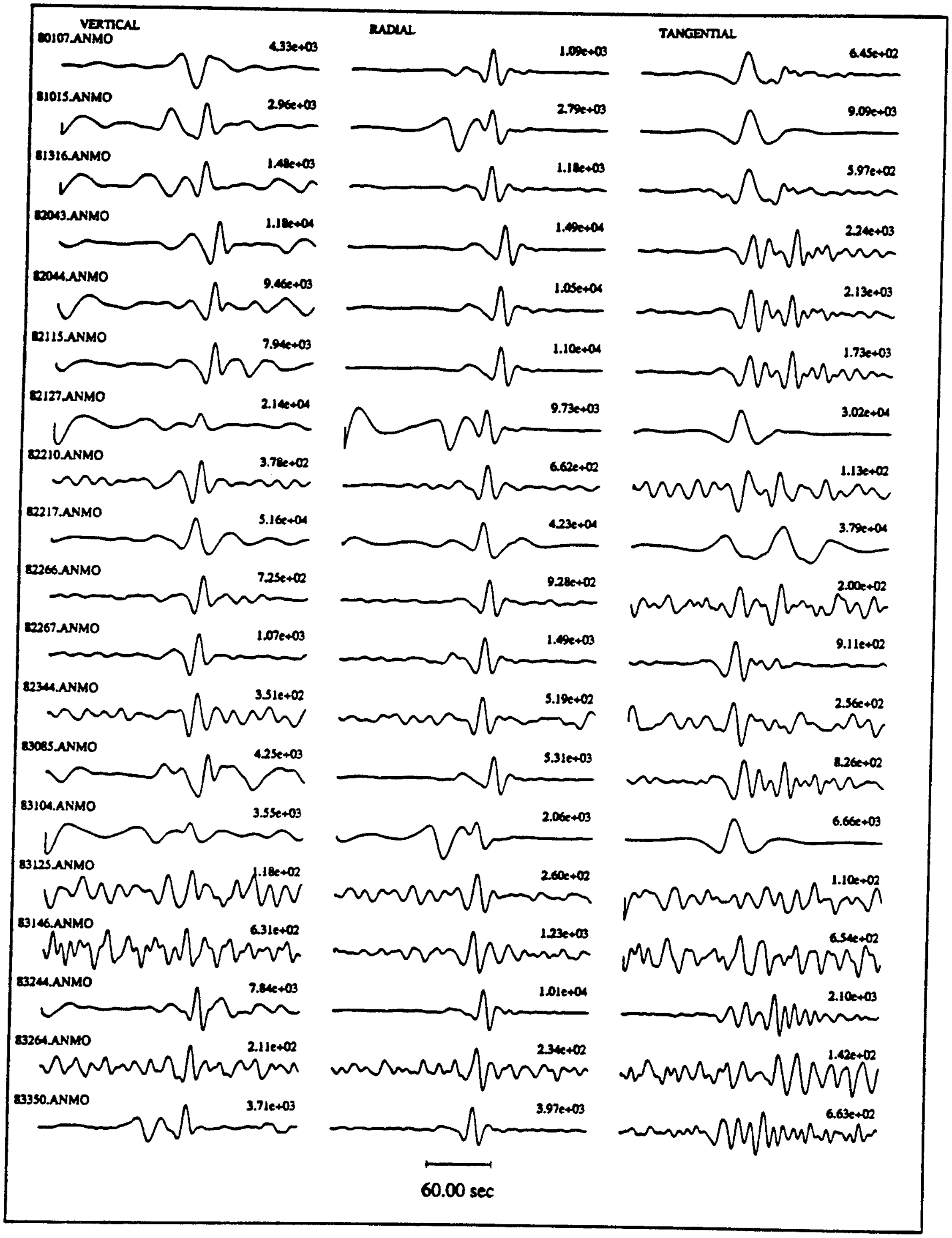
VERTICAL
RADIAL
TANGENTIAL
80107.ANMO 4.33e+03 1.09e+03 6.45e+02
81015.ANMO 2.96e+03 2.79e+03 9.09e+03
81316.ANMO 1.48e+03 1.18e+03 5.97e+02
82043.ANMO 1.18e+04 1.49e+04 2.24e+03
82044.ANMO 9.46e+03 1.05e+04 2.13e+03
82115.ANMO 7.94e+03 1.10e+04 1.73e+03
82127.ANMO 2.14e+04 9.73e+03 3.02e+04
82210.ANMO 3.78e+02 6.62e+02 1.13e+02
82217.ANMO 5.16e+04 4.23e+04 3.79e+04
82266.ANMO 7.25e+02 9.28e+02 2.00e+02
82267.ANMO 1.07e+03 1.49e+03 9.11e+02
82344.ANMO 3.51e+02 5.19e+02 2.56e+02
83085.ANMO 4.25e+03 5.31e+03 8.26e+02
83104.ANMO 3.55e+03 2.06e+03 6.66e+03
83125.ANMO 1.18e+02 2.60e+02 1.10e+02
83146.ANMO 6.31e+02 1.23e+03 6.54e+02
83244.ANMO 7.84e+03 1.01e+04 2.10e+03
83264.ANMO 2.11e+02 2.34e+02 1.42e+02
83350.ANMO 3.71e+03 3.97e+03 6.63e+02
60.00 sec

ANMO (d)

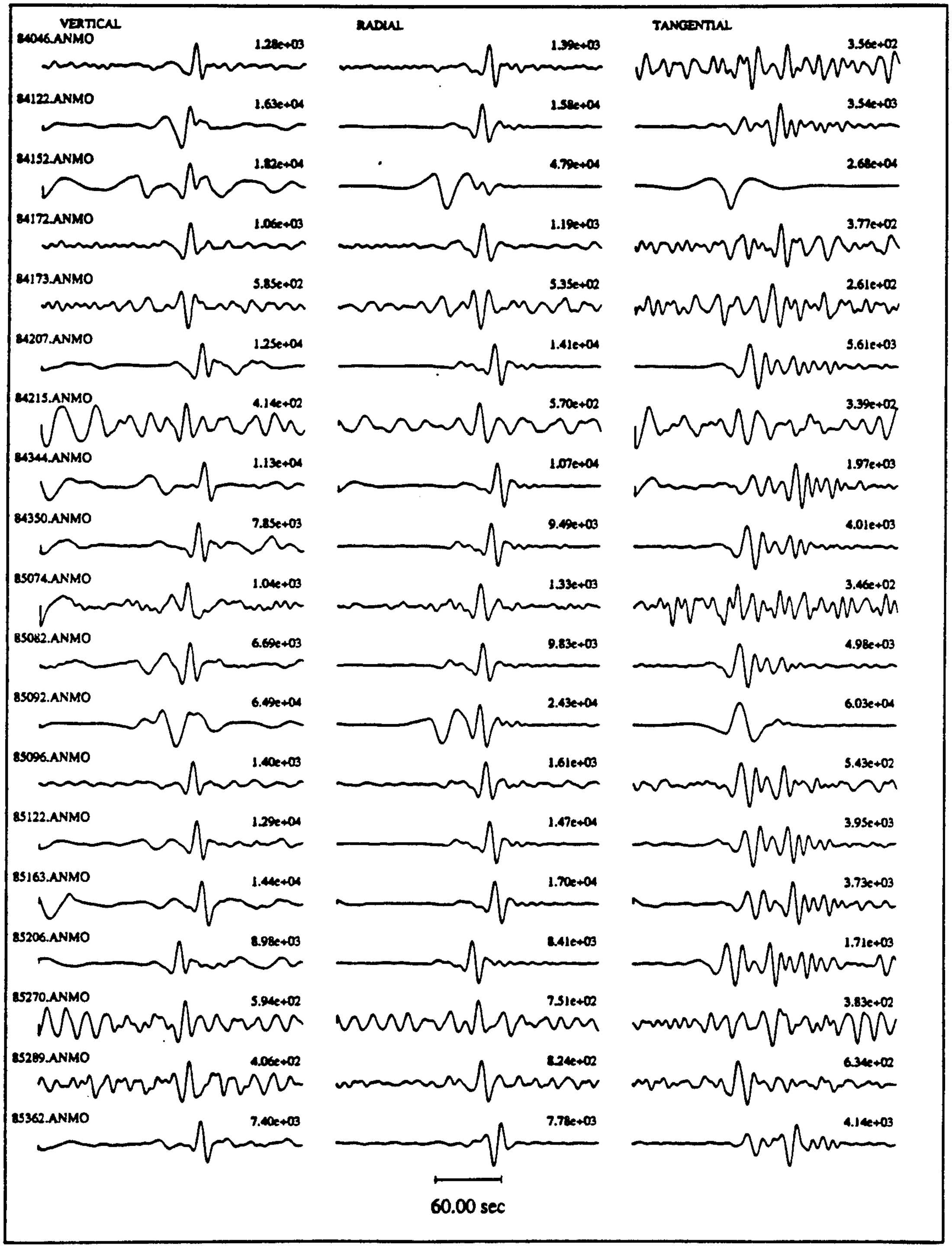
VERTICAL
RADIAL
TANGENTIAL
84046.ANMO 1.28e+03 1.39e+03 3.56e+02
84122.ANMO 1.63e+04 1.58e+04 3.54e+03
84152.ANMO 1.82e+04 4.79e+04 2.68e+04
84172.ANMO 1.06e+03 1.19e+03 3.77e+02
84173.ANMO 5.85e+02 5.35e+02 2.61e+02
84207.ANMO 1.25e+04 1.41e+04 5.61e+03
84215.ANMO 4.14e+02 5.70e+02 3.39e+02
84344.ANMO 1.13e+04 1.07e+04 1.97e+03
84350.ANMO 7.85e+03 9.49e+03 4.01e+03
85074.ANMO 1.04e+03 1.33e+03 3.46e+02
85082.ANMO 6.69e+03 9.83e+03 4.98e+03
85092.ANMO 6.49e+04 2.43e+04 6.03e+04
85096.ANMO 1.40e+03 1.61e+03 5.43e+02
85122.ANMO 1.29e+04 1.47e+04 3.95e+03
85163.ANMO 1.44e+04 1.70e+04 3.73e+03
85206.ANMO 8.98e+03 8.41e+03 1.71e+03
85270.ANMO 5.94e+02 7.51e+02 3.83e+02
85289.ANMO 4.06e+02 8.24e+02 6.34e+02
85362.ANMO 7.40e+03 7.78e+03 4.14e+03
60.00 sec

ANMO (e)

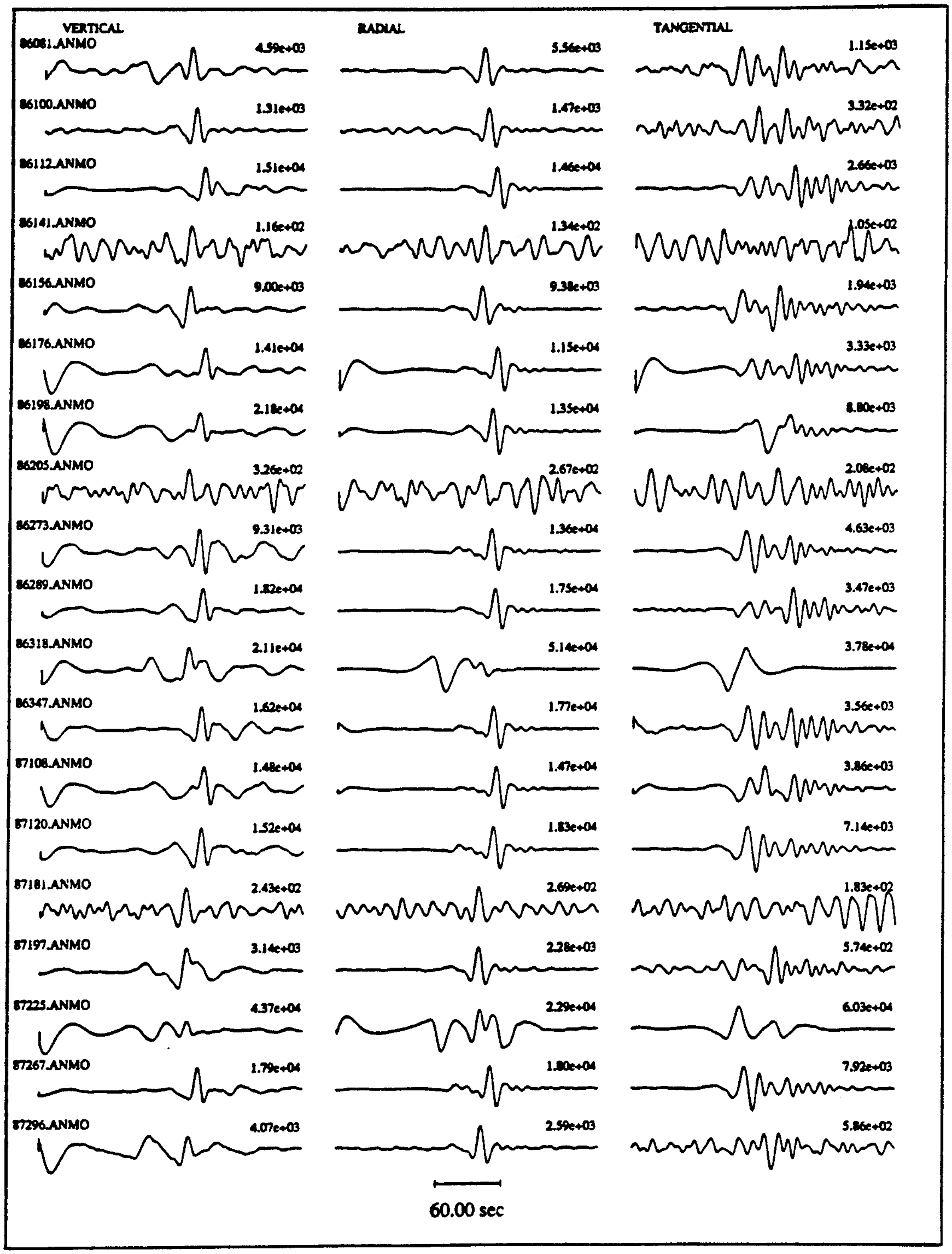

VERTICAL
RADIAL
TANGENTIAL
86081.ANMO
86100.ANMO
86112.ANMO
86141.ANMO
86156.ANMO
86176.ANMO
86198.ANMO
86205.ANMO
86273.ANMO
86289.ANMO
86318.ANMO
86347.ANMO
87108.ANMO
87120.ANMO
87181.ANMO
87197.ANMO
87225.ANMO
87267.ANMO
87296.ANMO
60.00 sec

LON (a)

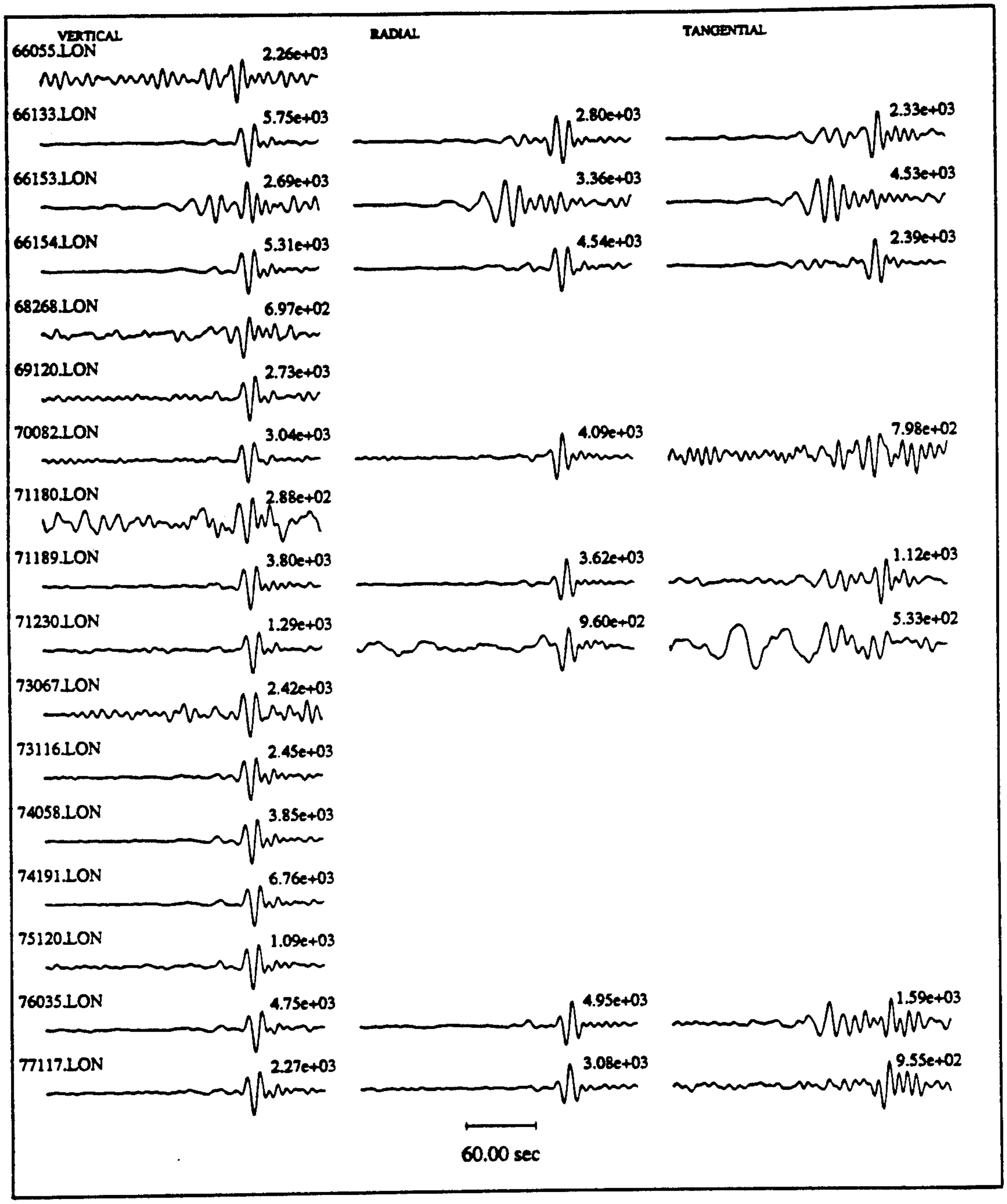

Figure .2: Explosion-generated surface waves observed at Longmire, WA (LON), some 1150 km from NTS.

LON (b)

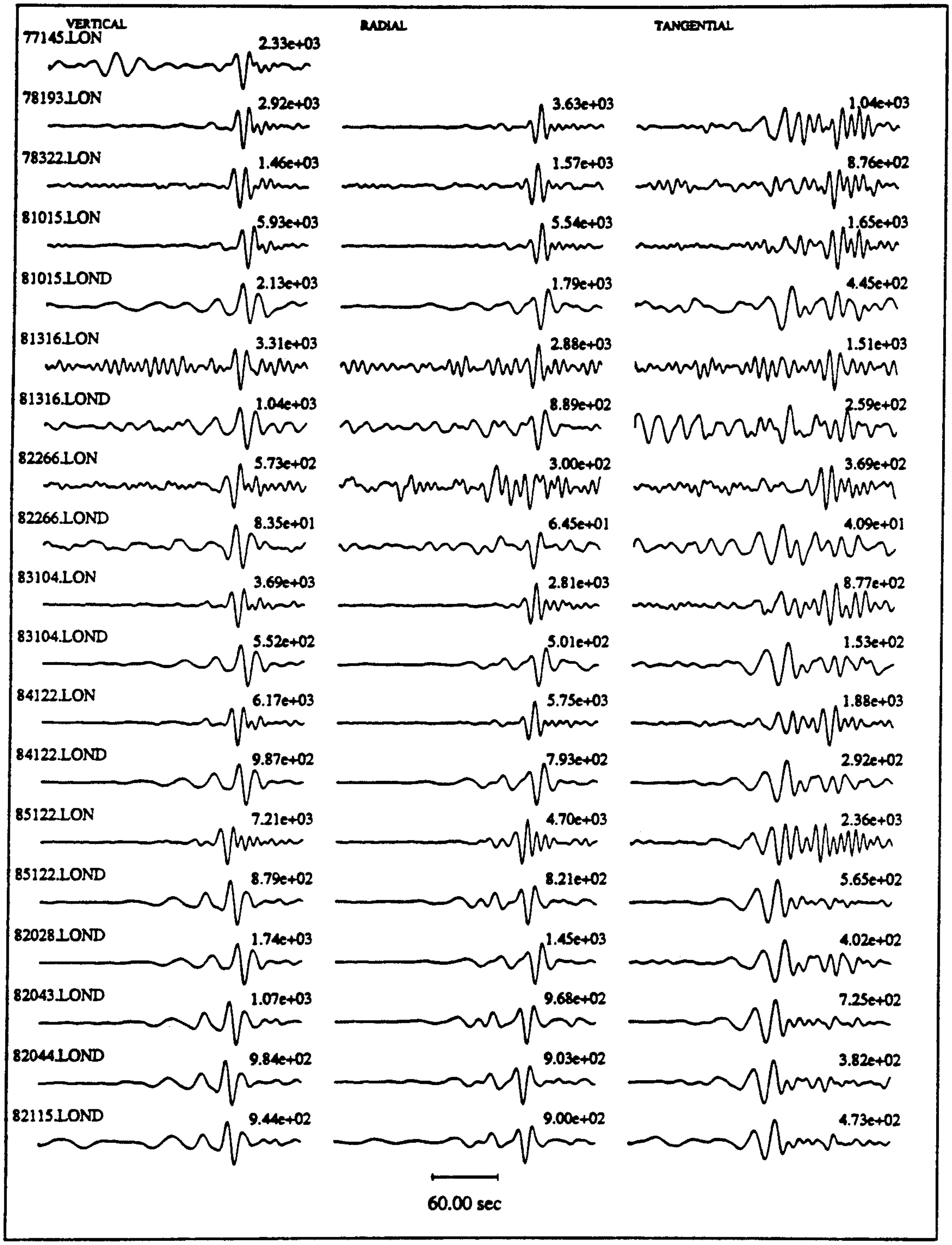
VERTICAL
RADIAL
TANGENTIAL
77145.LON
2.33e+03
78193.LON
2.92e+03
3.63e+03
1.04e+03
78322.LON
1.46e+03
1.57e+03
8.76e+02
81015.LON
5.93e+03
5.54e+03
1.65e+03
81015.LOND
2.13e+03
1.79e+03
4.45e+02
81316.LON
3.31e+03
2.88e+03
1.51e+03
81316.LOND
1.04e+03
8.89e+02
2.59e+02
82266.LON
5.73e+02
3.00e+02
3.69e+02
82266.LOND
8.35e+01
6.45e+01
4.09e+01
83104.LON
3.69e+03
2.81e+03
8.77e+02
83104.LOND
5.52e+02
5.01e+02
1.53e+02
84122.LON
6.17e+03
5.75e+03
1.88e+03
84122.LOND
9.87e+02
7.93e+02
2.92e+02
85122.LON
7.21e+03
4.70e+03
2.36e+03
85122.LOND
8.79e+02
8.21e+02
5.65e+02
82028.LOND
1.74e+03
1.45e+03
4.02e+02
82043.LOND
1.07e+03
9.68e+02
7.25e+02
82044.LOND
9.84e+02
9.03e+02
3.82e+02
82115.LOND
9.44e+02
9.00e+02
4.73e+02
60.00 sec

LON (c)

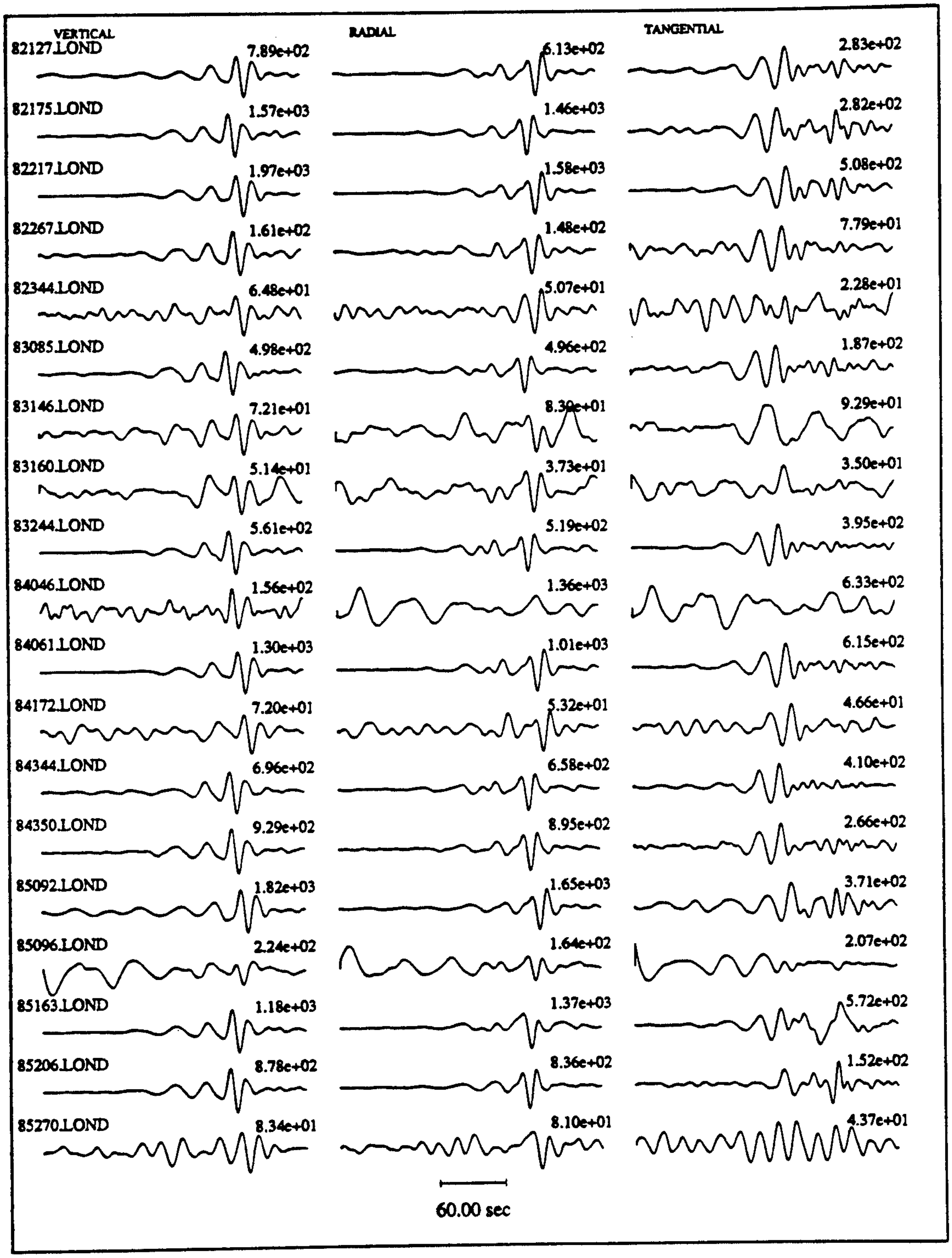
VERTICAL
RADIAL
TANGENTIAL
82127.LOND 7.89e+02 6.13e+02 2.83e+02
82175.LOND 1.57e+03 1.46e+03 2.82e+02
82217.LOND 1.97e+03 1.58e+03 5.08e+02
82267.LOND 1.61e+02 1.48e+02 7.79e+01
82344.LOND 6.48e+01 5.07e+01 2.28e+01
83085.LOND 4.98e+02 4.96e+02 1.87e+02
83146.LOND 7.21e+01 8.30e+01 9.29e+01
83160.LOND 5.14e+01 3.73e+01 3.50e+01
83244.LOND 5.61e+02 5.19e+02 3.95e+02
84046.LOND 1.56e+02 1.36e+03 6.33e+02
84061.LOND 1.30e+03 1.01e+03 6.15e+02
84172.LOND 7.20e+01 5.32e+01 4.66e+01
84344.LOND 6.96e+02 6.58e+02 4.10e+02
84350.LOND 9.29e+02 8.95e+02 2.66e+02
85092.LOND 1.82e+03 1.65e+03 3.71e+02
85096.LOND 2.24e+02 1.64e+02 2.07e+02
85163.LOND 1.18e+03 1.37e+03 5.72e+02
85206.LOND 8.78e+02 8.36e+02 1.52e+02
85270.LOND 8.34e+01 8.10e+01 4.37e+01
60.00 sec

LON (d)

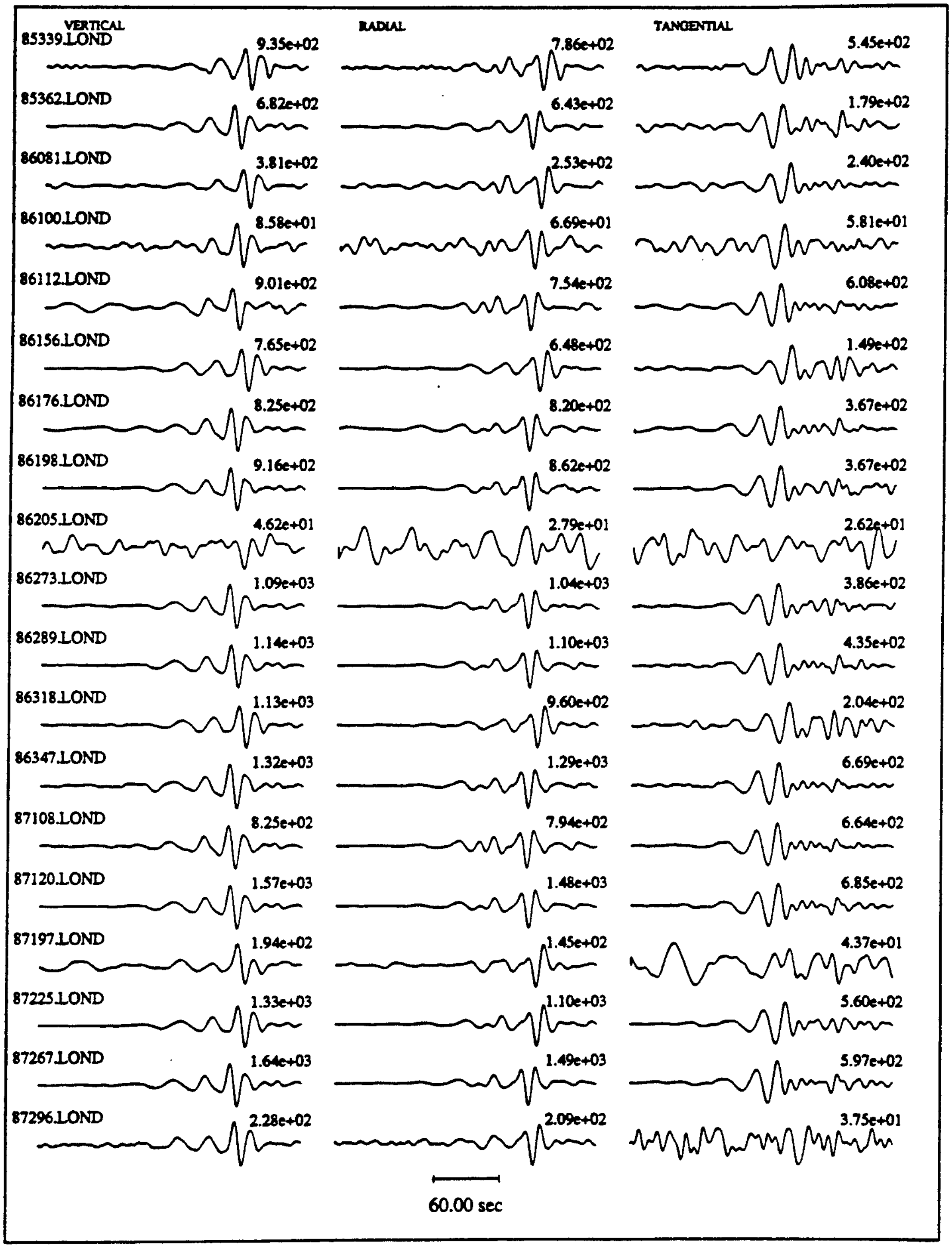
VERTICAL
RADIAL
TANGENTIAL
85339.LOND 9.35e+02 7.86e+02 5.45e+02
85362.LOND 6.82e+02 6.43e+02 1.79e+02
86081.LOND 3.81e+02 2.53e+02 2.40e+02
86100.LOND 8.58e+01 6.69e+01 5.81e+01
86112.LOND 9.01e+02 7.54e+02 6.08e+02
86156.LOND 7.65e+02 6.48e+02 1.49e+02
86176.LOND 8.25e+02 8.20e+02 3.67e+02
86198.LOND 9.16e+02 8.62e+02 3.67e+02
86205.LOND 4.62e+01 2.79e+01 2.62e+01
86273.LOND 1.09e+03 1.04e+03 3.86e+02
86289.LOND 1.14e+03 1.10e+03 4.35e+02
86318.LOND 1.13e+03 9.60e+02 2.04e+02
86347.LOND 1.32e+03 1.29e+03 6.69e+02
87108.LOND 8.25e+02 7.94e+02 6.64e+02
87120.LOND 1.57e+03 1.48e+03 6.85e+02
87197.LOND 1.94e+02 1.45e+02 4.37e+01
87225.LOND 1.33e+03 1.10e+03 5.60e+02
87267.LOND 1.64e+03 1.49e+03 5.97e+02
87296.LOND 2.28e+02 2.09e+02 3.75e+01
60.00 sec

to this time-domain windowing would be to phase-match-filter (Herrin & Goforth, 1977) the records, particularly the tangential component and all low SNR records, in order to remove noise and Rayleigh contamination, particularly for nearer stations where the fundamental-mode Rayleigh wave and Love wave group arrival times overlap.

Next, the spectral ratio of each windowed record and its appropriate synthetic is computed by averaging over the 0.167 to 0.0167 Hz bandwidth. The standard deviation in the spectral ratio estimate is taken as the error in the observation. Spectral ratio curves for Rayleigh waves were generally smooth and flat, implying a good fit between observed and synthetic spectra. Love wave data-to-synthetic spectral ratios were not as flat. It is suspected that the Rayleigh wavetrain energy, contaminating the Love wavetrain primarily is responsible for this effect.

The polarity of the waveform, used as phase information, was determined by visual inspection. This was primarily of importance for Love wave observations. Only in the case of PILEDRIVER were there any reversed-polarity Rayleigh waves. The resultant spectral ratios and phase information were used in the source inversion. The inversion technique is described in the "Synthetic Seismogram Generation and Moment Inversion Technique" section. The results of the source inversion are discussed later.

PATH MODELING

To determine accurate long-period source parameters it is necessary to correct for propagation effects along the surface wave travel-paths. This involves determining an average earth structure for each path from a general source region to a particular receiver. The paths are modeled as 1-dimensional laterally homogeneous structures. Paths from the Nevada Test Site (NTS) to 23 World Wide Seismic Station Network (WWSSN) and Canadian Seismograph Network (CSN) stations were determined for a surface wave study by Stevens (1986 and personal communication). These stations are shown as circles in Figure 3. The path Green's functions were determined by a two step inversion of shear wave velocity and Q as discussed in Stevens (1986). For other stations in the network (shown as triangles in Figure 3) path models were chosen or developed through a variety of means. Whenever possible, pre-existing models were used for path structures for any given NTS-station path. For some paths several models were tried. To determine whether or not a particular earth model was appropriate for a particular path, a synthetic seismogram was generated and compared to the highest SNR observed record. The quality of the fit was determined by visual inspection of time domain records. Absolute travel time and amplitude comparisons between observed and synthetic intermediate-period ($6<T<60$ sec.) Rayleigh waveforms as well as fundamental-mode dispersion data were the criteria used to judge the goodness of fit of the paths.

Most of the intermediate-range to distant station paths ($\Delta > 1500$ km) were successfully modeled using a structure from Stevens' ensemble of structures. However, for regional stations at lesser distances (i.e., the southwestern United States), alternative earth models were necessary. Station coverage in this area is especially important for several reasons. At regional distances the threshold magnitude for observing surface waves is lower than that of a more distant receiver, since the effects of geometrical spreading and attenuation (due both to anelastic absorption and scattering) are less for shorter paths. Amplitude errors due to using incorrect Q values for path corrections will also be less for shorter paths for the same reason. Because NTS is situated in the southwest corner of the U. S., the azimuthal coverage for more distant paths is limited, so that there are no seismographic stations 600 to 5000 km

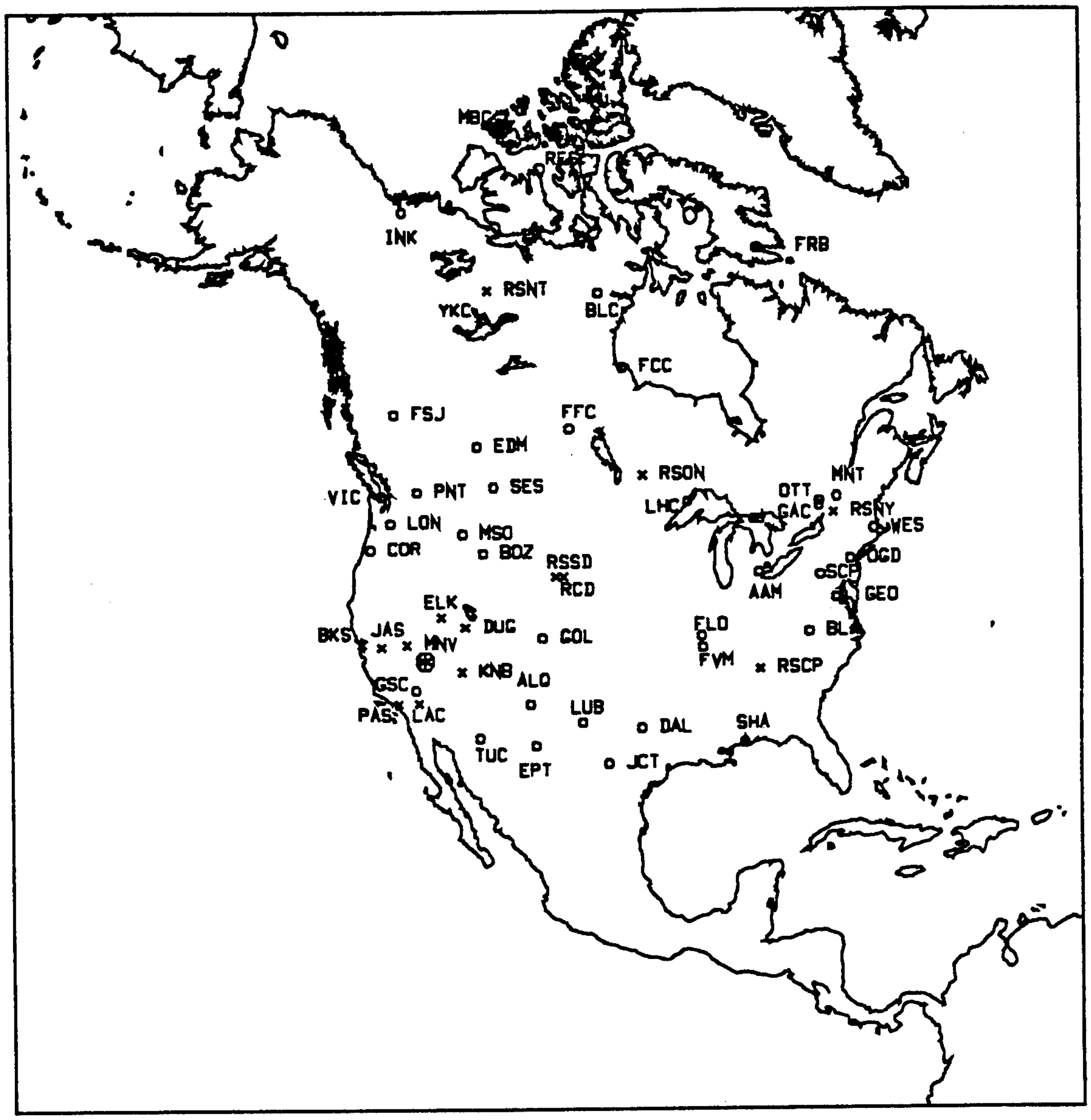

Figure 3: Map of North American station network used in this study. The "spoked wheel" is the Nevada Test Site.

to the west or southwest of NTS (i.e., in the Pacific Ocean). Station coverage to the south (for pure continental paths) is also very limited, as there were few long-period seismographic stations recording in Mexico and Central America during the time period in which events for this study were taken.

Broad azimuthal coverage is also important for constraining the seismic moment. For example, a vertical strike slip double-couple source, which has a $(\sin 2\phi)$ radiation pattern superimposed with an isotropic source will generate a Rayleigh wave radiation pattern with quadrants of increased and decreased amplitude, which is caused by the constructive and destructive interference of the two sources. For the case of perfect azimuthal coverage, the network-averaged scalar moment will be that of the isotropic source. Lack of coverage in one of these quadrants will cause the observed network-averaged moment to be larger or smaller than the actual value, depending upon whether constructive or destructive interference occurs in the unobserved quadrant. If phase and amplitude information are to be inverted to obtain the moment tensor, broad azimuthal coverage improves the constraints of the moment tensor inversion.

A large proportion of the regional stations in this study have paths which predominantly traverse the Basin and Range province. Fortunately this region has been the focus of many crustal and upper mantle structure studies, so that there are a good many earth structures derived from both surface wave and body wave studies available from which to choose to model the paths of interest in this study.

Mooney & Braile (1989) review P-wave velocity structures, determined from P-wave refraction studies, for the different physiographic regions of North America, including the Basin and Range province. Saikia & Burdick (1991) forward-modeled P_{nl} waveforms from NTS explosions to many of the same regional stations used in this study in order to determine a general crustal model for the area.

Press (1960) used a combined refraction, surface wave phase velocity, and gravity data to infer a seismic velocity structure for, primarily, the Mojave block. Hadley & Kanamori, in more recent studies, have interpreted this same area both in terms of P-wave refraction data (1977) and interstation phase velocities from teleseismic Rayleigh waves (1979).

Keller *et al.* (1976) used regional, explosion-generated, short-period (4 to 22 sec.) Rayleigh wave group velocities to determine crustal structure for several areas in the Western U. S., including the eastern Basin and range Province. Priestly & Brune (1978) made use of teleseismic, wide-band (4 to 120 sec.), interstation fundamental-mode Rayleigh wave and Love wave phase velocities to determine the shear-wave velocity structure for the Nevada and Western Utah Great Basin area. The dispersion results of this study are corroborated in a study by Patton (1982) in which single-station Rayleigh wave phase velocities were determined using regional, digital, broadband data.

Patton & Taylor (1984) determined shear-wave Q structure from regional Love wave and Rayleigh wave amplitude data. The shear velocity model used in their method is a hybrid of the Priestly-Brune (PB, 1978) upper mantle model and a NTS-TUC (Tuscon, Arizona) crustal model developed by Bache *et al.* (1978) discussed below. Their results imply a much lower Q in the crust and upper mantle than a more general study of attenuation in western North America by Mitchell (1975), which they attribute to partial melting in the upper mantle. This attenuation model was used in conjunction with all earth models examined in this study for paths in this region, which don't have an associated Q structure.

The model that generally best fit the Rayleigh wave and Love wave observed waveforms for the Basin and Range stations (DUG, GSC, ELK, KNB, LAC and MNV) from the above cited models was found to be the PB model. The Patton and Taylor (PT) Basin and Range attenuation model was used in conjunction with the PB velocity model.

Bache *et al.* (1978) determined flat-layered velocity structures for paths from NTS to ALQ and TUC using surface wave dispersion data. Attenuation values were taken from the previously cited study of regional Rayleigh attenuation study by Mitchell (1975). Langston & Helmberger (1974) also modeled the NTS-TUC path by forward-modeling body wave phases and by trial and error inversion of group velocity data. Both studies have similar crustal thicknesses for the NTS-TUC path, as body wave phases were used to constrain the depth to the Moho; however, the shear velocity is higher at the top of the mantle in the Langston-Helmberger model than in the other ($v_s = 4.6$, vs. $v_s = 4.42$). The Bache model was chosen for this study. Synthetic fundamental-mode surface waves generated with the Bache models match observed surface wave records significantly better than the Langston-Helmberger model. Comparisons of observed and syntethic surface wave waveforms for the NTS to ALQ and TUC paths, along with all others, are shown in Figure 4 (for Rayleigh waves) and Figure 5 (for Love waves).

Path structures determined in this study were arrived at through a combination of forward modeling and inversion of dispersion data for shear-wave structure. Compressional velocity and density were calculated from functional relationships with shear-wave structure as per Stevens (1986). The philosophy behind these path structures is to obtain earth models that will give accurate path corrections or Green's functions with which to generate synthetic seismograms which fit the observed waveforms with respect to amplitude and arrival times, rather than to recover the lithospheric structure or the earth along the path, although the

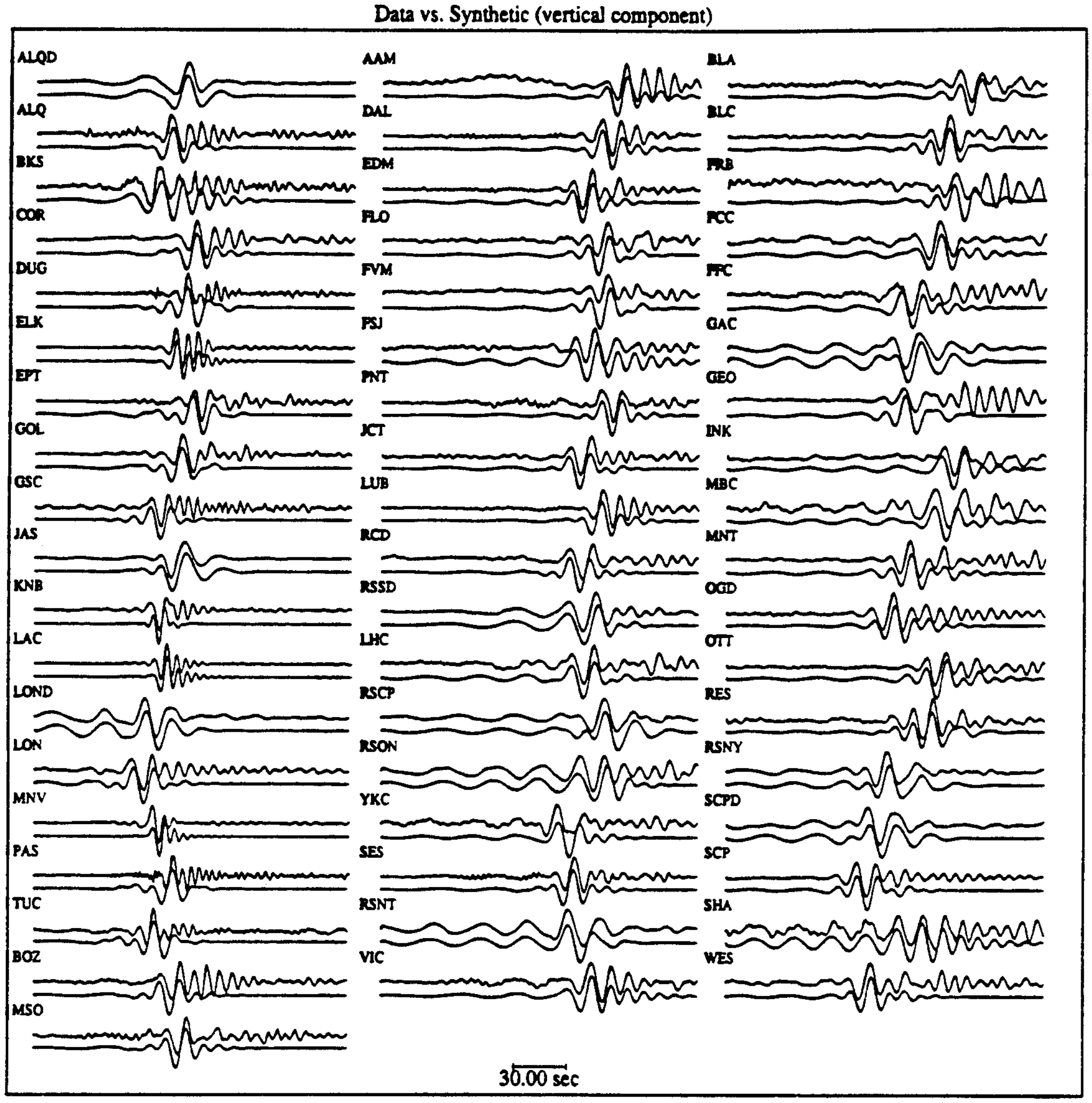

Figure Comparison of vertical component fundamental Rayleigh wave waveforms. The data time series are the upper, thicker traces; the lower trace in each case is the fundamental mode synthetic. All time series band-passed between 60 and 6 seconds.

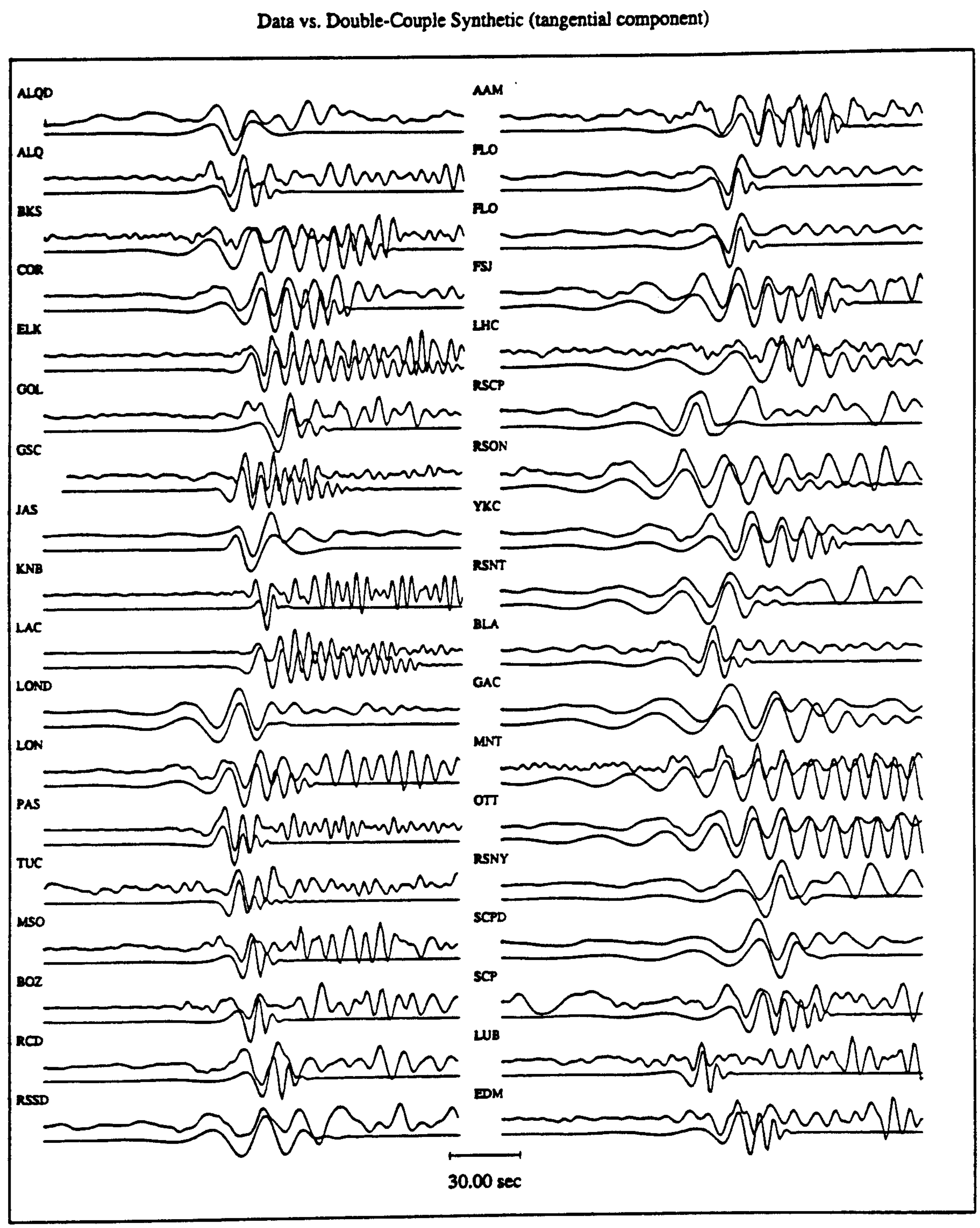

Figure Comparison of observed and synthetic fundamental-mode Love waves.

models also should not diverge too drastically from realistic gross earth structure. NTS surface waves for many of the stations in this study's network traverse several tectonic/geologic provinces. A flat-layered earth model obviously cannot accurately describe a crust and upper mantle cross-section traversing various portions of the Western Cordillera (the Basin and Range, Rocky Mountains, and the Colorado Plateau) and the North American craton. However, one can obtain a model which describes an average earth model for a given path which fits the observed dispersion data and spectral amplitude curves, as well as the time-domain waveforms.

The starting models used for this path determination scheme come from studies in which the earth structures for similar/nearby paths were inverted for using rigorous inversion procedures and resolution analysis and geophysical constraints. The first step was to see how well the initial structure modeled Rayleigh waveforms. As it turned out, none of these structures fit both arrival times and waveforms very well for the desired paths. Next, for each path the initial structure was perturbed in an effort to better fit synthetic seismograms generated with the structure to the observed waveforms. This included adding and removing low-velocity surface layers (representing sedimentary basins), increasing and decreasing the gross (or average) velocity in the crust and/or upper mantle, and increasing and decreasing the crustal thickness. This exercise also gives one a feel for the effects of these model changes. Perturbations to the initial model were retained if they improved the wave-train arrival and/or waveform.

The depth to the moho and the shear-velocity contrast there are the most important influences upon the surface wave-field. Independent geophysical constraints on these factors was desired. Mooney & Braile (1989) summarize crustal models for North America (NA) inferred from seismic refraction and reflection studies. Their map of NA crustal thickness and representative P-wave velocity structures for the various geologic regions were useful as guidelines for estimating average depths to the moho for the various paths investigated, as well as for inferring the crust-mantle shear-wave velocity contrast. In inverting for shear velocity structure, as described below, it was found that using a starting model with a correct crustal thickness (constrained by reflection and refraction data) was important in order to obtain earth structures which produced well-fitting dispersion values and time-series. Inverted shear-wave earth models obtained from starting models with crustal depths which differed from what was believed to be a reasonable estimate of the average crustal thickness (constrained by independent geophysical data) usually did not produce dispersion values compatible with the data or time series which adequately modeled observed seismograms.

As an independent test of crustal thickness, a stochastic inversion of the dispersion data was conducted with a generic model ($v_p = 7.0, v_s = 4.0$) to find the depth to the moho. It was found in each case that the structure converged, to first order, to a layer over a half-space. The depth of the basal crustal layer was found to agree with the values inferred from the Mooney & Braile (1989) map. In the case of JAS, where the travel path transverses the Sierra Nevada, it was unclear what the average crustal thickness should be, so the preliminary inversion inferred mantle depth of 37.5 km was taken to be representative of the average NTS-JAS path, and the Priestly-Brune Basin and Range based starting model was modified accordingly.

Paths from NTS to PAS, JAS, and RSTN stations were modeled in this study. Elastic parameters for these paths were determined by inverting fundamental-mode Rayleigh wave dispersion data to obtain the shear wave velocity (β) structure for the model. The surface wave analysis and velocity inversion computer codes used come from the Computer Programs in Seismology software package developed at the University of St. Louis (Herrmann, 1988). The shear-wave velocity (V_S) structure is found by simultaneously inverting for group and phase velocity data (for Rayleigh waves measured between 0.015 and 0.150 Hz) and minimizing the integral of $\|d\beta/dz\|$ over the structure, except across discontinuities at layer boundaries. This linear inversion scheme is similar to the one described in Bache *et al.* (1978) and Stevens (1986).

Q values for paths to RSTN stations were taken from the Stevens' attenuation model with the most similar path. All RSTN stations were on or near great circle paths of North American WWSSN or CSN stations. The PAS and JAS structures used the Patton & Taylor (1984) attenuation model. These two stations have paths to NTS which traverse a portion of the Basin and Range region.

Although Q structure was not determined by inversion, it was modified from the starting Q model by forward modeling of synthetic time series to be compatible with observations. For some paths it was necessary to create narrow, very high Q ($Q \approx 1000$) zones in the upper crust (5 to 15 km depth) in order to model the data. This was needed when the observed Airy Phase amplitudes ($8 < T < 15$) were considerably larger relative to the longer period data than the synthetic counterpart. The actual cause for these amplitude discrepancies are likely to be lateral variations in the waveguide which tend to generate shorter period surface waves, rather than extreme Q values in the crust or mantle. However, to model these paths with flat-layered models, amplitude discrepancies must be accounted for in the attenuation structure. The amplitude discrepancy between relative long period and shorter period Rayleigh waves is in all likelihood due to anomalous short-period energy, as it is much harder to account for differences in Q at longer periods, since the long-period wave-field completes fewer cycles for a given path distance than do the shorter period waves.

Surface wave dispersion is not strongly dependent on the compressional velocity (V_P) or density (ρ), hence they aren't directly solved for in the inversion, but rather treated as functions of the medium's shear velocity, to which surface wave velocities are most sensitive. The compressional velocity (V_P) is constrained to be consistent with a Poisson's ratio of 0.27, while the density is constrained by a Birch's law formula:

$$\rho = 0.65 \times \beta + 400.$$

This formula is an empirical relationship developed from data in Dobrin (1976) and is in MKS units.

The maximum depth of the inversion model was set to the approximate longest wavelength ($\lambda = c/f$) observations. For a 0.015 Hz Rayleigh wave phase velocity ($c \approx 4.0$), this depth would be 270 km. Little resolution is to be expected at the lower bounds of this depth estimate, however. Layer thicknesses in the crust were chosen to be 5 km, with the top-most layer being divided in two, allowing for some resolution of possible shallow sedimentary basins. The upper 40 km of mantle is divided into 10 km thick sections and below this to 200 km, it is divided into layers 20 km thick. These layer thicknesses are close in value to the resolution length.

Single-station group velocity (U) dispersion values were determined from multiple filter analysis (Dziewonski *et al.*, 1969) of vertical component Rayleigh waves. After obtaining group velocities ($U(\omega)$), the time series are iteratively phase matched filtered (Herrin & Goforth, 1977; and Stevens, 1986) to reduce scattered energy, noise and higher modes, so that the signal can be more accurately analyzed for phase and group velocity and amplitude information. The phase information obtained from the phased matched filter is used to obtain a phase velocity. Two iterations were made to obtain the final dispersion data used to invert for a shear velocity structure.

Seismograms used for dispersion analysis were chosen from large magnitude explosions with the least observed tectonic release. Events which did not show evidence of long-period tangential energy in the approximate Love wave time window were assumed to be good candidates. KEARSARGE data were used for PAS and JAS (CMB) to NTS paths. Dispersion analysis was done for other events, too. For all events examined, coherent spectral amplitudes were observed up to 30 sec. At periods greater than this, the error in velocity measurements are considerably larger. The propagation paths are less than 400 km in length, so longer-period surface waves have traveled very few wavelengths and thus are not yet fully developed and/or are not dispersed enough to measure their group energy packets.

For the RSTN stations, seismic waveforms came from a variety of events. For these stations at greater distances (D $<$ 230 km), coherent signal was observed up to 50 sec. The RSSD, RSCP, and RSNT paths used DARWIN data. The DARWIN group velocity curves for RSON and RSNY had several inflection points between 15 and 50 seconds. This feature is believed to be due to signal noise or processing artifacts. These two stations' deconvolved displacement records showed long-period noise throughout the records. For other larger events, with higher signal to noise ratios, this phenomenon may be due to tectonic-release generated signals. These deviations from the correct dispersion curve are significant and adversely affect inversion results.

The group velocity dispersion for a suite of seven events (both from Pahute Mesa and Yucca Flat) for the two paths were compared. The group velocity curves generally correlated quite well by visual inspection between 8 and 40 sec. Above and below these levels, only some events had coherent smoothly continuous dispersion curves. In the period range between 15 and 50 sec. perturbations from a smooth, near-constant slope group velocity curve varied in shape from event to event and sometimes were absent, implying that they are some sort of noise effect and not a propagation phenomenon. The final dispersion data came from BELMONT for RSON and HERMOSA for RSNY. Deconvolved displacement seismograms for these events show low long-period noise levels.

The best-fitting forward-modeled velocity structure was then used as the initial model for the shear-wave inversion procedure. A weighted, least-squares inversion of fundamental-mode Rayleigh wave group and phase velocity is performed. Details of the inversion method are given in Russell (1986). The procedure is non-linear in nature, so iterative solutions are obtained. Q structure was not inverted for these paths. Instead the attenuation model associated with the initial inversion model was used. Here the assumption is that the gross attenuation structure is the same between nearby paths. To robustly solve for attenuation, one must employ two-station attenuation measurements or joint moment-Q inversions. The combination of data and paths in this study does not lend it to the two-station method. For the shorter paths (JAS and PAS), attenuation effects are minimal for surface waves, as they propagate relatively few wavelengths and consequently undergo a corresponding low number of attenuation cycles.

The shear wave inversion is a non-linear process, so many iterations were performed. The weighting factors used for the dispersion observations were proportional to the inverse of the spectral amplitude at a given period. Approximately every fourth iterated model was saved in case later iteration models converged towards a "pathological" one with unrealistically large velocity-contrast low velocity zones in the crust. Early inversion attempts made, using a damped least-squares stochastic inversion, resulted in such low velocity zones. Applying a weighted, damped differential least-squares inversion produced "smoother" velocity models which were geophysically reasonable (*i.e.*, did not have oscillating high and low velocity zones or unreasonably large velocity contrasts). The final inverted models were obtained using the latter method.

As mentioned earlier, the criterion to determine the goodness of fit of an earth structure were visual comparisons of the observed and Green's Function derived dispersion and waveform fits of the fundamental Rayleigh wave. Figures 6 and 7 compare observed and modeled group and phase velocity dispersion for the seven paths. All dispersion curve fits are quite good. The largest mismatch between observed and inverted model dispersion values are at the longest and shortest periods. These periods had the lowest spectral amplitudes, so they are weighted least in the inversion scheme. It is somewhat surprising that such good fits were obtained, considering the significant lateral variations in the waveguide, particularly for the JAS and PAS paths which each traverse several mountain ranges and valleys.

Figure 4 compares observed to synthetic seismograms for the fundamental-mode, vertical component Rayleigh waves for the seven paths modeled in this study as well as for the other network paths used in this study. All time series were band-passed filtered between 60 and 6 seconds. Each path is well modeled with respect to waveform and arrival time ($\Delta t < 1.0$). A confirmation of how well the models reflect the average earth structure of the path are comparisons of observed and synthetic fundamental-mode Love waves. The error in timing of the Rayleigh wave-train is in all cases small and is estimated to be less than 2 seconds. Figure 5 compares observed and synthetic Love waves. Unlike the case of explosion generated

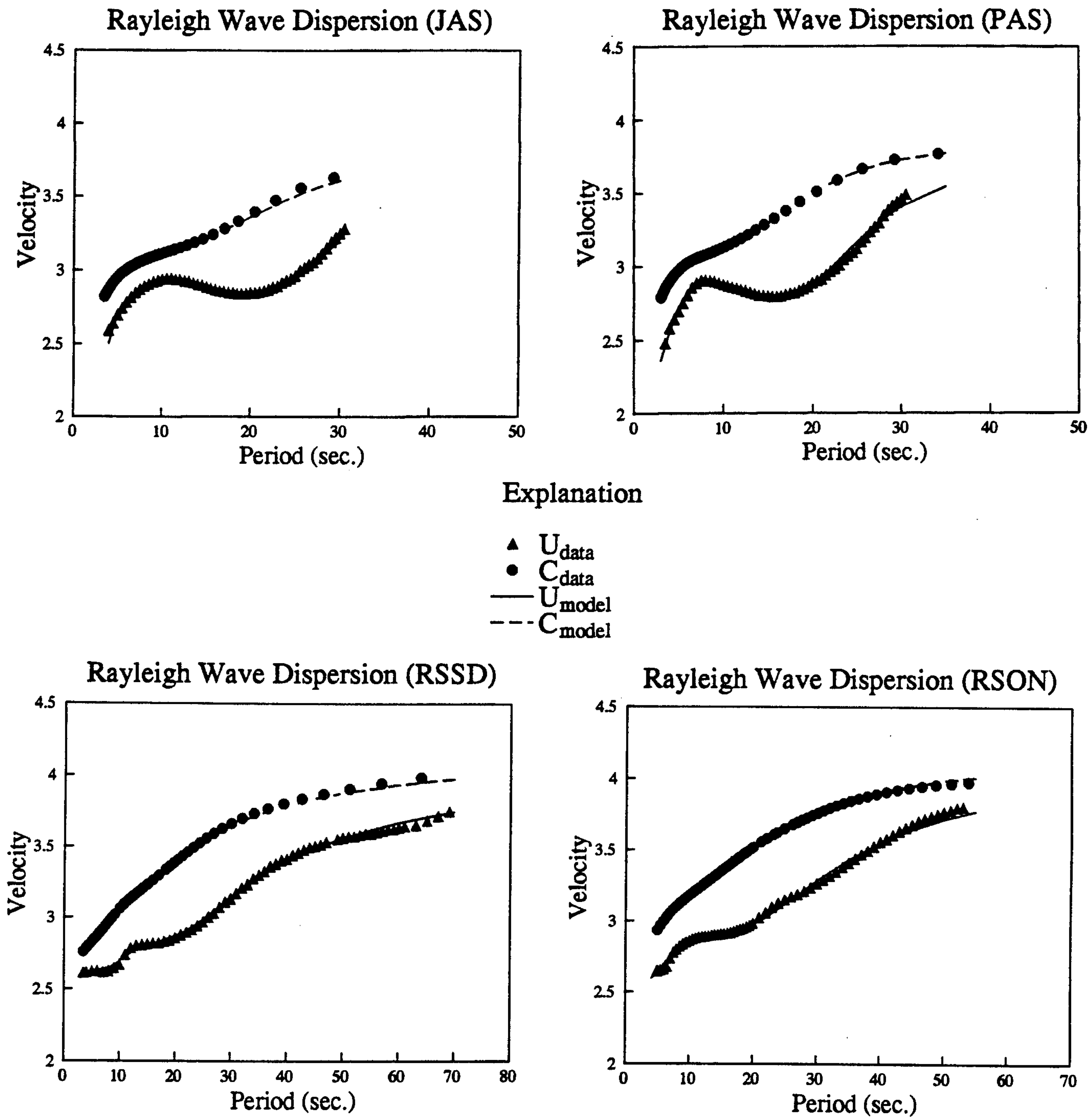

Figure 6: Fundamental-mode Rayleigh wave dispersion curves for JAS, PAS,RSSD and RSON.

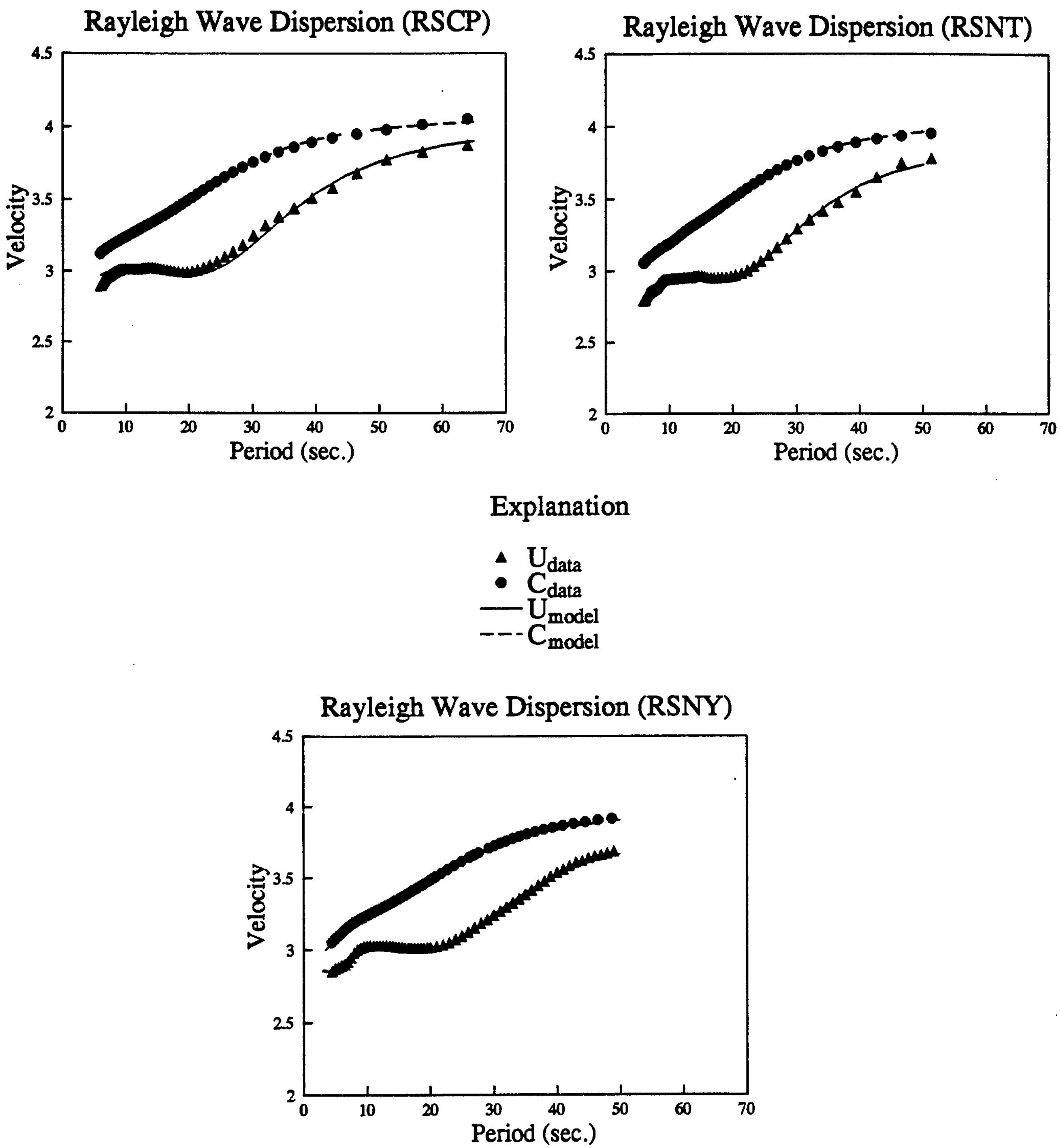

Figure 7: Fundamental-mode Rayleigh wave dispersion curves for RSCP, RSNT and RSNY.

Rayleigh waves, the polarity of tangential waves is ambiguous, because the source mechanism is not necessarily known. The correct polarity or phase was determined by comparing the best combined waveform fit/travel time residual minimum in conjunction with assumptions on the radiation pattern from previous studies. The waveform fits are sufficient for inversion purposes and aren't bad predictions of the observed Love waves, although the wave-train arrival time errors are larger (from 2 to 10 seconds), with the largest errors correlating, in general, to the more distant paths. Tables 2 lists the parameters for the final inverted path models.

Figure 8 displays the data/synthetic seismograms for the seven paths modeled in this study. Both fundamental-mode Rayleigh waves (vertical component) and Love waves are plotted. As discussed previously, the Q structures are based on pre-existing Q models, which are then modified by forward modeling the waveforms and only β was directly inverted. Estimated errors (1 standard deviation) in S velocity are on the order of 0.05 to 0.1 km/sec. Errors are smallest in the upper crust and largest in the lower crust and upper mantle. The resolving kernel widths were approximately 5 km in the upper crust and 10 to 15 km in the lower crust and upper mantle. Little or no resolution was found below 60 km. The P-wave and S-wave velocities, Q values and densities for these structures can be found in Woods (1993). These path models have typical continental path structures with crustal thicknesses in line with refraction and reflection constraints. No large low velocity zones are within the crust. Where an overlying layer does have a greater S velocity, the contrast is small ($\Delta V_S < 0.2$ km/sec.), and the errors in V_S are nearly of the same order of magnitude.

NTS to JAS Earth model				
Th km	α km/sec	β km/sec	ρ gm/cm^3	Q_β
2.5	4.06	2.35	2.33	30.0
5.0	6.00	3.51	2.70	103.4
5.0	5.96	3.49	2.69	171.6
5.0	6.20	3.63	2.76	171.6
5.0	6.11	3.58	2.73	171.6
5.0	5.95	3.48	2.69	171.6
5.0	6.36	3.71	2.81	103.4
5.0	6.33	3.69	2.80	103.4
4.0	7.55	4.36	3.26	103.4
5.0	7.60	4.38	3.27	90.0
10.0	7.66	4.42	3.29	80.0
10.0	7.73	4.46	3.22	70.0
20.0	7.80	4.12	3.24	70.0
20.0	7.86	4.15	3.26	80.0
20.0	7.91	4.08	3.28	93.4
20.0	7.98	4.09	3.30	106.8
20.0	8.04	4.40	3.33	106.8
20.0	8.13	4.43	3.36	106.8
20.0	8.22	4.45	3.39	106.8
∞	8.36	4.54	3.44	106.8

NTS to PAS Earth model				
Th km	α km/sec	β km/sec	ρ gm/cm^3	Q_β
1.0	3.09	1.75	2.16	30.0
3.0	5.62	3.21	2.62	54.6
5.0	6.07	3.51	2.72	74.6
5.0	6.02	3.48	2.71	131.6
5.0	6.08	3.52	2.73	171.6
5.0	6.19	3.58	2.76	131.6
4.0	6.27	3.62	2.78	103.4
5.0	6.80	3.93	2.93	103.4
5.0	7.78	4.49	3.24	103.4
5.0	7.74	4.47	3.22	74.6
5.0	7.68	4.43	3.20	49.6
5.0	7.61	4.39	3.18	49.6
10.0	7.54	4.35	3.15	49.6
10.0	7.48	4.31	3.13	49.6
10.0	7.44	4.29	3.12	31.2
20.0	7.43	4.29	3.12	31.2
20.0	7.48	4.32	3.13	63.4
20.0	7.58	4.37	3.16	93.4
∞	7.67	4.43	3.20	106.8

NTS to RSSD Earth model				
Th km	α km/sec	β km/sec	ρ gm/cm^3	Q_β
4.000	4.91	2.74	2.50	80.0
3.000	5.29	2.96	2.56	100.0
4.306	6.0	3.35	2.69	150.0
4.306	6.23	3.48	2.74	250.0
4.306	6.45	3.61	2.79	350.0
4.306	6.44	3.60	2.79	550.0
4.495	6.51	3.64	2.80	650.0
6.277	6.64	3.71	2.84	750.0
6.020	7.63	4.26	3.18	350.0
7.067	7.63	4.27	3.19	250.0
8.297	7.65	4.28	3.19	200.0
9.741	7.63	4.27	3.19	200.0
11.430	7.65	4.28	3.19	175.0
13.420	7.88	4.40	3.27	155.0
15.760	7.87	4.40	3.27	140.0
18.500	7.97	4.46	3.30	130.0
21.720	7.89	4.41	3.27	120.0
25.500	7.91	4.42	3.28	116.0
∞	7.91	4.42	3.28	116.0

NTS to RSON Earth model				
Th km	α km/sec	β km/sec	ρ gm/cm^3	Q_β
3.75	5.22	2.92	2.54	300.0
3.75	5.68	3.17	2.64	700.0
4.16	6.25	3.49	2.78	900.0
4.16	6.26	3.50	2.78	900.0
4.16	6.51	3.64	2.85	700.0
4.16	6.64	3.71	2.89	600.0
4.45	6.83	3.81	2.94	500.0
5.24	7.00	3.91	2.98	400.0
6.17	7.13	3.98	3.02	350.0
7.39	7.92	4.42	3.28	300.0
8.71	7.89	4.41	3.27	250.0
10.26	7.86	4.39	3.26	200.0
12.08	7.98	4.46	3.30	175.0
14.24	8.16	4.56	3.37	175.0
16.77	8.17	4.57	3.37	150.0
19.76	8.19	4.58	3.38	150.0
23.28	8.23	4.60	3.39	150.0
27.43	8.25	4.61	3.40	125.0
32.32	8.23	4.60	3.39	115.0
∞	8.23	4.60	3.39	115.0

Table 2a: NTS path models for JAS, PAS, RSSD and RSON

NTS to RSCP Earth model				
Th km	α km/sec	β km/sec	ρ gm/cm^3	Q_β
5.00	5.54	3.11	2.61	150.0
5.00	6.18	3.47	2.75	200.0
4.06	6.33	3.56	2.80	500.0
4.06	6.33	3.55	2.80	700.0
4.06	6.49	3.64	2.85	700.0
4.06	6.64	3.73	2.89	700.0
4.64	6.76	3.80	2.92	800.0
5.52	6.82	3.83	2.94	800.0
6.58	6.82	3.83	2.93	800.0
8.18	8.07	4.53	3.34	500.0
9.73	7.99	4.49	3.31	400.0
11.58	7.94	4.46	3.29	300.0
13.78	7.93	4.45	3.29	300.0
16.41	7.97	4.47	3.30	300.0
19.53	8.00	4.49	3.31	300.0
23.25	8.02	4.50	3.32	300.0
27.67	8.04	4.51	3.32	300.0
32.94	8.08	4.53	3.34	300.0
39.21	8.15	4.57	3.36	300.0
∞	8.15	4.58	3.37	300.0

NTS to RSNT Earth model				
Th km	α km/sec	β km/sec	ρ gm/cm^3	Q_β
5.00	5.57	3.11	2.61	217.4
5.00	5.96	3.33	2.69	219.9
4.45	6.36	3.55	2.80	275.4
4.45	6.43	3.58	2.79	344.3
4.45	6.54	3.65	2.84	466.0
4.45	6.76	3.78	2.86	631.4
7.09	6.97	3.90	2.87	770.2
7.06	7.00	3.91	2.87	723.0
6.70	8.13	4.54	3.34	634.9
7.98	8.11	4.53	3.33	441.2
9.50	8.00	4.47	3.34	310.3
11.31	7.88	4.40	3.35	229.2
13.46	7.99	4.46	3.35	181.0
16.03	7.98	4.46	3.36	152.3
19.08	8.03	4.49	3.36	133.5
22.72	8.07	4.51	3.36	120.2
27.05	8.15	4.55	3.38	118.6
32.20	8.22	4.59	3.37	119.0
38.33	8.26	4.61	3.39	119.3
45.63	8.26	4.62	3.39	119.5

NTS to RSNY Earth model				
Th km	α km/sec	β km/sec	ρ gm/cm^3	Q_β
2.00	5.92	3.31	2.54	844.0
3.00	5.92	3.31	2.54	815.0
4.00	5.90	3.30	2.54	932.0
1.00	6.01	3.36	2.54	965.0
4.06	6.42	3.59	2.73	964.0
4.06	6.44	3.60	2.74	902.0
4.06	6.50	3.63	2.76	881.0
4.06	6.58	3.68	2.79	752.4
4.64	6.69	3.74	2.83	520.0
5.52	6.78	3.79	2.86	436.1
6.58	6.83	3.82	2.88	318.5
8.18	8.14	4.55	3.36	243.4
9.73	8.10	4.52	3.34	194.3
11.58	8.04	4.49	3.32	160.5
13.78	8.03	4.49	3.32	135.1
16.41	8.06	4.50	3.33	116.0
19.53	8.12	4.54	3.35	113.4
23.25	8.18	4.57	3.37	114.1
27.67	8.23	4.60	3.39	114.6
32.94	8.27	4.62	3.40	115.0
39.21	8.31	4.64	3.42	115.0
∞	8.34	4.66	3.43	115.0

Table 2b: NTS path models for RSCP, RSNT and RSNY.

Synthetic Seismogram Generation and Moment Inversion Technique

Since the explosions are shallow sources ($h < 1$ km) and tectonic strain release is also thought to be not much deeper, higher modes are not strongly excited as the fundamental-mode Rayleigh wave at the periods of interest. Patton (1988) found that spall is an effectice generater of higher modes. However, such excited energy is relatively short-period, so that it's effect on the long-period function is minimal.

In the following we give the expressions for the Rayleigh and Love surface waves due to an explosion and a double couple (Ben-Menahem & Harkrider, 1964, Harkrider, 1970, Mendiguren, 1977, among many others), These epressions have been modified for a slowly varying laterally inhomogeneous medium as in Woods & Harkrider (1995), where the source region is one verticaly inhomogeneous medium and the propagation path and receiver are another.

For the vertical spectral displacement (positive down), the Rayleigh waves yield

$$\bar{w}_0 = \overline{M}_{\#} \left\{ \sin\lambda \, \sin 2\delta \, \overline{W}_{45} - \left(\cos\lambda \, \cos\delta \, \cos\phi - \sin\lambda \, \cos 2\delta \, \sin\phi \right) \overline{W}_{13} \right.$$

$$\left. + \left(\frac{\sin\lambda}{2} \sin 2\delta \, \cos 2\phi + \cos\lambda \, \sin\delta \, \sin 2\phi \right) \overline{W}_{12} \right\} + \overline{M}_{*} \, \overline{W}_{*} \tag{1}$$

The angles λ, δ, and ϕ are the standard rake, dip and azimuth measured from the fault strike. The double couple spectral components are

$$\begin{aligned}
\overline{W}_{12} &= -\frac{i}{2}\frac{\omega}{c_1} \, [A_{\#}]_1 \, \underline{A}_{Rm} \, H_2^{(2)}\left(\frac{\omega}{c_2} r\right) \exp[-\gamma_2 \, r] \\
\overline{W}_{13} &= -\frac{i}{2}\frac{\omega}{c_1} \, [C_{\#}]_1 \, \underline{A}_{Rm} \, H_1^{(2)}\left(\frac{\omega}{c_2} r\right) \exp[-\gamma_2 \, r] \\
\overline{W}_{45} &= -\frac{i}{4}\frac{\omega}{c_1} \, [B_{\#}]_1 \, \underline{A}_{Rm} \, H_0^{(2)}\left(\frac{\omega}{c_2} r\right) \exp[-\gamma_2 \, r)
\end{aligned} \tag{2}$$

and the explosion

$$\overline{W}_* = -i\frac{\omega}{c_1}\frac{\beta_1^2}{\alpha_1^2}\,[K_R]_1\,\underline{A}_{Rm}\,H_0^{(2)}\left(\frac{\omega}{c_2}r\right)\,\exp[-\gamma_2\,r] \tag{3}$$

where

$$K_R = y_3(h) - \frac{1}{2\mu k r}y_2(h),$$

$$A_\# = -y_3(h),$$

$$B_\# = -\left\{\left(3 - 4\frac{\beta^2}{\alpha^2}\right)y_3(h) + \frac{2y_2(h)}{\rho\alpha^2 k}\right\},$$

or in terms of the poisson ratio, σ,

$$B_\# = -\left\{\frac{(1+\sigma)}{1-\sigma)}y_3(h) + \frac{2y_2(h)}{\rho\alpha^2 k}\right\},$$

$$C_\# = \frac{y_4(h)}{\mu k},$$

$$k = \frac{\omega}{c}$$

and the $H_m^{(2)}$ are the cylindrical Hankel functions representing outward propagation over a distance r. The above spectral mixed path excitation is

$$\underline{A}_{Rm} = [\,\underline{A}_{R1}\,\underline{A}_{R2}\,]^{1/2} \tag{4}$$

with each subscripted

$$\underline{A} = \frac{1}{2cUI}$$

where the energy integral is

$$I = \int_0^\infty \rho(z)[y_1^2(z) + y_3^2(z)]dz,$$

$\rho(z)$ is the local density distribution in the medium and we have used Saito's (1967) Rayleigh wave eigenfunction notation, $y_i(z)$. The eigenfunctions are normalized in such away that the vertical displacement eigenfunction, $y_1(z)$ is equal to 1 at the free surface, $z = 0$. This results in the horizontal displacement eigenfunction, $y_3(z)$, being equal to the Rayleigh wave surface ellipticity at this boundary. $y_2(z)$ and $y_4(z)$ are the normal and shear stress eigenfuntions associated Rayleigh modes. U and c are respectively the local group and phase velocities. By local we mean the eigenvalues and eigenfunctions that one would obtain for a laterally homogeneous half-space consisting of the vertical elastic and density distribution at that location. The subscripted quantities other than the just mentioned eigenfunctions and Hankel functions are as follows: the subscript 2 denotes local quantities at the receiver location, which in this case is the same as the propagation path, and 1 is the point source location and quantities within the 1 or 2 subscripted square brackets are evaluated at these locations. γ is the frequency dependent attenuation coefficient due to the anelastic structure of the path, ie. $\gamma = \omega/(2QU)$, where Q is the attenuation quality factor.

For the azimuthal surface spectral displacement (positive for increasing azimuth), the Love waves yield

$$\begin{aligned} \bar{v}_0 &= \overline{M}_\# \Big\{ (2\cos\lambda \ \sin\delta \ \cos 2\phi \ - \ \sin\lambda \ \sin 2\delta \ \sin 2\phi)\overline{V}_{12} \\ &\quad + \ (\sin\lambda \ \cos 2\delta \ \cos\phi \ - \ \cos\lambda \ \cos\delta \ \sin\phi)\overline{V}_{13} \Big\} \end{aligned} \tag{5}$$

where the double couple spectral components are

$$\begin{aligned} \overline{V}_{12} &= -\frac{i}{2}\frac{c_2}{c_1} \, [y_1(h_\#)]_1 \, \underline{A}_{Lm} \, \frac{d}{dr} H_2^{(2)}\left(\frac{\omega}{c_2} r\right) \, \exp[-\gamma_2 \, r] \\ \overline{V}_{13} &= \frac{i}{2}\frac{c_2}{c_1} \, [G_\#]_1 \, \underline{A}_{Lm} \, \frac{d}{dr} H_1^{(2)}\left(\frac{\omega}{c_2} r\right) \, \exp[-\gamma_2 \, r] \end{aligned} \tag{6}$$

where

$$G_\# = -\frac{1}{\mu k} y_2(h)$$

and the eigenfunctions and eigenvalues are those for the fundamental Love wave mode and $\underline{A}_{Lm}$ is the mixed path excitation function for Love waves defined as its Rayleigh wave equivalent above with the exception that

$$I = \int_0^\infty \rho(z)[y_1^2(z)]dz.$$

where $y_1(z)$ is the surface azimuthal displacement eigenfunction and $y_2(z)$ is the Love wave shear stress eigenfunction, both normalized to surface displacement. Whenever the distinction between Rayleigh and Love wave quantities might be confusing, we will denote them with R or L subscripts or superscripts. The choice between subscript or superscript is made to reduce crowding.

Assuming that at the periods of interest ($T > 6sec$) the explosion and tectonic release source occur simultaneously and their respective moments can be considered as step function moments, $i.e.\overline{M} = M/(i\omega)$, the spectral far-field vertical components of the Rayleigh wave displacements and the tangential components of the Love waves are respectively

$$\bar{w}_0 = -ik_R\underline{A}_{Rm}\left(\frac{2}{\pi k_R r}\right)^{1/2}\exp[-ik_{R2}r + i\pi/4]\left[M_*\frac{\beta^2}{\alpha^2}K_R(h_*)\right.$$
$$+\frac{M_\#}{2}\left\{\frac{1}{2}\sin\lambda\sin 2\delta[B_\#(h_\#) - A_\#(h_*)\cos 2\phi]\right.$$
$$-\cos\lambda\sin\delta\sin 2\phi A_\#(h_\#) \tag{7}$$
$$\left.\left.-i(\cos\lambda\cos\delta\cos\phi - \sin\lambda\cos 2\delta\sin\phi)C_\#(h_\#)\right\}\right]\exp[-\gamma_{R2}\, r]$$

and

$$\bar{v}_0 = k_L\underline{A}_{Lm}\left(\frac{2}{\pi k_L r}\right)^{1/2}\exp[-ik_{L2}r + i\pi/4]\frac{M_\#}{2}$$

$$\cdot \left[\left(\cos\lambda \sin\delta \cos 2\phi - \frac{1}{2} \sin\lambda \sin 2\delta \sin 2\phi \right) y_1^L(h_\#) \right. \tag{8}$$

$$\left. +i(\sin\lambda \cos 2\delta \cos\phi - \cos\lambda \cos\delta \sin\phi) \frac{y_2^L(h_\#)}{k_L \mu} \right] \exp[-\gamma_{L2}\, r]$$

Assuming that h_* and $h_\#$, the respective explosion and double couple source depths, are shallow, then as $h \to 0$,

$$y_2^R(h) \to 0,$$

$$y_4^R(h) \to 0,$$

and

$$y_2^L(h) \to 0$$

and

$$K_R(0) = y_3^R(0) = -A_\#(0) = \frac{1}{3 - 4\beta^2/\alpha^2} B_\#(0)$$

and

$$C_\#(0) = 0$$

and

$$y_1^L(0) = 1.$$

Making use of these relations reduces the displacement equations to:

$$\bar{\mathrm{w}}_0 \cong -ik_R \underline{A}_{Rm} \left(\frac{2}{\pi k_R r} \right)^{1/2} \exp[-ik_{R2} r + i\pi/4] y_3^R(0) \frac{\beta^2}{\alpha^2}$$

$$\cdot \left\{ M_* + \frac{M_\#}{2} \frac{\alpha^2}{\beta^2} \left[\frac{1}{2} \sin\lambda \sin 2\delta \left(\cos 2\phi - 3 + 4\frac{\beta^2}{\alpha^2} \right) \right. \right. \tag{9}$$

$$\left. \left. + \cos\lambda \sin\delta \sin 2\phi \right] \right\} \exp[\gamma_{R2}\, r]$$

and

$$\bar{v}_0 \cong k_L \underline{A}_{Lm} \left(\frac{2}{\pi k_L r}\right)^{1/2} \exp[-ik_{L2}r + i\pi/4] \frac{M_\#}{4}$$

$$\cdot (2\cos\lambda \sin\delta \cos 2\phi - \sin\lambda \sin 2\delta \sin 2\phi) \exp[\gamma_{L2}\, r]. \tag{10}$$

At NTS the assumed mechanism for tectonic release is believed to be predominantly vertical, right-lateral strike slip in nature (Toksöz *et al.*, 1965;d Wallace *et al.*, 1983, 1985) ($\lambda = 180^\circ$ and $\delta = 90^\circ$). This assumption is made in part to help simplify the inversion procedure and leads to:

$$\bar{w}_0 \cong -ik_R \underline{A}_{Rm} \left(\frac{2}{\pi k_R r}\right)^{1/2} \exp[-ik_{R2}r + i\pi/4] y_3^R(0) \frac{\beta^2}{\alpha^2} \left[M_I - \frac{M_\#}{2} \frac{\alpha^2}{\beta^2} \sin 2\phi\right] \tag{11}$$

and

$$\bar{v}_0 = -k_L \underline{A}_{Lm} \left(\frac{2}{\pi k_R r}\right)^{1/2} \exp[-ik_{R2}r + i\pi/4] \frac{M_\#}{2} \cos 2\phi, \tag{12}$$

so that measured moment becomes a function of M_I, $M_\#$ and ϕ (three parameters), where ϕ is the azimuth measured clockwise from the strike of the fault plane. In the above we have replaced the actual explosion moment M_* with it's estimate M_I based on these assumptions.

To invert for the combined isotropic/double couple source mechanism, the measured fundamental Rayleigh and Love wave amplitudes are averaged over a spectral bandwidth between 10 and 60 seconds. For a receiver at azimuth θ, measured clockwise from North, and with a vertical strike slip fault with strike ψ, also measured clockwise from North, the observed Rayleigh amplitude will be:

$$A_{Ray} \propto M_I - \frac{M_\#}{2} \frac{\alpha^2}{\beta^2} \sin 2(\theta - \psi),$$

which can be simplified to:

$$A_{Ray} \propto M_I - \frac{M_\#}{2} \frac{\alpha^2}{\beta^2} [\sin 2\theta \cos 2\psi - \cos 2\theta \sin 2\psi]. \tag{13}$$

This equation can be formulated as a linear least-squares inversion problem of the form:

$$\mathbf{A} \cdot \mathbf{x} = \mathbf{b},$$

or

$$A_{Ray} = 1 \cdot x_1 - \frac{\sin 2\theta}{2} \frac{\alpha^2}{\beta^2} \cdot x_2 + \frac{\cos 2\theta}{2} \frac{\alpha^2}{\beta^2} \cdot x_3 \tag{14}$$

where $x_1 = M_I$, $x_2 = M_\# \cdot \cos 2\psi$, and $x_3 = M_\# \cdot \sin 2\psi$.

Similarly for the Love wave case, the amplitude is

$$A_{Lov} \propto M_\# \cos 2\phi = M_\# \cos 2(\theta - \psi),$$

or

$$A_{Lov} \propto M_\# [\cos 2\theta \cos 2\psi + \sin 2\theta sin 2\psi] \tag{15}$$

or in terms of a least-square problem in the form

$$A_{Lov} \propto \cos 2\theta \cdot x_1' + \sin 2\theta \cdot x_2' = \cos 2\theta \cdot x_2 + \sin 2\theta \cdot x_3. \tag{16}$$

The errors in this inversion can be calculated directly. For a function $x = f(u, v)$, the variance (σ_x^2) is defined as

$$\sigma_x^2 = \sigma_u^2 (\frac{\partial x}{\partial u})^2 + \sigma_v^2 (\frac{\partial x}{\partial v})^2 + 2\sigma_{uv}^2 (\frac{\partial x}{\partial u})(\frac{\partial x}{\partial v}). \tag{17}$$

For the case of u and v being uncorrelated $\sigma_{uv}^2 = 0$. σ_x is defined as:

$$\sigma_X = \sqrt{\frac{\sum (X_{obs}^i - X_{model}^i)^2}{N - m}}, \tag{18}$$

with N being the number of observations and m the number of parameters.

For the Rayleigh wave inversion (eq. (14)) case, the variance in the explosion estimate, x_1 is $\sigma_E^2 = \sigma_1^2$. For the tectonic release component ($TR = \sqrt{x_2^2 + x_3^2}$),

$$\sigma_{TR}^2 = \sigma_2^2 \cdot \frac{x_2^2}{(x_2^2 + x_3^2)} + \sigma_3^2 \cdot \frac{x_3^2}{(x_2^2 + x_3^2)}. \tag{19}$$

For the strike azimuth ($\psi = \frac{90^\circ}{\pi}\arctan(x_3/x_2)$),

$$\sigma_\psi^2 = \sigma_2^2 \cdot (\frac{90^\circ}{\pi})^2 \frac{x_2^2}{(x_2^2+x_3^2)} + \sigma_3^2 \cdot (\frac{90^\circ}{\pi})^2 \frac{x_3^2}{(x_2^2+x_3^2)}. \quad (20)$$

Since in the Love wave case $TR = \sqrt{x_2^2+x_3^2}$ as well, the variances σ_{TR}^2 and σ_ψ^2 are also given by eqs.(19) and (20), respectively.

Error Analysis of Assumptions

Since reducing the error in explosion moment estimates is critical to their worth, it is important to appreciate the margin of error introduced by assumptions in the analysis. One such question is how reasonable is the vertical strike-slip mechanism assumption for determining the tectonic release moment and what are the associated errors in the explosion moment estimate.

A theoretical source inversion study was conducted in order to get a handle on such errors. A hypothetical network with the same station azimuth make-up as that of the observed data set was used; however, all paths used the same structure and were of the same path length ($\Delta = 40^\circ$). An explosion of given moment ($10^{16} N-m$) is superimposed with a double-couple source of varying focal mechanism and F-factor.

Time-domain and spectral moments and isotropic moments and their standard deviations are calculated from the synthetic "data." The results are shown in Table 3. At the top of each box the rake (λ) and dip (δ) are given. A negative λ denotes a normal fault, a positive λ, a thrust fault. The left-most column gives the ratio of double-couple to isotropic moment. The first column gives the ratio of input tectonic release moment ($M_\#$) to explosion moment (M_I). For comparison, log-moments are converted to surface wave magnitudes by

λ=45° δ=90°						
M_s/M_*	M_S	s.d.	$\log M_0$	s.d.	$\log M_I$	s.d.
0.00	4.64	0.00	4.64	0.00	4.64	0.00
0.25	4.63	0.06	4.63	0.07	4.64	0.00
0.50	4.56	0.17	4.61	0.14	4.64	0.00
0.75	4.52	0.26	4.58	0.22	4.64	0.00
1.00	4.46	0.37	4.51	0.36	4.64	0.00
1.25	4.41	0.46	4.46	0.45	4.64	0.01
1.50	4.44	0.45	4.48	0.45	4.65	0.01
1.75	4.48	0.44	4.53	0.43	4.66	0.02
2.00	4.55	0.38	4.59	0.37	4.67	0.02

λ=45° δ=60°						
M_s/M_*	M_S	s.d.	$\log M_0$	s.d.	$\log M_I$	s.d.
0.00	4.64	0.00	4.64	0.00	4.64	0.00
0.25	4.56	0.08	4.56	0.08	4.57	0.00
0.50	4.41	0.24	4.45	0.21	4.50	0.00
0.75	4.06	0.70	4.13	0.65	4.42	0.00
1.00	4.31	0.33	4.34	0.33	4.32	0.02
1.25	4.36	0.38	4.39	0.36	4.20	0.04
1.50	4.42	0.38	4.45	0.37	4.06	0.07
1.75	4.49	0.36	4.52	0.34	3.78	0.17
2.00	4.54	0.36	4.58	0.33	5.03	0.05

λ=45° δ=75°						
M_s/M_*	M_S	s.d.	$\log M_0$	s.d.	$\log M_I$	s.d.
0.00	4.64	0.00	4.64	0.00	4.64	0.00
0.25	4.59	0.07	4.59	0.07	4.60	0.00
0.50	4.47	0.21	4.53	0.18	4.56	0.00
0.75	4.36	0.37	4.39	0.38	4.52	0.00
1.00	4.30	0.44	4.35	0.43	4.50	0.01
1.25	4.39	0.38	4.43	0.36	4.46	0.03
1.50	4.45	0.38	4.48	0.37	4.40	0.03
1.75	4.52	0.31	4.55	0.31	4.35	0.04
2.00	4.54	0.39	4.57	0.36	4.27	0.04

λ=45° δ=45°						
M_s/M_*	M_S	s.d.	$\log M_0$	s.d.	$\log M_I$	s.d.
0.00	4.64	0.00	4.64	0.00	4.64	0.00
0.25	4.55	0.07	4.56	0.07	4.56	0.00
0.50	4.42	0.20	4.43	0.20	4.47	0.00
0.75	4.08	0.60	4.13	0.57	4.38	0.00
1.00	4.24	0.36	4.29	0.33	4.27	0.04
1.25	4.31	0.37	4.35	0.36	4.03	0.03
1.50	4.41	0.31	4.45	0.30	3.68	0.12
1.75	4.47	0.33	4.51	0.31	4.92	0.04
2.00	4.54	0.30	4.57	0.28	4.95	0.06

Table 3: Source inversion results for theoretical study.

λ=−45° δ=90°						
M_s/M_*	M_S	s.d.	$\log M_0$	s.d.	$\log M_I$	s.d.
0.00	4.64	0.00	4.64	0.00	4.64	0.00
0.25	4.62	0.07	4.63	0.07	4.64	0.00
0.50	4.60	0.14	4.61	0.14	4.64	0.00
0.75	4.57	0.22	4.58	0.22	4.64	0.00
1.00	4.49	0.37	4.51	0.36	4.64	0.00
1.25	4.44	0.46	4.47	0.44	4.64	0.01
1.50	4.47	0.45	4.49	0.44	4.65	0.01
1.75	4.51	0.43	4.53	0.42	4.66	0.02
2.00	4.56	0.38	4.60	0.37	4.67	0.02

λ=−45° δ=75°						
M_s/M_*	M_S	s.d.	$\log M_0$	s.d.	$\log M_I$	s.d.
0.00	4.64	0.00	4.64	0.00	4.64	0.00
0.25	4.65	0.06	4.66	0.06	4.67	0.00
0.50	4.67	0.11	4.68	0.11	4.70	0.00
0.75	4.68	0.17	4.69	0.16	4.73	0.00
1.00	4.68	0.22	4.69	0.22	4.75	0.00
1.25	4.67	0.30	4.69	0.27	4.78	0.00
1.50	4.66	0.35	4.68	0.34	4.80	0.00
1.75	4.65	0.42	4.66	0.41	4.82	0.00
2.00	4.64	0.47	4.66	0.45	4.84	0.01

λ=−45° δ=60°						
M_s/M_*	M_S	s.d.	$\log M_0$	s.d.	$\log M_I$	s.d.
0.00	4.64	0.00	4.64	0.00	4.64	0.00
0.25	4.67	0.06	4.68	0.05	4.69	0.00
0.50	4.71	0.10	4.72	0.10	4.74	0.00
0.75	4.74	0.14	4.75	0.14	4.78	0.00
1.00	4.77	0.17	4.78	0.17	4.82	0.00
1.25	4.79	0.20	4.80	0.20	4.86	0.00
1.50	4.81	0.23	4.82	0.23	4.89	0.00
1.75	4.82	0.27	4.84	0.26	4.92	0.00
2.00	4.83	0.31	4.86	0.28	4.95	0.00

λ=−45° δ=45°						
M_s/M_*	M_S	s.d.	$\log M_0$	s.d.	$\log M_I$	s.d.
0.00	4.64	0.00	4.64	0.00	4.64	0.00
0.25	4.68	0.05	4.69	0.05	4.70	0.00
0.50	4.73	0.09	4.74	0.09	4.75	0.00
0.75	4.77	0.12	4.78	0.12	4.80	0.00
1.00	4.80	0.15	4.81	0.14	4.84	0.00
1.25	4.83	0.17	4.84	0.17	4.88	0.00
1.50	4.86	0.19	4.87	0.19	4.92	0.00
1.75	4.89	0.21	4.90	0.20	4.95	0.00
2.00	4.91	0.23	4.92	0.22	4.99	0.00

λ=−30° δ=90°						
M_s/M_*	M_S	s.d.	$\log M_0$	s.d.	$\log M_I$	s.d.
0.00	4.64	0.00	4.64	0.00	4.64	0.00
0.25	4.62	0.08	4.62	0.08	4.64	0.00
0.50	4.59	0.18	4.60	0.17	4.64	0.00
0.75	4.52	0.33	4.53	0.31	4.64	0.00
1.00	4.42	0.51	4.44	0.48	4.64	0.00
1.25	4.44	0.51	4.47	0.48	4.64	0.01
1.50	4.51	0.46	4.54	0.44	4.64	0.01
1.75	4.59	0.38	4.61	0.37	4.64	0.01
2.00	4.62	0.40	4.66	0.39	4.64	0.02

λ=−30° δ=75°						
M_s/M_*	M_S	s.d.	$\log M_0$	s.d.	$\log M_I$	s.d.
0.00	4.64	0.00	4.64	0.00	4.64	0.00
0.25	4.64	0.08	4.65	0.07	4.66	0.00
0.50	4.64	0.15	4.65	0.14	4.68	0.00
0.75	4.63	0.23	4.64	0.22	4.70	0.00
1.00	4.59	0.35	4.61	0.33	4.72	0.00
1.25	4.53	0.49	4.55	0.47	4.73	0.01
1.50	4.55	0.49	4.57	0.47	4.73	0.02
1.75	4.59	0.47	4.60	0.46	4.72	0.03
2.00	4.63	0.45	4.65	0.44	4.71	0.04

λ=−30° δ=60°						
M_s/M_*	M_S	s.d.	$\log M_0$	s.d.	$\log M_I$	s.d.
0.00	4.64	0.00	4.64	0.00	4.64	0.00
0.25	4.66	0.07	4.67	0.06	4.67	0.00
0.50	4.68	0.12	4.69	0.12	4.71	0.00
0.75	4.69	0.18	4.70	0.18	4.74	0.00
1.00	4.70	0.23	4.71	0.23	4.77	0.00
1.25	4.68	0.31	4.71	0.29	4.80	0.00
1.50	4.68	0.37	4.70	0.36	4.83	0.00
1.75	4.65	0.46	4.68	0.44	4.85	0.00
2.00	4.66	0.50	4.68	0.48	4.87	0.02

λ=−30° δ=45°						
M_s/M_*	M_S	s.d.	$\log M_0$	s.d.	$\log M_I$	s.d.
0.00	4.64	0.00	4.64	0.00	4.64	0.00
0.25	4.67	0.06	4.67	0.05	4.68	0.00
0.50	4.70	0.10	4.70	0.10	4.72	0.00
0.75	4.72	0.14	4.73	0.14	4.76	0.00
1.00	4.74	0.18	4.75	0.18	4.79	0.00
1.25	4.76	0.21	4.77	0.21	4.82	0.00
1.50	4.76	0.26	4.78	0.25	4.85	0.00
1.75	4.77	0.30	4.79	0.28	4.88	0.00
2.00	4.78	0.33	4.80	0.32	4.91	0.00

$\lambda=-15^o$ $\delta=90^o$						
M_s/M_*	M_S	s.d.	$\log M_0$	s.d.	$\log M_I$	s.d.
0.00	4.64	0.00	4.64	0.00	4.64	0.00
0.25	4.62	0.09	4.62	0.09	4.64	0.00
0.50	4.58	0.20	4.59	0.20	4.64	0.00
0.75	4.47	0.42	4.49	0.40	4.64	0.00
1.00	4.43	0.50	4.45	0.48	4.64	0.00
1.25	4.46	0.51	4.49	0.49	4.64	0.00
1.50	4.55	0.42	4.59	0.39	4.64	0.00
1.75	4.61	0.43	4.64	0.41	4.64	0.00
2.00	4.67	0.40	4.70	0.38	4.64	0.00

$\lambda=-15^o$ $\delta=75^o$						
M_s/M_*	M_S	s.d.	$\log M_0$	s.d.	$\log M_I$	s.d.
0.00	4.64	0.00	4.64	0.00	4.64	0.00
0.25	4.63	0.09	4.64	0.08	4.65	0.00
0.50	4.61	0.18	4.62	0.18	4.66	0.00
0.75	4.57	0.30	4.57	0.30	4.67	0.00
1.00	4.46	0.52	4.48	0.51	4.68	0.00
1.25	4.49	0.50	4.51	0.48	4.69	0.01
1.50	4.52	0.49	4.55	0.48	4.70	0.01
1.75	4.60	0.44	4.62	0.43	4.71	0.02
2.00	4.64	0.43	4.67	0.42	4.72	0.02

$\lambda=-15^o$ $\delta=60^o$						
M_s/M_*	M_S	s.d.	$\log M_0$	s.d.	$\log M_I$	s.d.
0.00	4.64	0.00	4.64	0.00	4.64	0.00
0.25	4.64	0.08	4.65	0.07	4.66	0.00
0.50	4.64	0.15	4.64	0.15	4.68	0.00
0.75	4.62	0.23	4.63	0.23	4.69	0.00
1.00	4.57	0.36	4.59	0.34	4.71	0.00
1.25	4.51	0.50	4.54	0.48	4.72	0.01
1.50	4.54	0.49	4.56	0.47	4.72	0.01
1.75	4.58	0.46	4.60	0.46	4.71	0.02
2.00	4.60	0.47	4.63	0.46	4.73	0.03

$\lambda=-15^o$ $\delta=45^o$						
M_s/M_*	M_S	s.d.	$\log M_0$	s.d.	$\log M_I$	s.d.
0.00	4.64	0.00	4.64	0.00	4.64	0.00
0.25	4.64	0.06	4.65	0.06	4.66	0.00
0.50	4.65	0.12	4.66	0.12	4.68	0.00
0.75	4.65	0.17	4.66	0.17	4.70	0.00
1.00	4.65	0.23	4.66	0.23	4.72	0.00
1.25	4.62	0.33	4.64	0.31	4.74	0.00
1.50	4.59	0.43	4.61	0.41	4.76	0.00
1.75	4.57	0.48	4.60	0.46	4.75	0.01
2.00	4.59	0.47	4.62	0.45	4.70	0.03

$\lambda=0^o$ $\delta=90^o$						
M_s/M_*	M_S	s.d.	$\log M_0$	s.d.	$\log M_I$	s.d.
0.00	4.64	0.00	4.64	0.00	4.64	0.00
0.25	4.62	0.09	4.62	0.09	4.64	0.00
0.50	4.58	0.21	4.58	0.21	4.64	0.00
0.75	4.47	0.44	4.47	0.44	4.64	0.00
1.00	4.45	0.49	4.45	0.49	4.64	0.00
1.25	4.53	0.45	4.49	0.52	4.64	0.00
1.50	4.60	0.39	4.60	0.39	4.64	0.00
1.75	4.63	0.48	4.63	0.47	4.64	0.00
2.00	4.71	0.37	4.71	0.37	4.64	0.00

$\lambda=0^o$ $\delta=75^o$						
M_s/M_*	M_S	s.d.	$\log M_0$	s.d.	$\log M_I$	s.d.
0.00	4.64	0.00	4.64	0.00	4.64	0.00
0.25	4.62	0.09	4.62	0.09	4.64	0.00
0.50	4.58	0.20	4.59	0.20	4.64	0.00
0.75	4.48	0.41	4.49	0.40	4.64	0.00
1.00	4.42	0.51	4.45	0.49	4.64	0.00
1.25	4.46	0.51	4.49	0.50	4.64	0.00
1.50	4.55	0.42	4.59	0.40	4.64	0.00
1.75	4.61	0.45	4.63	0.43	4.64	0.00
2.00	4.68	0.40	4.70	0.37	4.64	0.00

$\lambda=0^o$ $\delta=60^o$						
M_s/M_*	M_S	s.d.	$\log M_0$	s.d.	$\log M_I$	s.d.
0.00	4.64	0.00	4.64	0.00	4.64	0.00
0.25	4.62	0.08	4.62	0.08	4.64	0.00
0.50	4.59	0.17	4.60	0.17	4.64	0.00
0.75	4.52	0.31	4.53	0.31	4.64	0.00
1.00	4.41	0.52	4.43	0.50	4.64	0.00
1.25	4.43	0.52	4.46	0.50	4.64	0.00
1.50	4.50	0.47	4.53	0.45	4.64	0.00
1.75	4.57	0.41	4.61	0.38	4.64	0.01
2.00	4.61	0.42	4.65	0.40	4.64	0.01

$\lambda=0^o$ $\delta=45^o$						
M_s/M_*	M_S	s.d.	$\log M_0$	s.d.	$\log M_I$	s.d.
0.00	4.64	0.00	4.64	0.00	4.64	0.00
0.25	4.62	0.07	4.63	0.07	4.64	0.00
0.50	4.60	0.14	4.61	0.14	4.64	0.00
0.75	4.57	0.22	4.58	0.22	4.64	0.00
1.00	4.49	0.38	4.51	0.36	4.64	0.00
1.25	4.43	0.48	4.45	0.46	4.64	0.00
1.50	4.44	0.48	4.47	0.47	4.64	0.00
1.75	4.49	0.45	4.53	0.43	4.65	0.00
2.00	4.54	0.40	4.59	0.39	4.65	0.00

λ=15° δ=90°						
M_s/M_*	M_S	s.d.	$\log M_0$	s.d.	$\log M_I$	s.d.
0.00	4.64	0.00	4.64	0.00	4.64	0.00
0.25	4.62	0.09	4.62	0.09	4.64	0.00
0.50	4.57	0.22	4.59	0.20	4.64	0.00
0.75	4.46	0.43	4.49	0.40	4.64	0.00
1.00	4.42	0.51	4.45	0.48	4.64	0.00
1.25	4.46	0.52	4.48	0.50	4.64	0.00
1.50	4.57	0.41	4.59	0.40	4.64	0.00
1.75	4.62	0.42	4.64	0.41	4.64	0.00
2.00	4.67	0.39	4.70	0.39	4.64	0.00

λ=30° δ=90°						
M_s/M_*	M_S	s.d.	$\log M_0$	s.d.	$\log M_I$	s.d.
0.00	4.64	0.00	4.64	0.00	4.64	0.00
0.25	4.62	0.09	4.62	0.08	4.64	0.00
0.50	4.56	0.21	4.60	0.17	4.64	0.00
0.75	4.49	0.34	4.53	0.31	4.64	0.00
1.00	4.40	0.50	4.44	0.49	4.64	0.01
1.25	4.42	0.51	4.46	0.50	4.64	0.01
1.50	4.50	0.46	4.53	0.45	4.64	0.01
1.75	4.58	0.39	4.61	0.37	4.64	0.01
2.00	4.62	0.40	4.65	0.39	4.64	0.02

λ=15° δ=75°						
M_s/M_*	M_S	s.d.	$\log M_0$	s.d.	$\log M_I$	s.d.
0.00	4.64	0.00	4.64	0.00	4.64	0.00
0.25	4.60	0.09	4.61	0.09	4.62	0.00
0.50	4.55	0.21	4.56	0.21	4.61	0.00
0.75	4.37	0.53	4.40	0.50	4.60	0.00
1.00	4.38	0.53	4.40	0.51	4.58	0.00
1.25	4.47	0.45	4.50	0.44	4.57	0.00
1.50	4.56	0.36	4.59	0.35	4.56	0.00
1.75	4.62	0.36	4.65	0.35	4.54	0.00
2.00	4.66	0.35	4.70	0.34	4.53	0.00

λ=30° δ=75°						
M_s/M_*	M_S	s.d.	$\log M_0$	s.d.	$\log M_I$	s.d.
0.00	4.64	0.00	4.64	0.00	4.64	0.00
0.25	4.60	0.08	4.60	0.09	4.61	0.00
0.50	4.50	0.24	4.54	0.20	4.59	0.00
0.75	4.32	0.52	4.37	0.49	4.56	0.00
1.00	4.36	0.44	4.39	0.45	4.54	0.01
1.25	4.44	0.41	4.48	0.40	4.51	0.01
1.50	4.53	0.31	4.56	0.32	4.47	0.01
1.75	4.57	0.35	4.60	0.35	4.44	0.02
2.00	4.62	0.35	4.65	0.35	4.41	0.02

λ=15° δ=60°						
M_s/M_*	M_S	s.d.	$\log M_0$	s.d.	$\log M_I$	s.d.
0.00	4.64	0.00	4.64	0.00	4.64	0.00
0.25	4.60	0.08	4.60	0.08	4.61	0.00
0.50	4.54	0.20	4.54	0.20	4.59	0.00
0.75	4.38	0.48	4.40	0.45	4.57	0.00
1.00	4.34	0.52	4.38	0.49	4.54	0.01
1.25	4.42	0.47	4.46	0.44	4.52	0.00
1.50	4.52	0.32	4.56	0.32	4.50	0.01
1.75	4.57	0.34	4.61	0.33	4.47	0.02
2.00	4.59	0.41	4.64	0.39	4.45	0.02

λ=30° δ=60°						
M_s/M_*	M_S	s.d.	$\log M_0$	s.d.	$\log M_I$	s.d.
0.00	4.64	0.00	4.64	0.00	4.64	0.00
0.25	4.58	0.08	4.58	0.08	4.59	0.00
0.50	4.49	0.21	4.49	0.21	4.54	0.00
0.75	4.18	0.67	4.22	0.64	4.49	0.00
1.00	4.35	0.36	4.39	0.36	4.43	0.00
1.25	4.41	0.40	4.45	0.38	4.37	0.01
1.50	4.48	0.35	4.51	0.34	4.30	0.03
1.75	4.54	0.34	4.57	0.33	4.20	0.04
2.00	4.56	0.37	4.60	0.35	4.09	0.06

λ=15° δ=45°						
M_s/M_*	M_S	s.d.	$\log M_0$	s.d.	$\log M_I$	s.d.
0.00	4.64	0.00	4.64	0.00	4.64	0.00
0.25	4.59	0.07	4.60	0.07	4.61	0.00
0.50	4.54	0.16	4.55	0.16	4.58	0.00
0.75	4.44	0.33	4.46	0.31	4.56	0.00
1.00	4.30	0.52	4.33	0.50	4.54	0.01
1.25	4.40	0.40	4.42	0.39	4.53	0.02
1.50	4.45	0.34	4.50	0.32	4.48	0.01
1.75	4.48	0.34	4.55	0.32	4.47	0.02
2.00	4.53	0.34	4.59	0.33	4.42	0.04

λ=30° δ=45°						
M_s/M_*	M_S	s.d.	$\log M_0$	s.d.	$\log M_I$	s.d.
0.00	4.64	0.00	4.64	0.00	4.64	0.00
0.25	4.57	0.07	4.58	0.07	4.58	0.00
0.50	4.48	0.18	4.49	0.18	4.53	0.00
0.75	4.27	0.47	4.29	0.45	4.46	0.00
1.00	4.30	0.36	4.34	0.35	4.45	0.03
1.25	4.34	0.35	4.40	0.33	4.30	0.01
1.50	4.40	0.33	4.46	0.32	4.22	0.03
1.75	4.41	0.45	4.48	0.41	4.11	0.08
2.00	4.47	0.43	4.52	0.41	3.98	0.15

the relation

$$M_S = \log(M_0) - 11.36, \tag{21}$$

developed in Woods & Harkrider (1995) for the generic path, so that the correct M_S (or converted M_0) of the explosion alone should be 4.64 on this scale. Only Rayleigh wave synthetic data were used to determine the source information. Otherwise moments were determined using the same methods used on the data here and in Woods & Harkrider (1995). The M_s's in the second column were obtained by time domain measurements of the maximum peak to trough amplitude using the von Seggern (1977) formula for well dispersed Rayleigh waves as in Woods & Harkrider (1995).

$$M_S = \log(A/T) + 1.08 \times \log(\Delta) + 4.38, \tag{22}$$

Although the formula was chosen because the coefficient (1.08) more closely approximated the effect of attenuation along continental paths, it should be noted that Herak & Herak (1993) obtained a similar result for a set of 250 earthquakes mostly in the distance range of 20 to 150°. Their result

$$M_S = \log(A/T) + 1.094 \times \log(\Delta) + 4.429, \tag{23}$$

agrees with the standard Prague formula at 100°, where the data concentration was highest and reduces the significant distance dependence found in the 5514 Prague formula M_s readings that composed their data set.

The F factor results in Table 5 of the next section imply that for NTS, the $M_{\#}/M_I$ ratio is never above 0.6, so the maximum moment ratio of 2.0 was considered an extreme value for this area. The rake varied between -45 and 45 in 15 degree increments and the strike varied between 90 (vertical) and 45 degrees in 15 degree increments. These fault parameters are reasonable variations from the assumed vertical ($\delta = 0$), pure strike-slip (λ) mechanism for NTS tectonic release.

Unlike the observational results, there is a significant reduction in variance of the explosion moment estimate by inverting for the isotropic moment component over the average spectral moment estimate. For all but the most extreme deviations in source parameters and F factor, the estimated isotropic moments standard deviations are small, usually under 0.01 magnitude units. The actual data errors (Table 6) are somewhat bigger. This can be attributed to the fact that in the synthetic study case the seismograms have no noise contamination, hence there is no problem measuring the signal accurately. Also in the synthetic study case, far better azimuthal coverage was attainable, since only a small proportion of the network was available for any one event. In the theoretical case the synthetic seismograms are identical to the synthetic "data," so that there will be no error in the spectral ratio measurements, whereas in the observational case, errors in modeling the propagation path can lead to inaccuracies in moment estimates.

The average spectral scalar moment (M_0) standard deviations are significantly larger than those of the inverted moment estimates, being similar in size to errors in time-domain moment estimates. These errors are significant even for relatively low F-factor events ($M_\#/M_I < 0.75$), being, on average, 0.07 for $M_\#/M_I = 0.25$ events and 0.12 for $M_\#/M_I = 0.5$ events. For large F-factor events ($M_\#/M_I > 1$), the variances become exceedingly high, implying large scatter in the moment estimate.

The inverted isotropic moment is, in most all cases, closer in estimating the explosion moment than either average moment estimate. For all but the most extreme cases (say, $\lambda = -45^o$ and $\delta = 60^o$ and $M_\#/M_I > 0.75$), the difference between the estimated and actual isotropic moment is less than 0.1 magnitude units and is often less than 0.01 log units, whereas for the $M_{0(ptpk)}$ and $M_{0(\omega)}$, this difference is larger sometimes as great as 0.24 magnitude units. For a pure vertical strike-slip tectonic release mechanism, the average estimated moment or M_S determined from a network with complete azimuthal coverage should be that of the explosion, with the variations due to the tectonic release canceling itself out, on average (Helle & Rygg, 1984). However, the network used does not have equal coverage for each lobe of the $\sin 2\theta$ radiation pattern, so that the apparent moment or magnitude differs from the actual value for even the smaller F factor cases. For the case of $M_{\#}/M_I = 0.75$, this difference is 0.17 (48 percent). These canonical test results show that estimating the explosion moment by inverting for the isotropic component, in conjunction with a double-couple component, should yield the most accurate measurements.

The error in moment estimate due the difference between the modeled source depth (600 m) and actual source depth (between 300 and 750 m) is minimal (0.25 percent), unless the difference in depth should place the shot in a medium with a significantly different α^2/β^2 ratio. The error in using one generic centralized NTS location to calculate the distance for all station-path synthetic is also minimal, being at the most 0.5 percent for the extreme case of short regional paths ($d_o \approx 400$ km, $\delta d = 20$ km).

Another source of error in explosion moment determinations is caused by mis-modeling the near-source region, in particular the shot-point medium elastic properties, since, by eq. (3), the displacement generated by an explosion is inversely proportional to α^2/β^2 which, in turn, is related to Poisson's ratio (σ). Various studies have determined the P-wave velocity structure for the various NTS sub-regions; however, the S-wave velocity structure is far less well constrained. Depending on the shot depth and particular model, α^2/β^2 varies between

3.25 and 2.75 (3 for a Poisson solid), leading to potential systematic errors on the order of 8 percent (0.035 log units).

This effect is significant and could be corrected for in terms of sub-site coupling coefficients or calibration constants. In a global nuclear monitoring environment, this factor may only be ascertainable by indirect means (such as estimating α^2/β^2 from the ratio of $M_{DC(Ray)}/M_{DC(Lov)}$). This effect is investigated, as in Woods & Harkrider (1995), by examining the moment-m_b and moment-yield scaling relationships for various explosion populations and sub-populations at NTS. Unfortunately the spectral moment data set is significantly smaller and less comprehensive than the data set used in Woods & Harkrider (1995), since many of those moments/M_S's were determined from historical analog data. However, the available data set does contain events from Rainier Mesa as well as smaller events from the other sub-sites, down to $m_b = 4.9$, and in a few cases down to the $m_b = 4.4$ level, whereas previous (Stevens, 1986; Given & Mellman, 1986) studies have only examined $m_b = 5.5$ and larger events. Hence the moment scaling relationships can be better constrained for Pahute Mesa and Yucca Flats, and the Rainier Mesa long-period scaling relationships can be established using this data set. Including the large-yield explosions from the previous studies makes the data set even more comprehensive in scale range. By comparing the relationships obtained from these three NTS sub-sites, one can get a handle on the effect of near-source structure and shot medium effects on these scaling relationships.

Source structure significantly affects absolute surface wave amplitudes, hence surface wave magnitudes or moments. For all of the synthetic seismograms generated, we used the Stevens (1986) NTS source elastic structure, which was also used by Given and Mellman (1986) and is basically a Pahute Mesa velocity structure. Since there are known shot point source velocity structure variations at NTS, we estimated the error in log moment which would occur by assuming the common NTS source structure instead of the actual structure. Using the same approximations, synthetic Rayleigh waves were generated for various shot point structures reported for NTS. These were compared with synthetics using the Stevens (1986) NTS source region to obtain relative moment corrections. The NTS sub-site source structures and the log moment corrections are given in Table 4. The correction values are all positive. Thus, if the event actually occured in this structure, the log moment obtained using the Stevens's NTS source structure would be too small by the amount given in the tables. On the average, the corrections for Yucca are about 0.10 units greater than Pahute. This implies that the log explosion moment obtained for these Yucca structures using the NTS source region is 0.10 units less than the Pahute structures. This does not explain the entire difference observed by Given and Mellman but it is in the right direction. It is interesting to note that South Yucca model yields moment values closer to those of the Pahute models than the North Yucca model.

In order to reduce the effect of differing shot point velocity ratios, Stevens (1986) suggested a new explosion moment, M_0', defined by

$$M_0' = 3\frac{\beta^2}{\alpha^2}M_0 \tag{24}$$

For a shot point medium with Poisson's ratio of 0.25 (α^2/β^2=3), the value of the moment is unchanged. If we had used the same value of M_0' for each source model instead of M_0 , we would have obtained log moment corrections that are the difference in value between the two entries for each source structure. The variation of this value over the test site is small and is a measure of the effect of the vertical velocity structure and not the shot point medium. At long periods the difference in spectra from the standard NTS structure is given by this ratio

NTS (Stevens)			
Th km	α km/s	β km/s	ρ gm/cm^3
0.5	2.00	1.00	1.70
1.0	3.30	2.00	2.10
1.5	4.50	2.70	2.40
1.0	5.90	3.40	2.75
8.0	5.96	3.52	2.78
9.0	6.11	3.61	2.80
10.0	6.37	3.76	2.84
14.0	7.90	4.42	3.20
20.0	8.05	4.50	3.30
15.0	8.10	4.50	3.30
40.0	8.00	4.40	3.30
30.0	7.90	4.30	3.25
30.0	7.90	4.30	3.25
40.0	8.00	4.40	3.30
∞	8.50	4.70	3.50

Pahute Rhyolite			
Th km	α km/s	β km/s	ρ gm/cm^3
0.36	2.30	1.35	1.90
0.20	2.80	1.50	2.00
0.10	3.30	1.50	2.25
0.50	4.00	1.90	2.30
1.00	4.45	1.97	2.37
0.75	4.60	2.00	2.40
0.80	5.30	2.50	2.50
2.25	5.50	2.95	2.70
6.04	6.00	3.50	2.75
9.00	6.11	3.61	2.80

Pahute Tuff			
Th km	α km/s	β km/s	ρ gm/cm^3
0.36	2.30	1.35	1.90
0.40	2.80	1.50	2.00
0.70	3.30	1.50	2.25
0.70	4.00	1.90	2.30
0.75	4.60	2.00	2.40
0.80	5.30	2.50	2.50
2.25	5.50	2.95	2.70
6.04	6.00	3.50	2.75
9.00	6.11	3.61	2.80

Pahute (Leonard-Johnson)			
Th km	α km/s	β km/s	ρ gm/cm^3
0.05	1.50	0.99	1.90
0.10	1.90	1.25	1.90
0.10	2.30	1.48	1.90
0.10	2.50	1.57	1.90
0.10	2.70	1.66	2.00
0.10	2.91	1.74	2.00
0.10	3.11	1.82	2.25
0.50	3.64	2.01	2.30
0.30	3.90	2.12	2.37
0.30	4.10	2.20	2.37
0.25	4.29	2.27	2.37
0.16	4.37	2.29	2.37
0.75	4.60	2.35	2.40
0.80	5.30	2.50	2.50
2.25	5.50	2.95	2.70
6.04	6.00	3.50	2.75
9.00	6.11	3.61	2.80

Yucca North			
Th km	α km/s	β km/s	ρ gm/cm^3
0.20	1.65	0.90	1.60
0.20	2.14	1.14	1.80
1.10	3.70	2.00	2.30
0.50	4.60	2.50	2.70
2.00	5.90	3.40	2.75

Yucca South			
Th km	α km/s	β km/s	ρ gm/cm^3
0.40	1.34	0.64	1.50
0.25	2.14	1.14	1.80
0.45	3.00	1.60	2.05
0.90	4.57	2.64	2.50
2.00	5.90	3.40	2.75

Yucca (Ferguson)			
Th km	α km/s	β km/s	ρ gm/cm^3
0.25	1.34	0.64	1.00
0.25	2.14	1.14	1.80
0.30	3.00	1.60	1.80
1.20	4.57	2.64	2.50
2.00	5.90	3.40	2.75
8.00	5.96	3.52	2.78

Yucca (Bache)			
Th km	α km/s	β km/s	ρ gm/cm^3
0.40	1.65	0.90	1.60
0.60	2.35	1.30	1.86
0.50	4.80	2.60	2.65
0.50	4.80	2.60	2.65
2.00	5.90	3.40	2.75

Yucca (Geotech)			
Th km	α km/s	β km/s	ρ gm/cm^3
0.25	1.34	0.603	1.00
0.25	2.14	0.963	1.80
0.30	3.00	1.50	1.80
1.20	4.57	2.285	2.50
2.00	5.90	3.48	2.75
8.00	5.96	3.52	2.78

Log Moment Corrections For Various NTS Sub-Area Models					
Yucca	$\Delta \log M_o$	$2 \log \left(\frac{\beta_o}{\alpha_o} \frac{\alpha}{\beta} \right)$	Pahute	$\Delta \log M_o$	$2 \log \left(\frac{\beta_o}{\alpha_o} \frac{\alpha}{\beta} \right)$
South	+0.08	+0.11	Tuff	+0.03	+0.10
North	+0.14	+0.10	Leonard-Johnson	+0.06	+0.08
Bache	+0.07	+0.08	Rhyolite (0.5)	+0.06	+0.11
Ferguson	+0.15	+0.11	Rhyolite (0.6)	+0.20	+0.25
Geotech	+0.19	+0.17	Rhyolite (0.7)	+0.18	+0.21

Table 4: Various NTS sub-area models and their log moment corrections

and if we had used the frequency range of Given and Mellman (1986) instead of Stevens, who uses more high frequency values to average the spectra, we would have obtained an even smaller effect using M_0'. The use of M_0' for these source structure models effectivly removes the effects of differing local shot point properties. None of this however addresses coupling or how yield is related to M_0 through the shot point material properties.

Thus, by numerical simulations using a variety of different NTS structures, we found that for the frequencies of interest and sources in the upper 6 kilometers, the primary effect was due to the difference in shot point velocity ratios. The size of the effect can be predicted extremely well from their explicit presence in the mixed-path expression, eq. (3). As an example, our Green's functions are computed for an explosive source at a depth of 600 meters. In the NTS (Stevens) source structure, the second layer starts at a depth of 500 meters. There is a significant difference between the Poisson's ratio of the surface and second layer in the source earth structure. The log difference between the square of their compressional to shear velocities would predict from eq. (3) M_S difference of 0.17. The actual difference between the Ms of a surface explosion and our Green's function is 0.16 with the near surface explosion smaller as predicted.

RESULTS

Several variations of spectral source inversions were conducted. First a weighted average spectral moment was calculated assuming only a scalar moment from an explosive source. No station corrections were included in these calculations. Variance reciprocals were used as the weighting coefficients. These source parameters are given in Table 5; for each event the upper entry is the source parameter and the lower one is its standard deviation. Moment values are in units of 10^{15} Newton-meters $(N-m)$ and the strike angle is in degrees. In the second column the upper entry is the number of Rayleigh observations and the lower entry is the number of Love wave observations used.

Next, the isotropic (M_I) and double-couple ($M_{\#}$) moment components and strike angle (ϕ) were then determined using the least-squares inversion method described in the previous section. Separate inversions were performed for the Rayleigh waves ($M_{*(R)}$, $M_{DC(R)}$, and $\phi_{(R)}$), Love waves $M_{DC(L)}$ and $\phi_{(L)}$), and the combined data ($M_{*(R+L)}$, $M_{DC(R+L)}$, and $\phi_{(R+L)}$). The values and standard deviations are also listed in Table 5. Again variance reciprocals were used as the weighting coefficients in the inversion. In the last column is the F factor, defined by Toksöz *et al.* (1965) as:

$$F = \frac{M_{\#}}{M_I}\frac{\alpha^2}{2\beta^2} \approx \frac{3}{2}\frac{M_{\#}}{M_I} \tag{25}$$

for near-Poisson solids ($\alpha^2/\beta^2 \approx 3$).

The different inversion schemes, with a few exceptions, all yield similar explosion moment estimates for a given event. Also, most strike angles for the double-couple source are in the Northwest quadrant ($280°$ E $< \phi < 5°$ E). The $15° - 20°$ NW strike angle inferred/observed by other studies of NTS tectonic release lies within the 2σ confidence levels for most events, implying that the results obtained here are consistent with others' observations. In general, for a given event, $\phi_{(R)}$ and $\phi_{(L)}$ correlate reasonably well and $M_{DC(R)}$ and $M_{DC(L)}$ are within a factor of two of each other. Notable exceptions to these observations are PILEDRIVER (66153), HURONLANDING-DIAMONDACE (82267) and MIZZEN (75154). PILEDRIVER is the only event in this data set detonated at Climax Stock, a granite pluton and is believed to have generated tectonic release with a thrust-like mechanism (Stevens, 1986), so the inversion scheme employed here would not accurately model it. HURONLANDING-DIAMONDACE was a double event, which is a possible explanation for its anomalous radi-

Table 5 (a): Inverted Explosion and Tectonic Release Source Parameters											
Event	# obs.	M_0	$M_{I(R)}$	$M_{dc(R)}$	$\phi_{(R)}$	$M_{dc(L)}$	$\phi_{(L)}$	$M_{I(R+L)}$	$M_{dc(R+L)}$	$\phi_{(R+L)}$	$F_{(R+L)}$
65062	13	1.762	2.220	0.804	335.3	1.395	340.9	2.261	0.900	342.4	0.597
	4	0.345	0.223	0.263	9.6	0.207	4.4	0.208	0.145	4.6	0.111
66018	4	1.740	1.650	0.693	307.2			1.661	0.629	307.9	0.568
	1	0.438	0.323	0.315	15.6			0.237	0.190	12.1	0.189
66055	7	0.965	1.725	1.	342.7	2.696	353.9	1.760	1.155	344.7	0.984
	2	0.382	0.175	0.206	4.9	0.178	2.4	0.211	0.255	4.9	0.247
66133	16	5.952	5.672	0.702	334.1	1.544	329.8	5.493	1.021	331.3	0.279
	7	0.363	0.416	0.359	14.9	0.323	5.6	0.369	0.252	7.0	0.071
66153	26	4.242	4.846	1.269	51.5	6.032	326.0	3.811	1.023	330.8	0.403
	13	0.416	0.407	0.395	7.5	1.507	6.3	0.949	0.769	19.8	0.319
66154	19	5.544	5.368	0.384	325.2	0.826	330.7	5.243	0.656	329.1	0.188
	8	0.331	0.378	0.335	26.4	0.482	19.1	0.390	0.252	12.2	0.073
67177	3	0.697	0.628	0.054	320.2	0.388	346.8	0.248	0.378	345.4	2.288
	2	0.018	0.018			0.016	0.6	0.064	0.	2.5	0.638
67243	1	0.195									
	0										
67312	8	1.110	0.954	0.206	295.4			0.871	0.315	296.4	0.543
	1	0.101	0.234	0.206	27.8			0.193	0.163	14.6	0.306
68060	5	0.647	0.721	0.261	344.0						0.543
	0	0.165	0.101	0.087	11.3						0.196
68268	7	0.694	0.639	0.233	335.6						0.546
	0	0.133	0.127	0.115	13.7						0.290
69015	8	2.578	2.942	0.654	5.2	2.012	358.8	2.871	1.237	357.4	0.646
	2	0.245	0.711	0.250	25.5	0.710	3.3	0.886	0.300	16.3	0.253
69043	1	0.451									
	0										
69120	15	3.131	3.007	0.173	332.0			2.944	0.262	333.6	0.134
	1	0.203	0.299	0.251	45.0			0.265	0.214	25.3	0.110
70042	1	0.582									
	0										
70082	14	5.360	5.713	1.289	297.3			5.605	1.357	301.6	0.363
	1	0.572	0.597	0.588	13.5			0.540	0.472	11.2	0.131

Table 5: Source parameters for explosions and associated tectonic release.

Table 5 (b): Inverted Explosion and Tectonic Release Source Parameters											
Event	# obs.	M_0	$M_{I(R)}$	$M_{dc(R)}$	$\phi_{(R)}$	$M_{dc(L)}$	$\phi_{(L)}$	$M_{I(R+L)}$	$M_{dc(R+L)}$	$\phi_{(R+L)}$	$F_{(R+L)}$
70125	3 2	0.856 0.122	70.761 0.122	63.643	79.7	0.431 0.109	346.2 3.8	0.386 0.235	0.431 0.168	350.5 8.0	1.675 1.209
70146	2 0	0.354 0.041									
71180	7 0	0.291 0.048	0.362 0.028	0.103 0.022	354.5 8.0						0.427 0.096
71189	15 3	3.561 0.212	3.896 0.299	0.567 0.315	58.4 14.6	1.007 0.216	1.1 7.3	3.433 0.286	0.400 0.209	346.2 16.3	0.175 0.092
71230	18 5	1.426 0.068	1.370 0.079	0.109 0.072	339.0 18.5	0.582 0.071	356.3 3.3	1.276 0.	0.286 0.075	347.7 6.5	0.336 0.091
72123	5 1	0.444 0.127	0.712 0.101	0.265 0.078	354.0 10.9			0.655 0.114	0.255 0.093	343.6 11.3	0.584 0.237
72140	3 1	0.573 0.043	0.607 0.043	0.184	313.1			0.576 0.081	0.049 0.075	29.6 36.8	0.127 0.197
72202	5 0	0.477 0.095	0.475 0.049	0.138 0.046	347.9 11.8						0.436 0.150
73067	10 1	3.228 0.199	3.353 0.428	0.270 0.273	81.5 37.6			2.785 0.365	0.455 0.280	321.2 14.0	0.245 0.154
73116	20 1	2.851 0.279	2.865 0.296	0.124 0.304	351.6 60.2			2.886 0.299	0.287 0.269	339.3 25.9	0.149 0.141
73156	6 0	0.634 0.071	0.574 0.	0.140 0.022	357.9 6.2						0.367 0.061
74058	15 8	6. 0.474	5.533 0.385	1.390 0.342	328.9 8.1	2.078 0.209	345.2 2.7	5.333 0.341	1.761 0.239	336.5 3.9	0.495 0.074
74170	7 1	0.690 0.123	0.761 0.083	0.228 0.091	344.2 10.2			0.830 0.079	0.314 0.067	356.1 5.7	0.568 0.134
74191	21 6	10.389 0.806	10.422 0.724	1.692 0.652	315.0 12.3	3.168 0.359	347.5 3.0	10.427 0.681	1.935 0.543	323.8 8.8	0.278 0.080
74269	12 1	2.265 0.136	2.194 0.157	0.150 0.144	315.7 28.0			2.169 0.164	0.236 0.143	325.4 17.5	0.163 0.100
75066	15 0	2.692 0.156	2.470 0.192	0.300 0.161	298.2 16.0						0.182 0.099

Table 5 (c): Inverted Explosion and Tectonic Release Source Parameters

Event	# obs.	M_0	$M_{I(R)}$	$M_{dc(R)}$	$\phi_{(R)}$	$M_{dc(L)}$	$\phi_{(L)}$	$M_{I(R+L)}$	$M_{dc(R+L)}$	$\phi_{(R+L)}$	$F_{(R+L)}$
75095	1	0.649									
	0										
75120	12	1.492	1.486	0.236	325.1						0.238
	0	0.122	0.107	0.098	14.9						0.101
75154	20	8.947	8.503	1.682	284.4	11.806	20.5	8.613	1.299	290.6	0.226
	3	0.737	0.714	0.748	10.8	4.249	10.2	0.787	0.679	14.5	0.120
75297	1	0.289									
	0										
76035	13	7.244	7.740	1.076	282.6	1.682	351.7	7.254	1.534	319.4	0.317
	4	0.665	0.701	0.902	23.6	1.967	29.8	0.680	0.393	8.0	0.086
76133	1	0.853									
	0										
76363	7	4.736	4.411	1.211	282.9						0.412
	0	0.403	0.364	0.524	8.4						0.181
77117	16	3.297	3.926	0.896	274.7			3.154	0.395	323.1	0.188
	1	0.248	0.329	0.337	6.5			0.359	0.267	21.5	0.129
77145	8	4.051	4.664	0.901	80.9						0.290
	0	0.366	0.466	0.368	12.5						0.122
78193	21	4.728	5.275	1.288	297.5	0.462	342.7	5.186	1.025	302.0	0.296
	4	0.408	0.318	0.286	6.7	1.140	69.9	0.394	0.294	8.8	0.088
78322	12	1.889	1.923	0.301	288.3						0.234
	0	0.188	0.240	0.219	19.0						0.173
79039	18	2.611	4.389	1.886	332.4						0.644
	0	0.594	0.709	0.601	11.1						0.230
80107	17	3.118	3.201	0.982	84.7	0.777	319.3	3.103	0.514	282.9	0.249
	3	0.419	0.378	0.446	9.5	0.122	5.7	0.437	0.338	15.8	0.167
80305	5	0.526	0.611	0.374	329.3			0.812	0.354	352.1	0.654
	1	0.193	0.188	0.194	12.1			0.132	0.089	10.7	0.196
81015	10	7.871	7.504	0.760	337.1			7.414	0.916	339.1	0.185
	1	0.626	0.834	0.763	29.1			0.676	0.512	15.6	0.105
82028	8	11.200	11.512	0.895	335.8	1.939	344.9	11.436	1.548	349.5	0.203
	4	0.520	0.402	0.509	17.4	0.292	5.3	0.389	0.324	5.4	0.043

Table 5 (d): Inverted Explosion and Tectonic Release Source Parameters											
Event	# obs.	M_0	$M_{I(R)}$	$M_{dc(R)}$	$\phi_{(R)}$	$M_{dc(L)}$	$\phi_{(L)}$	$M_{I(R+L)}$	$M_{dc(R+L)}$	$\phi_{(R+L)}$	$F_{(R+L)}$
82043	4	10.253	10.199	1.714	299.9	3.326	335.2	8.253	3.236	335.2	0.588
	4	1.379	1.748	1.401	30.7	0.160	1.3	0.960	0.319	2.6	0.090
82044	7	7.402	6.958	1.493	355.2	1.870	345.6	7.046	1.612	349.6	0.343
	7	0.652	0.590	0.704	8.7	0.094	1.9	0.366	0.151	3.4	0.037
82107	4	0.210	0.197	0.086	351.0	0.250	47.2	0.210	0.045	342.0	0.325
	3	0.054	0.031	0.033	9.3	0.081	2.3	0.056	0.032	24.1	0.248
82115	7	6.638	6.633	0.302	306.2	1.925	337.0	6.594	1.213	348.3	0.276
	5	0.362	0.398	0.384	76.7	0.151	2.2	0.469	0.186	6.1	0.047
82126	4	0.109	0.111	0.009	287.2						0.120
	0	0.007	0.012	0.022	52.6						0.296
82127	8	4.896	4.969	0.648	345.2	1.351	339.1	5.	1.023	345.3	0.306
	8	0.353	0.314	0.429	14.0	0.107	2.4	0.267	0.127	4.1	0.041
82175	8	9.711	9.151	1.956	13.0	1.592	3.9	9.	1.666	9.4	0.275
	8	0.711	0.515	0.460	5.6	0.112	7.6	0.433	0.120	4.5	0.024
82210	8	0.280	0.274	0.096	322.4	0.188	334.1	0.261	0.132	337.6	0.755
	3	0.057	0.029	0.033	20.8	0.008	1.1	0.031	0.014	3.1	0.121
82217	8	12.794	12.692	0.666	340.8	2.152	341.5	12.559	1.571	348.0	0.188
	5	0.547	0.561	0.717	27.1	0.077	1.1	0.529	0.343	5.9	0.042
82266	5	0.590	0.632	0.061	86.2	0.227	339.0	0.387	0.172	339.7	0.666
	3	0.	0.255	0.189	84.0	0.008	1.0	0.133	0.079	13.4	0.382
82267	4	0.969	0.951	0.202	15.0	0.510	353.6	0.737	0.436	359.4	0.886
	4	0.131	0.223	0.198	23.7	0.	0.9	0.144	0.063	5.7	0.215
82272	4	0.096	0.092	0.013	15.1						0.214
	0	0.005			0.3						0.003
82344	7	0.352	0.317	0.047	356.1	0.092	2.1	0.282	0.089	4.4	0.474
	5	0.024	0.031	0.028	15.1	0.016	16.8	0.028	0.	7.1	0.072
83085	11	3.452	3.293	0.790	2.3	0.944	34	3.068	0.789	345.2	0.386
	10	0.284	0.139	0.109	4.8	0.078	2.5	0.171	0.081	3.5	0.045
83104	10	3.564	3.631	0.596	352.1	0.697	333.4	3.583	0.608	344.1	0.255
	7	0.312	0.311	0.372	12.1	0.	2.9	0.235	0.167	7.2	0.072
83125	6	0.121	0.189	0.084	287.0						0.662
	0	0.025	0.027	0.022	7.4						0.199

Table 5 (e): Inverted Explosion and Tectonic Release Source Parameters

Event	# obs.	M_0	$M_{I(R)}$	$M_{dc(R)}$	$\phi_{(R)}$	$M_{dc(L)}$	$\phi_{(L)}$	$M_{I(R+L)}$	$M_{dc(R+L)}$	$\phi_{(R+L)}$	$F_{(R+L)}$
83146	7	0.545	0.528	0.081	331.9			0.525	0.084	335.7	0.240
	1	0.066	0.	0.076	32.1			0.062	0.068	24.6	0.197
83160	6	0.296	0.301	0.087	341.8	0.084	7.5	0.301	0.103	348.9	0.512
	4	0.047	0.017	0.019	5.7	0.048	41.8	0.028	0.012	5.5	0.078
83244	13	3.855	4.301	1.671	338.0	1.533	334.8	4.272	1.547	335.4	0.543
	13	0.514	0.204	0.191	3.3	0.094	1.6	0.176	0.086	1.5	0.038
83264	2	0.162									
	0	0.003									
83265	4	0.078	0.	0.031	284.0			0.087	0.015	287.9	0.259
	1	0.004	0.018	0.028	18.1			0.018	0.023	37.7	0.409
83350	10	1.983	1.887	0.233	335.2	0.278	352.2	1.863	0.281	345.9	0.227
	5	0.144	0.134	0.132	16.7	0.112	28.0	0.111	0.071	8.6	0.058
84046	7	0.594	0.631	0.307	331.3			0.631	0.307	331.2	0.731
	1	0.137	0.036	0.035	2.9			0.032	0.	2.5	0.081
84061	10	8.401	8.009	1.893	346.5	2.656	338.4	7.975	2.179	344.8	0.410
	7	0.722	0.335	0.353	4.5	0.219	2.4	0.312	0.229	3.0	0.046
84122	10	7.374	6.373	1.282	336.5	1.318	333.5	6.374	1.315	334.5	0.309
	9	0.510	0.582	0.507	11.1	0.114	2.5	0.333	0.190	4.1	0.048
84152	10	8.081	8.132	0.935	352.6	1.147	330.3	8.084	0.920	336.5	0.171
	7	0.476	0.467	0.750	12.2	0.144	3.7	0.404	0.228	7.2	0.043
84172	4	0.660	0.507	0.217	337.5			0.507	0.217	337.5	0.642
	1	0.134	0.058	0.051	6.8			0.039	0.035	4.6	0.114
84207	9	3.637	4.839	2.736	354.5	3.344	351.0	4.927	2.952	354.2	0.899
	9	0.838	0.234	0.245	1.8	0.186	2.1	0.201	0.150	1.4	0.059
84215	5	0.210	0.206	0.043	349.2	0.104	342.6	0.203	0.	354.5	0.445
	3	0.022	0.013	0.018	8.1	0.129	45.7	0.022	0.018	7.7	0.143
84243	3	0.359	0.389	0.104	291.2			0.388	0.099	291.5	0.384
	1	0.055	0.055					0.003	0.004	1.0	0.014
84257	4	1.179	1.190	0.223	356.3	0.395	348.9	1.207	0.328	358.3	0.407
	4	0.055	0.048	0.199	5.7	0.031	3.9	0.028	0.026	1.6	0.034
84315	4	0.125	0.140	0.029	306.1	0.478	316.6	0.157	0.066	295.5	0.626
	2	0.017	0.012	0.	13.1	0.013	0.7	0.048	0.035	14.4	0.384

Table 5 (f): Inverted Explosion and Tectonic Release Source Parameters											
Event	# obs.	M_0	$M_{I(R)}$	$M_{dc(R)}$	$\Phi_{(R)}$	$M_{dc(L)}$	$\Phi_{(L)}$	$M_{I(R+L)}$	$M_{dc(R+L)}$	$\Phi_{(R+L)}$	$F_{(R+L)}$
84344	13	4.334	4.332	1.225	346.1	1.528	336.3	4.338	1.258	342.6	0.435
	11	0.371	0.178	0.199	3.8	0.102	1.9	0.157	0.111	2.5	0.041
84350	13	5.255	5.123	1.680	6.6	1.691	351.3	4.897	1.603	358.9	0.491
	10	0.524	0.323	0.298	4.8	0.233	4.6	0.325	0.195	3.8	0.068
85074	5	0.837	0.795	0.173	353.1						0.326
	0	0.106	0.437	0.206	68.1						0.427
85082	3	4.251	-1.623	5.157	318.3	3.008	350.6	3.012	2.487	344.3	1.239
	3	1.233	1.233			0.524	4.3	0.861	0.509	6.1	0.435
85092	11	12.581	13.191	1.409	345.8	1.758	324.6	13.327	1.653	341.8	0.186
	5	1.	1.219	1.562	22.3	0.246	6.0	0.912	0.871	12.8	0.099
85096	3	1.125						0.598	0.440	345.2	1.106
	1	0.208						0.901	0.418	32.6	1.970
85122	13	6.448	5.892	2.473	351.3	2.438	346.6	5.734	2.407	348.6	0.630
	13	0.685	0.512	0.540	4.8	0.163	2.1	0.342	0.211	2.4	0.067
85163	14	8.196	8.239	1.330	356.4	1.777	340.5	8.450	1.262	346.3	0.224
	13	0.502	0.429	0.414	8.0	0.106	1.9	0.318	0.155	4.4	0.029
85206	13	3.139	4.300	2.184	43.0	0.745	353.0	3.426	0.847	24.4	0.371
	11	0.690	0.515	0.495	5.5	0.168	6.8	0.556	0.342	11.4	0.161
85270	3	0.514	-1.462	2.375	356.8						*****
	0	0.095	0.095								0.159
85289	2	0.553									
	1	0.073									
85339	7	5.167	5.140	2.560	353.6	1.976	336.5	5.012	2.076	350.7	0.621
	4	1.178	0.962	0.881	9.1	0.736	10.4	0.777	0.486	7.8	0.174
85362	9	4.671	4.301	1.573	348.1	0.895	357.3	4.477	0.997	351.3	0.334
	3	0.606	0.506	0.527	8.3	0.199	10.6	0.455	0.224	8.0	0.082
86081	5	3.197	2.908	0.500	310.7	1.071	342.7	2.216	1.032	340.8	0.698
	3	0.337	0.652	0.311	39.8	0.254	7.6	0.337	0.187	5.2	0.165
86100	7	0.651	0.600	0.162	338.0	0.276	340.6	0.592	0.199	341.5	0.504
	2	0.099	0.	0.084	14.9	0.	9.3	0.078	0.059	8.5	0.162
86112	13	4.784	6.023	2.531	341.1	2.404	334.6	5.957	2.297	337.7	0.578
	10	0.698	0.377	0.344	3.8	0.186	1.9	0.294	0.177	2.2	0.053

Table 5 (g): Inverted Explosion and Tectonic Release Source Parameters											
Event	# obs.	M_0	$M_{I(R)}$	$M_{dc(R)}$	$\phi_{(R)}$	$M_{dc(L)}$	$\phi_{(L)}$	$M_{I(R+L)}$	$M_{dc(R+L)}$	$\phi_{(R+L)}$	$F_{(R+L)}$
86141	1 0	0.115									
86156	8 4	4.633 0.847	4.611 0.805	1.436 0.803	353.1 14.3	0.536 0.146	347.0 11.6	4.622 0.662	0.676 0.308	353.0 19.0	0.219 0.105
86176	9 8	4.002 0.510	5.229 0.510	1.584 0.417	347.2 8.3	1.191 0.124	343.0 3.3	4.875 0.307	1.233 0.138	344.5 3.6	0.379 0.049
86198	11 7	6.852 0.799	6.704 0.534	2.003 0.521	336.2 7.3	1.589 0.202	320.9 4.2	6.704 0.489	1.625 0.263	329.0 4.7	0.363 0.064
86205	1 0	0.264									
86273	9 9	7.362 1.	6.697 0.286	2.175 0.199	0.2 6.0	2.092 0.226	358.5 3.5	6.689 0.321	2.122 0.144	358.6 2.6	0.476 0.040
86289	7 7	6.947 0.712	7.683 0.312	2.018 0.299	340.8 4.4	1.766 0.103	338.5 1.7	7.554 0.242	1.786 0.100	339.1 1.7	0.355 0.023
86318	6 3	8.049 0.668	9.990 1.439	2.595 1.269	296.1 13.7	1.009 1.635	340.6 45.0	9.950 1.076	2.582 0.914	298.0 10.1	0.389 0.144
86347	8 8	9.412 1.039	8.703 2.089	1.747 1.783	1.3 23.0	2.780 0.268	347.2 3.8	7.687 1.	2.391 0.409	351.2 6.9	0.467 0.102
87108	5 5	7.904 0.688	6.126 0.579	1.797 0.455	336.5 7.4	3.019 0.151	340.7 1.5	5.201 0.404	2.826 0.251	340.8 2.6	0.815 0.096
87120	8 6	11.109 0.962	8.724 0.629	3.177 0.436	5.9 3.7	4.186 0.589	4.8 6.3	7.957 0.703	3.958 0.368	4.2 3.5	0.746 0.096
87181	2 0	0.148 0.009									
87225	4 3	10.809 1.051	11.835 0.159	1.797 0.176	278.4 2.2	4.340 0.470	311.7 3.1	10.454 1.262	2.782 0.704	325.6 7.4	0.399 0.112
87267	4 4	10.772 0.495	10.134 0.247	1.361 0.229	3.6 3.2	3.769 0.071	0.6 0.7	8.644 0.640	3.294 0.391	357.8 3.5	0.572 0.080
87296	4 0	1.650 0.119	1.996 0.031	0.474 0.033	78.9 1.1						0.356 0.025

ation pattern. It is also very close in location to the PILEDRIVER shot, so that the tectonic release faulting mechanisms may be similar. The Rayleigh and Love wave double-couple moments vary by a factor of seven and the strikes are off by 90 degrees for this Rainier Mesa event. However, the Love wave source solution is poorly constrained having only a minimum number of observations. It may be that the tectonic release mechanism for this event may vary significantly from the assumed vertical strike-slip one. MIZZEN belongs to subgroup of Yucca shots north of latitude 37.09 N, many of which yield double-couple mechanisms with strikes near $N80^oE$. Given & Mellman (1986) found an offset in the M_0 vs. m_b curves between northern and southern Yucca Flat, which was interpreted as a difference in Poisson ratios between shot sites or as having different stress regimes which would give rise to differing tectonic release mechanisms.

In most cases, the double-couple moment determined from Love wave observations is within a factor of two of the moment determined from Rayleigh waves alone. The relative errors of the double-couple moment estimates are appreciably larger than those of the isotropic moment estimates, so the 2σ confidence levels of the two independent double-couple moment estimates overlap and are thus compatable. The joint inversion results in significantly better constrained $M_{\#}$ estimates.

Many of the Rainier Mesa shots were relatively small ($m_b \approx 5.0$) and consequently not enough observations were available to invert for a source, so it is hard to ascertain the predominant tectonic release mechanism at this sub-site. However, barring the double event HURONLANDING-DIAMONDACE, all events with sufficient observations for inversion yielded strikes appropriate for a vertical strike-slip fault with the strike angle in the North West quadrant. Patton (1988) speculates that block thrust or rotation may be the

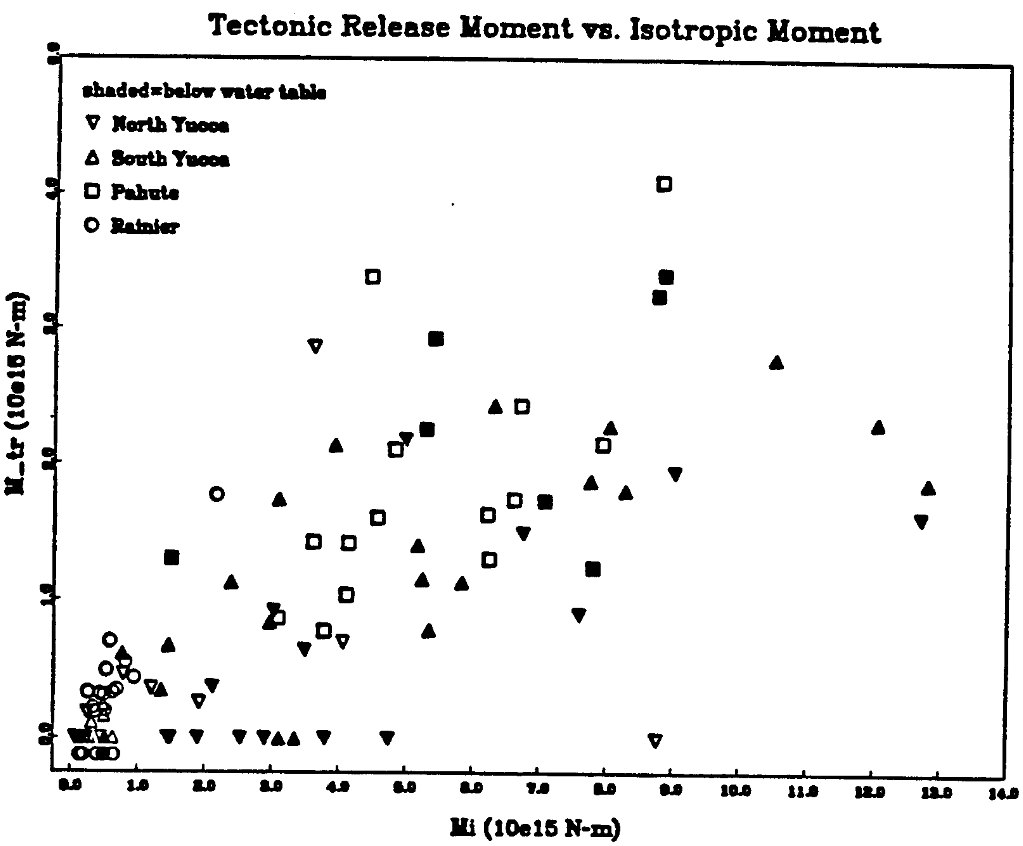

Figure .: Tectonic release moment plotted vs. isotropic moment.

prime mechanism at Rainier Mesa; however, the results here imply that strike-slip motion can explain the fundamental-mode surface wave radiation pattern observations adequately.

Figure 9 plots the estimated tectonic release (from combined Rayleigh and Love wave inversion) vs. the isotropic moment. Events with no observed Love waves or too few observations to invert for a double-couple source are treated as having no tectonic release ($M_{\#} = 0$). For all events $M_I > M_{\#}$. All Pahute events show evidence of tectonic release. Only about half of the Yucca events do so. Otherwise, there are no clear trends in the data. The amount of tectonic strain release does not appear to depend on whether the shot takes place above or below the water table, either.

The explosion moments and errors were converted to log_{10} units and listed, along with time domain moments (and their errors) for overlapping events determined in Woods & Harkrider (1995), in Table 6. The time-domain moments are plotted versus the spectral moments in Figure 10. Spectral domain moment errors are significantly smaller than those of time-domain moments by over 0.1 magnitude units on average, resulting in a reduction in standard deviation from 41.3 to 12.2 percent. However, the time-domain log-moments are in close agreement with the scalar spectral log-moments; yielding estimates within 15 to 30 percent of one another. There is no discernible improvement in error reduction between the different types of spectral moment estimates. Differences between constrained explosion (M_0) and inverted isotropic (M_I) log-moments are generally less than 0.1 log units (25 percent); often the difference is much smaller.

Figure 11a plots all final explosion moments from this study vs. teleseismic m_b taken from, or calculated using the method of Lilwall & Neary (1985). Vertical error bars on the data points are the estimated error (standard deviation, s.d.) of the data (note that

Figure : Time domain log moments regressed against spectral domain moments. In the top figure spectral moments were determined assuming an isotropic source only, while in the bottom figure the spectral moments were determined by inverting for an isotropic source + a double-couple source. The regressions were constrained to a slope of unity.

Mo(PPA) vs Mo(spectral)

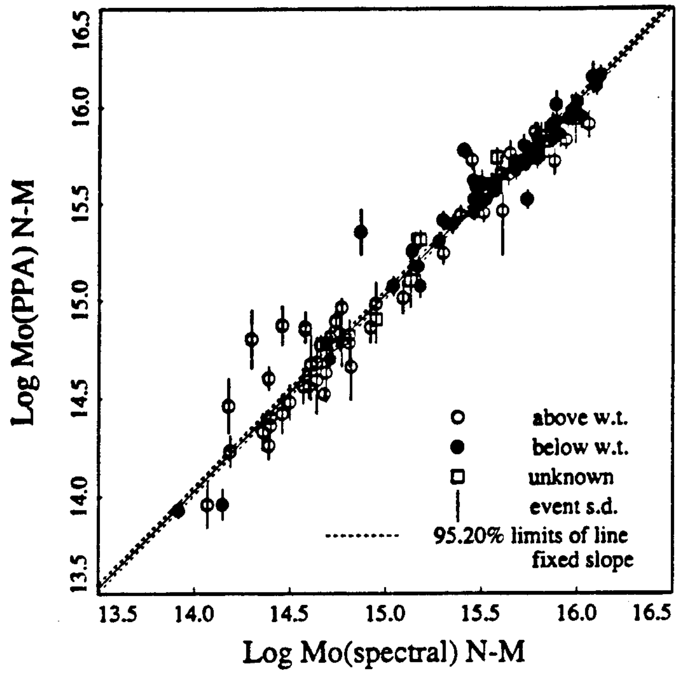

Log Mo(PPA) N-M =1.00 x Log Mo(spectral) N-M + 0.03

(s.d.=0.11)

Mo(PPA) vs Mi(spectral)

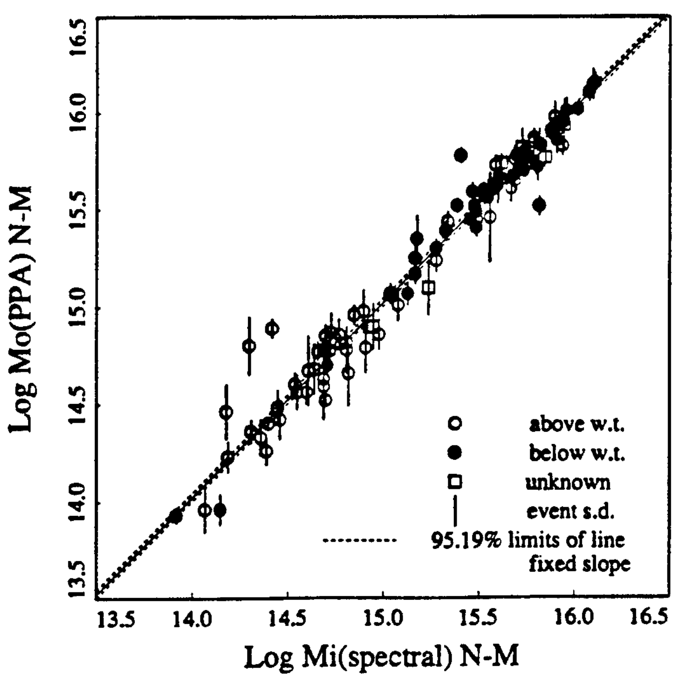

Log Mo(PPA) N-M =1.00 x Log Mi(spectral) N-M + 0.02

(s.d.=0.10)

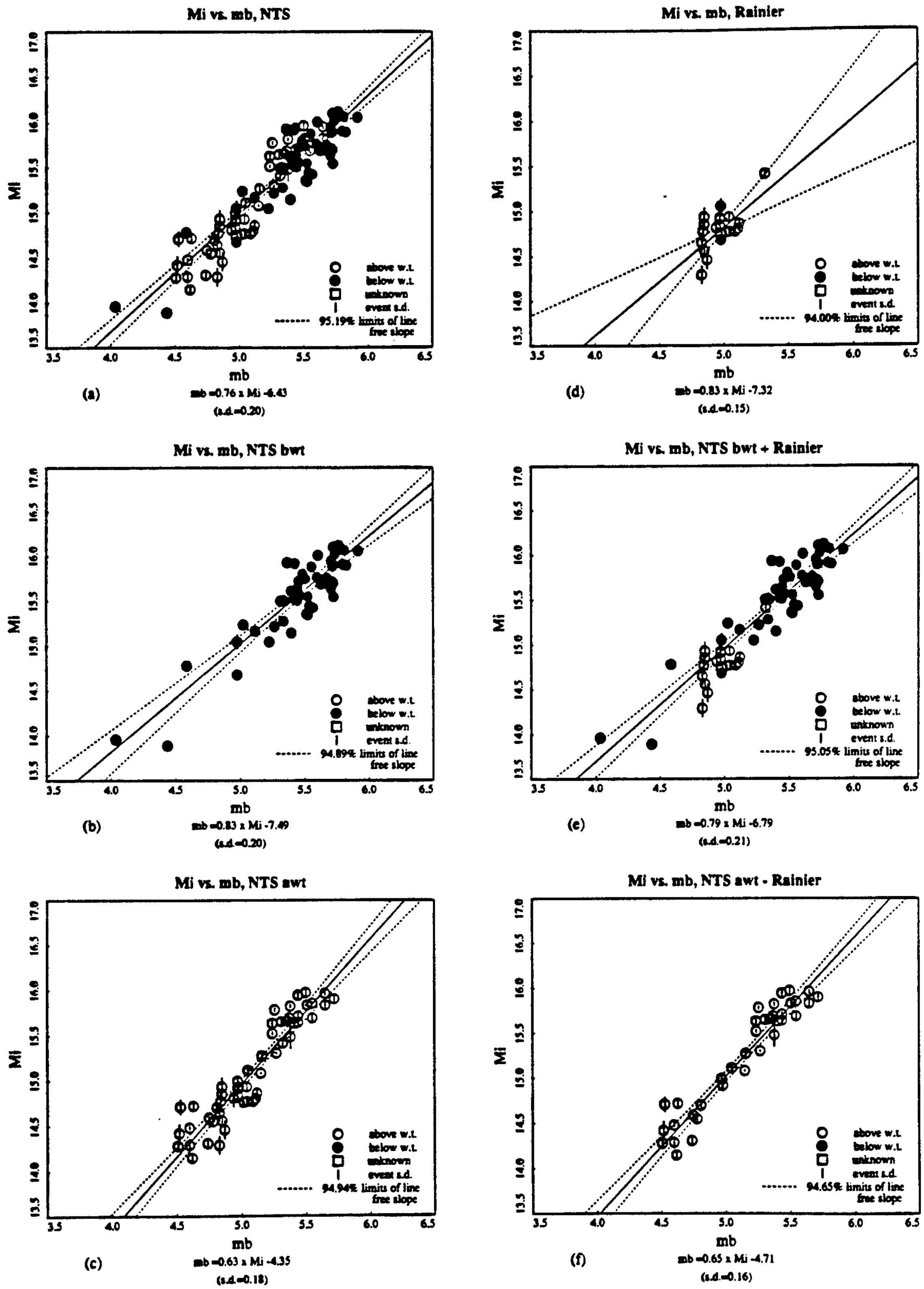

Figure : M_0 vs. m_b regression curves for the aggregate NTS population and for Rainier Mesa.

for most solid points the scaled errors are smaller than the symbols and hence are not viewable). A weighted linear least-squares regression was performed to obtain the M_0:m_b scaling relationship. Below the curve is the regressed scaling relationship and below that, in parentheses, is the standard deviation in the fit of the data to the curve. Given & Mellman (1986) formulate the M_0:m_b (or M_I:m_b) scaling law as a function of M_0, so for consistency in comparisons the same is done here. Here, unlike in their study, the slope is not set to 0.9, an artificial constraint, needed because of the narrow range of data and based on assumptions in m_b:yield and moment:yield scaling laws. The solid line is the fit to the data and the dashed lines are the 2σ error bars for this line. The scaling relationship is well constrained; however, the standard deviation is large, being 0.2 log-moment units (58 percent). Separating the events into populations detonated below and above the water table (Figures 11b and 11c, respectively) does not reduce the scatter significantly, but it does change the slope of the curve some (10-15 percent), giving an indication of how well the regression curves are constrained.

Figure 11d is a regression-curve plot of Rainier Mesa explosions. Although the curve is not well-constrained, the slope is close in value to that of the other curves. Rainier shots are detonated in large horizontal tunnels, unlike other shots which are detonated in boreholes. So there is some question as to the complexity of Rainier sources. As discussed in Woods & Harkrider (1995), the M_S-yield relationship is similar to that of well-coupled Pahute detonations below the water table (BWT) from which it is assumed that the Rainier shots can be treated as being in saturated rock. This inference is substantiated by Taylor (1983), who reports that the Mesa sports a perched aquifer. Treating the Rainier detonations as having been below the water, the entire NTS data set is again separated into shots occurring below and above the water table populations in Figures 11e and 11f, respectively. The inclusion or exclusion of Rainier events does not appreciably change either curve, so it not clear from these results whether Rainier shots are detonated in water-saturated rock or not.

Figure 12a is the moment-m_b regression curve for Yucca Flats explosions. Figures 12b and 12c separate the Yucca population into shots below and above the water table. All three of these curves are well-constrained and have slopes near 0.8, similar to the complete NTS population curves. The standard deviations of these curves are slightly smaller than that of the aggregate NTS data curves, indicating that the sub-sites do have relative excitation levels for surface waves and body wave.

Figures 12d, 12e and 12f are analogous curves for Pahute Mesa. These curves are poorly constrained, because of the limited data set, and have quite different slopes. To obtain useful scaling relationships for Pahute Mesa, more data is necessary. In an effort to better constrain these curves, Rainier shots were added to this population under the premise that the two source regions have similar geology (volcanic mesas of tuff and rhyolite). Although the resultant curves are well-constrained (Figures 13a, 13b and 13c), their slope values are quite different from the other populations. It appears that the Rainier shots have a larger m_b for a given moment than Pahute events. This point will be further examined after examining the moment:log-yield scaling laws.

In order to better constrain the m_b:moment scaling relationships, data from the Stevens (1986) and Given & Mellman (1986) studies were included after correcting for their modeled shot points. Figures 14 and 15 are regression curve plots for the combined data sets analogous to Figures 11 and 12. The main improvement is to better constrain the Pahute Mesa curves (Figures 15d and 15e) which have slopes in line with the regression curves for the other

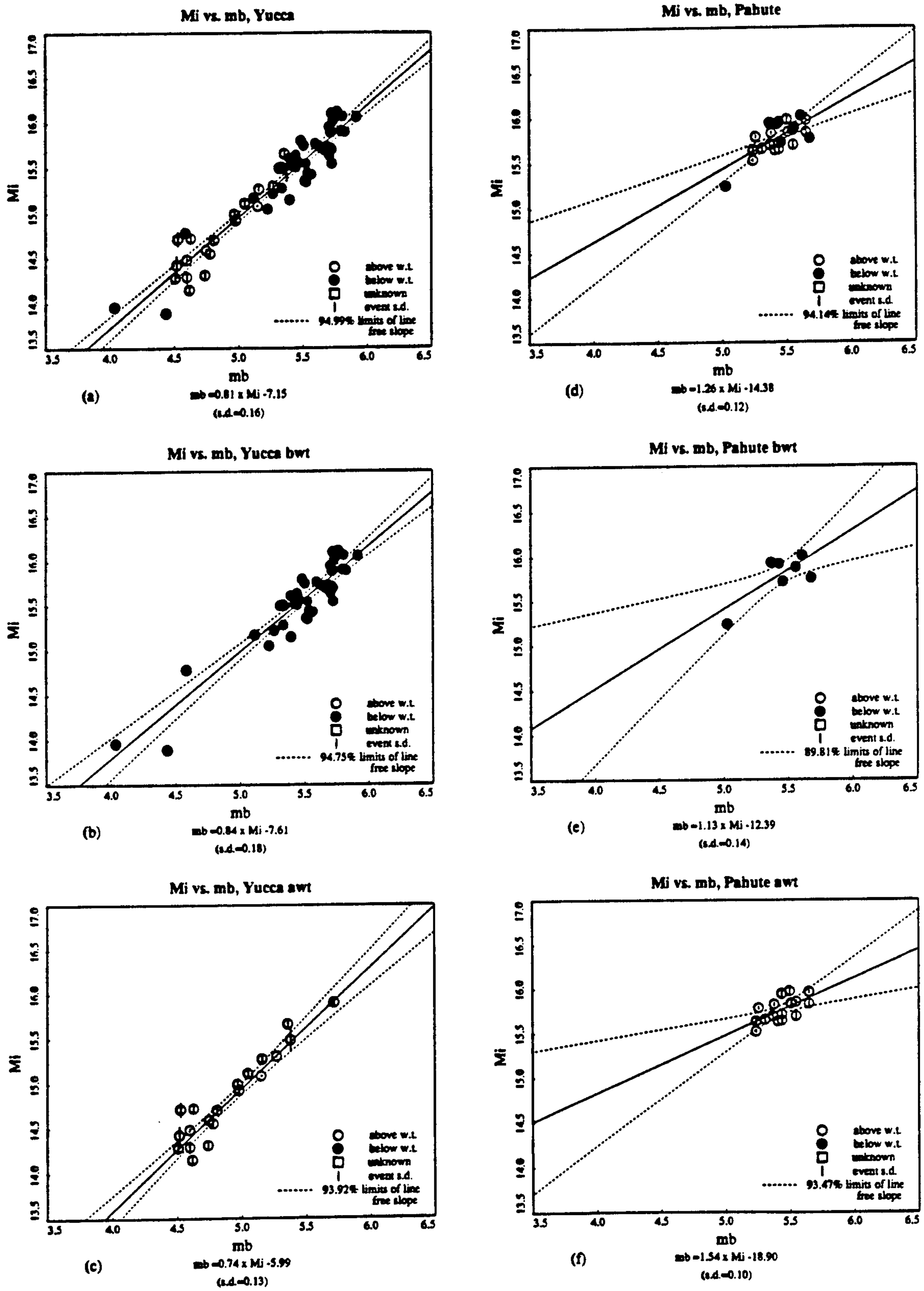

Figure : M_0 vs. m_b for regression curves Yucca and Pahute Events.

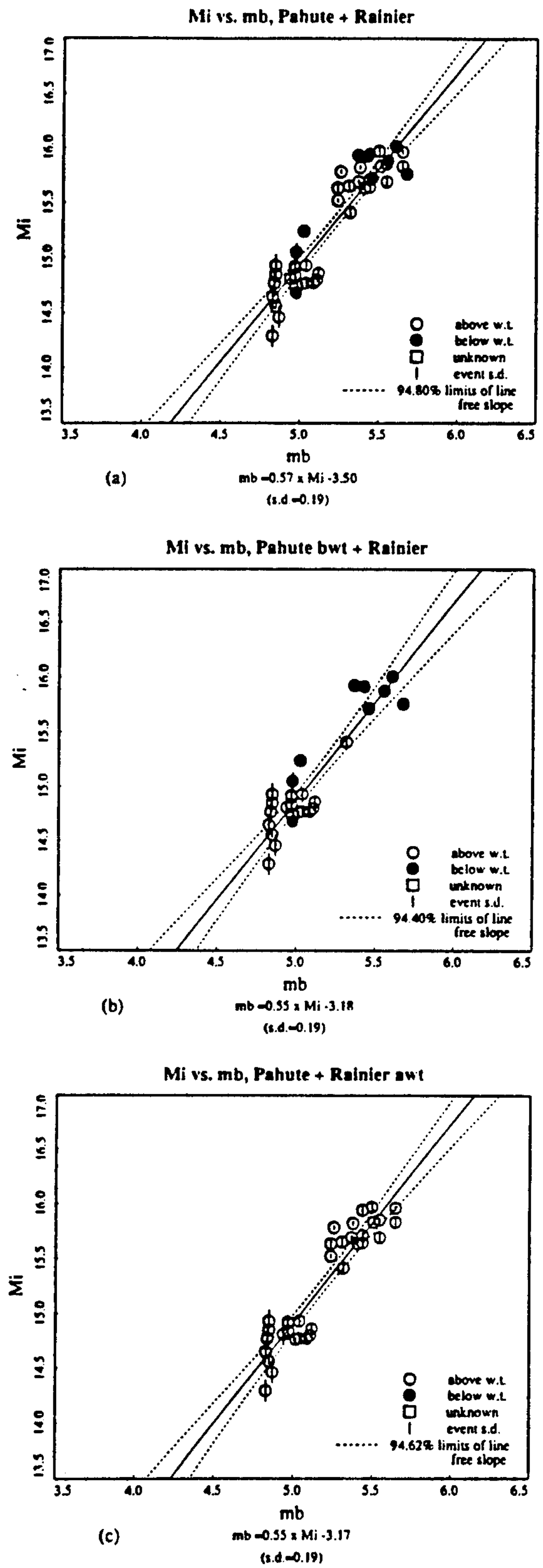

Figure .3: M_0 vs. m_b regression curves for Pahute and Rainier events.

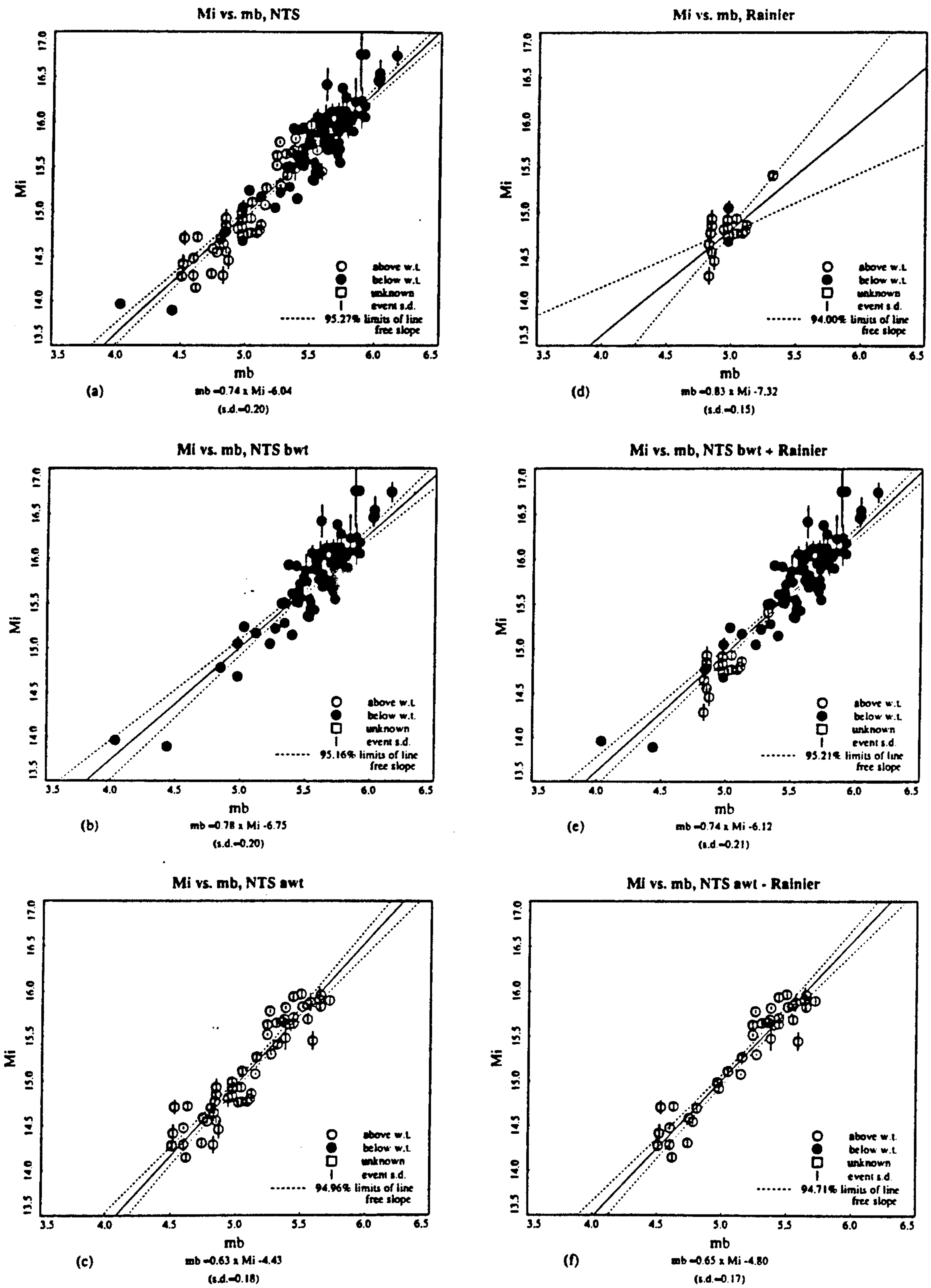

Figure .4: M_0 vs. m_b regression curves for all NTS events and for Rainier events. Data from Stevens (1986) and Given and Mellman (1986) are included.

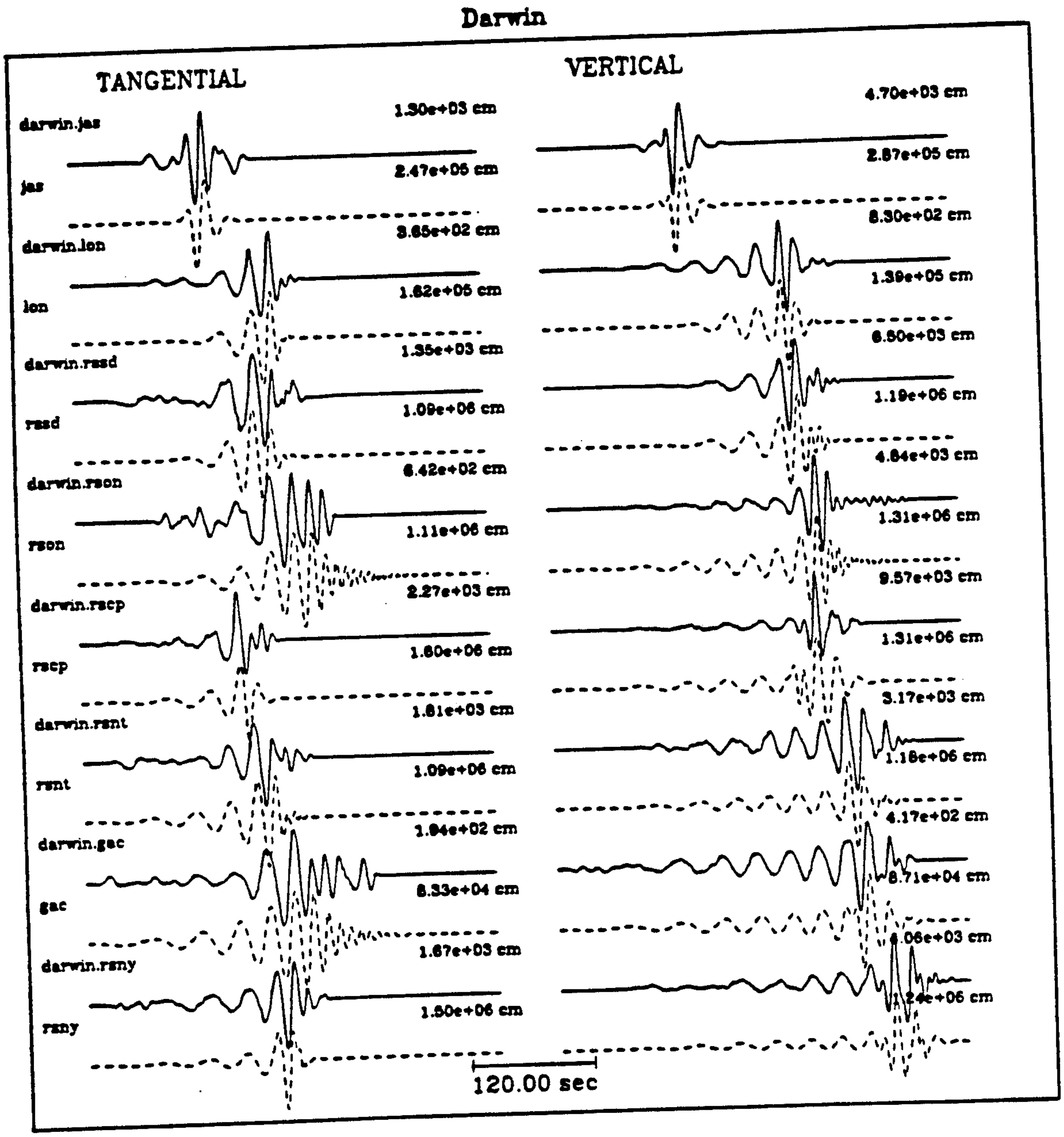

Figure : Comparison of observed and synthetic seismograms for paths modeled in this study.

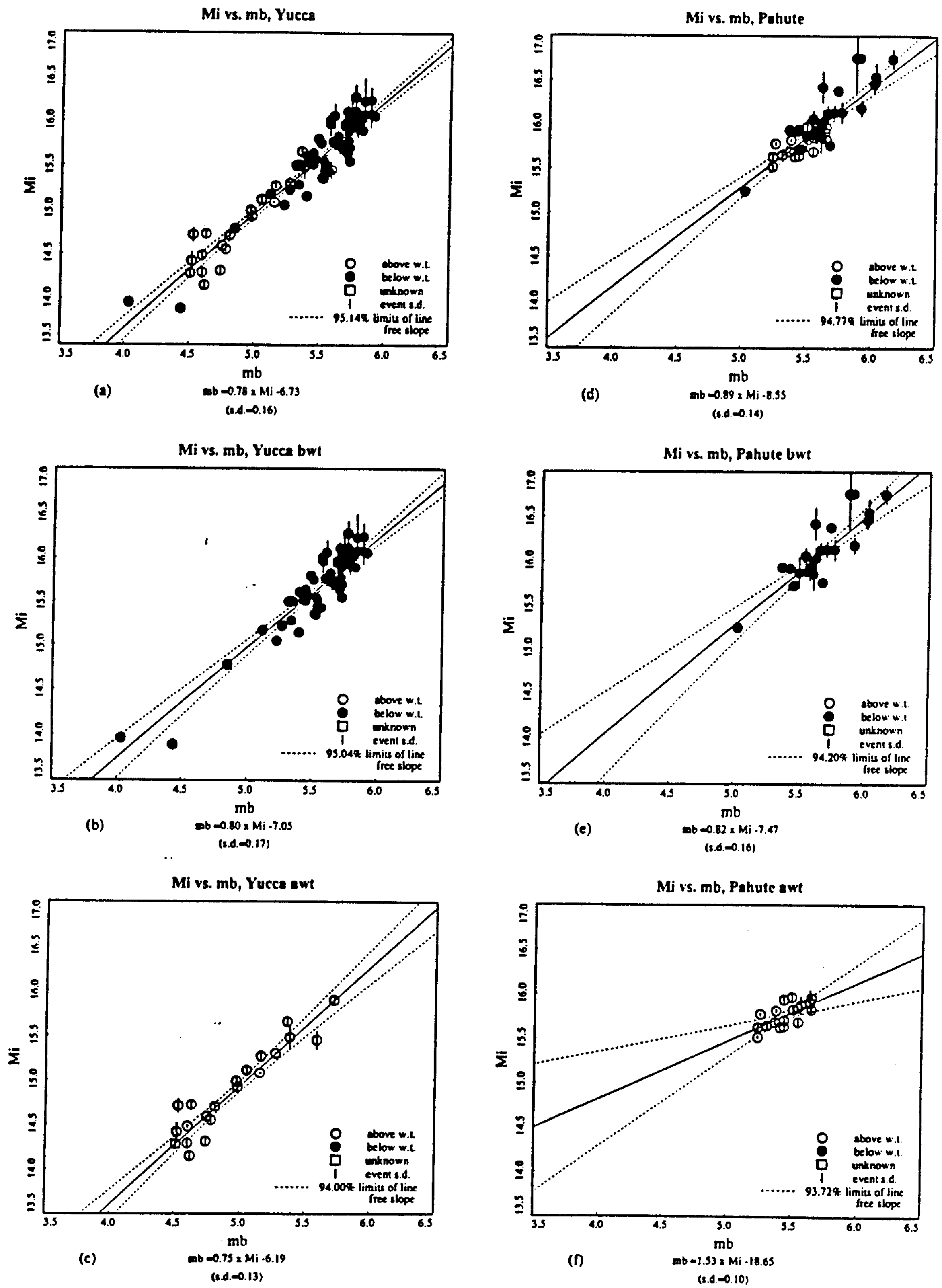

Figure 5: M_0 vs. m_b regression curves for Yucca and Pahute events. Data from Stevens (1986) and Given and Mellman (1986) are included.

populations (≈ 0.8). The Pahute awt curve is no better constrained however.

From these results it appears that the m_b:moment scaling relationship curve slope is near to 0.8 for all well-constrained cases. The data sets were then regressed again with a fixed slope of 0.8. The difference in off-sets, relative to the aggregate NTS curve, are given in Table 7, with a positive value meaning that for a given moment, the m_b value will be larger by that many magnitude units. The standard deviation of the data fit to the curve is also given, so that goodness of fit of the unconstrained and constrained curves can be compared. In all cases, except for Pahute events alone, this difference is negligible. For Pahute the errors are slightly smaller for the unconstrained curve. For the entire NTS data set the fixed-slope scaling relationship is

$$m_b = 0.8 \times M_0 - 7.0. \tag{26}$$

Here the M_0 can be interchangeably used with M_I. There is no appreciable off-set between shots detonated above or below the water table at an individual site implying that P-wave and Rayleigh wave coupling effects are very similar. There are differences between sites, however, the largest difference being between Pahute and Rainier. From these results Pahute Mesa will have the smallest m_b for a given moment, followed by Yucca and then Rainier, implying that it is the richest in long-period energy excitation. The scaling curve off-set difference between shots above and below the water table are negligible.

In order to determine seismic coupling effects and moment-scaling independent of another seismic scale, the seismic moments were also regressed against yield. Figures 16, 17 and 18 are log-moment vs. log-yield regression plots analogous to the M_0 vs. m_b plots of Figures 11, 12 and 13, respectively.

For the complete NTS data set (Figure 16a) the curve is well-constrained, with a slope near

$m_b = 0.8 \times log\,(M_0) - 7.0 + D$			
Site	Case	D	s.e.
NTS	all	0.0	0.02
NTS	bwt	0.0	0.03
NTS	awt	-0.01	0.03
Rainier	all	0.15	0.03
Yucca	all	0.04	0.02
Yucca	bwt	0.04	0.03
Yucca	awt	0.05	0.03
Pahute	all	-0.17	0.03
Pahute	bwt	-0.18	0.06
Pahute	awt	-0.17	0.03

Table 7: Offsets in Mo:mb regression curves for NTS subsites

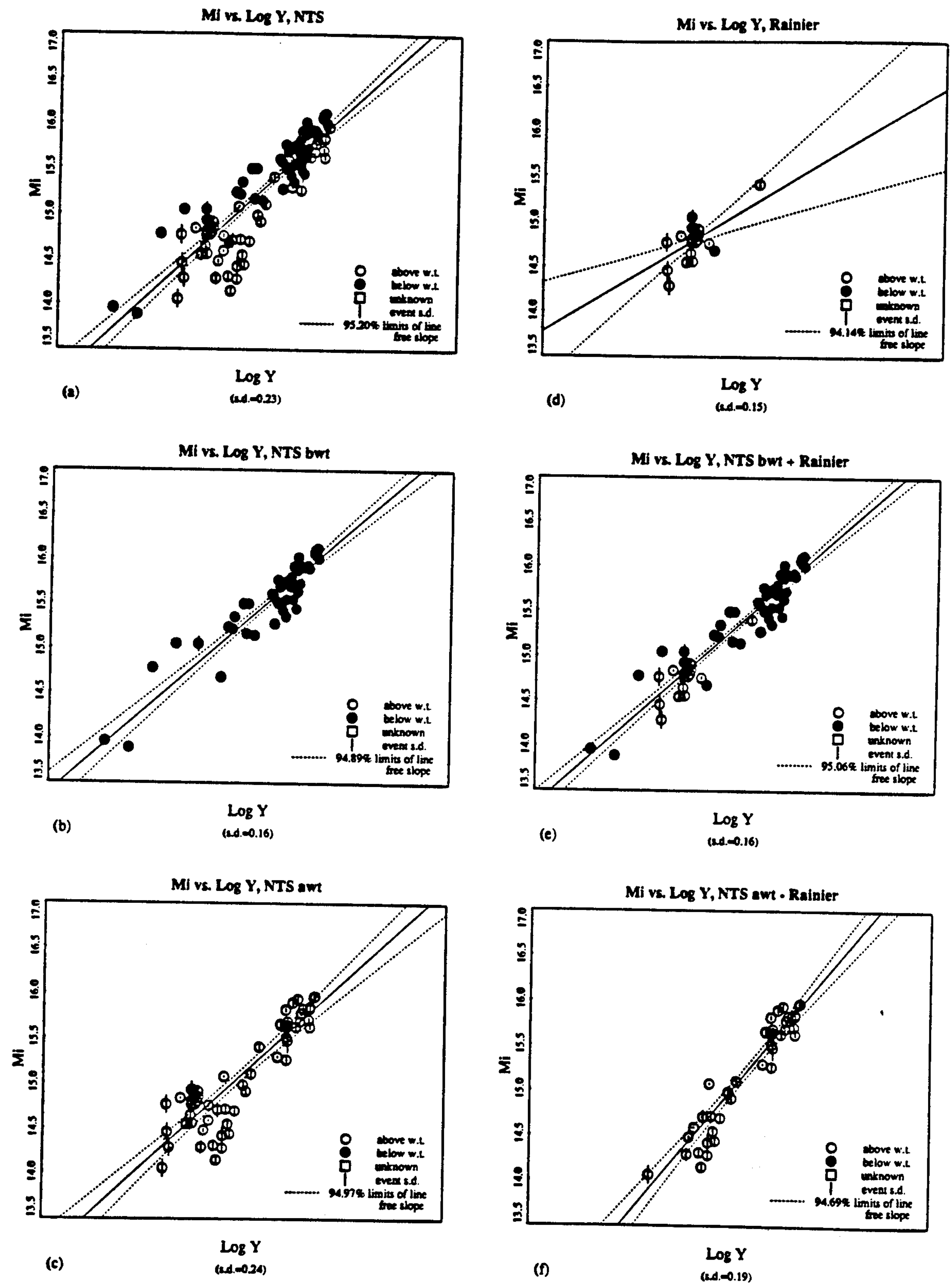

Figure 9: M_0 vs. log-yield for aggregate NTS and Rainier data sets.

unity (1.04). The group of data points grouped away from the regression curve are Yucca Flat explosions detonated above the water table (AWT), about half of these were detonated in alluvium as well. Werth *et al.* (1963), in a previous study of P-wave coupling found that alluvium had the lowest seismic coupling coefficient amongst the shot medium rock types that were studied. It is also known that saturated rock tends to be a more effective medium for seismic coupling. Compressional velocity tends to increase with decreasing dry porosity, as the bulk modulus increases, so by equation (3) an increase in α lowers the observed displacement for a given moment, M_I. So it is not surprising that bombs detonated in such muffling material will give lower apparent moments. Splitting the NTS population into shots detonated in water-saturated or unsaturated rocks leads to similar sloping curves, with values near unity (0.98, 1.03 and 1.00 for curves b, c and e, respectively) but with different intercepts. The scaling relationship for Rainier events (Figure 16d) is poorly constrained; however, a slope of unity is within the 2σ confidence level of the curve.

For the case of AWT explosions, excluding Rainier shots (Figure 16f), the slope of the curve is considerably larger than for any of the other cases. This data set falls into two clusters (above and below $\log(M_I) = 15.5$), the upper group being predominantly Pahute events and the lower being all Yucca events. If there is a difference in coupling between the two sites, there should be a corresponding offset in scaling curves. So the best-fitting curve for the combined data set will give a very skewed, incorrect curve (slope=1.35).

Separated Yucca and Pahute population log-moment:log-yield curves are shown in Figures 17a through 17f. The variance is significantly smaller for the Pahute populations, particularly for BWT events (Figure 17e). The slope for this curve (0.86) is heavily-constrained by the one low-yield event (REX), where as the Pahute and Pahute AWT curves both have slopes

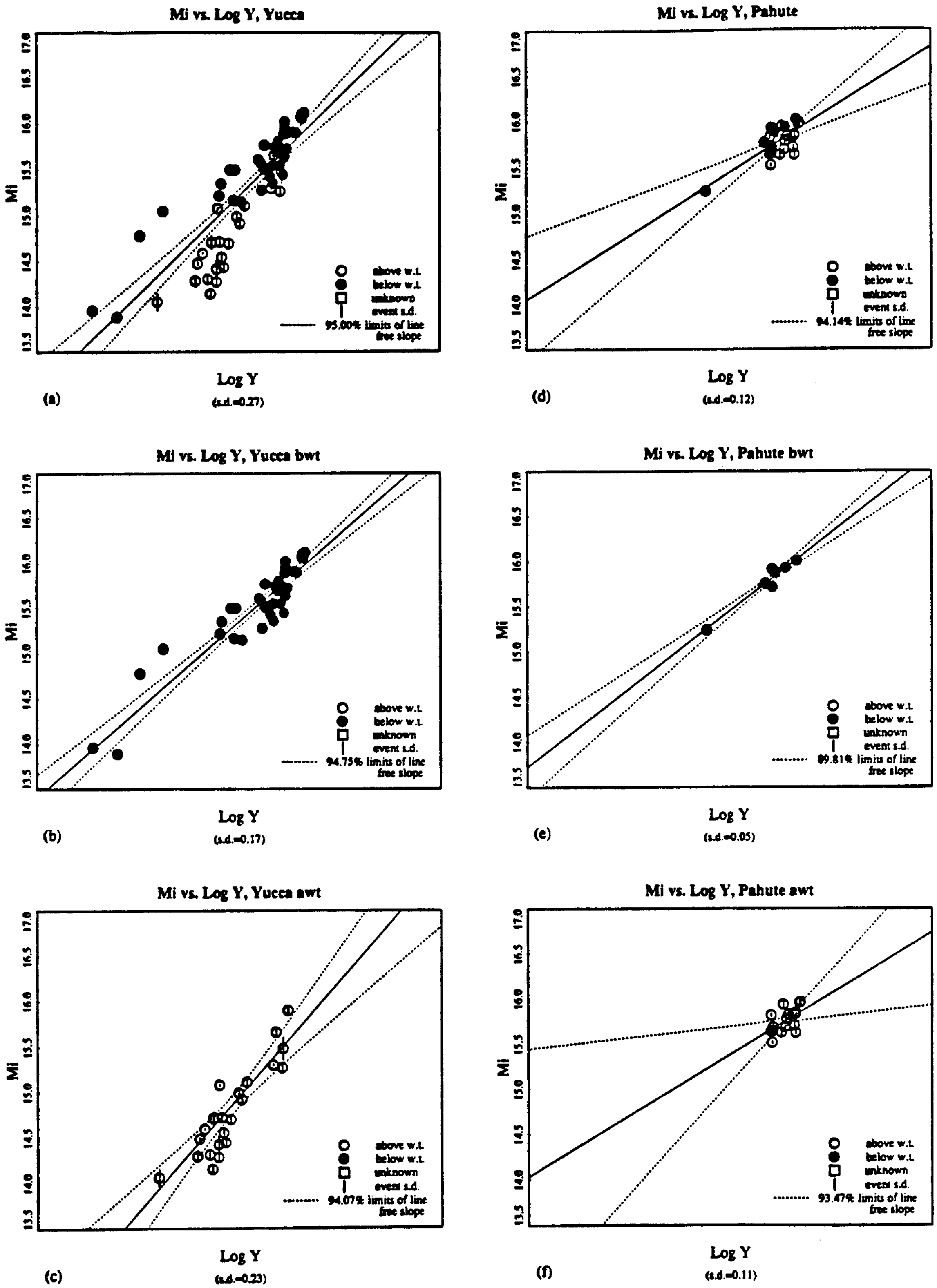

Figure : M_0 vs. log-yield for Yucca Flats and Pahute Mesa data sets.

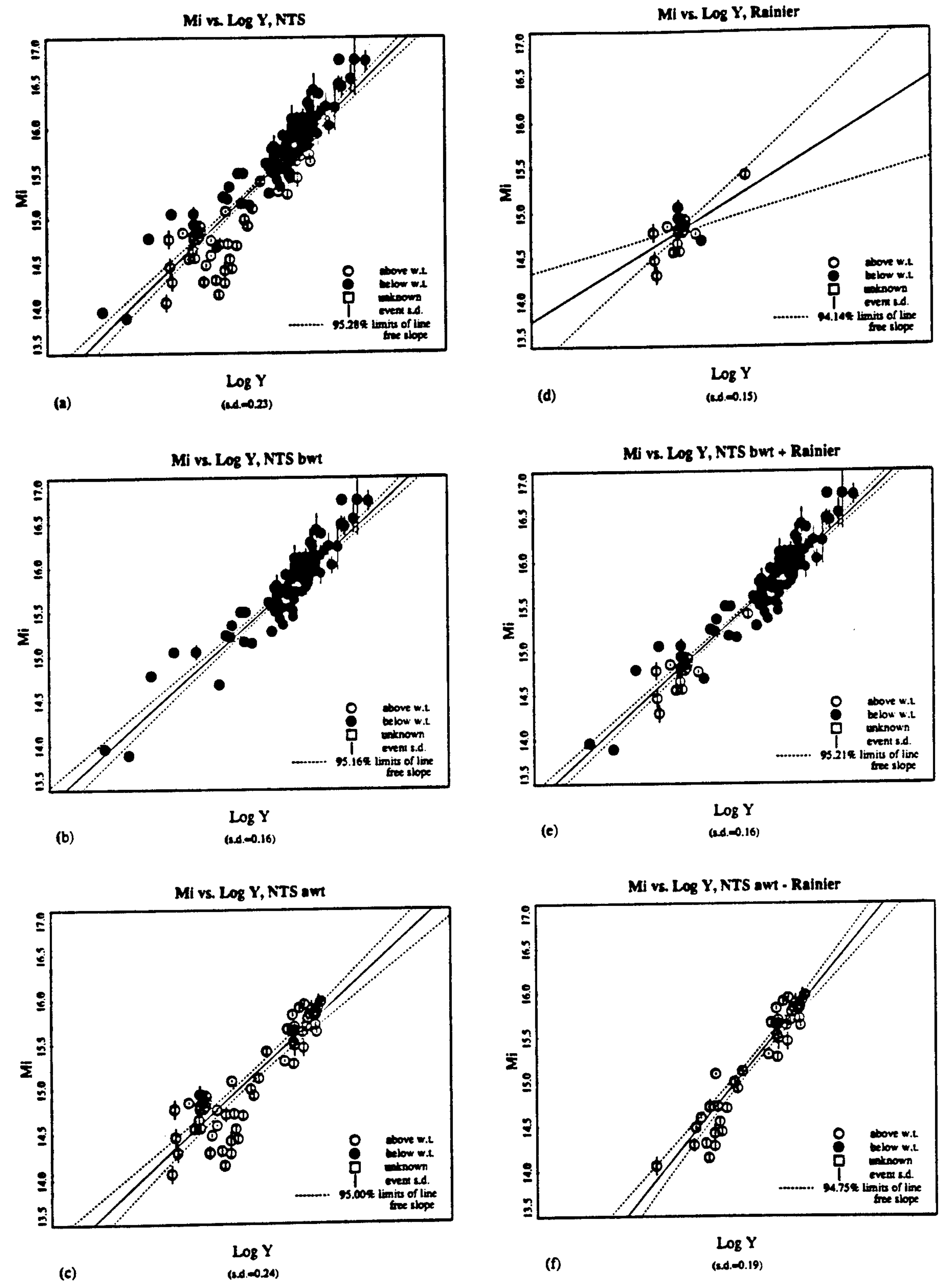

Figure 8: M_0 vs. log-yield for combined Yucca Flat and Pahute Mesa data sets.

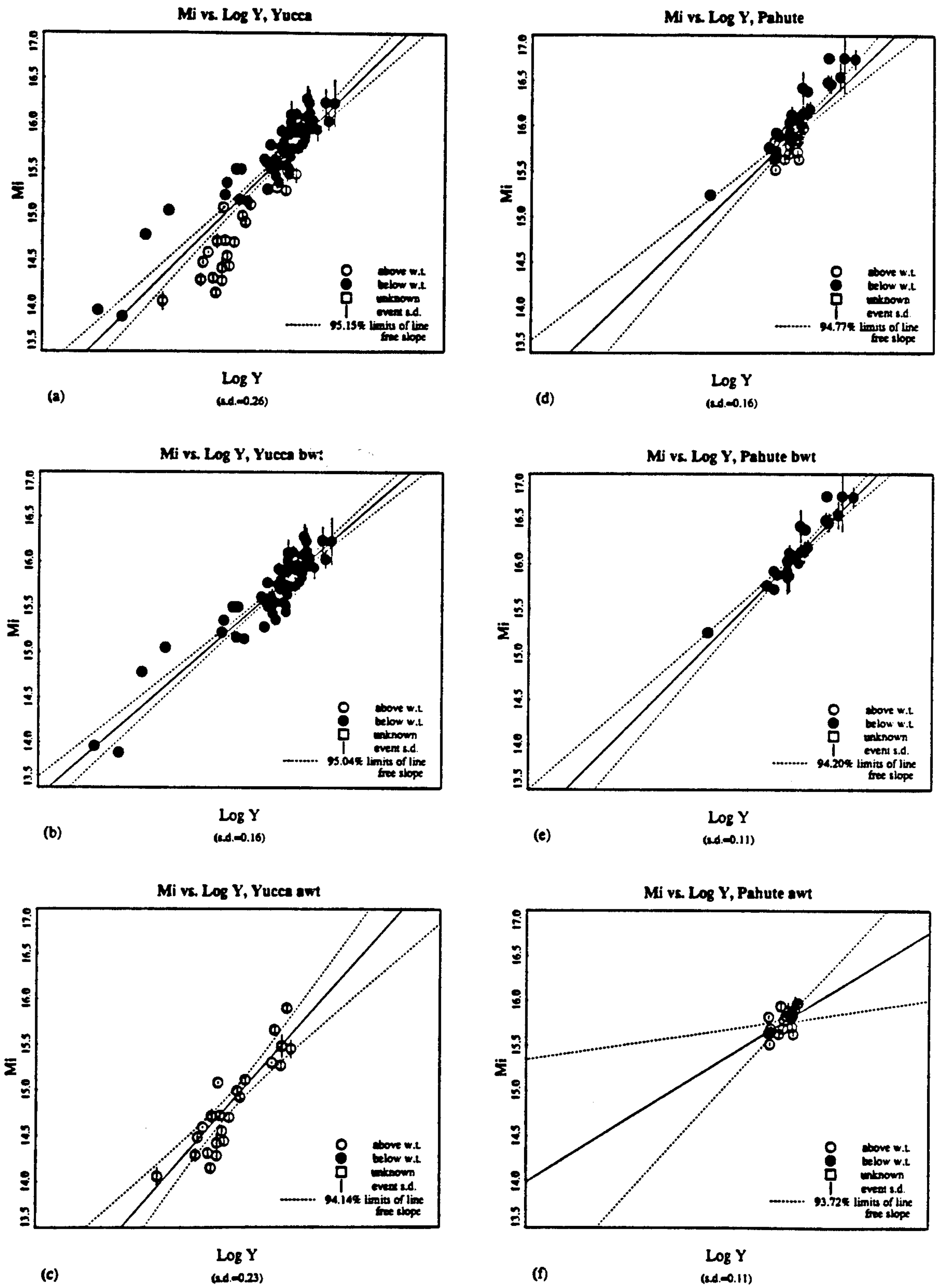

Figure .9: M_0 vs. log-yield for the Rainier and complete NTS data sets which include moment data from Stevens (1986) and Given and Mellman (1986).

near 0.69 in value. In fact, the best-constrained curve is for Yucca BWT shots (Figure 17)b, slope=0.97). The Yucca AWT regression curve (slope=1.27) is not well-constrained, due to the highly scattered nature of the data.

Combining the Pahute and Rainier data leads to a better constrained curve for BWT events by making the assumption that all of the Rainier shots are fired in saturated rock. For all events above and below the water table, the slope is 0.95 (Figure 18a). For the case of BWT shots, the slope is 1.06 (Figure 18b). Combining Pahute AWT shots with Rainier shots gives a slope of 0.90 (Figure 18c). The fact that the Pahute AWT + Rainier slope is furthest from unity is interpreted to mean that the Rainier events couple intermediate to Pahute shots detonated below and above the water table.

In order to better constrain the larger-yield portion of the regression curves (particularly for Pahute events), the other studies' moments are also added to the data set, bringing the total number of events to 155 from 109. Figure 19a is for all NTS BWT events; the slope of the scaling relationship is 1.01. Including Rainier shots leads to a slope of 1.03 (Figure 19b).

None of the AWT curves are appreciably changed by the addition of only a few points (1 to 3) at most. The most improvement in constraining the data is for those data sub-sets including Pahute events. Figure 19c is for all Pahute alone and the slope, 1.09, is better constrained than that of the curve in Figure 17d. Including Rainer data gives a slope of 1.01 (Figure 19d). The Pahute BWT data and corresponding scaling curve are shown in Figure 19e (slope=1.14), unfortunately the lower end of the scale is still poorly constrained. Figure 19f is for Yucca BWT data. Its slope (0.96) is close to the case for this study's data only (Figure 17b).

From these results the estimated average slope of the moment:yield scaling curves is near unity, with a 2σ margin of error of 0.05. A constrained (fixed-slope) least-squares regression for each data set was also performed. The tabulated results for this study's data set and the combined data set are in Table 8 and Table 9, respectively. The first column of each table describes the data set sub-population. The second column is the off-set relative to the complete NTS data set determined in this study (δD). The last column is the standard deviation for each fix-slope regression curve, which are generally not appreciably larger than for the free-slope regression curves. The standard error, $\sigma_{\bar{X}}$, defined as

$$\sigma_{\bar{X}} = \frac{\sigma}{\sqrt{n}},$$

with σ being the standard deviation and n being the number of observations, is between 0.01 and 0.04 for δD in all cases. So δD's larger than this amount are statistically significant.

Using either data set (this study's or the combined data set) a large offset is seen in the log-moment:log-yield intercept between shots detonated above and below the water table. For Pahute this offset is 0.22 log units (a difference of 66 percent). For Yucca the offset is 0.41 log units (a 275 percent difference). The difference in apparent coupling between Pahute and Yucca shots detonated in saturated rock is only 0.08 log units or 20 percent. The Rainier scaling curve intercept appears to be intermediate to that of the Pahute BWT and Pahute AWT curves. Yucca AWT shots have the lowest apparent coupling, being 0.3 log units (200 percent) lower than that of the aggregate NTS data curve. The difference in offset between composite (BWT+AWT) data sets is small for all subsites, being less than 0.07 (17 percent) in all cases. Hence, site source effects are relatively small; however, whether or not the shot occurs in saturated material is a significant effect.

$\log(M_0)=\log(\text{yield}) + D$		
dataset: this study		
Case	ΔD	s.e.
NTS (all)		0.02
NTS bwt	0.11	0.16
NTS awt	-0.12	0.03
Rainier	0.04	0.03
NTS bwt+Rainier	0.10	0.02
NTS awt-Rainier	-0.18	0.03
Yucca (all)	-0.03	0.03
Yucca bwt	0.10	0.03
Yucca awt	-0.30	0.05
Pahute (all)	0.03	0.03
Pahute bwt	0.14	0.02
Pahute awt	-0.04	0.03

Table 8: Offsets in constrained Mo:yield regression curves for NTS sub-sites.

$\log(M_0)=\log(\text{yield}) + D$		
combined data set		
Case	ΔD	s.e.
NTS (all)	0.02	0.02
NTS bwt	0.14	0.02
NTS awt	-0.12	0.03
NTS bwt+Rainier	0.13	0.01
NTS awt-Rainier	-0.16	0.04
Pahute (all)	0.08	0.02
Pahute bwt	0.21	0.03
Pahute awt	-0.1	0.02
Pahute+Rainier	0.08	0.02
Pahute bwt+Rainier	0.14	0.02
Pahute awt+Rainier	0.0	0.02
Yucca (all)	0.01	0.03
Yucca bwt	0.13	0.02
Yucca awt	-0.28	0.05

Table 9: Offsets in constrained Mo:yield regression curves for NTS sub-sites using the combined data set.

CONCLUSION

Spectral moments were determined for 109 NTS explosions using regional surface wave data. This data set is significantly larger and more comprehensive than previous published studies of long-period explosion sources. Whereas these studies (Stevens, 1986 and Given & Mellman, 1986, for example) are confined to explosions greater than $m_b = 5.4$; in this study, events down to $m_b = 4.9$ were consistently observed and analyzed (in some cases even smaller). With this extensive data set it is possible to make more robust inferences concerning long-period source scaling for underground nuclear explosions.

The reduced magnitude threshold is due, in part, to the inclusion of near-regional (d<700 km) surface wave records for source inversions. Only with such data were the smallest events ($m_b \leq 4.9$) measurable. Systematic errors due to incorrectly modeling path attenuation effects are minimized using such stations as well. It was also found that regional digital long-period stations, specifically RSTN and DWWSN stations, were superior for observing the smaller events than were the earlier-model analog WWSSN stations.

Moment estimates assuming a pure explosion source (*i.e.*, the average of the station moments) do not vary significantly, in almost all cases, from estimates determined from joint isotropic + double-couple inversions. Moment standard errors (1σ) are also comparable, being on average approximately 7 percent (0.03 log units), with the smaller events tending to have larger errors. This is a significant improvement over the time domain moments determined in Woods & Harkrider(1995) ($\bar{\sigma} = 0.15$). Past investigations of surface wave magnitudes and seismic moments did not achieve this level of accuracy, even when secondary path corrections (or more exactly station corrections) were incorporated. The improvement in accuracy in the moment estimates found in this study are attributed to using near-regional stations and having better azimuthal coverage.

The results of the canonical source inversion study predict errors for the joint source inversion compatible with observations; however, the observed errors for the constrained explosion source estimates are smaller than the predicted values. A possible explanation for this fact is that the path Green's functions were inverted from bomb data contaminated with tectonic release energy, so that azimuthal radiation effects are incorporated into them. Thus azimuthal amplitude variations will be smeared-out, making the observed non-isotropic component appear smaller.

The constrained tectonic-release moment results are not as well resolved, with standard deviations varying from 10 to 50 percent (0.04 to 0.18 log units). Moment estimates determined separately by Rayleigh wave and Love wave varied by as much as a factor of 2.5. The inferred strike angles obtained from the constrained moment inversion generally were found to confirm earlier studies that found the predominant tectonic release mechanism could be modeled as a near-vertical strike-slip double-couple source with a strike near N20°W.

As a goal of this study was to re-evaluate the utility of surface wave measurements to quantify explosions for yield and discrimination purposes, particular attention was paid to error analysis of the moment estimates. To this end it is important to determine how much near-source effects can modify apparent moments. Moment scaling relationships for the various NTS sub-sited were determined using this study's analyzed events in conjunction with larger yield explosion data from other studies in order to better constrain their curves. It was found that $m_b \propto 0.8(\pm 0.05) \times \log(M_0)$, while $M_0 \propto Y^{(1.0 \pm 0.05)}$.

The off-set in scaling curve intercept between sub-sites is at most 0.07 log units (17 percent) for the super data set and only 0.02 log units (5 percent) when only data from this study was considered. A much greater difference in scaling curve intercepts exists between events detonated above and below the water table, being between 0.22 log units for Pahute Mesa and 0.41 log units for Yucca Flats. This coupling affect appears to be similar for P-wave amplitudes. If this coupling effect cannot be accounted for in practice, then predicted yield estimates could off by a factor of two. Gupta *et al.* (1989) found that the spectral content of P-waves could be used to determine whether a shot occurred above or below the water table. In an actual monitoring environment where only remote-sensing may be possible, employing this technique would enable one to correct explosion moment estimates for the shot medium coupling, thus significantly improving surface wave moment estimates, as well as body wave magnitudes.

The improvement in estimating the long-period source spectrum of explosions found in this study makes such measurements more useful for seismic nuclear monitoring. The resolution attained in this study makes surface wave moment estimates a prime candidate as companion measurement to L_g magnitude ($m_{b(Lg)}$) (Nuttli, 1986; Patton, 1988). The magnitude threshold for L_g is lower than that of surface wave measurements, being near $m_b = 3.1$ for comparable distances; however, for paths in which the L_g wavetrain is "pinched out," a term for which is "L_g blockage," other methods are necessary.

Acknowledgments. This research was supported by the Air Force Office of Scientific Research through Grant Number F49620-93-1-0221. Contribution No. xxxx, Division of Geological and Planetary Sciences, California Institute of Technology, Pasadena, California.

REFERENCES

Aki, K., & Tsai, Y.-B., 1972. Mechanism of Love-wave excitation by explosive sources, *J. Geophys. Res.*, **77**, 1452-1475.

Archambeau, C. & Sammis, C., 1970. Seismic radiation from explosions in prestressed media and the measuremnt of tectonic stress in the Earth, *Rev. Geophs. and Space Phys.*, **8**, 473-499.

Bache, T. C., Rodi, W. L., & Harkrider, D. G., 1978. Crustal structures inferred from Rayleigh-wave signatures of NTS explosions, *Bull. Seism. Soc. Am.*, **68**, 1399-1413.

Ben-Menahem, A. & Harkrider, D. G., 1964. Radiation patterns of seismic surface waves from buried dipolar point sources in a flat stratified earth, *J. Geophys. Res.*, **69**, 2605-2620.

Brune, J. N. & Pomeroy, P. W., 1963. Surface wave radiation patterns for underground nuclear explosion and small-magnitude earthquakes, *J. Geophys. Res.*, **68**, 5005-5028.

Dobrin, M. B., 1976. *Introduction to Geophysical Prospecting*, McGraw-Hill, New York.

Ekström, G.& Richards, P. G., 1994. Empirical neasurements of tectonic moment release in nuclear explosions from teleseismic surface waves and body waves, *Geophys. J. Int.*, **117**, 120-140.

Evernden, J. F., 1971. Variation of Rayleigh-wave amplitude with distance, *Bull. Seism. Soc. Am.*, **67**, 405-411.

Given, J. W. & Mellman, G. R., 1986. Estimating explosion and tectonic release source parameters of underground nuclear explosions from Rayleigh and Love wave observations, *DARPA Report AFGL-TR-86-0171*, Sierra Geohysics Inc., Kirkland, WA.

Gupta, I. N., Lynnes, C. S., Chan, W. W., & Wagner, R. A., 1989. A comparison of the spectral characteristics of nuclear explosions detonated below and above the water table, *Teledyne Geotech Rept. No, TGAL-89-04*, GL-TR-89-0151, Alexandria, VA.

Hadley, D. & Kanamori, H., 1977. Seismic structure of the Transverse Ranges, California, *Geo. Soc. Am. Bull.*, **88**, 1469-1478.

Hadley, D. & Kanamori, H., 1979. Regional S-wave structure for Southern California from the analysis of teleseismic Rayleigh waves, *J. Geophys. Res.*, **58**, 655-666.

Harkrider, D. G., 1964. Surface waves in multilayered media I. Rayleigh and Love waves from buried sources in a multilayered elastic half-space, *Bull. Seism. Soc. Am.*, **54**, 627-679.

Harkrider, D. G., 1970. Surface waves in multilayered elastic media. Part II. Higher mode spectra and spectral satios from point sources in plane layered earth models. *Bull. Seism. Soc. Am.*, **60**, 1937-1987.

Harkrider, D. G., 1981. Coupling near source phenomena into surface wave generation, *Identification of Seismic Sources - Earthquake or Underground Explosion*, pp 277-326, eds Husebye & Mykkeltveit, D. Reidel, Dordrecht. 277-326.

Harkrider, D. G., Stevens, J. L. & Archambeau, C. B., 1994. Theoretical Rayleigh and Love waves from an explosion in prestressed source regions. *Bull. Seism. Soc. Am.*, **84**, 1410-1442.

Haskell, N. A., 1967. Analytic approximation for the elastic radiation from a contained underground explosion, *J. Geophys. Res.*, **72**, 2583-2586.

Helle, H. & Rygg, E., 1984. Determination of tectonic release from surface waves generated by nuclear explosions in Eastern Kazakhstan, *Bull. Seism. Soc. Am.*, **74**, 1883-1898.

Herak, M. & Herak, D., 1993. Distance dependence of M_s and calibrating function for 20 second Rayleigh waves, *Bull. Seism. Soc. Am.*, **83**, 1881-1892.

Herrin, E. & Goforth, T., 1977. Phase matched filtering: Applications to the study of Rayleigh waves, *Bull. Seism. Soc. Am.*, **76**, 1259-1275.

Herrmann, R. B., 1988. Computer Programs in Seismology, *Proceedings of the 10th Annual DARPA/AFGL Seismic Research Symposium*, 126.

Kanamori, H. and Given, J. W., 1981. Source parameters determined from long period surface waves, *Phys. Earth Planet. Inter.*, **11**, 312-332.

Langston, C. A. and Helmberger, D. V., 1974. Interpretation of body and Rayleigh waves from NTS to Tucson, *Bull. Seism. Soc. Am.*, **64**, 1919-1929.

Levshin, A. L., 1985. Effects of lateral inhomogeneities on surface wave amplitude measurements, *Annales Geophysicae*, **3**, 511-518.

Lilwall, R. C. and Neary, J. M., 1985. Redetermination of earthquake body-wave magnitudes using ISC Bulletin data, United Kingdom Atomic Energy Authority, *AWRE Rept. No. O 21/85*, H.M.S.O. London.

Mendiguren, J. A., 1977. Inversion of surface wave data in source mechanism studies, *J. Geophys. Res.*, **82**, 889-894.

Mitchell, B. J., 1975. Regional Rayleigh wave attenuation in North America, *Geophys. J. R. astr. Soc.*, 80, 4904-4916.

Mooney, W. D. and Braile, L. W., 1989. The seismic structure of the continental crust and upper mantle of North America, *eds., Bally, A. W. and Palmer, A. R., The Geology of North America v. A: An overview*, ch. 4; Geological Society of America, Boulder, Colorado.

Nuttli, O.W., 1986. Yield estimates of Nevada Test Site explosions obtained from seismic Lg waves, *J. Geophys. Res.*, **78**, 2137-2151.

Oliver, J., 1962. A summary of observed surface wave dispersion, *Bull. Seism. Soc. Am.*, **52**, 81-86.

Patton, H. J., 1982. Measurements of Rayleigh-wave phase velocities in Nevada: Implications for explosion sources and the Massachusetts Mountain Earthquake, *Bull. Seism. Soc. Am.*, **72**, 1329-1349.

Patton, H. J. and Taylor, S. R., 1984. *Q* Structure of the Basin and Range from surface waves, *J. Geophys. Res.*, **89**, 6929-6940.

Patton, H. J., 1988. Source models of the HARZER Explosion from regional observations of fundamental-mode and higher-mode surface waves, *Bull. Seism. Soc. Am.*, **78**, 1133-1157.

Patton, H. J., 1991. Seismic moment estimation and the scaling of the explosion source, *Geophysical Monograph 65: Explosion Source Phenomenology*, editors: S. R. Taylor, H. J. Patton and P. G. Richards; AGU, Washington, D. C., 171-183.

Patton, H. J. and Zandt, G., 1991. Seismic moment tensors of Western U. S. earthquakes and implications for tectonic stress field, *J. Geophys. Res.*, **96**, 18,245-18,259.

Peppin, W. A. and McEvilly, T. V., 1974. Discrimination among small magnitude events on Nevada Test Site, *Geophys. J. R. astr. Soc.*, **37**, 227-243.

Pomeroy, W. P., Best, W. J., and McEvilly, T. V., 1982. Test Ban verification with regional data - A review, *Bull. Seism. Soc. Am.*, **72**, s89-s129.

Press, F. and Archambeau, C., 1962. Release of tectonic strain by underground nuclear explosions, *J. Geophys. Res.*, **67**, 337-343.

Priestly, K. and Brune, J., 1978. Surface waves and the structure of the Great Basin of Nevada and Western Utah. *J. Geophys. Res.*, **83**, 2265-2272.

Richards, P. G. and Zavales, J., 1990. Seismic discrimination of nuclear explosions, *Annu. Rev. Earth. Sci.*, **18**, 257-286.

Richter, C. F., 1935. An instrumental magnitude scale, *Bull. Seism. Soc. Am.*, **25**, 1-32.

Richter, C. F., 1958. *Elementary Seismology*, W.H. Freeman, San Francisco.

Romanowicz, B. A., 1982. Moment tensor inversion of long period Rayleigh waves: A new approach, *J. Geophys. Res.*, **87**, 5395-5407.

Russel, D. R. 1986. Mutli-channel processing of dispersed surface waves, *Ph.D. Dissertation*, Saint Louis University, St. Louis, MO.

Saikia, K. C., Kafka, A. L., Gnewuch, S. C., and McTigue, J. W., 1990. Shear velocity and intrinsic Q structure of the shallow crust in Southeastern New England from R_g wave dispersion, *J. Geophys. Res.*, **95**, 8527-8541.

Saikia, C. K. and Burdick, L. J., 1991. Fine structure of P_{nl} waves from explosions, *J. Geophys. Res.*, **96**, 14,383-14,401.

Saito, M., 1967. Excitation of free oscillations and surface waves by point sources in a vertically heterogeneous earth. *J. Geophys. Res.*, **72**, 3689-3699.

Savino, J. L., Sykes, L. R., Lieberman, R. C., and Mollnar, P., 1971. Excitation of seismic surface waves with periods of 15 to 70 seconds for earthquakes and underground explosions, *J. Geophys. Res.*, **76**, 8003-8020.

Schlittenhardt, J., 1988. Seismic yield estiamtion using teleseismic P- and PKP-waves recorded at the GRF-(Gräfenberg) array, *Geophys. J.*, **95**, 163-179.

Springer, D. L., 1966. P-wave coupling of underground explosions, *Bull. Seism. Soc. Am.*, **56**, 861-876.

Springer, D. L. and Kinnaman, R. L., 1971. Seismic source summary for U. S. underground nuclear explosions, 1961-1970, *Bull. Seism. Soc. Am.*, **61**, 1073-1098.

Stevens, J. L., 1986a. Estimation of scalar moments from explosion-generated surface waves, *Bull. Seism. Soc. Am.*, **76**, 123-151.

Stevens, J. L., 1986b. Reply to Z. Der's "Comments on the paper 'Estimation of scalar moments from explosion-generated surface waves,'" *Bull. Seism. Soc. Am.*, **76**, 1825-1829.

Stevens, J. L., 1991. Seismic source characteristics of cavity decoupled explosions in salt and tuff, *Bull. Seism. Soc. Am.*, **81**, 1272-1291.

Stump, B. W. and Johnson, L. R., 1984. Near-field source characteristics of contained nuclear explosions in tuff, *Bull. Seism. Soc. Am.*, **74**, 1-26.

Stump, B. W., 1985. Constraints on explosive sources with spall from near-source waveforms, *Bull. Seism. Soc. Am.*, **75**, 1312-1325.

Sykes, L. R. and Cifuentes I. L., 1984. Yields of Soviet underground nuclear explosions from seismic surface waves: Compliance with the Threshold Test Ban Treaty, *Proc. natl. Acad. Sci.*, U.S.A., 1922-1925.

Taylor, S. R. and Toksöz, M. N., 1982. Measurement of interstation phase and group velocities and Q using Wiener filtering, *Bull. Seism. Soc. Am.*, **72**, 73-91.

Taylor, S. R., 1983. Three-dimensional crust and upper mantle structure at the Nevada Test Site, *J. Geophys. Res.*, **88**, 2220-2232.

Taylor, S. R. and Patton, H. J., 1986. Shear-velocity structure from regionalized surface-wave dispersion, *Geophys. Res. Lett.*, **16**, 211-214.

Taylor, S. R. and Randall, G. E., 1989. The effects of spall on regional seismograms, *Geophys. Res. Lett.*, **16**, 211-221.

Thio, H. K. and Kanamori, H., 1991. A surface wave study on the structure of the crust and upper mantle under Southern California, (abstract) *Eos Trans AGU*, **72**, No. 44, 324.

Thio, H. K. and Kanamori, H., 1992. Moment tensor inversions in Southern California using surface waves recorded by TERRAscope, *Eos Trans AGU*, **73**, No. 43, 376.

Toksöz, M. N., Harkrider, D. G., and Ben-Menahem, A., 1965. Determination of source parameters by amplitude equalization of seismic surface waves, *J. Geophys. Res.*, 907-922.

Toksöz, M. N., Thomson, K. C., and Ahrens, T. J., 1972. Generation of seismic waves by explosions in prestressed media, *Bull. Seism. Soc. Am.*, **61**, 1589-1623.

Toksöz, M. N. and Kehrer, H. H., 1972. Tectonic strain release by underground nuclear explosions and its effect on sesimic discrimination, *Geophys. J. R. astr. Soc.*, **31**, 141-161.

U.S. Congress, 1988. *Seismic Verification of Nuclear Testing Treaties*, Office of Technology Assessment, OTA-ISC-361, U.S. Goverment Printing Office, Washington, D.C.

Vergino, E. S. and Mensing, R. W., 1989, Yield estimation using regional mb(Pn), *Lawrence Livermore National Laboratory* Report UCID-101600.

Viecelli, J. A., 1973. Spallation and the generation of surface waves by an underground nuclear explosion, *J. Geophys. Res.*, **78**, 2475-2487.

Vidal, A. and Munguia, L., 1991. Local magnitude and source parameters for earthquakes in the Peninsular Ranges of Baja California, Mexico, *Bull. Seism. Soc. Am.*, **81**, 2254-2267.

Von Seggern, D., 1977. Amplitude distance relation for 20-Second Rayleigh waves, *Bull. Seism. Soc. Am.*, **67**, 405-511.

Wallace, T. C., Helmberger, D. V., and Engen, G. R., 1983. Evidence of tectonic release from underground nuclear explosions in long-period P waves, *Bull. Seism. Soc. Am.*, **73**, 593-613.

Wallace, T. C., Helmberger, D. V., and Engen, G. R., 1985. Evidence of tectonic release from underground nuclear explosions in long-period S waves, *Bull. Seism. Soc. Am.*, **75**, 157-174.

Werth, G. C. and Herbst, R. F., 1963. Comparison of amplitudes of seismic waves from nuclear explosions in four mediums, *J. Geophys. Res.*, **68**, 1463-1475.

Woodhouse, J. H., 1974. Surface waves in a laterally varying layered structure. *Geophys. J. R. astr. Soc.*, **37**, 461-490.

Woods, B. B., 1993. Regional surface wave magnitude and moment determination methods applied to nuclear explosions at the Nevada Test Site: Implications for yield estimation and seismic discrimination, *PhD thesis*, California Institute of Technology.

Woods, B. B., Kedar, S., and Helmberger, D. V., 1993. M_L:M_0 as a regional seismic disriminant, *Bull. Seism. Soc. Am.*, **83**, 11677-1183.

Woods, B. B. and Harkrider, D. G., 1995. Determining surface wave magnitudes from regional NTS data, *Geophys. J. Int.*, **120**, 474-498.

Yacoub, N. K., 1983. "Instantaneous amplitudes": A new method to measure seismic magnitude, *Bull. Seism. Soc. Am.*, **73**, 1345-1355.

Yelin, T. S. and Patton, H. J., 1991. Seismotectonics of the Portland, Oregon region, *Bull. Seism. Soc. Am.*, **81**, 109-130.

Yomogida, K., 1985. Surface waves in a laterally slowly-varying media. *Geophys. J. R. astr. Soc.*, **82**, 511-533.

Zhao, L. S. and Harkrider, D. G., 1992. Wavefields from an off-center explosion in an imbedded solid sphere, *Bull. Seism. Soc. Am.*, **82**, 1927-1955.